Universidad del País Vasco Euskal Herriko Unibertsitatea

FACULTY OF ENGINEERING BILBAO
UNIVERSITY OF THE BASQUE COUNTRY

Université Polytechnique HAUTS-DE-FRANCE

PhD Thesis

CHARACTERIZATION OF THE CBN WHEEL WEAR AND MODELLING OF ITS INFLUENCE ON NGV GRINDING

Presented by

Dipl. Ing. Gorka Vidal Irusta

At the

Department of Mechanical Engineering of the
University of the Basque Country
and
University of Valenciennes

For obtaining the degree on

International PhD in Mechanical Engineering

Supervised by

Dr. Naiara Ortega
Prof. Dr. Mirentxu Dubar

November 2019

Nenikekamen!

Acknowledgements

Me gustaría mencionar y agradecer a todas las personas que me han ayudado durante la tesis y que en cierto modo han hecho posibles las siguientes doscientas y pico páginas:

A los alumnos internos del taller, de los cuales la primera ya es doctora: Leire, Jonatan, Gorka, Hodei, Asier, Marina, María, Oihane, Amaia y Marcos. He intentado no olvidarme de nadie, si lo he hecho, os pido disculpas y haced vuestro este agradecimiento. Vuestra ayuda ha sido parte imprescindible de este trabajo. Con vosotros he aprendido, trabajado y reído. ¡Muchas gracias a todos!

A mis compañeros del sótano de doctorandos. Gracias por los buenos momentos que hemos pasado y por hacer que los años de la tesis hayan sido menos duros e intentar afrontar cada miseria que tenemos los doctorandos con una sonrisa.

A mis anfitriones en la universidad Carlos III durante mis dos estancias de dos semanas cada una. En especial a José y Héctor. Me acogisteis como si fuera uno más y me enseñasteis todo lo que fui capaz de aprender en tan poco tiempo. Sin vuestra ayuda, seguiría sin ser capaz de hacer correr una simulación. Todo el mérito es vuestro. Para cualquier cosa, tenéis un contacto en Eibar.

Damien and Cedric. Thanks for your help. I really appreciate your efforts, time and patience during my several stays in France. It is not needed to say that without your help, this thesis would not be finished.

Juan! Eskerrik asko zure laguntzagatik. Gure telefono elkarrizketek diruditen baino gehiago lagundu egin didate. Milesker!

Mirentxu, thanks a lot for your help and mainly for your attention during my stays in Valenciennes. You have always tried to teach and help me not only in my work but in everything you could. Definitively your help has made my stays much easier. I feel that I am really lucky to have you as my supervisor in France. Thanks.

Naiara, un simple gracias puede parecer corto, pero no sé cómo resumir todo lo que tengo para decir sin tener que escribir otro capítulo más de la tesis. Siempre me has intentado ayudar y enseñar, aunque a veces me haya costado verlo y eso es algo que seguro que no te he agradecido lo suficiente. Además de todo eso, quedan los momentos al margen de la tesis, de los cuales espero no olvidarme nunca y que todavía quede alguno más. Muchas gracias por todo.

A la cuadrilla. Por esa gran habilidad de simplificarlo todo y hacer que la tesis deje de existir durante el tiempo que estoy con vosotros. Eskerrik asko!

A Ane. Por tener toda la paciencia y comprensión que una persona puede tener. Siempre confiando en que podía acabar la tesis y dejándome que pasara fines de semana en el camarote sin sentirse celosa de las palomas. Eskerrik asko guapísima.

A la familia, pero en especial a la Ama. Por todo en general. De pequeño, quizás por la imaginación que se tiene o porque no se es consciente de todo, pensaba que eras capaz de cualquier cosa. Con el tiempo, uno se hace mayor y se da cuenta de que realmente es así, has

hecho y haces posible que TODO funcione. Eres capaz de sacar tiempo y fuerzas de dónde sea para cualquier cosa que necesite sin hacer ruido ni esperar nada a cambio. Algo impagable que necesitaba mencionar en estas líneas. Eskerrik asko, Ama.

Por último, me gustaría acordarme de ti, tía. La mayoría de gente no tiene ni idea del esfuerzo y trabajo que hiciste durante tanto tiempo. Este último año y medio me ha tocado vivir una pequeña parte de eso, lo que ha hecho que mi admiración y respeto por ti sea mayor todavía. Esta tesis va a medias, un abrazo muy fuerte. Se te echa de menos.

Summary

This thesis is focused on improving a paramount grinding process used in the aeronautic industry. The process is one of the last manufacturing steps of the nozzle guide vanes, which form the stator of the exhaust of aeroengines. The enhanced physical properties of the materials which these components are made of, result in adverse conditions during the grinding process in terms of thermal and mechanical loads. Besides, the short cycle time needed for accomplishing the high productivity of this sector promotes the appearance of issues related with these loads, such as thermal damage and vibration marks.

That being said, the scrapping of the nozzle guide vanes at this late state of their manufacturing process involves significant economical loses because of the accumulated work carried out with expensive advanced technologies. The methodology of this thesis has been established in order to understand the influence of the affecting parameters and thus, improve the productivity while the good quality of the parts is ensured.

The wear suffered by the wheels is considered as one of the most influential aspects on the grinding performance. Therefore, at first, a topographic analysis of the grinding wheel surface was conducted on different moments of the grinding wheel life. In this way, the wear types and their evolution could be detected and measured from a brand-new wheel to a totally worn wheel.

Secondly, the process was studied in detail through experiments. Due to the complexity of the industrial process, a test bench was specially designed for reproducing the grinding conditions in a controlled manner. In order to enhance the consistency with the industrial process, the same superabrasive material and workpiece alloy were used. In addition, the value of the input parameter was calculated taking the industrial process as a reference. In this way, not only the input, but also the outputs could be controlled and measured. Thus, the forces and the surface quality were measured in order to understand the influence of the input parameters such as the grinding speed and contact depth.

Finally, the information gathered in the previous two steps was used for developing a numerical model based on the finite element method. The model reproduced the contact between a multigrain surface and the workpiece material. Both of them were defined with the physical properties of the materials used in the industrial process. In addition, the model addressed accurately the geometry of the grinding wheel since the real topography was imported into the model through a procedure specially developed for this study.

The results obtained from this study revealed that there was a coherency between the experiments and the model that can be explained through mechanical and thermal principles mentioned previously by other authors. Thus, the results obtained from this study allows to understand the influence of the input parameters on the process. On this basis, the methodology developed in this thesis present a useful scenario for the study of grinding processes by means of experiments and numerical models that comprises some aspects that have not being comprised previously in bibliography.

CONTENT

INDEX OF FIGURES

INDEX OF TABLES

STATE OF THE ART

1 STATE OF THE ART

1.1 INTRODUCTION

This chapter gathers the state of the art of the most relevant research works related to the subject of this thesis.

First of all, an introduction of general concepts of grinding processes is carried out. In this section, the background knowledge needed for understanding the topics that are going to be addressed in the following chapters is summarized. The works mentioned in the first section, 1.2, are those related with the case study of this research work in terms of grinding technology, grinding wheel or workpiece material.

In the next section, 1.3, the most relevant methodologies and publications in the field of grinding wheel characterization are introduced and commented. The characterization method depends on the feature to be evaluated and on the grinding wheel type, hence, the research works related with EP CBN wheels are analyzed more carefully. The particular case of study of this work comprises a combination of EP CBN wheels, nickel base superalloy as workpiece material and CFG conditions, therefore, works that addressed similar works are discussed in detail.

Following to this, in section 1.4, a review of the state of the art of experimental tests benches is done. This section is focused on different research works where a specific setup or test bench have been used. The input and output variables together with the setup are analyzed with the purpose of evaluating their suitability with this work and having some references in case any special development must be done.

Finally, the most relevant numerical simulations carried out in the field of grinding are gathered in the last section of this chapter, 1.5. There, the different methods used for simulating grinding processes during the years are explained and the main research works are discussed. The scope of each method and the possibilities concerning the input and output variables are analyzed in order to find the most appropriate for the scope of the current work.

1.2 GRINDING BASICS

In this section basic information on grinding processes is summarized with the aim of facilitating the understanding of the reader on the topics discussed all along the manuscript. That being said, this section does not gather an extensive state of the art of the various topics explained. Instead, some publications are mentioned where the explained concepts can be better understood.

1.2.1 Grinding process

1.2.1.1 Grinding wheels

The vast majority of grinding wheels are formed by three elements. The abrasive grains can be considered the most representative one. So much so, that grinding wheels are usually

differentiated in accordance with the material of the abrasive grains. They can be made of materials such as alumina, silicon carbide (SiC), CBN or diamond, whilst the application of the wheel will depend strongly on the abrasive material. The abrasive grains are the unique element of the wheel expected to be in contact with the workpiece during the grinding process. Any other situation is a result of an incorrect grinding. Therefore, they are considered responsible for the material removal.

The abrasive grains must be significantly harder than the workpiece material for being able to remove material without suffering an extreme wear. This aspect is related with the material of the grains. However, for a given abrasive grain material, there are other characteristics that can be used to distinguish them. The friability (related with the microstructure of the grain), the size and the shape are also paramount features to take into account when a wheel must be designed for a specific process [1],[2].

Regarding the abrasive materials mentioned before, they can be distinguished in conventional and superabrasive materials. From the softest to the hardest, they can be arranged as Alumina, SiC, CBN and Diamond, the first two are considered conventional abrasives while the last two superabrasive materials. Although SiC and diamond are the hardest in each group, it should be mentioned that their use is often limited by their chemical affinity with some workpiece materials [3],[4]. Apart from this, the grains of each material can be manufactured with different microstructure and shapes, which affects the friability of the grain itself and eventually to the grain performance [5],[6].

The second element is the bonding material. This is the responsible of keeping the grains joined. They can be made of different materials, the most commonly used in industry are vitreous, resinoid, galvanic and metallic bonds. The bonding material dictates some properties of the grinding wheel; hence, the selection of the bonding material must depend on the application of the wheel. However, not only the bonding material but also their composition and quantity affect the wheel performance. Although this element is the responsible of keeping the grains joined, it is also the responsible of releasing the grains when it is needed. In this way, if the bonding material is chosen correctly for a specific grinding process, the grains will be released when they are no longer able to removed material in good conditions. In this way, they leave space for new grains revealed from beneath. If the bonding material is too hard, the grains will be kept in the grinding wheel surface even after they are too worn for removing material, what may lead to workpiece damages or accuracy errors. By contrast, if it is too soft, the grains will be released too easily, when they are still capable of removing material, which accelerates the wheel wear and reduces the wheel life[1],[5],[7].

That being said, only specific abrasive grains can be used together with each bonding material. Vitreous material is the most used bonding material and can be used with any of the four abrasive grains mentioned before. Resinoid bonding can also be used with any abrasive material although it is not very common to be used with CBN. Finally, galvanic and metallic bonding materials are exclusively used with superabrasive materials because they provide a higher retention force [8]. The superabrasive materials are significantly harder but also notably more expensive, therefore, normally harder bonding materials than in conventional abrasive are used. Moreover, superabrasive wheels only have abrasive grains and bonding material on one or few layers on the periphery of the grinding wheel, while conventional abrasive wheels are usually completely made of the mixture of abrasive grains and bonding material.

Finally, the last element of the grinding wheels is the porosity. This element can be defined as void spaces in the bonding material. The porosity of a grinding wheel can be achieved naturally by the manufacturing process or can be induced artificially by different techniques. The pores are responsible for several helpful phenomena. They provide free space for storing the chips generated during the process, specially during the cutting length, where the chip cannot be evacuated. In addition, thanks to the pores, the cutting fluid can be taken more easily to the contact zone, which helps to keep the temperatures within safe values, to reduce the friction between the abrasive grains and the workpiece and to reduce the risk of having workpiece material stuck to the wheel surface. However, the presence of pores depends on the bonding material. For instance, galvanic and metallic bonded wheels do not have pores as a part of their structure, although some experimental works have been done for creating pores in metal bonded grinding wheels [9],[10].

Regarding the particular case of EP CBN grinding wheels, they are formed by a solid body and a single layer of abrasive grains and bonding material. On the one hand, the solid body can be made of aluminum, steel or even carbon fiber, each one has its own weak and strong points. On the other hand, the grains are stuck to the body by a nickel layer that is plated by a galvanization process. The nickel junction between the grains and the body is only mechanical, no chemical reactions take place during the plating process. In this way, the grains are covered up to the half of their size. Two particularities make this type of wheel different to the conventional wheels. At first, due to the manufacturing process and their structure, they have no pores. Secondly, they cannot be dressed since they have a single abrasive layer, the dressing process is introduced in section 1.2.3.

The reason why this grinding wheels are used for the grinding process of aeronautic parts such as NGV comes from the complexity of the process. For grinding the numerous surfaces of an NGV, up to 80 different grinding wheels must be used in a single grinding machine. Therefore, the size of the grinding wheels is a key point in terms of machine capacity and productivity. The lower the wheel size is, the more wheels can be loaded in the tool charger and the less time is needed for changing the wheel. In addition, several operations require a specific grinding wheel geometry and a specific trajectory of the wheel during the grinding operation. If dressable wheels are used, the size and shape of the wheel will change after subsequent dressings. Hence, non-dressable wheels are more appropriate for this process. Finally, conventional abrasive on a single layer wheel for grinding such complicated aeronautic materials would lead to a short wheel life and thus, to an unproductive process. Taking this aspect into account, diamond would be the most appropriate abrasive material. However, diamond abrasive grains cannot bear grinding temperatures above 500 ^{o}C because they become graphite and their mechanical properties drop drastically [4]. This demanding grinding process involves extremely high temperatures, as it is demonstrated by the thermal damage seen in some ground parts, Fig. 1. Hence, CBN is the most suitable abrasive material for this process.

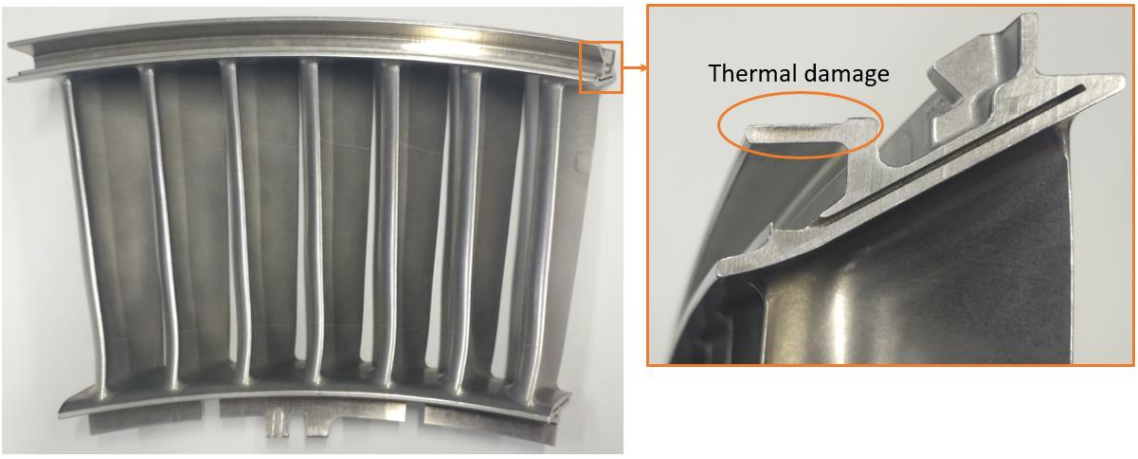

Fig. 1 On the left there is a Nozzle Guide Vane. On the right there is a detail of a face of the NGV where thermal damage is marked in orange.

Taking everything into account, EP CBN grinding wheels are the most appropriate option for this process. However, the progressive wear suffered in these wheels as a consequence of being a non-dressable wheel, leads to some problems that this work aims to understand and solve.

1.2.1.2 Material removal in grinding

The main particularity of grinding lies in the way in which the chip is created. For addressing this topic, what takes place at the contact zone must be analyzed.

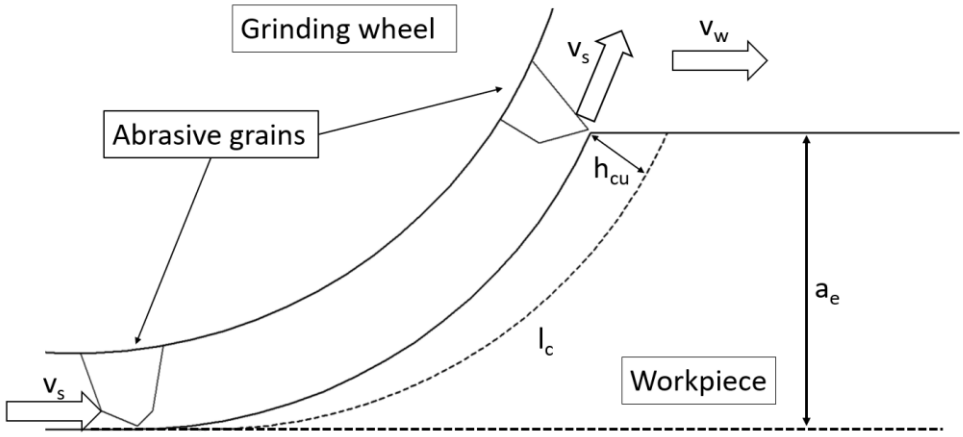

Fig. 2 A depiction of the contact zone during a grinding operation.

Fig. 2 shows a depiction of the contact zone during a plane grinding operation. The continuous path represents the shape created by the exiting grain while the discontinuous arc represents the path to be travelled by the next abrasive grain. Therefore, the gap between the continuous and discontinuous arcs contains the material that is going to interact with the next abrasive grain. The length of the arc is called contact length, l_c, and is calculated through Eq. (1), where d_e is the diameter of the grinding wheel and a_e is the cutting depth.

$$l_c = d_e \cdot a_e \tag{1}$$

The thickness of the gap increases from the tangent point to the end of the contact length, the maximum value of the thickness is marked in the drawing as h_{cu}. This is called undeformed chip thickness and can be calculated with Eq. (2), where v_s is the wheel peripheral speed, v_w is the feed speed, C is the active grain density and r is the ratio of width to thickness of the chip.

$$h_{cu} = \sqrt{\frac{1}{C \cdot r} \cdot \frac{v_w}{v_s} \sqrt{\frac{a_e}{d_e}}} \tag{2}$$

The chip thickness determines the reaction of the material. In this way, three different phases are differentiated along the contact length in every grinding operation. These phases are known as cutting mechanisms and are explained in the following lines.

- Rubbing. This mechanism covers the very first zone right after the tangent point, i.e. the lowest thickness values. In this phase, the contact depth is not enough for the grain to penetrate the material. It is considered that only elastic deformations take place as a result of the interaction grain-workpiece. In consequence, there is only a friction phenomenon (rubbing) between both surfaces. The energy spent in this mechanism does not contribute to the chip formation, instead, it is considered to be converted exclusively into heat [11].
- Plowing. This mechanism occurs when the contact depth is deep enough for the grain to penetrate the material. The penetration starts when the normal stress at the contact interface exceeds the resistance of the material. As the grain advances in the contact length, the material is plastically deformed (plowing) by the interaction with the grain. Although no chip is formed in this mechanism, the plastic deformation is needed for the material removal since one part of that will later become chip. Therefore, the energy consumed in this process does not contribute directly to the chip formation. Instead, it is mainly transformed in heat through plastic deformation and friction [11].
- Cutting. This mechanism occurs when the shear stress on the deformed material results in the failure of the material (cutting) and hence, the creation of the chip [12]. However, during the plowing, the material flowed also to the sides of the grain path. This, material is not removed during the cutting mechanism and remains as part of the workpiece until subsequent grains reach the contact zone. The chip thickness when the failure material starts is called critical chip thickness [13]–[15]. In terms of efficiency, the cutting mechanism is the one where the energy consumption results actually in chip generation. Therefore, the objective of many research work has been to maximize the influence of the cutting mechanism in the overall energy consumed during the contact [1],[9],[10],[14],[16]–[21].

The combined effect of the three cutting mechanisms is evaluated by a single parameter called specific grinding energy, e_c. This parameter is defined as the energy required for removing a mm^3 of workpiece material.

The dependence of the material response on the chip thickness is called size effect [14],[16],[18],[21]. From Eq. (2) it can be deduced that there are several process parameters that affects the chip thickness. Furthermore, additional parameter as workpiece material properties or the type of cutting fluid [22],[23] have also influence on the grinding process performance. However, the ideas explained in this section are sufficient to understand the issues addressed in the following sections.

1.2.1.3 Material removal in Creep Feed Grinding

CFG improves the productivity by means of increasing significantly the cutting depth in comparison of conventional grinding processes. The increase in the cutting depth reduces the number of passes of the grinding process and can even permit to remove the milling operation from the manufacturing sequence. See indicative values of process parameters for conventional grinding and CFG in Table 1.

Table 1 Indicative values for process parameters of conventional grinding and CFG.

	Conventional grinding	*Creep feed grinding*
Depth of cut [mm]	0.001-0.05	0.5-30
Feed speed [mm/s]	100-500	0.1-40
Cutting speed [m/s]	20-60	30-120

However, in CFG, feed and cutting speed must be adapted with the purpose of maintaining the h_{cu} in the same range. As a result, the e_c increases because the fraction of the cutting length where the chip is thinner than the critical chip thickness increases. Hence, the contribution of plowing and rubbing mechanisms to overall energy consumption increases in comparison with conventional grinding. Although h_{cu} is maintained, l_c is increased because of the modification of a_e. As a consequence, not only plowing and rubbing mechanisms cover more fraction of the contact length, but also the contact length itself is longer. These two factors lead to an increase in temperatures in the contact zone [24]. Thermal damage is one of the main problems that grinding can cause on a workpiece, however, CFG reduces the risk of thermal damage even though having higher grinding temperature than conventional grinding [25],[26]. This phenomenon occurs because the hottest point in the contact length is moved away from the ground surface to a further position [27], see Fig. 3.

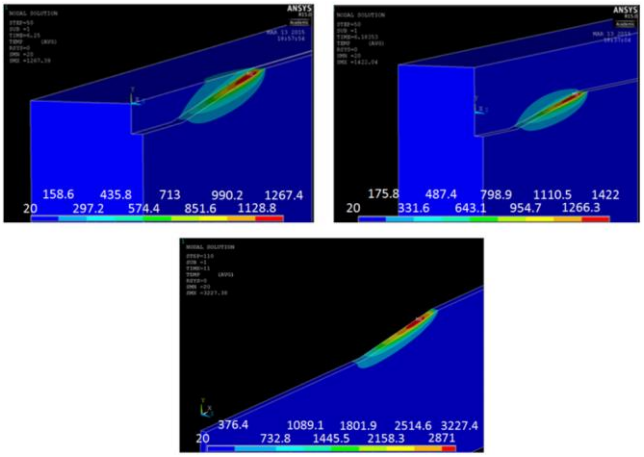

Fig. 3 The location of the hot spot during a creep feed grinding operation [27].

In this way, it is more likely that only the material to become chip is thermally affected. Nevertheless, the cutting fluid is a key factor for avoiding the thermal damage, it must be supplied at a pressure high enough for matching the peripheral speed of the wheel [28]. A brief review of the state of the art of the research work on CFG is carried out in following lines with the purpose of addressing the advantages of this technology.

Zhang et al. [29] carried out an interesting study about CFG back in 1995. In that study, the performance of CBN and alumina vitrified wheels was compared in grinding metallic materials and the performance of vitrified diamond wheel was evaluated grinding different types of ceramic materials.

The performance was evaluated in terms of grinding forces, specific energy and workpiece roughness from where coherent conclusions were drawn. The CBN grinding wheel presented a lower specific energy than alumina for the same R_a roughness values achieved on the workpiece. In addition, finer roughness was obtained with CBN wheel. The workpiece material attached to the wheel during the grinding process was also observed due to its influence on the process. Less attached material was found in the CBN vitrified wheel than in the alumina wheel, which may explain the lower specific energy. However, it should be mentioned that the CBN wheel had a special configuration with radial slots from where cutting fluid was supplied directly to the contact zone, what can be considered as a proof of the importance of the cooling in CFG. Apart from this aspect, the grain size and porosity between both wheels were also different, hence, a comparison in similar conditions could not be carried out.

Uhlmann and Spur [30] studied the influence of ultrasonic vibration (USV) assistance in CFG by means of single-grit tests, these tests are introduced in section 1.4. The USV was produced by a special sonotrode, the frequency was 22 kHz and the amplitude of the wave was 4 µm. The tests were carried out with a single diamond grain on polished ceramic samples.

Through the analysis of the scratches created, they determined that USV assistance provided a ductile fracture of the workpiece. This is specially important in the grinding process of brittle fracture materials such as ceramics. In addition, USV assisted grinding led to discontinuous contact unlike conventional grinding, this resulted in lower contact length but deeper penetration of the grain. In consequence, the thermal loads were reduced and the mechanical

loads increased. These two conclusions together with some more were summarized by the authors in Fig. 4.

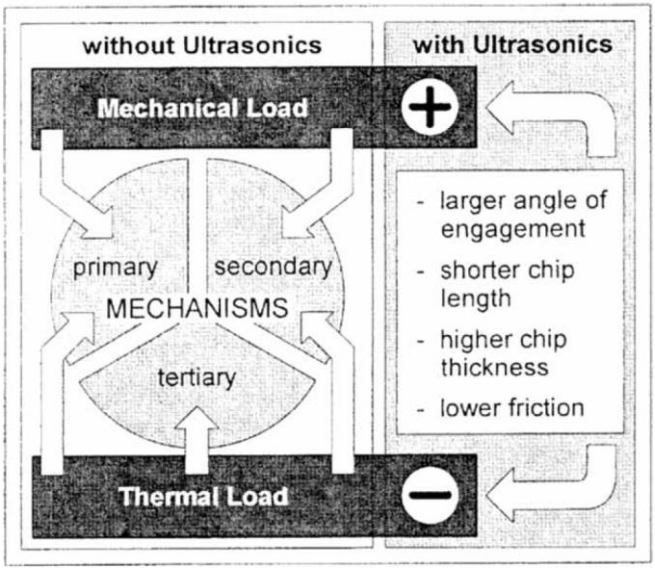

Fig. 4 The conclusión drawn by Ulhmann and Spur regarding the ultrasonic assistance in CFG [30].

However, the cutting speed used for the tests was in the range of 5 to 35 m/s, which is significantly lower than the cutting speed used for CFG. This aspect together with the use of a single abrasive grit, arises the need for further understanding of the USV assistance for CFG.

Ichida et al. [6] studied the performance of polycrystalline CBN grains with respect to monocrystalline CBN grains in CFG of nickel-based superalloys. As explained previously, often in this application the grinding wheel must carry out grinding operations with specific forms. This situation makes the CFG process even more demanding because the access of the cutting fluid to the contact zone is more difficult, the temperatures are higher and the working load on all the width of the grinding wheel is unequal. Ichida et al. addressed this case study in their work by the grinding tests shown in Fig. 5.

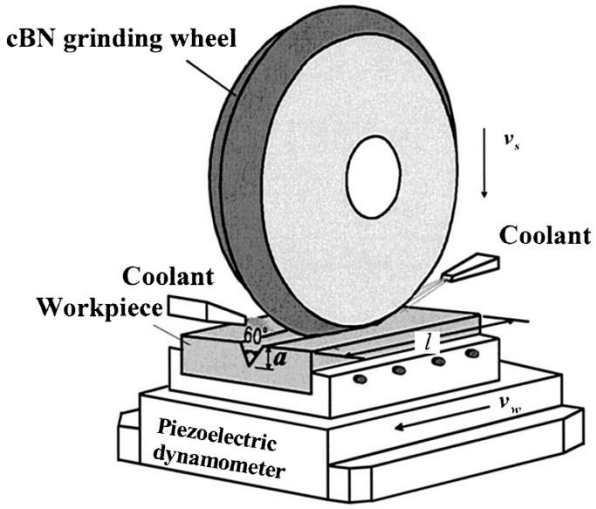

Fig. 5 CFG tests carried out by Ichida et al. [6].

The V-shape grinding operation allowed to evaluated the wear of both types of CBN grains in terms of wheel profile retention. In addition to this, the forces and specific energy where compared and analyzed. The results revealed that the new polycrystalline CBN grains presented a better performance in terms of the profile retention, volumetric wear and energetic efficiency.

Upadhyaya and Fiecoat [31] carried out a similar experimental research work. In this case, they studied the influence of the toughness of the grains and the grain protrusion height in CFG process of stainless steel.

Five different CBN grains where compared in the first study. From that comparison, it was concluded that the toughest grains showed less radial wear of the wheel and less power consumption while no appreciable influence could be seen on the roughness on the workpiece.

The second study was carried out with two different CBN grains, namely the one of the toughest and the softest. Those grains were covered up to three percentages, namely 35%, 50% and 65%. The best results were achieved by the toughest grain with the thinnest bond layer.

Therefore, it was concluded that if the right grain toughness is chosen, the CFG process improves with a higher grain protrusion height. Moreover, the wheel with the thinnest bond layer presented a higher amount of dislodged grains, i.e. pull-out, but lower radial wear than thicker bonded wheels. This phenomenon reveals the fact that a high gain concentration may be a detrimental factor while the grain protrusion height should be maximized for a more efficient CFG process.

Nevertheless, authors did not provide information about the grain concentration and the differences between de CBN grain types. An additional test for evaluating the right grain concentration would have been of great interest for CFG applications.

As it can be deduced, the influence of the grinding wheels in CFG has been extensively studied. Mohamed et al. [32] published a research work focused on the same topic, but using alumina wheels. More exactly, they studied the influence on the process of grooved wheels with different parameters, see Fig. 6.

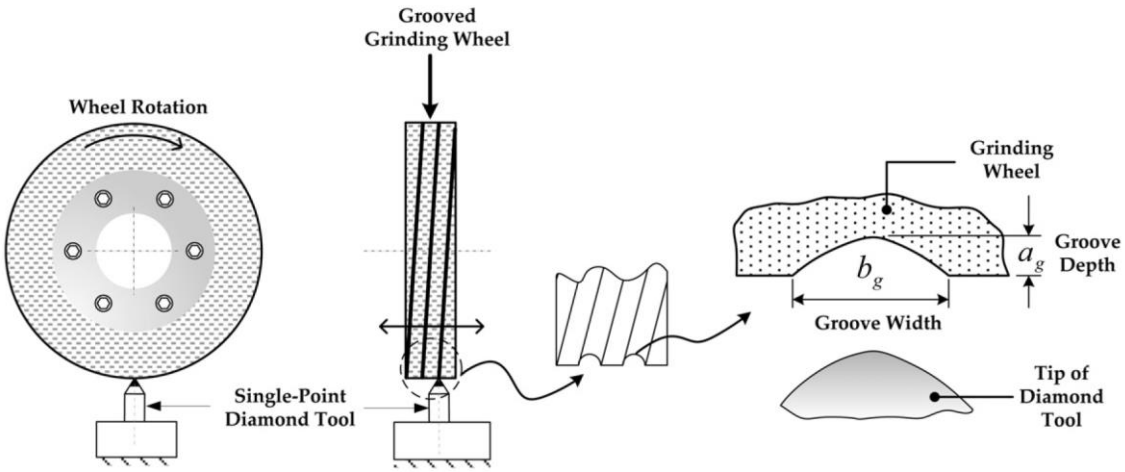

Fig. 6 Groove pattern created on alumina wheels by Mohamed et al. [32].

They tried three combination of groove width and helix angle and also a normally dressed wheel. The performance was evaluated in terms of forces, power and energy consumption for a wide range of cutting depths.

The best efficiency was achieved with the wheels that had the maximum percentage of the surface covered by the helix. Among those wheels, the thinner groove width led to better results. In addition, the roughness of the workpiece was not hindered by the grooved wheels.

As in the previous work, the efficiency of the CFG improves as the number of grains on the wheel surface decreases. This phenomenon indicates that in CFG it is convenient to reduce the grain density with the purpose of enhancing the distance between the grain. In this way, the uncut chip thickness is enlarged and the space for the cutting fluid and chip storage is improved.

D. Bhaduri et al. published two subsequent works, [33],[34], based on USV assisted CFG process. However, unlike Uhlmann et al. [30], they carried out experimental tests with grinding wheels. The setup was formed by an alumina wheel, an Inconel 718 workpiece, the equipment necessary for inducing USV and a force piezoelectric sensor, see the whole setup in Fig. 7. The vibrations were induced in a direction parallel to the feed speed.

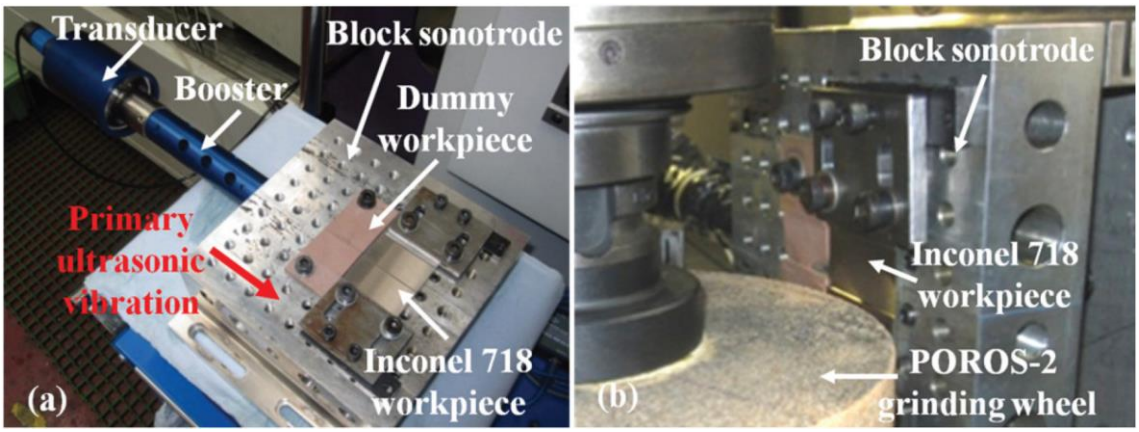

Fig. 7 The setup used by Bhaduri et al. for studying the ultrasonic assisted CFG [12].

In the first study they analyzed the influence of the cutting speed and the feed speed on the CFG process with and without USV. The USV was induced with a frequency of 20 kHz and an amplitude of 4 µm. The tests were analyzed in terms of normal and tangential forces, workpiece roughness and wheel radial wear and surface roughness after the tests.

In general terms, the forces were lower, the roughness was finer and the wheel radial wear was lower when the workpiece was ground with USV. This was caused by the increase in the contacting abrasive grains in the contact length and by the higher overlapping between the grains. Despite the finer mean roughness with USV, the peaks on the workpiece surface were higher, which indicated that there was more plastically deformed material.

Regarding the state of the grinding wheel after the process, the roughness of the wheel was studied through grinding graphite blocks and the peaks density through resin replicas. In general terms, the roughness of the wheel surface was finer and the density of the grains was higher.

These results explain the results of workpiece roughness while the reduction of the force must be attributed to the beneficial effect of the USV.

In the second work, the amplitude of the USV was modified with the aim of understanding its influence and hence, finding the best combination. Thus, they tried 7.8, 2.4 µm and 0 µm (no USV) at different cutting depth, namely 0.1, 0.5 and 1 mm. The evaluation methods were the same, i.e. forces, roughness and the state of the wheel surface.

Authors concluded that the increase in the vibration amplitude led to lower forces, but created a rougher workpiece surface. This was consistent with the observations of the wheel surface, where the higher amplitude led to more void spaces on the wheel and thus, to lower forces and higher roughness.

Following with conclusions of the previous work about the void spaces on the wheel surface, Zhenzhen et al. [9] studied the influence of alumina bubbles on the Cu-Sn-Ti alloy bonded CBN grinding wheels used in CFG applications. The study was divided in two parts. On the one hand, the resistance of the bonding was studied with the help of a mechanical numerical model. The maximum stress under a *P* load for different pore size was calculated. The larger the pore size, the higher the stress created by the *P* load. However, it did not vary in a linear progression, instead, it was quite stable until 0.7 mm, from that size on, the maximum stress increased drastically. Therefore, a pore size of 0.5 was chosen for avoiding a weak behavior of the bond while having a significant pore size. Once selected the pore size for the next analysis, the influence of the distribution of the pores was studied in terms of bending strength, see Fig. 8. They found out that an arranged pattern had a better performance.

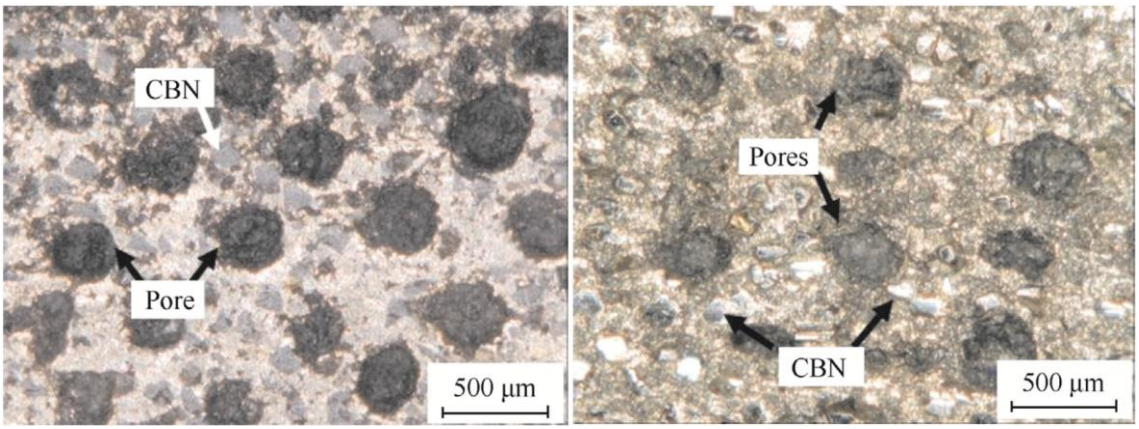

Fig. 8 Two porosity patterns compared by Zhenzhen et al. [9].

On the other hand, the performance of the wheel with the selected pore size and pattern was compared with a vitrified CBN wheel's. The forces were registered using a piezoelectric sensor and the temperatures with semi-artificial thermocouples.

As expected, the forces and the specific energy were higher with the vitrified wheel. In addition, the temperature was nearly a 25% lower with the metallic wheel due to the better access of the cutting fluid to the contact zone and to the better thermal conductivity of the Cu-Sn-Ti alloy. Finally, the workpiece presented a homogeneous surface when ground with the metallic wheel

while some flaws where on the workpiece ground with the vitrified wheel. This phenomenon was caused by workpiece material adhered to the vitrified grinding wheel surface.

One of the last innovative research works carried out about CFG was developed by Paknejad et al. [35]. In this work, authors studied the influence of USV in CFG in dry conditions. Under this configuration, authors wanted to study the influence of USV on the temperature of the process. According to authors, the optimum method for measuring the temperature is a thermographic camera. Unlike thermocouples and laser pyrometer, it can provide data exactly from the needed point and do not suffers any delay in the acquisition. However, for a clear access to the desired zone, the grinding process must be carried out in dry conditions, otherwise, the cutting fluid would make it impossible.

The grinding tests were carried out with an alumina wheel on stainless steel. The USV was applied in two directions and the effect on the temperature was analyzed as a function of the cutting depth, feed speed and cutting speed.

The increase in the cutting depth led to an increase in the temperature, nevertheless, for a given cutting depth, the temperature was lower if USV was used. Similarly, when the feed rate increased, the temperature increased as well, but for a given feed speed, the use of USV resulted in lower temperature. Finally, although cutting speed did not have a significant influence on the temperature in dry CFG, USV led to a lower temperature for a given cutting speed.

The highest temperature registered in that work was slightly above 600 ^{o}C, what makes possible to use a dry CFG process for that material. However, the cutting temperature is significantly higher in productive CFG processes of nickel-based alloys, thus, the use of cutting fluid is completely necessary.

As a summary, the importance of CFG has been demonstrated by the numerous research works carried out with the aim of improving it. It is a productive process widely used in demanding sectors such as aeronautics and automotive where not only the productivity must be achieved, but also demanding quality standards are required.

One of the aspects of the previously mentioned works to be improved is the cutting speed, since it was hardly in the range of the speed of actual CFG process. The present works aims to continue the efforts of understanding and improving this particular process by means of understanding the phenomena that take place in the contact zone at cutting conditions as close as possible to the real CFG process of nickel-based alloys.

1.2.2 Wear types and mechanisms

Although the wear suffered by the grinding wheels can be overcome in most cases by dressing, the wear has been a case of study in numerous research works [6],[7],[36]–[52]. Here, it must be differentiated between the wear mechanisms and wear types. The former determine the causes through the wheel gets worn while the latest determine the result of those causes.

1.2.2.1 Wear mechanisms

The main wear mechanisms can be divided in three groups according to the classification done by Marinescu et al. [8].

Abrasive wheel wear takes place as a consequence of the interaction itself. In a grinding process there are two bodies in contact with a relative velocity between them. The fact of having a contact between two surface entails a normal force. If the friction coefficient is higher than zero, a tangential force results from the normal force and the relative movement. The tangential force creates elastic and plastic deformation that eventually may lead to the failure of one or both bodies. The physical properties of the bodies will determinate which one suffers the most material loss. In grinding, the abrasive material must be chosen with the purpose of being the workpiece the weakest of the bodies in contact.

The second wear mechanism is the adhesive wheel wear. The adhesive wear refers to a mechanical adhesion between the loss particles of one body to the other body. This adhesion is so strong that the adhered material remains attached during the subsequent interactions. Consequently, the contact conditions of the subsequent interactions are modified. In grinding processes, this wear mechanisms normally takes place when grinding metallic materials. The high temperatures in the contact zone may cause the melting of the workpiece material during the process of chip formation. If these molten chips are not evacuated by the cutting fluid, they can get adhered to the wheel.

The last wear mechanism is the tribochemical wear. This wear occurs after a chemical reaction between the different elements that form the both bodies. In consequence, particles of one of the bodies joins the other body. However, unlike the previous wear mechanism, the attachment is chemical rather than mechanical. Therefore, the composition of the existing material changes where this mechanism takes place. This mechanism occurs when there is a chemical affinity between wheel and workpiece material although it can be facilitated by high temperatures.

1.2.2.2 Wear types

As explained, the wear types are the results of the previous wear mechanisms. In this section, the wear types detected in EP CBN grinding wheels are introduced. The works cited in the following lines are discussed later in section 1.3.

The CBN grains can be fractured as a consequence of the forces and crashes during grinding process. Usually, the fractures are differentiated in microfractures and fractures as a function of the magnitude. The effect of this wear type on the material removal process is considered as beneficial because new sharp edges are created on the fractured grains. However, this wear type must take place in a controlled way, otherwise, the wheel working life will be shorter than expected [6],[43],[44],[47],[50],[53]. See an example in Fig. 9

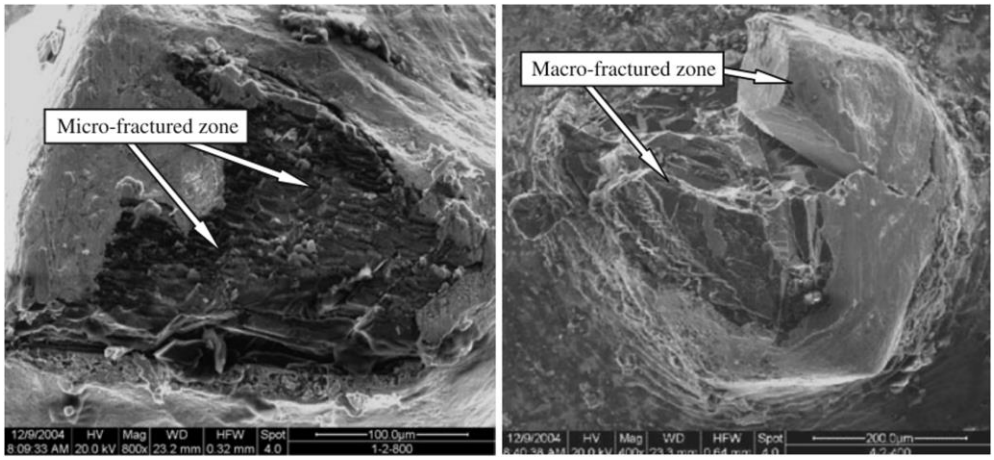

Fig. 9 Micro and macrofractures detected by Ding et al. [43].

When the forces of the grinding process exceed the retaining force that the bonding material has over the grains, the grains are dislodged from the wheel. This phenomenon is called grain pull-out. In multilayer grinding wheels, this wear type can be beneficial and necessary for the process since new sharp grains are revealed from lower layers. However, in single layer grinding wheels such as EP wheels, this wear type must not take place since there are no grains in lower layers for replacing the lost grains. Usually, the EP CBN wheels have enough grains for bearing a certain level of grain pull-out, but an excessive loss may lead to a catastrophic failure of the wheel. High temperatures may affect the resistance of the bonding material and facilitate the appearance of this wear type [44],[47],[51],[53]. See an example in Fig. 10.

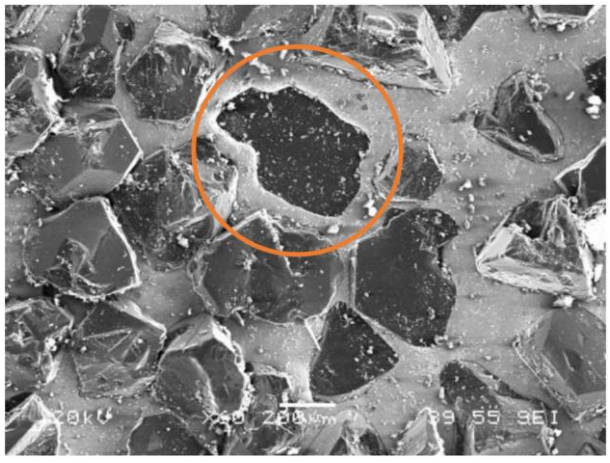

Fig. 10 A CBN grain pull-out in an EP wheel detected by Yu et al. [51]

By contrast, when the grinding forces are low, the load on the grains are too low for the grain pull-out and for fracture. Then, the grains become duller and duller instead of being fractured or pulled-out. Eventually, the grain tip becomes in a flat surface, this is called wear flat. The effect of this wear on the process is detrimental in terms of mechanical and thermal loads. Firstly, the normal force needed for reaching the stress required for penetrating the material increases. Secondly, the friction between the grain and the workpiece is larger because of the larger contact surface of the grain. Thirdly, the temperature on the contact zone is higher as a consequence of the higher friction. Finally, the roughness achieved in the workpiece surface

tends to be lower with the presence of wear flat [38],[43]–[45],[47],[53]. See an example in Fig. 11.

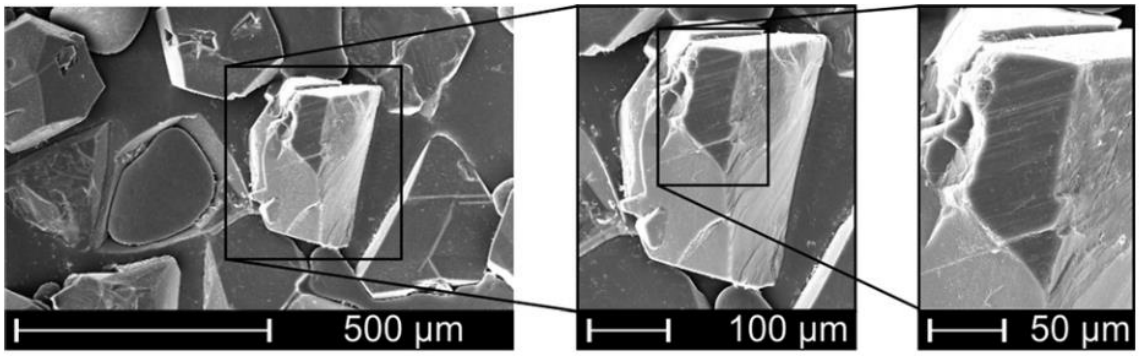

Fig. 11 A wear flat found by Puerto et al. on an EP CBN grinding wheel [45]

The last wear type found in EP CBN grinding wheels is the adhesion phenomenon, also called wheel loading. These wheels are prone to suffer this wear type due to the lack of pores and the little void space between the grains. In addition, the high temperatures of the CFG of nickel-based alloys and the ductility of these materials present an appropriate scenario for the appearance of this wear type. Taking everything into account, if the grinding parameters and cutting fluid delivery are not correct, wheel loading is likely to appear. The adhered material can fill the void space between the grains or can even cover the abrasive grains. The first situation reduces the space for the cutting fluid and chip while the second results in a contact metal-metal. In both cases the temperature of the contact zone rises and may cause a regenerative effect [43],[45]. See an example in Fig. 12.

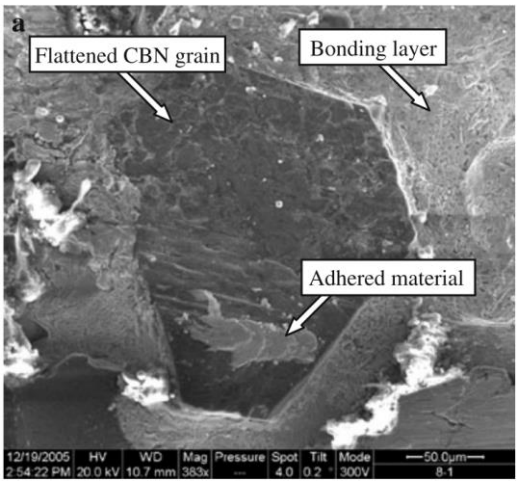

Fig. 12 Adhered material found by Ding et al. on a CBN grain on an EP grin wheel [43].

From a global point of view, the effect of the wear types can be summarized in a loss of the profile of the grinding wheel, a loss of the roundness of the grinding wheel and a loss of the cutting ability. However, in the particular case of single layer EP CBN grinding wheels, only the effect of the loss of the cutting ability must be considered.

1.2.3 Truing, dressing and conditioning

There are three processes used for modifying the grinding wheel surface by removing material from it, each one has its own objective. Truing is carried out for removing geometrical errors in the wheel periphery. This process must be conducted on every wheel right after being mounted in the machine with the purpose of removing the radial runout and irregularities that may appear when the wheel is put in rotation.

Dressing is a similar operation in terms of tools and kinematics, but the objective is different. The main target of dressing is to modify the cutting capacity of the grinding wheel. It is commonly used for recovering the cutting ability of the wheel that has been lost due to the wear. Through this process, new sharp edges are created on the grinding wheel either by fracturing old grains or by removing worn grains and revealing new grains from lower layers. However, this process is not suitable for single layer grinding wheels such as EP CBN because there are not grains in lower layers for substituting the removed grains. Therefore, the single layer grinding wheels are considered as non-dressable.

The main handicap of these wheels is that the wear increases progressively during their working life and, consequently, also their performance. With the purpose of mitigating the adverse effect of this aspect, several conditioning processes have been developed and studied. A conditioning process is carried out for modifying superficially either the existing grains or the bonding material with the purpose of adapting the wheel performance to the needs of the process.

The latest and most relevant research works about conditioning of EP CBN wheels are summarized in the following lines.

As mentioned before, a conditioning process can be focused on modifying the grains or the bonding material. The physical properties of both materials, CBN and nickel respectively, are completely different. Hence, specific methods have been developed for each case. Those methods are gathered and explained in the work published by [54]. These methods can be divided roughly in three groups as follows.

1.2.3.1 Mechanical conditioning

This method can be carried out with static or rotary tools and can be coupled with USV. The tools used are similar to the tools used for conventional dressing operations.

Ghosh and Chattopadhyay released two consecutive works [55],[56] based on mechanical conditioning of single layer CBN wheels. The conditioning was focused on minimizing the runout of the wheel and sharpen the grains. In this method, homemade diamond blocks were used with a shallow depth of cut, in the range of microns, in order to touch only the grain tips. In the first work [55], they studied the influence of conditioning three brazed CBN wheels, each one with a different grain distribution pattern, see Fig. 13. The performance of the wheels was evaluated by the surface finishing of the steel workpiece and by the grinding forces. The dressing tool was intentionally formed by dull diamonds brazed on a flat block.

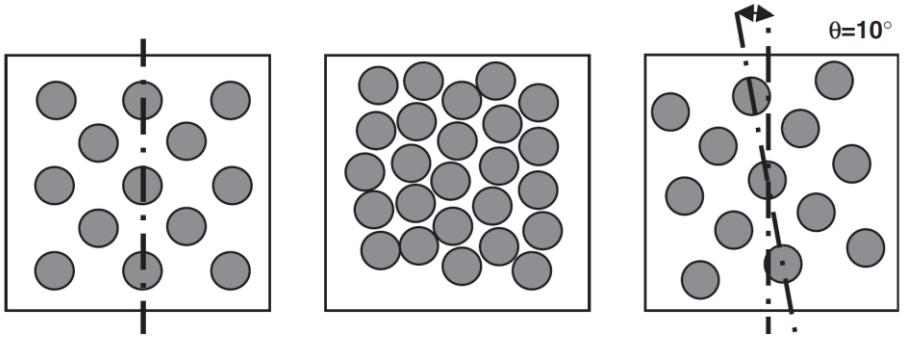

Fig. 13 3 grain distribution patterns conditioned by Ghosh and Chattopadhyay [55].

They tested the performance of the three different patterns after subsequent conditioning passes of 2 µm. At first, during the first conditioning passes, the roughness depended strongly on the initial pattern of the wheel. However, when the cumulative conditioning depth got close to 20 µm, the roughness achieved by the three patterns was in the range of 1 to 1.5 µm Ra. This was caused by the leveling of the grain protrusion grain, thus, they concluded that this aspect has more influence than the grain concentration and pattern. However, regarding the forces, they noticed that despite the conditioning, the more space between the grains, the lower grinding forces were needed for the process.

Later they performed [56] the same study for different grain sizes, see Fig. 14, with similar results. Similar surface roughness was achieved either with coarse and fine grains while the grinding performance was still better with coarser grains thanks to the separation of the grains.

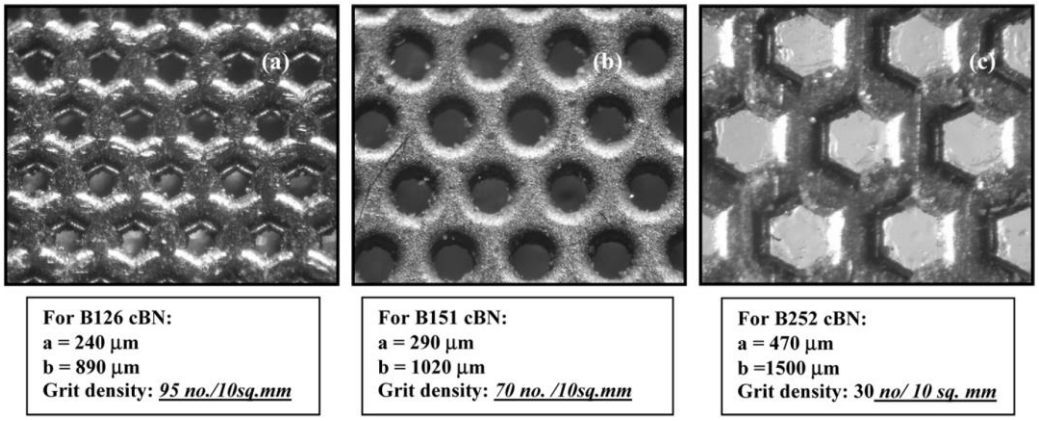

Fig. 14 3 grain sizes conditioned by Ghosh and Chattopadhyay [56].

Through these works, authors were able to modify the performance of CBN single layer wheels with the aim of reducing the roughness. However, the significant increase in the forces, reveal that the efficiency of the process drops with the reduction of the roughness. This is an important aspect if this methodology is wanted to introduce in the industry. In addition, they worked with brazed wheels, which have a grain protrusion height larger than EP wheels because of a different bonding process.

Ding et al. [10] used mechanical conditioning as part of their experimental work for evaluating the performance of metal bonded CBN wheels. They included alumina bubbles in the bonding

material with the purpose of improving the performance of metallic wheels thanks to the porosity.

However, before being used for grinding, authors conditioned the wheel with two objectives. On the one hand they wanted to remove the excess of bonding material. On the other, they wanted to break the alumina bubbles to create the porosity. Later, during the grinding process, the alumina bubbles were supposed to be broken at the first contact with the workpiece. A zirconia corundum wheel was used for that purpose, see Fig. 15.

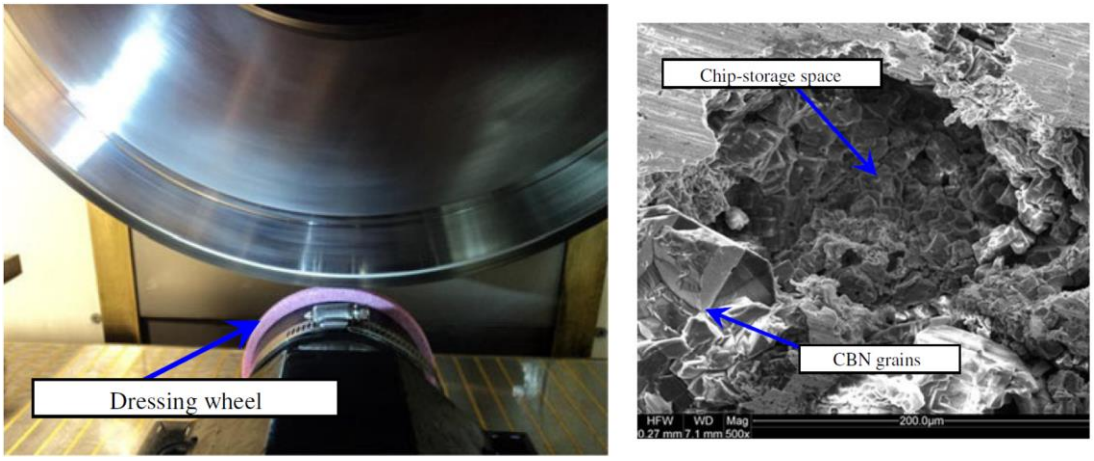

Fig. 15 On the left, the setup used by Deng et al. [10] for conditioning the metal bonded CBN wheel. On the right, a picture of the surface of the grinding wheel after being conditioned.

The bonding material was softer than the zirconia corundum, hence, the bonding material was removed easily. The forces during the conditioning were high enough for breaking the alumina bubbles but not too high for removing the CBN grains form the wheel surface. Despite the interesting results, the influence of the conditioning process on the CBN grains was not studied. It is evident that CBN is significantly harder than zirconia corundum, but this aspect should have been addressed for a complete study.

Finally, although the CBN wheel analyzed in this study had several layers of abrasive grains, no grain pull-out was detected after the conditioning process. The nickel layer also provides a good retention force; therefore, this conditioning process may be suitable for EP CBN grinding wheels.

Kitzig et al. [57] applied USV on a single diamond dresser for conditioning EP grinding wheels. This method had been widely used for dressing vitrified and resin bonded grinding wheels but not for monolayer grinding wheels. The vibration was transmitted to the dresser in radial direction of the grinding wheel. The rotation of the wheel during the conditioning was 0.5 m/s with the purpose of having a hammering effect instead of a conventional dressing effect. The amplitude of the vibration was in the range of 2 to 10 µm.

The objective of the experimental work was to reduce the roughness achievable with a coarse EP diamond wheel by means of conditioning. Through subsequent conditionings, the difference in height of the grains was reduced and thus, the resulting roughness of the tungsten carbide workpiece reduced as well to the half. However, as expected, the grinding forces increased more than 100%.

From this review, it has been noted that mechanical conditioning can be carried out either for improving the cutting ability of the wheel or for improving other aspects as the roughness.

1.2.3.2 Laser conditioning

Laser touch conditioning (LTC) is widely used for dressing multilayer grinding wheels and it was introduced to monolayer wheels by Dold et al. [58] who used a picosecond laser source for conditioning electroplated diamond wheels. Thus, they compared LTC with mechanical conditioning of electroplated diamond wheels used for dressing SiC grinding wheel. While a mechanical conditioning can hardly be controlled, the LTC allowed to create a defined pattern on the diamond wheel surface, see Fig. 16.

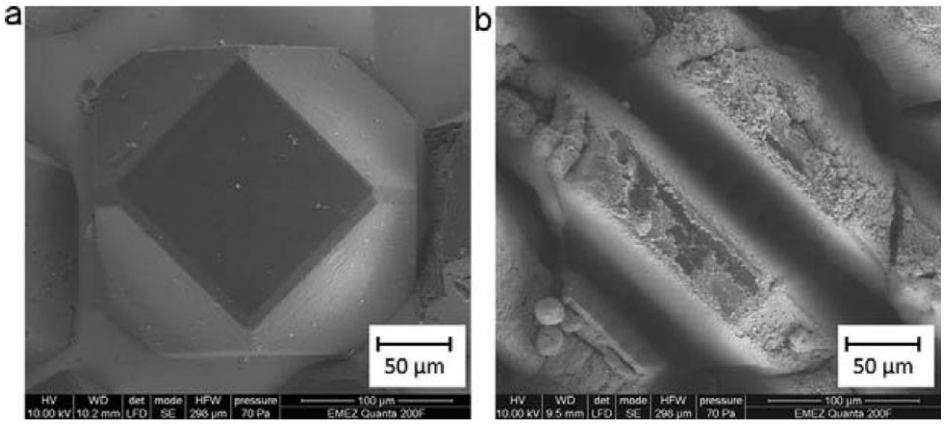

Fig. 16 a) A diamond grain before the conditioning process. b) The surface of the after LTD, [58].

The SiC wheel dressing process was evaluated in terms of normal and tangential forces. Besides, the diamond wheel topography was measured before and after being conditioned and also after the dressing process. Regarding the forces, the laser conditioned wheel presented significantly lower forces, which was considered as a better performance. However, the result of the dressing process on the SiC wheel was not analyzed.

Regarding the diamond wheel topography, mechanical conditioning left a smoother surface than LTC, what explains the higher forces. However, the roughness on the diamond wheel surface after dressing the SiC wheel was comparable in both cases. These results indicate that there is a difference between both methods, but after a certain work load, the roughness of the diamond wheel surface may tend to the same value. This aspect must be studied further.

Apart from this, authors concluded that the LTC was conducted without remarkable graphitization of the diamond grains.

Later, Deng et al. published two research works based on LTC of bronze diamond wheels, [59],[60]. The first work was a first approach to the application of this conditioning method to bronze diamond wheels. Unlike the previous work, the laser was used in two directions with respect to the grinding wheel. On the one hand it was applied tangentially for profiling the wheel surface. On the other hand, it was applied radially for sharpening the grains, the two configurations are shown in Fig. 17.

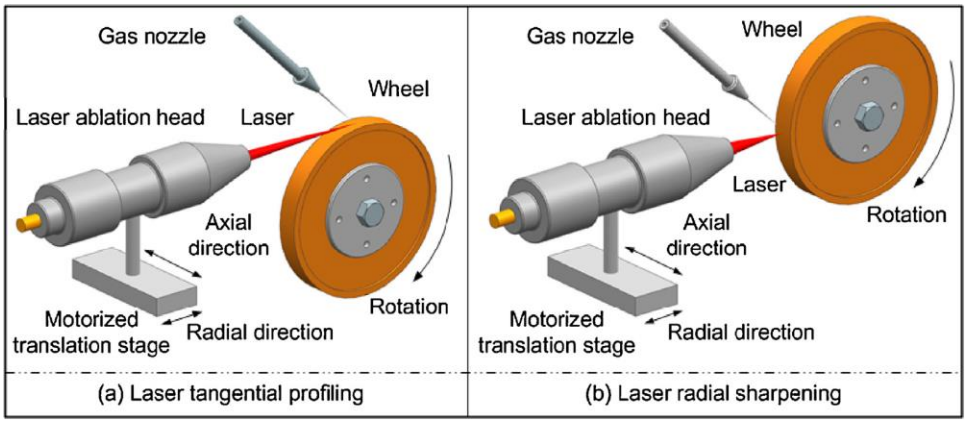

Fig. 17 The two LTC applications investigated by Deng et al. [58].

Different parameters and trajectories were tried in each process with the purpose of finding the most appropriate combination. In his works, authors did not evaluate the performance of the grinding wheel, only observed the effect on the wheel surface of the different combinations.

Through the numerous trials carried out in that work, authors were able to find most influential laser parameters, namely the laser power density, the spot overlap ratio, the laser scanning track line overlap ratio and the number of laser scanning cycles. Regarding the tangential profiling, they found the parameters for enhancing the roundness of the grinding wheel. Finally, concerning the sharpening, they found the parameters for maximizing the sharpness of the wheel surface.

In the second work, [59], Deng et al. analyzed the performance of the LTC bronze diamond wheel by means of grinding experiments. At first, they adjusted again the conditioning parameters. In this work, they payed special attention to maximizing the grain protrusion height without weakening excessively the junction between the grains and the bond. A high grain protrusion height enhances the grinding process. However, if too much bonding material is removed from the base of the grain, the retention force drops and the risk of pull-out increases.

Once this part of the work was conducted, they carried out grinding tests on alumina samples with the laser conditioned wheel and with a mechanically conditioned wheel. The forces acquired for different cutting depths indicated that LTC created a sharper wheel than mechanical conditioning.

Pfaff et al. [61] carried out a similar study with EP CBN wheels. They compared the LTC with conventional conditioning. Through observations of the grinding wheels surface, they were able to differentiate the effect of LTC and conventional conditioning on the grains. LTC created flat surfaces on the top of the grains with an average clearance angle of 4.3°. However, conventional conditioning created aleatory grain geometries due to the crashes between the conditioning tool and the CBN grains. A picture of grains conditioned by both methods is shown in Fig. 18.

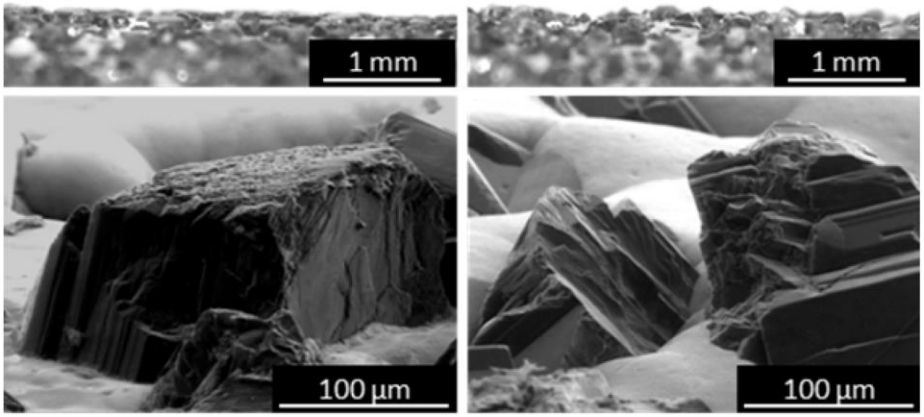

Fig. 18 On the left a CBN grain conditioned by LTC. On the right a CBN conditioned by conventional conditioning system by Pfaff et al. [61].

After conditioning they used those wheels for grinding hardened steel. Similar to other authors, the used the forces and the resulting roughness on the sample for evaluating the process. As it could be expected form the observed grain geometry, the forces obtained with the LTC were higher, while the roughness was lower. In addition, authors mentioned that the grains conditioned by LTC were likely to have more endurance because they had more bearing area. Nevertheless, this aspect was not studied by further experimental works.

LTC can be used for conditioning either the grains and the bond. It is more precise than mechanical conditioning, since defined patterns can be easily created on the wheel surface.

1.2.3.3 Electrochemical conditioning

The methods included in this group are more complex to use in an industrial process because of the special conditions required.

Zhao and Guo [62] combined this method with two different mechanical conditioning methods for achieving an appropriate wheel surface for superfinishing optical glasses. They designed a complex conditioning process for enhancing the performance of EP diamond wheels in this application. That process had three phases. At first, the wheel was conditioned by a diamond wheel. The objective of this phase was to reduce the runout of the wheel and to equalize the grain protrusion height. In this way, they could ensure that they were not going to surpass the critical cutting depth for causing a brittle fracture of the optical glasses. However, at the end of this phase, the diamonds were at the same height as the nickel bonding layer. In the second phase, an electrolytic in-process conditioning method was used for removing the nickel between the grains. In this way, a certain grain protrusion height was achieved while the low runout values were maintained. Finally, the wheel was conditioned by an alumina stick with the purpose of removing the oxide created by the electrolytic conditioning. The surface state through the whole process is shown in Fig. 19.

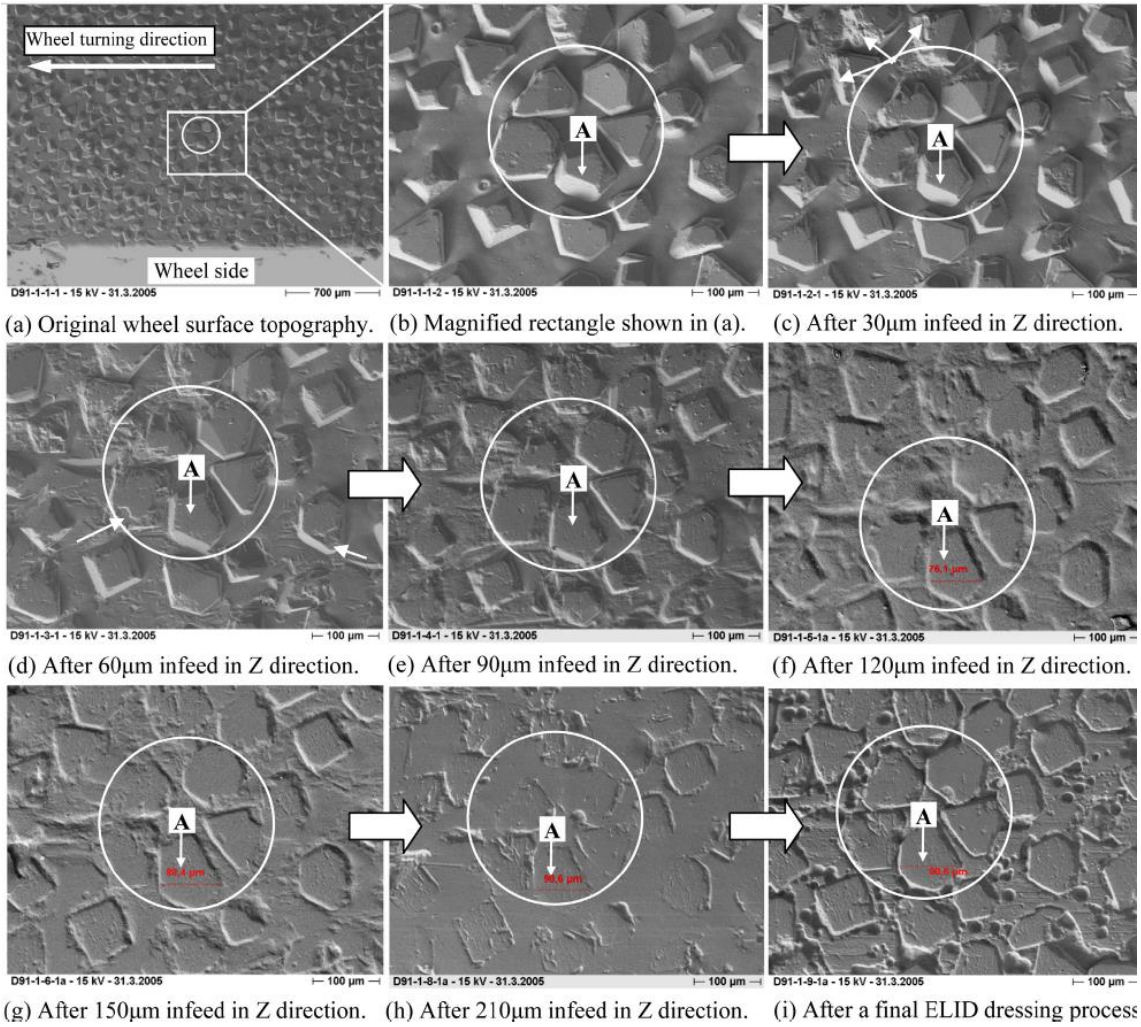

Fig. 19 The EP diamond wheel surface through the conditioning process designed by Zhao and Guo [62].

It should be noted that in the works cited previously, the mechanical, LTC, and non-contact methods were used for different purposes such as equalizing the grain protrusion height while keeping a rough surface on the grains, flattening the grains for a better finishing, and cleaning the bonding layer.

1.3 GRINDING WHEEL CHARACTERIZATION

The wear of the EP CBN wheels has been acknowledged as the major reason of the recurrent problems in the CFG process of the NGVs. However, it is needed to detect and measure the wear evolution on the wheels surface, with the purpose of understanding the true origin.

The wear of the grinding wheels has been the case study of several authors and consequently, different methods have been developed for the extensive variety of grinding wheels and wear types. In this section, different methods for characterizing the wheel surface are gathered.

The measurement of the wheel surface has been performed for different purposes, namely the effect of the dressing [5,6], the achievement of the number of active grains [3,7] and the

assessment of the wheel wear, among others. This section presents a review of the work focused on the measurement of wheel wear and wheel topography characterization.

They can be divided in online and offline methods. Online wheel wear measurement is not always possible because the working zone inside a grinding machine could be a hostile environment and the tools required for the measurement often need specific and delicate conditions. In these situations, offline methods should be used.

Brinskmeier and Werner [40] developed a system based on the triangulation of a laser beam which was able to obtain 2D roughness parameters of a corundum grinding wheel surface. Nonetheless, this system, as any optical system, was very sensitive to external factors such as grinding fluid and chips. In addition, the reflectivity of the bond and the grains is very different, therefore this method should be calibrated for each wheel geometry and the oil rests on the wheel surface should be also removed.

Furutani et al. [37] used a pressure sensor to record the hydrodynamic pressure generated by a nozzle between a vitrified alumina wheel and a plate installed for this purpose. The plate had a hole to allow the fluid to reach the sensor. The variations on the pressure indicated the radial wear of the wheel while the variation on the frequency was related to the dulling and loading of the wheel. This method was used at a first time to optimize the dressing of the wheel in an external grinding machine and later [49] to compensate the grinding depth with the same grinding wheel in a surface grinding machine with favorable results. However, this method needs to have an appropriate adjustment between the sensor and the wheel surface. Therefore, it is not suitable for the current case study, although it appears an interesting method for an online monitoring of the sharpness of the grains. As mentioned previously, the CFG process of an NGV needs up to 80 different wheels for roughing and finishing operations of the numerous faces to be ground. There is almost a specific grinding wheel geometry for each of those faces, where the width, the profile and the shape vary. In consequence, this online method cannot be used for the current study.

Other authors, Sutowski et al. [46] and Liao et al. [36] among others, used Acoustic Emissions (AE) to detect online the dull state of the wheel. The former calibrated their method for a vitrified alumina wheel comparing AE measurement with the variation of a parameter called ratio of cutting ability K_{AFGW}, see Eq. (3)

$$K_{AFGW} = \frac{w_i * a_{zsr} * l_w}{l_s * B_{kr}} \tag{3}$$

Where w_i is the mean amount of abrasive grain vertex, a_{zsr} is the elementary cutting depth per one abrasive grain, l_w is the mean distance between abrasive grain vertices, l_s is the mean abraded length of abrasive grain vertex profile and B_{kr} is the active grinding wheel length.

The later used a minimum distance classifier for alumina and silicon nitride wheels as a weak learner boosted with two different algorithms (AdaBoost and A-Boost) in order to enhance the results. In spite their satisfactory results, these methods did not provide a real sight of the wheel state. Thus, in case of an incorrect performance of the wheel, the reason will remain unknown.

Regarding the offline methods, they provide a further knowledge of what actually is occurring on the wheel. However, these methods require to extract the wheel from the grinding machine, which affects negatively the productivity. In 1996 Blunt and Ebdon [65] were pioneers on the 3D wheel surface measurement with a 3D stylus-based measuring system. A stylus with a 2µm tip radius was used for measuring two different grain sizes of vitrified alumina wheels. This measuring technique was unable to measure the lowest zone of the wheel surface because of physical interference of the stylus with the upper part of the grains. This error was called convolution error. Hence, they focused the study on the characterization of the cutting edges.

Prior to digitalize the wheel surface, they established a criterion for calculating the optimum spacing between each acquired point by the stylus, also called optimum sample size. In this way, they were able to optimize the digitalization with the minimum necessary number of acquired points. This criterion was calculated through Eq. (4), where d_g is the diameter of the grain and ss_{opt} the optimum sample size.

$$3 \leq \frac{d_g}{ss_{opt}} \leq 4 \tag{4}$$

Later, in 2002, Butler et al. [66] used the same system to assess dressing operation on aluminum oxide wheels. They used the optimum sample spacing expression and set three 3D roughness parameters needed for the wheel characterization, namely S_{ds}, S_{sc} and S_q. S_{ds} is the summit density, where a measured point can be considered as a summit if it is surrounded by 8 lower points. S_{sc} is the summit curvature and it is calculated with Eq. (5) and S_q is the root mean square roughness, calculated through Eq. (6).

$$S_{SC} = \frac{1}{N} \iint_{Summit-Area} \left(\frac{\partial^2 z(x,y)}{\partial x^2} \right) + \left(\frac{\partial^2 z(x,y)}{\partial y^2} \right) dxdy \tag{5}$$

$$S_q = \sqrt{\frac{1}{A} \iint_A z^2(x,y) dxdy}. \tag{6}$$

In 2006, Shi and Malkin [44] characterized electroplated CBN grinding wheels by means of three measuring devices.

SEM was used for obtaining the grain density by counting the grains. Optical microscopy was used for addressing the state of the grains, with this method, the wear flat area was measured and the pulled-out grains were counted. Finally, a stylus profilometer was used for measuring the radial wear of the wheel. For this purpose, one part of the wheel width was not used during the grinding trials. Then, the whole width was used for grinding a sample where print of both zones of the wheel could be measured for calculating the radial wear.

Advances in optical devices and software complements have allowed many recent studies in this area. Darafon et al. [67], Cui et al. [68] and Ye et al. [69] used different optical system to digitalize the wheel surface or grain morphology. The first one used white-light axial chromatic depth technique to digitalize a typical vitrified aluminum oxide grinding wheel. They used a hole filling operation to fill the non-measured point and compared the measurements with a SEM and

Nanovea PS50 profiler with similar results. They converted the 3D digitalization into binary images in order to count the active cutting edges with a questionable criterion. They wanted to count cutting edges but due to the nature of the wheel and depending on the threshold depth, they only could detect amalgamations of grains and bonding material.

In the second work, authors used white light interferometry for differentiating the grains and the bond on a resin bonded diamond grinding wheel. At first, they scanned the surface in a range of height. After that, the analyzed the light intensity of each acquired point. Through this analysis they were able to distinguish the bond from the diamond as a function of the light intensity. Then, coupling this information with the height at where the data was acquired, the shape of the grain could be created. This process was not proved with the wheel loading phenomenon detected by Ding et al [43] in Fig. 12, where there is workpiece material adhered to the grain surface. In addition, authors only proposed a methodology for digitalizing the surface of the wheel, no analysis was carried out on the digitalized surfaces.

The last of the three works mentioned previously, realized a 3D motif analysis on vitrified alumina wheels to identify the most significant features of a wheel surface, namely peaks, saddle and pits. The authors used a 6-point criterion to identify each of them. They used this criterion because 4-point criterion and the most used 8-point criterion did not satisfy Euler criterion, Eq. (7). They evaluate each point and classified in one of the three previous features.

$$Euler\ criterion: \#peaks - \#saddles + \#pits = 2 \tag{7}$$

They regarded the same problem that the previous authors did, i.e., the number of peaks is not the number of cutting grains since more than one peak could be found in one grain. They applied Wolf's pruning method to avoid this problem. Once this method was calibrated, they set as the most significant ISO 25178 roughness parameter the density of peaks, S_{pd}, the mean hill area, S_{ha}, and the mean hill volume, S_{hv}.

However, the authors only proposed these parameters for the characterization of their grinding wheel. They did not use them for a wheel wear measurement, and therefore their suitability for the purpose of this study should be verified.

Taking everything into account, the offline methods provide more information of the state of the grinding wheel surface. During the study, the productivity of the process is affected because the wheels must be taken out from the machine to the measuring devices. However, the complete understanding of the wear phenomena allows to detect the wear types and their effect in the grinding process. Consequently, any incorrect performance of the grinding process occurred later can be linked with the corresponding wear without the need of measuring again the wheel. In this way, corrective actions can be taken more efficiently.

Among the offline methods introduced in the previous lines, the optical methods are the most versatile. They allow to have information from the highest to the deepest point of the wheels surface. The information obtained with the optical devices must be analyzed with powerful analysis software in order to detect and quantify the wear. Fortunately, this point should not be an issue thanks to the numerous commercial software designed for this kind of analysis.

These conclusions, matches with the methods used in the research works cited in section 1.2.2.2, hence, optical measuring devices are considered for the wear analysis explained in chapter 2. In addition, the suitability of standardized roughness parameters according to ISO 25178 is going to be analyzed as other authors did, [66],[69]. In this way, the parameters used for quantifying the wear are univocally defined and can be applied to other grinding wheel specifications.

1.4 EXPERIMENTAL APPROACHES IN GRINDING

Machining industrial processes are commonly replicated by means of laboratory tests when they are being studied. In doing so, on the one hand, the authors of the research work have more control over the input variables. On the other hand, more output parameters can be obtained from the process since the test bench has previously been designed for being more accessible for the measuring devices. In addition, the specific and costly equipment used in the industry for productive applications are substituted by more economical options. For this purpose, the scope of the research work must be defined and the test bench configuration must be accordingly selected. In this way, the industrial processes are commonly simplified in terms of trajectories or tool and workpiece geometry.

Grinding is also studied by means of experimental test carried out in laboratories. However, in comparison with other machining processes, the material removal occurs at a significantly smaller scale. This particularity has led the authors to develop very specific laboratory test as a function of the case study. In consequence, some experimental works are carried out through grinding operations and some others through specific tests where the kinematics and the tools are different from a grinding process, but the results can be extrapolated to real processes.

The current study is focused on how the evolution of the wear affects the material removal. This means that the interface between the grinding wheel and the workpiece must be studied in detail. Grinding tests, if they are correctly controlled, allow to study the process form a macro point of view, however, this is insufficient considering for the previously mentioned focus. Thus, with the aim of maximizing the information from the contact zone, specific tests must be carried out using nickel based aeronautic material as the workpiece and EP CBN wheel surface as the abrasive.

A review of the experimental tests carried out in the field of grinding is gathered in the following lines. The focus of each study is analyzed with the purpose of finding the most suitable tests configuration for the current study.

Thus, laboratory tests are revealed as more appropriate for this case study. Among the research works based on laboratory tests, the vast majority carried out single grit tests, although other test configurations were also used with remarkable results.

One of these setup was developed by Bifano et al [70] back in 1991. This test bench was called PEGASUS (Precision Engineering Grinding Aparatus for Super-finishing Ultrahard Surfaces) and was developed for studying the ductile regime grinding in brittle materials, the setup is shown in Fig. 20.

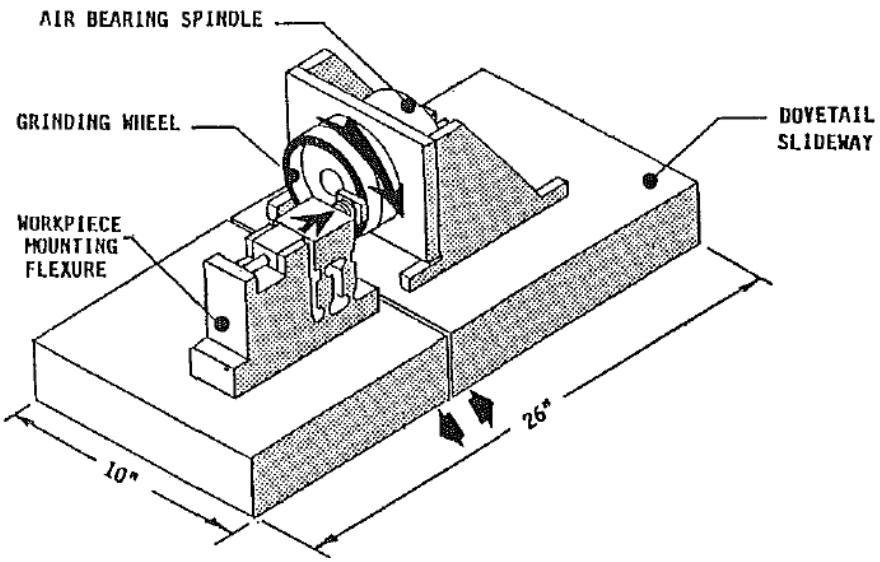

Fig. 20 PEGASUS test bench developed by Bifano et al. [70]

Grinding in ductile regime is achieved by diminishing extremely the cutting depth, up to the range of nanometers under the assumption that the energy required for plastic yielding is lower than the energy required for crack propagation. This process is also called microgrinding. In this way, the material flows instead of being removed like polishing and lapping processes. However, grinding provides more flexibility in terms of workpiece geometry than the rest of superfinishing processes. Given the small cutting depths, PEGASUS simplified the microgrinding process with the purpose of enhancing the precision. Only movement in two directions were allowed in the test bench, namely rotational speed of the wheel and infeed movement to the workpiece.

Through this method, they analyzed the behavior of several ceramic materials under the effect of a diamond wheel at different infeed rates. They analyzed the obtained surfaces by means of a scanning electron microscope (SEM) and managed to develop a mathematical expression for calculating the critical cutting depth that indicated the transition from brittle to ductile behavior as a function of the material properties. However, the PEGASUS test bench was designed for microgrinding conditions

Zhang et al. [71] developed a test bench for validating a force prediction model as part of a more complete model that comprised the grinding operation and the machine stiffness. The setup was mounted inside a 5-axis grinding machine, it can be seen in Fig. 21.

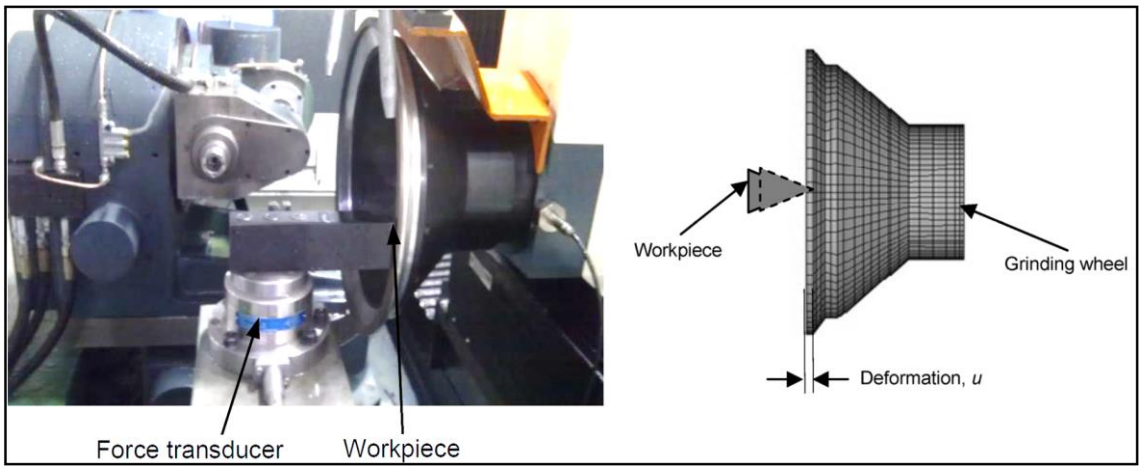

Fig. 21 Test bench used by Zhang et al. [71] *for validating a force prediction model.*

The setup was formed by a piezoelectric force sensor, an indexable cemented carbide workpiece and a diamond cup wheel. Grinding tests were conducted under different parameter combinations. During those tests, the normal force was measured and later it was compared with the force predicted by their model. Although a special test bench was used in this work, no particular attention was put on the contact zone between grains and workpiece.

Despite the fact that valuable information was taken from the laboratory tests mentioned before, the contact zone cannot be evaluated in detail as it is required in this work. For that purpose, the grinding process must be simplified further such as single grit tests do.

Single grit test is a configuration commonly used for reproducing the contact of grinding processes. There, a single grit is used for creating a grove on the workpiece material, which allows to have a more detailed view of the contact zone.

Numerous works based on single-grit tests have been released in the field of grinding. Kita et al. [72] presented one of the first research works based on this configuration using a specifically developed test bench, see Fig. 22.

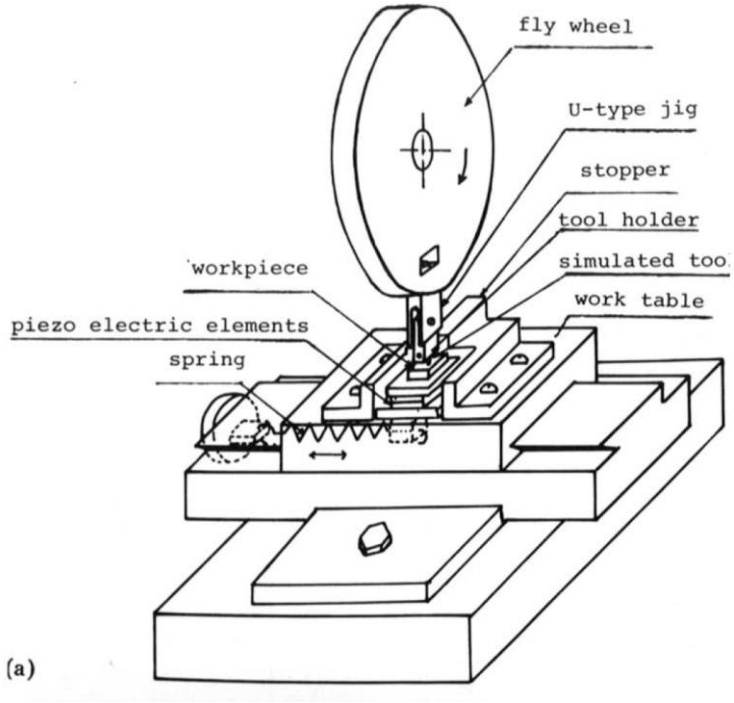

Fig. 22 Test bench developed by Kita et al. [72].

In this device an abrasive grain was attached to a rotating disk, this is called fly wheel, and the sample was mounted on a special support. This support had a stopper that released the sample during the contact with the grain. This technique is called quick stop and allows to have a view of the chip formation during the contact, see Fig. 23. Finally, a piezoelectric force sensor was located below the support of the sample.

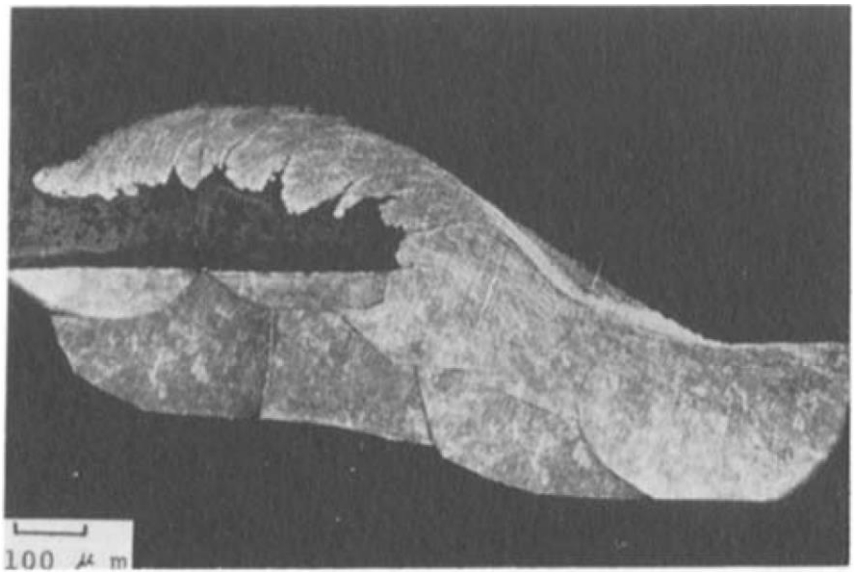

Fig. 23 A picture of the chip generation in a quick stop test carried by Kita et al. [72].

In this work, authors studied the influence of the apex angle on the chip generation in terms of the angle at which the chip flows, the tangential force and the normal force.

The work commented in the previous lines was released in 1978. Afterwards, several single-grit works have been published. In this section, the latest single-grit works are analyzed.

Wang et al. developed a pendulum-like device for single grit scratch tests, see the device and the attached measuring systems in Fig. 24.

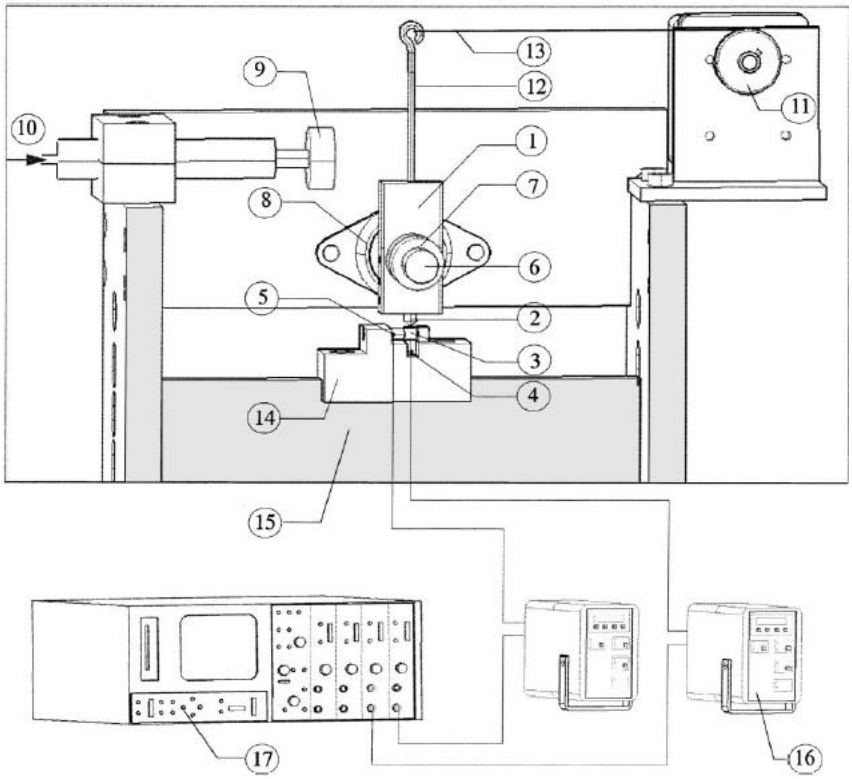

Fig. 24 Pendulum developed and used by Wang et al., [73] *and* [74]*, and Subbash et al.,* [75]*. 1) Pendulum. 2) Diamond tool. 3) Sample. 4) Normal load cell. 5) Tangential load cell. 6) Arbor. 7) Ring. 8) Precision bearing. 9) Hitting disc. 10) Nitrogen gas. 11) Motor wheel. 12) Bar. 13) Rope. 14) Sample base. 15) Support beam. 16) Dual mode amplifier. 17) Nicolet oscilloscope.*

The pendulum could be activated by two mechanisms. On the one hand, the movement could be transmitted by a pneumatic cylinder located on the left. The operating pressure was from 0.345 to 2.069 MPa, this resulted in a speed range on the diamond tip from 1 to 4 m/s. When the pressure of the cylinder was in the range of 0.069 to 0.345, partial scratches could be created on the sample. In this way, the abrasive grain got stopped at an intermediate point of the scratch and the chip formation could be studied.

On the other hand, the pendulum could be activated by a rope attached to a motor on the right. This mechanism provided lower test speed, but better control of the speed by means of controlling the rotating speed of the motor, for instance, 55 rpm resulted in 0.01 m/s.

The sample was mounted on a piezoelectric load cell for measuring the force in normal and tangential directions. Both the sample and the load cell were mounted on a base that could be adjusted in height in order to select the depth of the scratch.

They used this device for two consecutive research works [73] and [74]. In the first one, they performed scratches with a diamond conical grain on titanium samples with the purpose of

investigating the material removal mechanisms on that material. At the same time, they used this work for validating the new test bench. They performed numerous tests where partial and complete scratches were carried out, see Fig. 25.

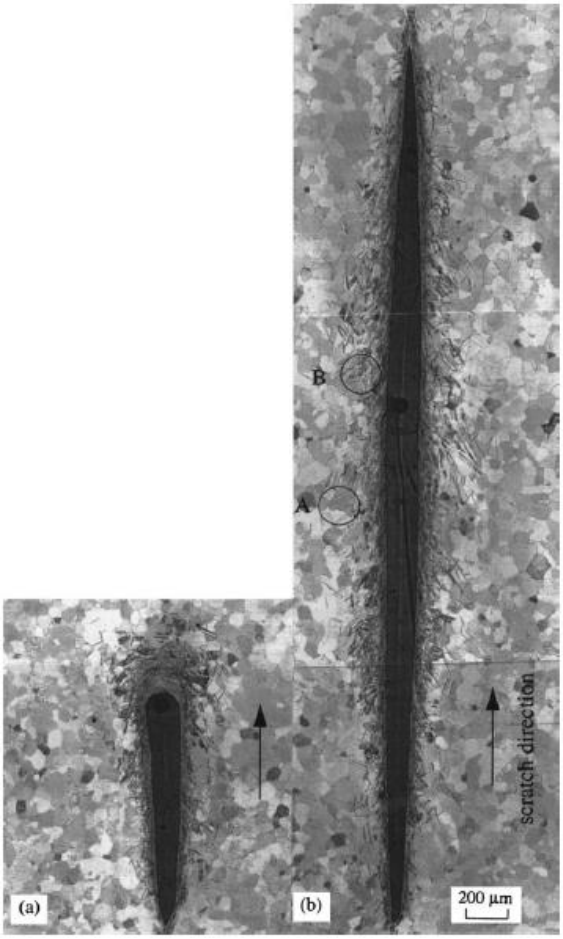

Fig. 25 Partial and complete scratches carried out by Wand et al. [73].

Thanks to the information given by the force sensor connected to the sample base, the tests were analyzed in terms of normal and tangential force and also in terms of the friction coefficient calculated from the division of both force components. They compared their results with those obtained by Kita et al. [72] in their single grit scratch tests. The same phenomena were observed, although the difference in speed, 40 times higher in the work of Kita et al., led to different results. For a deeper understanding of the material removal process, the overall specific energy was calculated using the work of Briscoe et al. [76] with the purpose of addressing the size effect.

After having evaluated all the results, authors concluded that they developed a functional test bench for the analysis of the material removal mechanisms of metals in grinding operations. Thanks to the partial scratches, they were able to separate 4 different zones in the deformed workpiece material ahead the grain. The influence of the attack angle of the diamond grain could also be addressed by plotting the forces versus the scratch length. Finally, they concluded that instantaneous specific energy and instantaneous material hardness were more appropriate than the overall specific energy for evaluating the size effect in this type of tests.

In the second work, [74], they analyzed in detail the geometry of the process, see Fig. 26, with the aim of developing an analytical model of the material removal. The model was called UBA (upper bound analysis), it was validated through the results of force and overall friction coefficient obtained in pendulum tests on pure titanium. Once validated, the model provided information about the power consumption and material behavior. Through the modelization of the material behavior, different features of the deformation could be predicted as well as the material removal. They could also detect the three cutting mechanisms and locate them along the scratch, i.e. rubbing and plowing were more important in the first half of the scratch while cutting played a more important role in the second half.

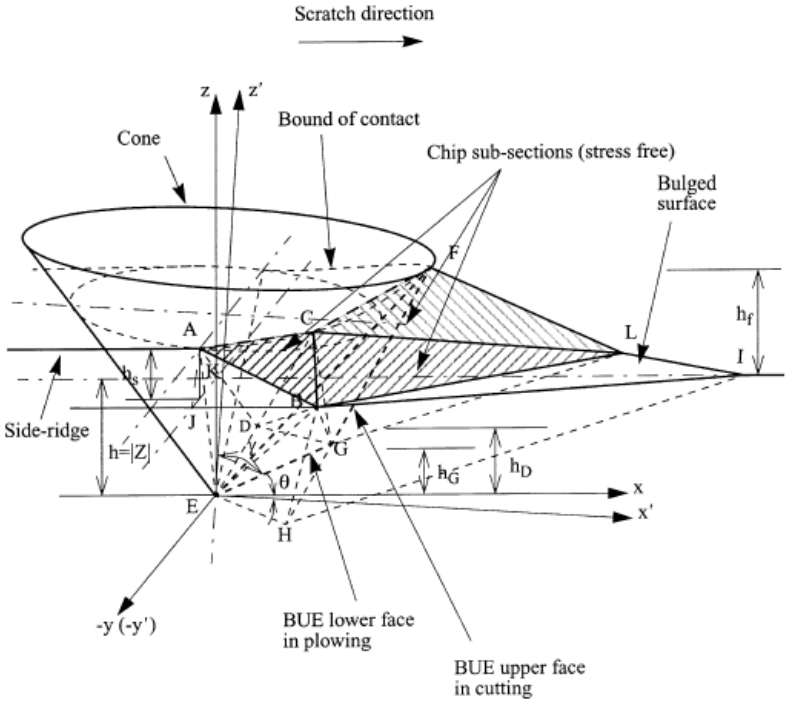

Fig. 26 Geometrical analysis of the single-grit test [74].

The analytical model requires a deep analysis of the deformation of the workpiece material at specific conditions and it can be hardly used for other materials without the previous extensive analysis.

In between, Subbash et al. released a scientific article using the same test bench, [75]. In that work, authors proposed a data dependent system method for evaluating the fracture modes observed in single-grit scratch tests. In this case they used the pendulum device for performing single-grit scratch tests on ASTM 1018 steel at first and later on brittle materials such as Homalite-100 and Pyrex glass. The difference on the scratch and forces of a ductile and a brittle material are shown in Fig. 27.

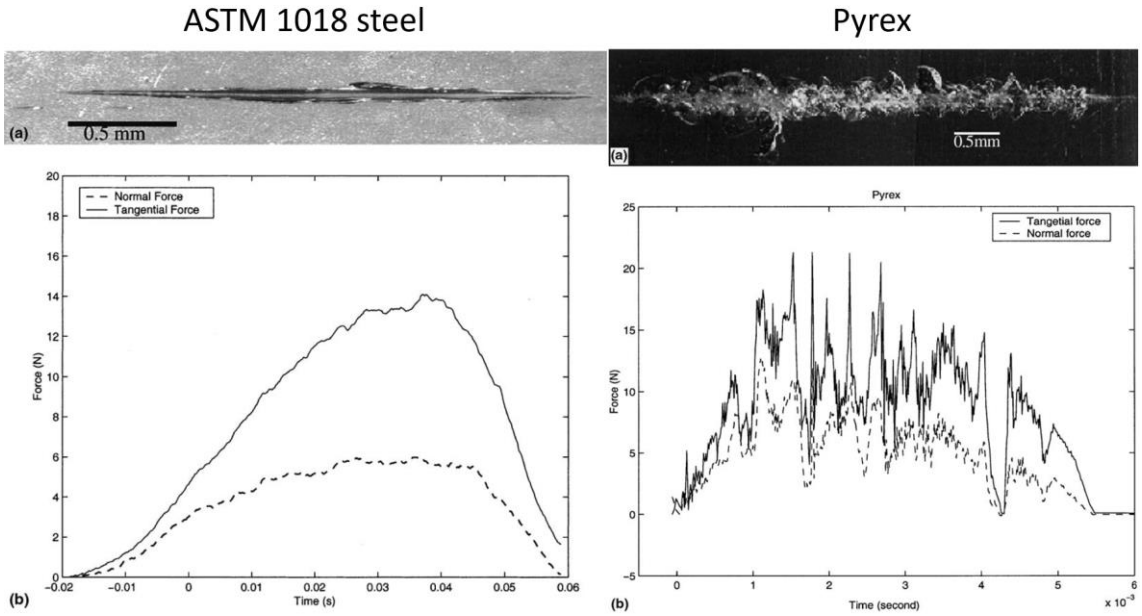

Fig. 27 On the top, the scratches on ASTM 1018 steel (left) and Pyrex (right). On the bottom, the normal and tangential force signals on ASMT 1018 steel (left) and Pyrex (right), [75].

Data dependent system method is explained in detail by Pandit and Wu in [77]. In short terms, it is an autoregressive model of a specific order adjusted with the information of the experimental test that gives information of the nature of the material removal process. For this purpose, the force signals were compared with the scratches in order correlate them.

This model could be developed due to the possibility of relating the force signal to the features observed along the scratches. In general terms, the pendulum developed for these works allowed to do interesting research works in the field of material behavior under the effect of a scratching grain. However, the efforts of increasing the precision of the test bench, limited its range of application mainly in terms of speed. It is mentioned before that a maximum speed of 4 m/s could be reached, while in grinding processes the speed is commonly above 10 times higher. The influence of the speed was acknowledged by these authors when they compared their results with the work of Kita et al.

Brinksmeier et al. [16] investigated the material removal mechanisms of the finishing process of gears. This grinding process is carried out at low cutting speed, in the range of 0.3 to 5 m/s. For reproducing those cutting conditions, they used a fly wheel configuration setup. They inclined the sample with the purpose of obtaining a chip geometry similar to the chip obtained in the grinding process, the setup can be seen in Fig. 28.

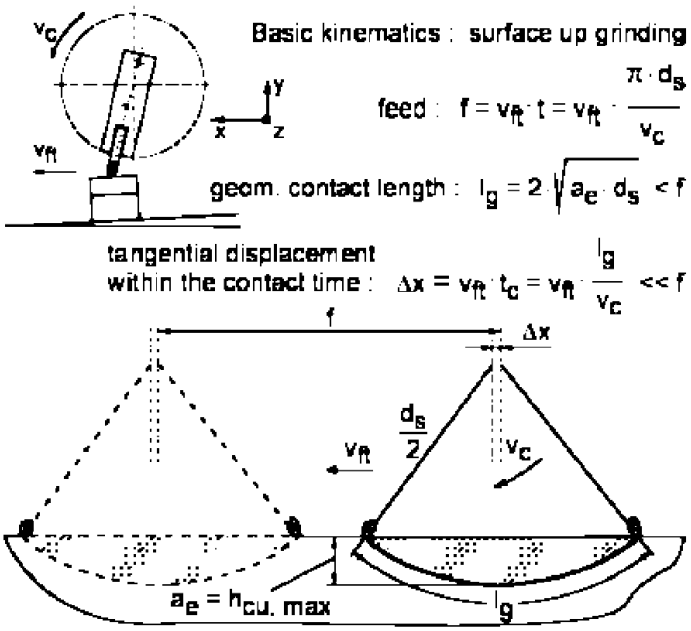

Fig. 28 Fly wheel single-grit test setup used by Brinksmeier et al. [16].

The tests were carried out using a diamond grain on hardened steel samples that had already been polished for a better control of the cutting depth.

Two parameters were used for evaluating the tests. On the one hand the specific scratching energy was calculated using the force signals registered by a force sensor located below the sample and the digitalizations of the scratches made by an atomic force microscope. On the other hand, the relative chip volume calculated through Eq. (8), [78], where A_r is the section of the groove and A_1 and A_2 are the sections of the piled material.

$$f_{ab} = \frac{A_R - (A_1 + A_2)}{A_R} \tag{8}$$

The results obtained for different cutting depths and different cutting speeds were replicated by grinding tests maintaining the same cutting speeds and substituting the cutting depth by the equivalent chip thickness. Through this comparison they wanted to verify the results observed in the single-grit tests.

Although the results did not show a very close relationship in quantitative terms, the trends of material removal and specific energy observed as a function of the cutting speed and cutting depth matched satisfactorily. It should be mentioned that the chip thickness in single-grit tests equals the cutting depth, but this calculus is far more complicated in real grinding due to the multigrain surface of the wheel.

Through this work, authors detected the speed and size effect and had important information for improving the gear finishing process.

Durgumahanti et al, [79] carried out single grit scratch tests as a part of their work for developing a force model. They used a fly wheel configuration were alumina grains of different sizes were

attached by means of a holding screw for several scratch tests on steel, see a depiction of the setup in Fig. 29.

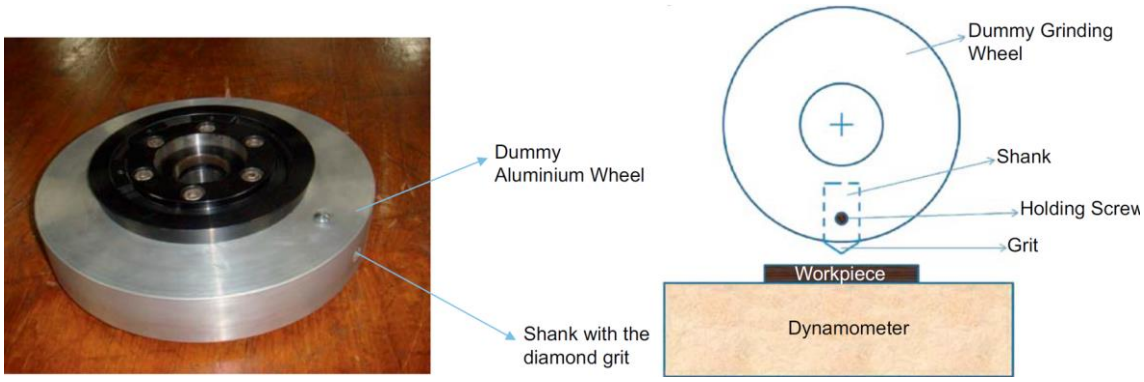

Fig. 29 Pin on disk setup used by Durgumahanti et al. [79].

During the tests, the forces were measured and after the tests, the scratches were scanned in order to measure the groove depth and the height of the piled material. They used this empirical data for establishing some constants of their model through a regression method. However, they did not provide further information and results of the measurements of single-grit tests.

The same test configuration was later used by Singh et al. [80] for developing a specific energy model.

In 2011 Aurich et al., [81], and Chen et al., [82], presented two works based on single-grit tests, both under a fly wheel configuration.

The setup developed by Aurich et al. was designed for high speed tests, up to 120 m/s, see Fig. 30.

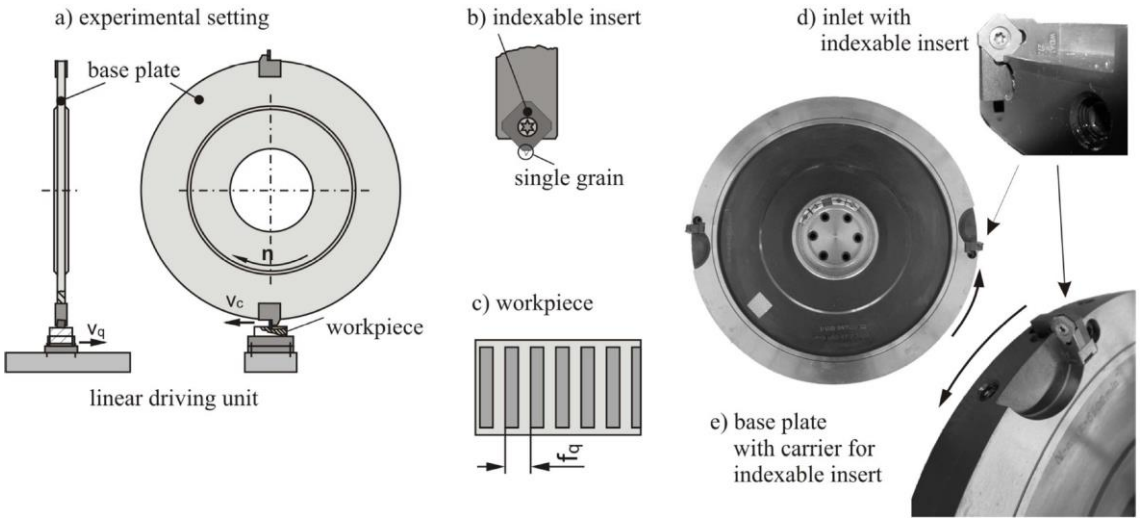

Fig. 30 A depiction of the test setup used by Aurich et al., [81].

They performed scratches with CBN grains on AISI 4140H steel. The CBN grain was attached to the indexable insert by galvanization and the fly wheel was moved axially during the tests for achieving separated scratches. The high speeds required a special attention to the balancing of

the fly wheel. Therefore, an additional place for another indexable insert was manufactured on the opposite side of the fly wheel and even an insert was placed, however, only one of the two inserts had a CBN grain.

Before attaching the grains on the indexable insert, they were digitalized in 3D. In this way, they could compare the shape of the grains with the groove created. Thus, the difference between the groove section and the grain section was a consequence of the elastic deformation occurred during the contact. As it can be deduced, they also digitalized the scratches in 3D, but not only with the purpose of measuring the groove, but also the piled material on the sides of the grooves. Through this geometrical analysis, they drawn the following conclusions: there was not elastic deformation below the grain; the higher angle between the sample surface and the grain the more piled material; and the higher cutting speed, the less proportion of plastically deformed material.

Through this setup, speeds in the range of CFG were achieved, unlike the previous works. However, the mechanical and thermal part of the process was not addressed since no measurement was carried out on these magnitudes. In addition, authors mention in the last part of their work that the tests should be repeated with a multigrain surface for obtaining more consistent values with a real grinding process.

The work carried out by Chen et al. [82] had some similarities with the work carried out by Aurich et al. The setup was also designed for reaching high speed, up to 150 m/s, and the fly wheel was also moved in axial direction during the tests for creating independent marks. However, the materials used for the tests and the measurement conducted were different. The abrasive grain used in this case was made of diamond and the workpiece material was a nickel-based alloy called GH4169. In addition, as it can be seen in Fig. 31, the sample was mounted on a dynamometer and a chip container was placed right after the sample.

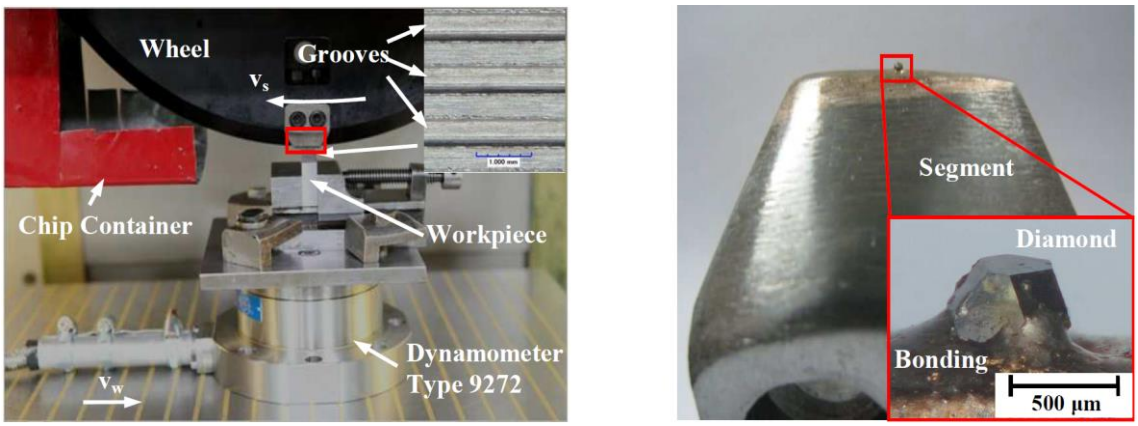

Fig. 31 Single-grit test configuration used by Chen et al. [82].

The scratches were digitalized in 3D and also observed by a SEM. The first measurement allowed to evaluate the groove section and the piled material and the second measurement allowed to evaluated the surface of the groove.

As a result of this complete study they concluded that the roughness improves with the cutting speed and the force decreases when the speed increases. However, the work is incomplete since

the efficiency of the process was not assessed in terms of specific energy. Moreover, as for the previous work, a multigrain surface is needed for a better approach to the real grinding.

Öpoz et al. [83] carried out single-grit tests with a fly wheel configuration with the purpose of analyzing the influence of the grain shape and the cutting depth. For this purpose, they used an inclined surface in the axial direction, unlike Brinksmeire et al. [16], see an example of their setup in Fig. 32.

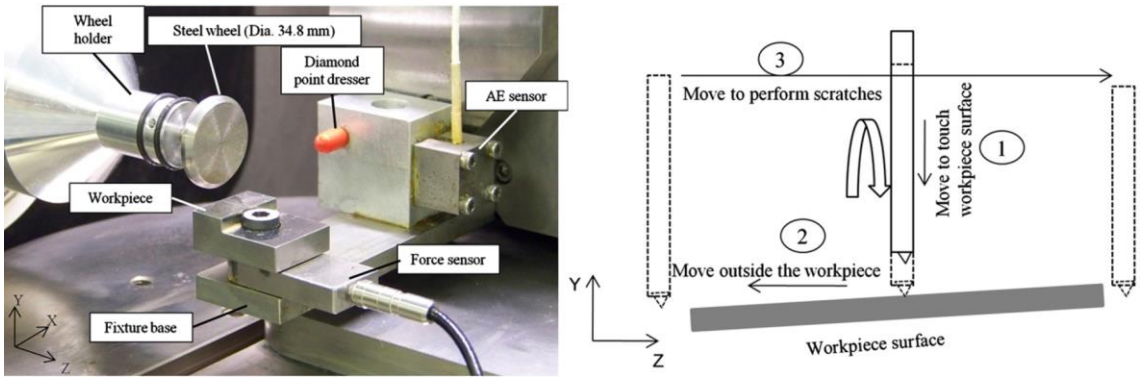

Fig. 32 Setup and methodology used by Öpoz et al. for single-grit tests [83].

Although Aurich et al. [81] already investigated the influence of the shape of the grains, the change in shape as a consequence of the wear was not studied. In this work, the grains CBN grains are used for scratching polished steel samples until they get dislodged from the disk or too worn for further tests.

Among the grain geometry created automatically by the wear, they could study the case of blunt grains that have suffered wear flat and fractured grains with more than one cutting edges, in addition to the case of new sharp grains with a single cutting edge.

From the geometrical analysis carried out of the scratches, they concluded that the most efficient scenario for reducing the plastically deformed material is a sharp grain with a single cutting edge. In comparison with a multiple cutting edged grain, the results of the pile-up ratio are lower although there is a similar trend when the cutting depth is increased. In both cases the pile-up ratio decreases when the cutting depth increases. However, flat grains presented a better result at low cutting depths than multiple edged grains, but the pile-up ratio increased when the cutting depth increased.

In this work, the authors demonstrated that the pile-up ratio is a good indicator of the efficiency of the material removal in terms of plastic deformation versus real material removal. However, they do not provide information of the mechanical loads in spite of having a force sensor in the setup.

Later, in 2013, the same authors presented a work based on the same experimental work [84]. In that work, the geometrical results were used as empirical data for a finite element model of the single-grit tests.

Tian et al. [14] used the same single-grit test bench as the one used by Chen et al. [82] but with a different configuration. On the one hand, they designed the preparation of the tests with the

purpose of obtaining an uncut chip geometry similar to the real grinding process, as tried by Brinksmeier et al. [16]. This was achieved by grinding the sample at an intermediate point in order to create the contact length corresponding with the equivalent wheel diameter of the fly wheel and cutting depth, see Eq. (1). On the other hand, that grinding operation was carried out at a specific angle for achieving the effect of increasing progressively the cutting depth, as tried by Öpoz et al. [83]. The ground path is marked in red in Fig. 33 while the single-grit tests are marked in blue.

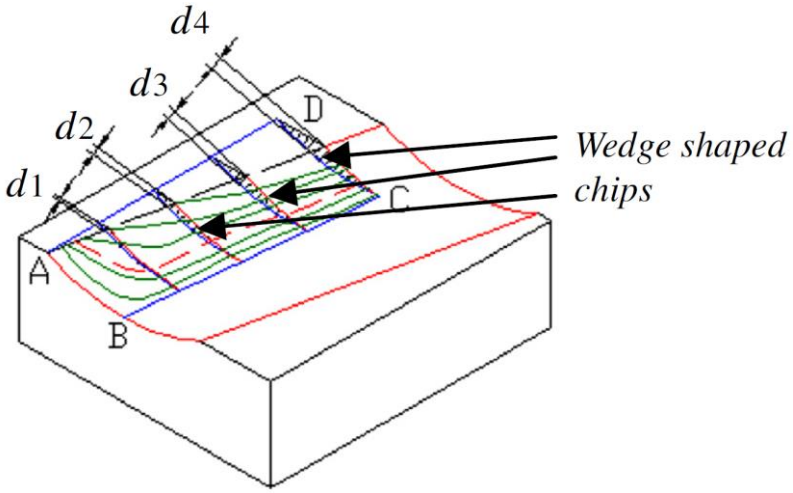

Fig. 33 A depiction of the samples used in the work of Tian et al. The geometry of the sample created for the tests is marked in red. The material to be removed during the single-grit tests is marked in blue.

The grain was a diamond with a defined shape and the workpiece was made of a nickel-based alloy. They performed an extensive work where they analyzed the roughness of the scratches, the profile of the scratches, the forces during the tests and the shape and geometry of the chips.

By means of observations on the surface appearance of the sample after the tests, three zones could be clearly differentiated, namely the rubbing, plowing and cutting zones. The extension of each of these zones varied as a function of the cutting speed and uncut chip thickness. The uncut chip thickness at the border between plowing and cutting zones was acknowledged as the critical chip thickness.

In addition, the values of the forces and pile-up ratio for a given uncut chip thickness at a wide range of speeds were compared, from 20 to 160 m/s. Two different regions were detected from this comparison, which demonstrated the presence of the speed effect. Below 100 m/s the material behavior progressively became more brittle as the cutting speed increased, however, above 100 m/s, the material behavior became more ductile when the cutting speed increased. The tests were repeated without cutting fluid and the behavior of the material became more ductile when the speed increased above 20 m/s, which reveals the importance of the temperature in the speed effect.

This research work showed a new test configuration and interesting results. However, the wear of the diamond is not mentioned in the whole article, despite the significant amount of material removed by the single grain during the preparation of the sample and the performance of the tests.

More recently, Rasim et al. [85] proposed a new concept for single-grit tests. In the majority of the works mentioned in the previous lines, the grain was attached to a fly wheel and the sample was placed on a table connected to force sensors. This configuration made difficult the observation of the chip generation process. Rasim et al. developed a test bench where the abrasive grain was fixed on the table and the sample was fixed on the rotating component. With the purpose of having a chip thickness corresponding with the trochoidal geometry of a grinding process, the uncut chip thickness was calculated and modified for being reproduced consistently on the rotating component, see the process in Fig. 34.

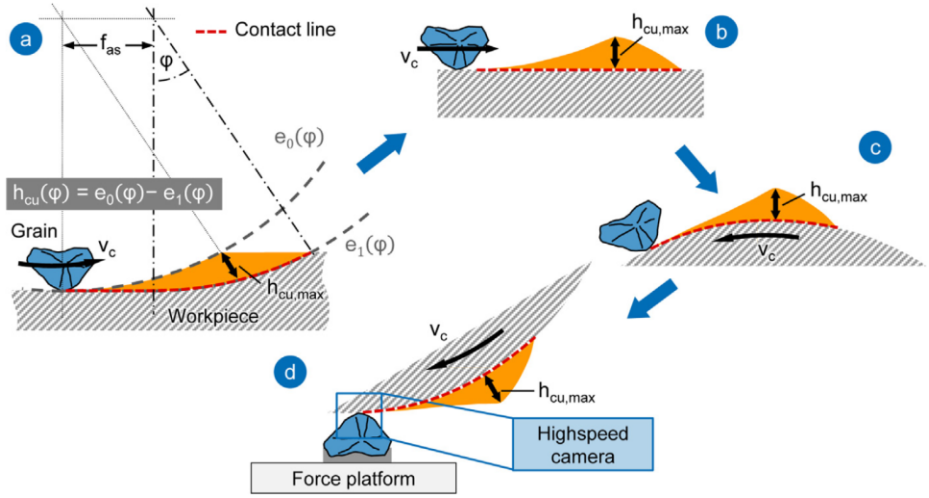

Fig. 34 Conversion of the uncut chip thickness from a flat surface to a circular surface [85].

Since the abrasive grain was fixed to an immobile surface, all the action occurred at the same place. This feature allowed to add a high-speed camera to the measurement devices also seen in the previous works, namely a force sensor and a microscope.

This study focused on studying the influence of the grain shape on the chip formation. For this purpose, the grain geometry was digitalized by a SEM and three angles were established as a method for classifying, namely the rake angle, the apex angle and the opening angle, see Fig. 35.

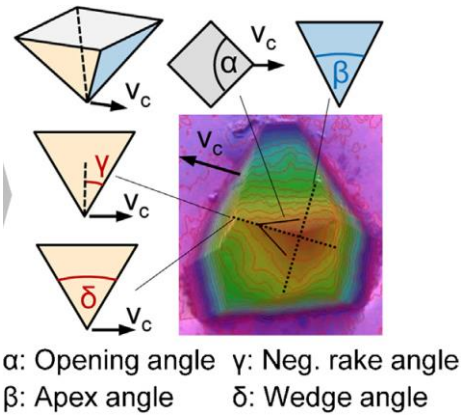

Fig. 35 The angles defined by Rasim et al. [85] *for studying the influence of the geometry.*

Thanks to the setup, authors could differentiate the onset of the plastic deformation and chip generation and relate to the geometry of the grains. After having analyzed all the outputs,

authors concluded that the opening angle was the one with the least influence in the chip formation. The increase of the other two angles resulted in a deeper cutting depth for starting the plastic deformation, by contrast, the increase of the cutting speed required lower cutting depth.

Despite the advantages of the new single-grit methodology developed it that work, it must be taken into account that the preparation of the tests is far more complicated and time consuming. On the one hand, the uncut chip thickness must be created on a circular body, this process is not explained in the published article, but a high accuracy is needed since the uncut chip thickness is in the range of microns. In addition, it is mentioned that after achieving the right geometry, the sample was polished to $R_z < 0.03$ µm. On the other hand, each time the chip thickness wants to be modified, the whole process must be repeated. In addition, even with this configuration, a single grain is used instead of a multigrain surface.

Akbari et al. [86] carried out also single-grit tests focused on grinding process, but with different kinematics. Instead of having a rotating and a still component, they proposed a linear movement between both components. The setup is shown in Fig. 36.

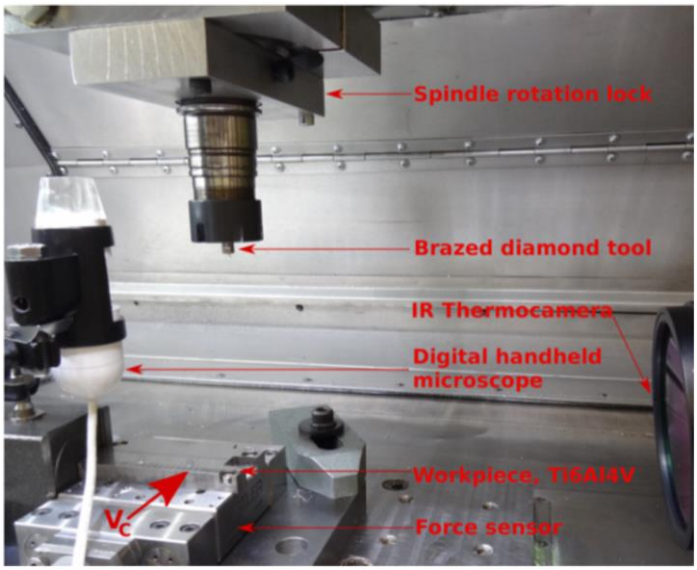

Fig. 36 The setup developed by Akbari et al. [86] *for liner single-grit tests.*

They digitalized the diamond grain with the purpose of relating the results obtained with the rake angle. The rest of the output, namely the forces acquired by the force sensor and the recordings of the thermographic camera, were used as empirical data for a numerical thermomechanical model.

Through that model, authors were able to adjust a failure criterion for grinding TI6Al4V with negative rake angles. However, linear relative movement hampers to reach speed in the range of conventional grinding processes, for instance, the relative speed used in this work was 0.8 m/s.

Chen et al. [87] used as well linear single-grit tests for studying the ductile-brittle transition during the microgrinding process of single crystals silicon. This process is carried out with grinding tools whose diameter is below 1 mm. Therefore, the cutting speeds are significantly

lower than in conventional grinding, namely below 1 m/s. Thus, the maximum sliding speed of the test bench used for this work, see Fig. 37, was 12.6 m/s.

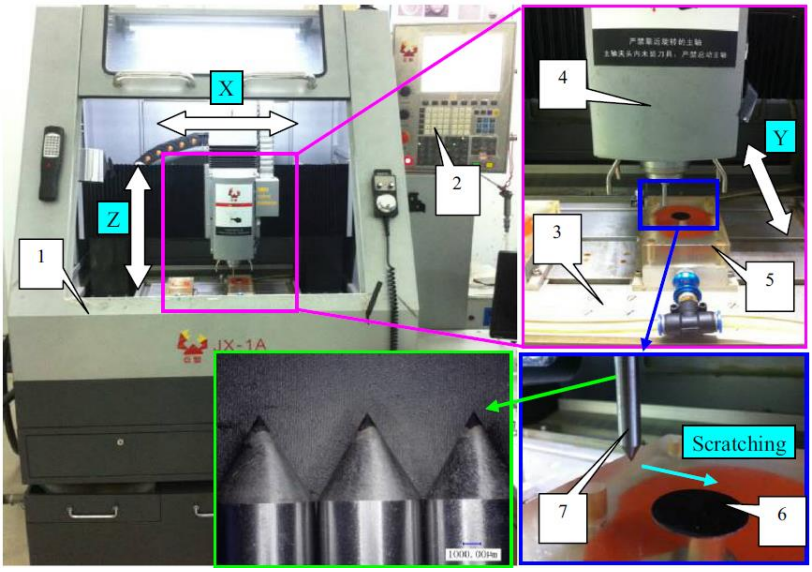

Fig. 37 Single-grit test setup used by Chen et al. [87].

The objective of the research study was to avoid the cracks created below the grain. For that purpose, authors wanted to shift the brittle behavior of crystal materials into a ductile behavior.

They based the study on the apex angle of the diamond grit, on the cutting speed and on the cutting depth. As evaluation method, they observed and measured the scratches by means of different microscopy devices.

They concluded that the higher the speed and cutting depth are, the more prone to have brittle behavior and hence, to fracture the material. However, regarding the shape of the grains, the sharper grains led to brittle fracture more easily than the blunt grains. That is to say that the ductile regime can be maintained at deeper cutting depth with the blunt grains.

Later, Wang et al. [88] published a research work focused also on the microgrinding of brittle materials. They used a cutting depth below or equal to 2 µm and a grinding speed below or equal to 1.667 m/s. The particularity of their test bench is that they included an interferometer inside the machine, see Fig. 38

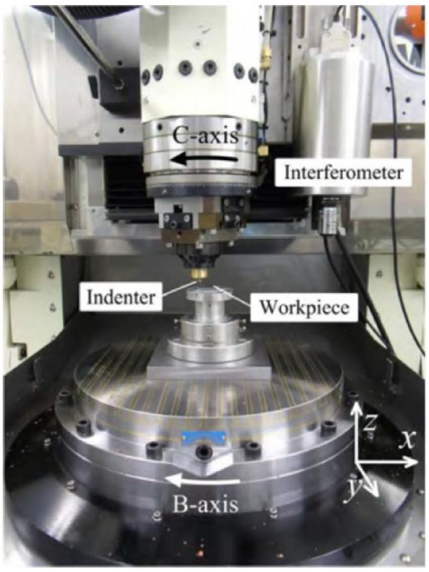

Fig. 38 Single-grit test setup used by Wang et al. [88].

In this research work, the experimental tests were used as an empirical source for validating an analytical model for the crack propagation.

The single-grit tests carried out for studying the microgrinding process of silicon, ceramics and optic materials are carried out on special machines where the resolution of the axes is fine, 1 nm, but the available linear speed is too low for reproducing CFG or even conventional grinding materials. Therefore, they cannot be taken as a reference for the work presented in this manuscript.

Finally, in 2019, Suya Prem Anand et al. [89], carried out rotating single-grit tests with the typical configuration, where the abrasive grain is on a fly wheel and the sample is on a piezoelectric force sensor and everything is positioned on the table of the machine, as it is shown in Fig. 39.

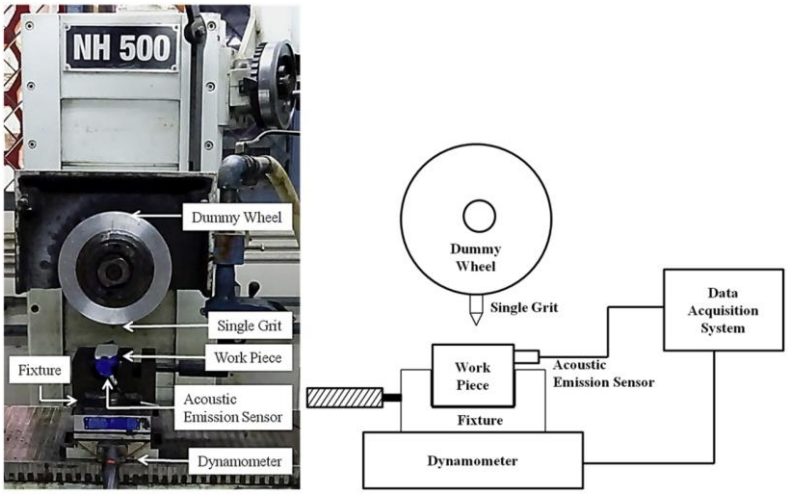

Fig. 39 The fly wheel single-grit tests bench used by Suya Prem Anand et al. [89].

In addition to the forces, they measured the scratches with a microscope for calculating the removed material and the specific energy. With all that information they evaluated the influence

of the rake angle and cutting depth on the chip formation of sintered and presyntered zirconia bioceramic material. It should be mentioned that the cutting and feed speed were kept constant, 16 m/s and 6 m/min respectively.

It can also be concluded that the influence of the grain shape and the cutting depth can be addressed by single-grit scratch tests without the need of special evaluation techniques. However, it is not common to reproduce grinding processes where the requirements in terms of speed or forces are specially demanding.

Taking everything into account, it can be stated that single-grit tests have been carried out in rotational and linear configuration. Linear configuration provides a better control on the cutting depth. The phenomena at a specific cutting depth can be analyzed in more details since the interaction at the desired cutting depth can be carried out for longer time and distance. However, it must be kept in mind that the interaction between the grain and the sample is not the trochoidal path that takes place during a grinding operation, where the contact depth varies and the three cutting mechanisms occur. In addition, they are used for very specific processes where the cutting speed is rather low in comparison with conventional grinding and the cutting depth is in the range and below microns. The issue of the speed can hardly be solved because there is no space in the machine to accelerate.

By contrast, rotational single-grit tests, allow to have grinding speeds in the range of industrial grinding operations. However, the preparation of the tests may be more tedious than linear tests. For instance, different efforts have been made for enhancing the control over the cutting depth, which demonstrates the complexity and importance of this aspect.

Both test configurations have been successfully used for different purposes. They have been mainly used studying the different stages of the material removal as a function of the cutting parameters and shape of the abrasive grains. Nevertheless, they have also been used for obtaining empirical data for as input parameters or for validating several types of models. These two features reveal the suitability of this methodology for the current work. However, it must be taken into account that every work has been done with a single abrasive grit. In consequence, the effect of the adjacent grains has not been addressed.

1.5 GRINDING MODELIZATION

The importance of empirical results for a research work has already been explained in the previous section. However, in complex processes, a numerical modelization is commonly used for completing the work. In the following lines the benefits of coupling an empirical experiment with a numerical modelization are listed.

Laboratory tests are normally designed for reproducing accurately a specific phenomenon in such a way that the control on the affecting parameters is maximized and the outputs can be measured properly. In this way, the original phenomenon can be studied; nevertheless, laboratory tests have also their limitations. Thus, the aim of a numerical modelization is to cover these limitations. Although, the experiments have been correctly designed and a customized test bench has been developed for those experiments, there are some physical magnitudes that cannot be measured. This situation occurs as a result of too high inertias, either mechanic or

thermal, of measuring devices, difficult access to the zone where the magnitude must be measured, or insufficient resolution, accuracy and repeatability of the measuring devices among other possible reasons. A numerical modelization avoids those problems.

Here, the measuring devices are not a limiting aspect, therefore, magnitudes that cannot be directly measured in the experiments, can be measured in the model. This implies that there is more information about the process itself and thus, it is easier to understand the resulting phenomena. In addition, the performance of empirical tests requires significant efforts in terms of preparation of the setup, materials, and gathering the results from different sources, which means important economic and time costs. These downsides are avoided at some extent if the process is numerically modelized, although it must be kept in mind that an empirical source of information is always needed for adjusting and validating the model. In this way, once the model is correctly validated, the range of the research work is enhanced. It is easier to isolate the input parameters so that their influence can be better addressed. Besides, the spectrum of the study can be expanded since a wider range of input parameter can be used, without any physical limitation of the test bench. Although, it must be mentioned that the further the input conditions move from the conditions used in the empirical test, the higher the uncertainty of the model.

Taking everything into account, the advantages of the numerical modelizations takes importance given the particular process studied in this work. First of all, the EP CBN grinding wheels used in the industry for the CFG process of NGV have a significant cost, around 2000 € each, and long delivery times. Apart from this, the aeronautic alloys used for the NGVs have also an important cost and even longer delivery times. Secondly, as it is going to be explained in chapter 3, the preparation of the materials for the tests takes a long time since they have to be manufactured and adapted specially to the test bench. Thirdly, given the grinding parameters characteristic of CFG, the main limitation of the test bench regarding the input parameters was to reach the high grinding speeds, not only because of machine capacity, but also for safety reasons. Finally, this work is focused very specifically on the contact between the abrasive layer and the material. The dimension and kinematics of the process makes impossible to obtain all the desirable outputs of the tests.

Thus, the process should be modeled by means of a method that allows to address the following aspects:

- Geometry. The performance of the grinding process depends strongly on the state of the grinding wheel surface. Therefore, the model must be capable of reproducing to the closest the features of the grinding wheel surface in terms of grain geometry and wear state, grain concentration and grain protrusion height.
- Kinematics. The model must reproduce the kinematics of the experiments.
- Materials. The model must allow to define the physical properties of the different materials used in model itself.
- Material removal. The material must be removed during the modelization as a consequence of the interaction between the abrasive grains and the workpiece material.

- Outputs. The model must give information about the mechanical and thermal aspects of the process through several parameters. Some of them may be used for validating the model and some others may be used as additional information for the experiments.

Because of the reasons mentioned before, grinding processes have been extensively modeled by many authors through different types of modelization. The most important modelization works have been reviewed with the purpose of evaluating the suitability of the different type of modelization with the case study presented in this work. They are separated in four groups as follows.

1.5.1 Analytic models

Since the 70's analytical simulations have been used for different purposes. They can be based on deterministic [90] or stochastic [39],[91]–[94] determination of the inputs. The deterministic simulations were defined by Gibb et al. [95] as simulation without randomness where all the inputs have a known origin and lead to a unique output. The stochastic simulations are often based on statistical measurements.

Steffens and König [90] developed a closed loop model where the force and the temperature were calculated iteratively. In that model, the thermal and mechanical inputs were defined as a function of the results leading to a non-linear problem that only could be solved by means of iterations. Therefore, the simulation must be repeated until a thermomechanical equilibrium was found.

Koshy et al. [91] developed a model for reproducing the surface of freshly dressed resin or metal diamond wheels of different grain sizes. They simplified the wheel as a hexahedron made of bonding material where the grains were located randomly under the following assumptions. The grains were defined as spheres, this approach was considered valid due to the negative rake angle of the abrasive grains. The size of those spheres was an average value based on the sieves used for classifying the abrasive grains in industry. Finally, the grains were distributed randomly and homogenously in the cube. The dressing process was considered as a progressive loss of bonding material until the bearing of the grain not strong enough for supporting the forces of the dressing process, then, pull-out occurred.

They modelized cubes with different grain sizes and compared the results with experimental works found in bibliography with the purpose of validating the model. The model was validated in terms of grain protrusion height and static grain count. Static grain count is defined as the number of grains protruding from the wheel surface. Afterwards, they used the model for calculating the intergrain spacing and the projected area. Despite the fact that it showed an acceptable coherence with the work used for its validations, they were only punctual empirical values, which may not be sufficient for a consistent validation of the model.

Guo and Malkin [92],[93] presented two works focused on the modelization of the heat flux during a surface grinding operation. In the first paper three different models for that purpose were introduced, namely the temperature matching method, the integral method and the sequential method. Each model was based on different equation and principles; hence, the input data were also different.

The suitability of each method was tested in the second article. where the contact length could be calculated as well. In that work they conducted three different grinding experiments, with three workpiece materials and three grinding wheel configurations. During those experiments, the temperature was measured by a thermocouple in order to gather the input data for the models. They concluded that the actual heat flux shape was triangular with the highest energy flow close to the leading edge of the grinding wheel. Despite the good correspondence with the measured values, they were also able to measure the contact length through the heat flux. This was achieved thanks to the three zones distinguished on the workpiece surface during the grinding operation as a function of the sense of the heat flux. There was a zone where the heat flux was negative, i.e. outwards the workpiece; there was another zone with positive heat flux, i.e. towards the workpiece, and the last zone where no heat flux was considered. They considered the surface length with positive heat flux as the actual contact length, which included the effect of deflections.

The workpiece roughness was also addressed in terms of R_a by Agarwal and Venkateswara [94] for ceramic grinding applications. The model used the undeformed chip thickness, h_{cu}, as the base for predicting the end roughness. For that purpose, a statistical recreation of the wheel surface was intersected with the workpiece and some assumptions were established before evaluating the scratches. Those assumptions, although necessary for the study, conditioned strongly the work since no plastic or elastic deformations were allowed and no overlapping of between the scratches created by different grains was allowed. Although these are actual phenomena in a grinding process, it is true that both plastic and elastic deformation plays a less important role in ceramic grinding than in metallic grinding.

Finally, they carried out grinding tests with a diamond wheel on silicon carbide for evaluating the correspondence of the modeled values for a range of feed speeds and cutting depth. The coherence of the results for a given cutting depth varied with the feed speed from low errors at low speeds to higher errors for higher speeds.

With the advances in the computational power of the computer, more complex analytical models were developed.

Yu et al. [39] presented an analytical model formed by four modules for simulating the grinding wheel surface, the forces, the temperature and finally the grain pull-out. Firstly, they calculated the grinding power from the workpiece material removal and plowing. The grinding power was used for determining the thermal loads thanks to assumptions about the energy partition taken from bibliography. The mechanical and thermal information obtained in the previous two steps was used for a grit thermomechanical model whose results were finally the input of a fatigue law. The results of a previous work were used as empirical data [51] and a finite element method (FEM) model was also used for finding the maximum stress concentration point of the bond layer.

In these simulations, the surface of the wheel has to be created by means of mathematical expressions, which are usually based on statistical measurements of the wheel surface. In this work, a model with a real wheel surface was pursued; therefore, the use of analytical simulations was dismissed.

1.5.2 Kinematic models

Grinding process can also be simulated by kinematic simulations. These simulations require a higher computational power than the analytical simulation.

Chen and Rowe [11],[48],[96],[97] developed a kinematic model coupled with analytical equations that addressed the wheel dressing, the surface roughness, the grinding forces and the wheel wear.

In the first work the dressing process was modelized. The wheel characteristics, the diamond geometry and the dressing parameters where used for calculating the surface of the wheel after being dressed. On the one hand, the wheel was created by using spherical grains of a specific size due to the characteristic negative rake angle, as Koshy et al. did [91]. The position of the grains was established randomly through an algorithm that included the grain size, and the grain density of the wheel specification. On the other hand, the diamond dresser was created as a paraboloid. Finally, the dressing parameters where used for finding the interferences between the dressing tool and the grinding wheel. However, the interferences where coupled with an aleatory function that controlled the result of the interference. Through this function, the fracture of the grain could be larger equal or smaller than the geometrical interference with the diamond. This function was adjusted according to experimental experiences. See an example of the effect of this function in Fig. 40 where the dressing trace and the fractured area are not the same.

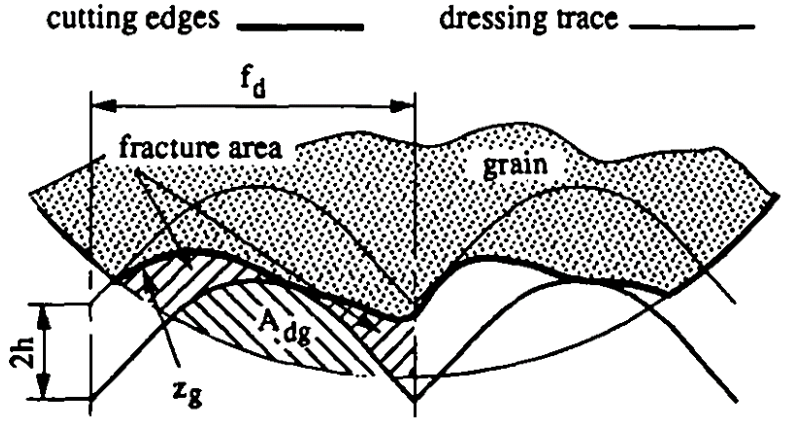

Fig. 40 Difference between the dressing trace and the grain shape in the kinematic model of Chen and Rowe [11].

In the second work, the dressed wheel surface was used as input for a kinematic model where the force per grain and the roughness of the workpiece where predicted. Both results were based on the interference of the dressed profile with the workpiece surface. However, some additional phenomena were added to the model with the purpose of enhancing its accuracy, namely the elastic deformation caused in the engagement workpiece-grain, the plastic deformation of the undeformed chip thickness and the workpiece material properties.

In the third work, the results of the models were compared with cylindrical grinding experiments carried out with an alumina wheel on hardened steel. The correspondence of the model with the experiment in terms of specific power and R_a were considered correct although the accuracy

of the model was significantly better for some grinding parameters. By both experimental and modelized results, authors concluded that the dressing depth had more influence on the grinding power than the dressing speed, while the contrary trend was observed concerning the roughness.

Finally, the fourth work addressed the wear of the grinding wheel. Attritious wear, grain fracture and bond fracture were considered. The grain fracture and the attritious wear were differentiated by a specially designed function. This function was empirically adjusted so as to determinate randomly when a grain-workpiece interaction yield grain fracture or attritious wear. By contrast, when the grinding force generated in the grain was higher than the retention force provided by the bonding material, the grain was directly pulled-out as a consequence of bond fracture. Again, the experiments and the model where compared in terms of specific power and Ra with some differences. The experimental values were plotted versus the accumulated stock removed by the wheel, while the model results were plotted versus the radial wear of the wheel. With this into account, the trends presented a good accordance but numerically, the results were far for some grinding conditions.

Warnecke and Zitt [98] developed a complex macro-micro kinematic model coupled with a FEM model for calculating the grinding forces. See the concept of the model in Fig. 41.

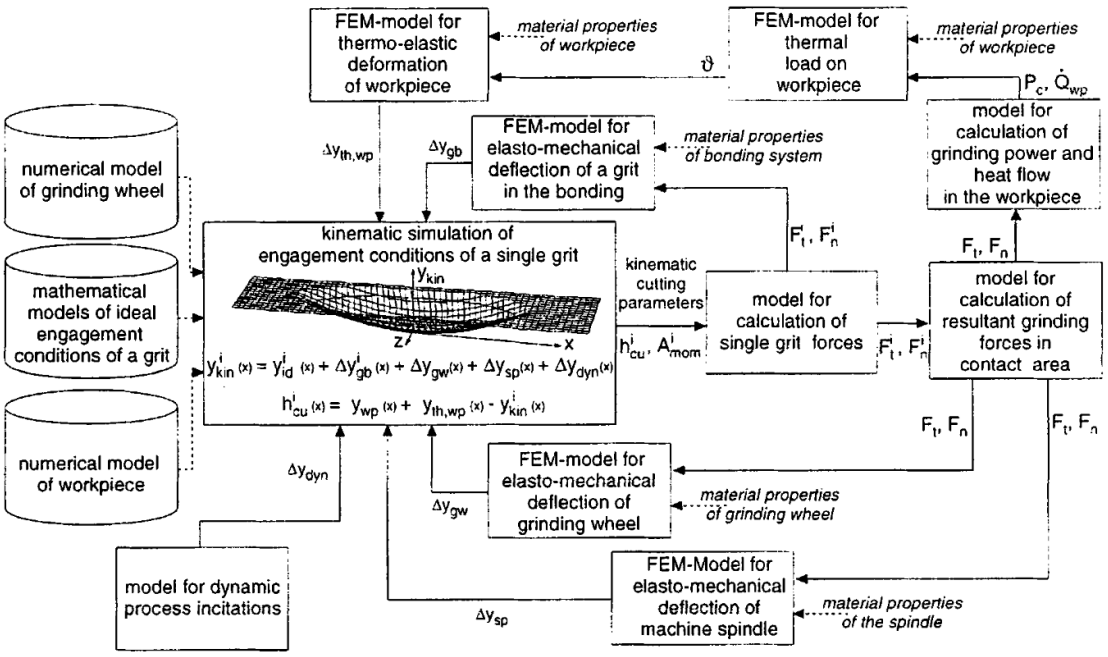

Fig. 41 The concept of the kinematic model developed by Warnecke and Zitt [98].

The model had several steps. At first the macrogeometry of the wheel was created. There, roundness errors were included for addressing their influence on the cutting process. Secondly, the microgeometry of the wheel was created using information taken from SEM observations. Statistical measurements were carried out during those observations in order to establish the grain size and grain distribution.

Thirdly, the kinematic interference between the wheel and the workpiece was conducted. In this step, the forces, the grinding power and the heat flux were calculated as a function of the undeformed chip thickness. The fourth step used that information from the ideal kinematic model to feed additional finite element models for addressing the deflections caused by the mechanical and thermal loads. The compared the model results with two grinding experiments where the single difference was the body material of the CBN grinding wheel. The model was capable to predict the grinding forces for both wheel body materials during a single lap of the wheel. The results were compared during a single lap with the purpose of evaluating at the same time the effect of the roundness error. However, during a single lap, the grinding process is not able to reach a steady state during the grinding process, mainly in thermal terms. Therefore, a comparison for a longer time should conducted for verifying completely the accuracy of the model.

Nguyen and Butler [99],[100] presented a work divided in two articles with the aim of predicting the workpiece roughness. In the first one, they generated the surface of three different grinding wheels from statistical measurements. They developed a mathematical procedure for creating the wheel surface. Two transformation methods were applied to that procedure and the results were compared with actual grinding wheel surfaces of different specifications. The similarity between the real and the modeled surfaces was assessed in terms of several roughness parameters. The result of both transformation methods showed coherent results with the digitalized wheel surfaces.

In the second work, they calculated the workpiece roughness considering the plastically deformed material during the plowing and cutting phases. The three cutting mechanisms, namely, rubbing ploughing and cutting, were set as a function of the grain attack angle instead of chip thickness. The model was then compared with grinding experiments carried out on two workpiece material. The same roughness parameters as the ones used in the previous work were obtained from the real and modeled workpiece profiles. The agreement of the results on the majority of parameters for the both materials indicated that the developed kinematic model was suitable for desired task.

Aurich and Kirsch [101] developed also a kinematic model coupled with a FEM with the purpose of predicting the grinding forces accounting the deflections of the whole setup. As Warnecke and Zitt [98], they also created the macro and micro geometry of the grinding wheel. On the one hand. extensive observations by SEM were conducted before creating the microgeometry. Through those observations, the average grains shapes were detected and adapted to the model as it can be seen in Fig. 42.

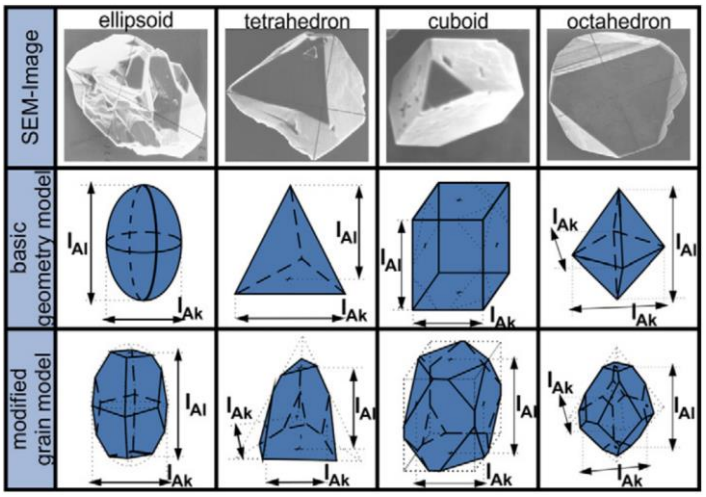

Fig. 42 Abrasive grain geometry used for the kinematic simulation by Aurich and Kirsch [101], *based on actual shape of real grains.*

In addition to the different grain geometries used for the grains, author also addressed the wear flat phenomenon by cutting the grains as it is shown in Fig. 43.

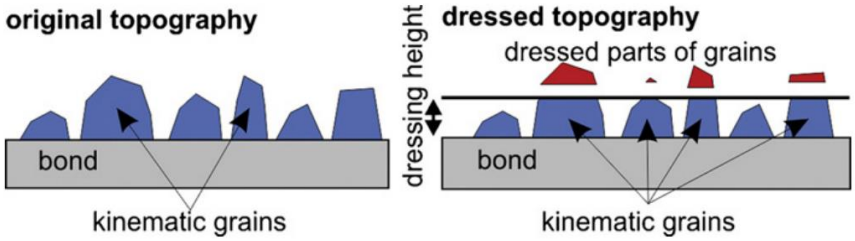

Fig. 43 Wear flat creation in the kinematic model developed by Aurich and Kirsch [101].

On the other hand, the macrogeometry was designed for considering influence of the roundness error. After having defined the wheel geometry, the kinematic model was conducted by turning two laps the grinding wheel. The first one was used to prepare the roughness of the workpiece for the second lap. In this way, the output parameters were obtained from the second lap.

The results obtained from the kinematic model were used by a finite element method model for calculating the deflections. Then, the kinematic model was run again with the deflections calculated by the finite element method model. This iterative process was carried out until the convergence occurred. However, this research work was focused on introducing the kinematic model, no experimental validation was shown in that work. Therefore, the effectiveness of this model was not verified.

Finally, Mohamed et al. [102] presented a work where an analytical model and a kinematic model were compared with grinding experiments. The target of the work was to predict the surface texture created with grooved wheels. It should be clarified that the roughness of the workpiece was not addressed in this study, only the texture left by the geometrical interference by the grooved wheel and the workpiece. For this purpose, only the macrogeometry of the grinding wheel surface was created.

The accuracy of the models was proved under several conditions, namely several cutting and feed speeds, different relative motions between the cutting and feed speeds and also reciprocating grinding. The geometric results of the models were in good accordance with the result of the grinding experiments.

In contrast to analytical simulations, in kinematic approaches are better controlled in terms of wheel surface where even the wear of the wheel can be simulated comparing it directly with the real surface. 3D surface can be created using statistical data for the grain shape, size and distribution. However, the simulation must be complemented with analytical equations or FE models when more information than the geometrical intersection is the aim of the simulation.

1.5.3 Finite element models

In some of the previously mentioned works, FEM was used as a complementary tool but it can also be used for studying the contact. However, these approaches are incomplete because the contact has been mainly studied by single grit simulations.

Öpöz and Chen [84] were able to simulate the groove geometry obtained by rotating single grit scratch test through a 3D model of a spherical grain. The model comprised the two bodies involved in the contact of the single grit tests, namely the grain and a plate as the workpiece. Both bodies and the model were defined in Abaqus® commercial software, as shown by Fig. 44.

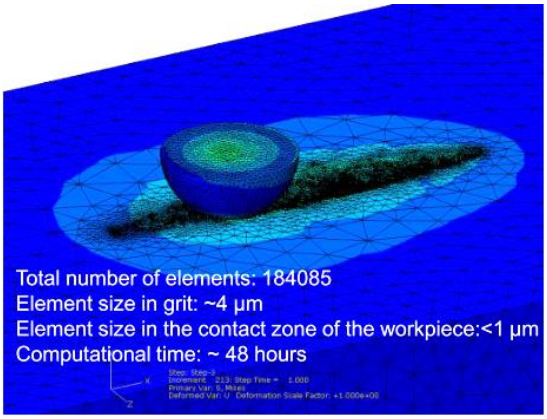

Fig. 44 A capture of the 3D model developed by Öpöz and Chen [84].

While the grain was defined with the physical properties of CBN the properties of the plate were different from the material used for the experiments. Instead of the properties of mild steel, some modifications were done with the purpose of approximating the results of the model and experiments. In addition to the material properties, the magnitude of the cutting speed was also modified in the model without providing any reason. The speed was reduced from 327.6 m/min to 100 µm/s.

With all these modifications, the model was able to reproduce qualitatively the deformation observed in the single-grit tests.

Ding et al. [103] calculated the residual stress distribution on a brazed CBN grain after several conditions. It should be explained that brazing is bonding method for single layer grinding wheels, as electroplating. However, brazing provides higher grain protrusion height and higher

grain retention force thanks to the chemical junction between the grain and the bond itself. This method is carried out at higher temperatures, unlike electroplating. Therefore, the stress analysis was carried out after the brazing process, after grinding with different embedding and wear percentages. The model was developed in Abaqus®, where a hexagonal CBN grain and the bond were created in 2D environment, see Fig. 45 were two models with different embedding percentage are shown. The grain wear was achieved by removing layers of elements.

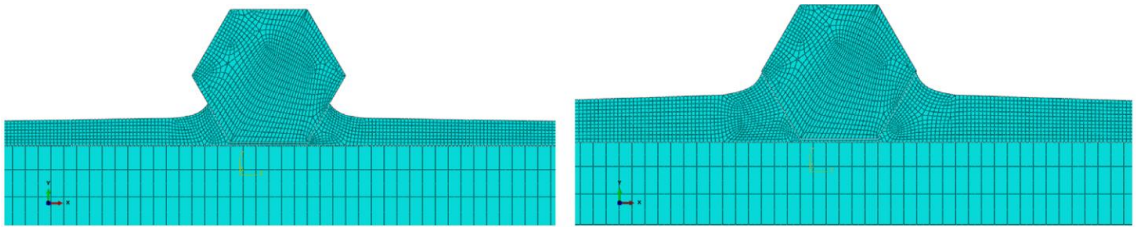

Fig. 45 Two different embedding percentages in the model developed by Ding et al. [103].

The stresses after the brazing process were calculated from the cooling phase right after the bonding material is solidified around the grain. This occurs at 800 °C. By contrast, the stress analysis after grinding process considered the thermal stresses form the cooling process and the mechanical stresses created by the grinding forces. Nevertheless, they did not carry out any experimental validation of the simulation.

Sun et al. [104] addressed the grinding process of alumina ceramic material through a single-grit 3D FEM model developed in Abaqus®, see Fig. 46.

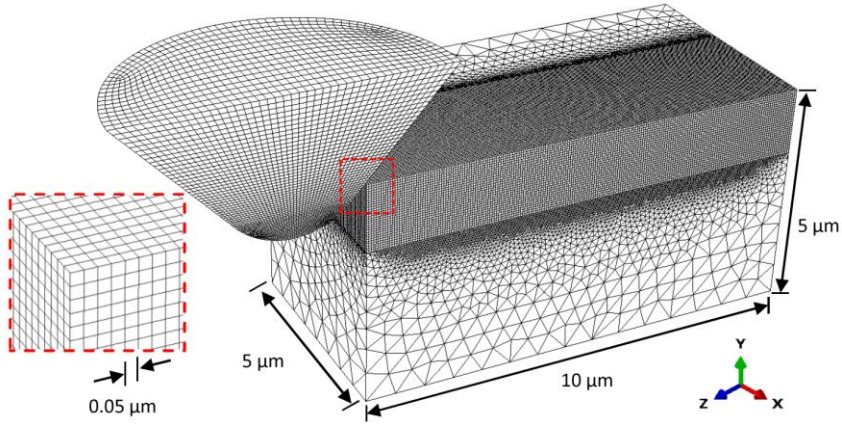

Fig. 46 A picture of the model developed by Sun et al. [104].

The constitutive model for reproducing correctly the behavior of the alumina under the effect of the abrasive grain was carefully selected. In addition, the criterion that determined when the elements failed was accompanied with another criterion that determined when the elements where finally deleted from the model. This additional criterion was called failure strain. In this way, the effect of loose workpiece particles could be taken into account.

The effect of different values of the failure strain was analyzed in terms of workpiece surface, grinding forces and subsurface residual stresses. However, only a visual comparison was carried out between a real alumina sample and the model.

Dai et al. [105] studied the effect of the grinding speed and undeformed chip thickness on the grinding process of Inconel 718. For this purpose, they developed a single grit 2D model in Abaqus®, see Fig. 47.

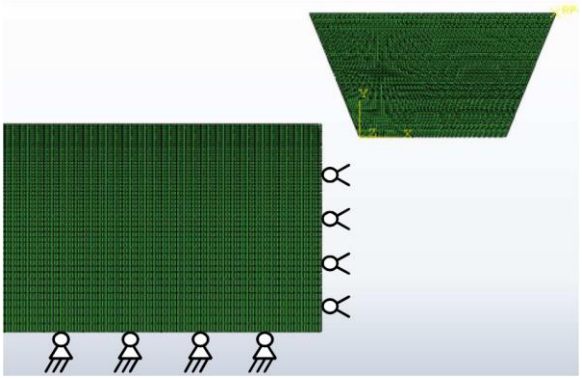

Fig. 47 A picture of the 2D model proposed by Dai et al. [105].

The kinematics of a grinding were simplified by a linear relative movement between the grain and workpiece instead of the trochoidal movement. The workpiece was a reproduced as a square plate and the CBN grain was reproduced as a semi-hexahedron. Calculations with a wide range of cutting speed were carried out, from 20 to 400. The contact depth was considered equivalent to the undeformed chip thickness of a real grinding process. At each grinding speed, undeformed chip thicknesses equal to 1, 2, 4, 6 and 8 µm were used. Later, these uncut chip thicknesses were extrapolated to cutting depth and feed speed of the real grinding process through Eq. (9), where d_{eq} is the grinding wheel diameter, v_w is the feed speed, v_s is the cutting speed and a_p is the cutting depth.

$$a_{gmax} \approx 2 \cdot \pi \cdot d_{eq} \left(\frac{v_w}{v_s}\right) \sqrt{\frac{a_p}{d_{eq}}} \tag{9}$$

Thanks to an appropriate meshing, they were able to reproduce the important plastic deformation occurred in this process before the chip formation. The morphology of the deformed material together with the grinding forces, flow stresses in the material and temperature were analyzed for understanding the speed effect in the range of undeformed chip thickness mentioned before.

The results concluded that on the one hand, the speed effects were more noticeable at high undeformed chip thicknesses. On the other hand, the speed effect caused a progressive hardening effect until 150 m/s and a progressive softening effect for faster speeds. However, these interesting results were not supported by experimental tests.

Akbari et al. [86] developed also a single-grit linear model. Nevertheless, in this case, the model was created in a 3D environment with MSC software®, see Fig. 48.

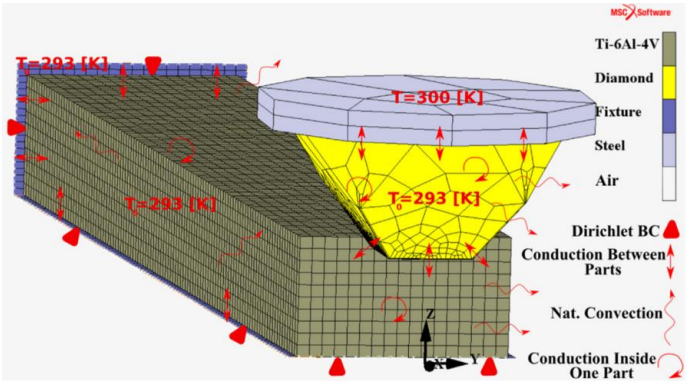

Fig. 48 A picture of the model proposed by Akbari et al. [86].

The purpose of the authors was to develop a damage criterion for the machining of Ti6Al4V with negative rake angles. Thus, at first, they carried out single-grit linear tests in order to have empirical data for supporting their simulation. The geometry of the diamond was digitalized with the aim of using the same geometry in the model. Finally, the values of forces, temperature distribution and plastic deformation were used for adjusting the model.

The forces obtained in the model matched with the forces obtained in the experiments but the comparison was only done at a single test parameter combination. As a consequence of the good agreement, authors mentioned that the model together with the damage criterion will help to design the tools and the process parameters in order to improve the productivity and minimize the tool wear. However, further work must be done in order to see if the model reproduce correctly the process under other grinding parameters.

Apart from these approaches using single grit configuration, Zhang et al. [71] simulated the contact with a multigrain surface. The virtual grinding wheel surface was created by hexahedral blocks with random distribution and orientation. The grain size and grain density were used for making the virtual multigrain surface equivalent to a real grinding wheel surface, see the virtual surface in Fig. 49.

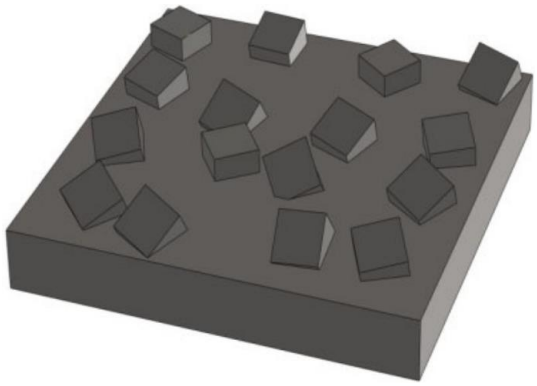

Fig. 49 The multigrain Surface created by Zhang et al for their FEM model [71].

As it can be seen, the abrasive grains were defined as hexahedron that did not match the assumptions of other authors about the high negative rake angle of abrasive grains. Once the surface was designed it was imported to Deform® commercial software where the grinding

process of tungsten carbide was modeled. Complementary to this model, the machine structure was also modeled in Ansys® software for a closed-loop model. In this way, the grinding forces where used for calculating the deflection of the machine and then, the deflections were used for running again the grinding model. At least, three iterations were needed for reaching the equilibrium between both models. See a schema in Fig. 50.

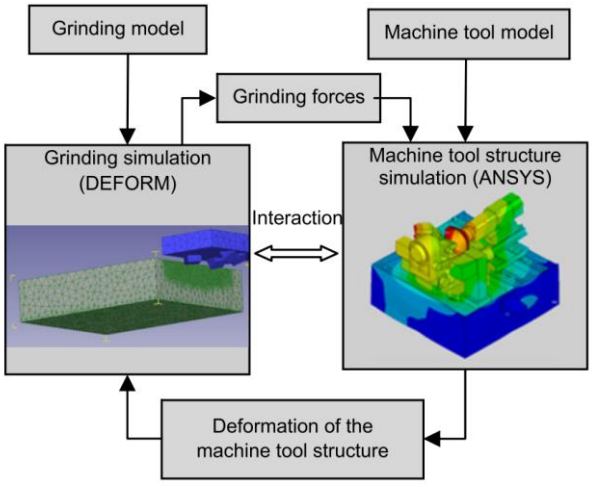

Fig. 50 The schema of the methodology proposed by Zhang et al. [71].

The force obtained during the grinding simulation was compared with the force registered during experimental tests. The experimental tests were carried with the same materials as those defined in the model in order to have as close situation as possible. The kinematics were also the same, the linear relative movement was reproduced by means of a cup diamond wheel and a specific workpiece material shape as explained back in section 1.4. However, cutting fluid was used during the tests while no mention was done in the model regarding this aspect.

Despite the efforts done on the proposed methodology, only the mechanical loads were addressed. The thermal loads may cause deflections also in the machine structure that may affect the accuracy of the grinding process. For a complete model, the thermal aspect should also be comprised by both models.

Taking everything into account, it has been acknowledged that in a grinding operation, the result of the interaction between the wheel and the workpiece depends strongly on the wheel surface and the cutting parameters. Despite the fact that the works mentioned previously addressed several scenarios, a thermo-mechanical model where the contact is studied with a multigrain surface with real geometry has not been carried out.

FEM provides some advantages with respect to the previously introduced model types. On the one hand, there is a complete control on the geometry of the abrasive surface. On the other hand, mechanical and thermal analysis can be carried out in the same environment without the need of coupling several models.

TOPOGRAPHIC CHARACTERIZATION AND WEAR ANALYSIS OF ELECTROPLATED CBN GRINDING WHEELS

2 TOPOGRAPHIC CHARACTERIZATION AND WEAR ANALYSIS OF ELECTROPLATED CBN GRINDING WHEELS.

2.1 INTRODUCTION

This thesis addresses the contact between EP CBN grinding wheel and Inconel 718 under CFG conditions. One of the aspects that determines the grinding performance is the specifications of the wheel. Depending on the process requirements and the workpiece material, the wheel is defined for increasing the productivity, minimizing the wear and ensuring a good performance during the grinding process. However, as a consequence of wear, the topography of the grinding wheel changes as the workpiece removed volume increases. Therefore, for a given process configuration, it can be stated that the contact and the wheel performance will vary as a function of wear. The wear was introduced back in section 1.2.2.

The influence of wear on the grinding wheel performance is controlled by dressing the wheel. The dressing process is used for recovering the original wheel topography and thus, the optimal situation of the grinding process. There are numerous ways for dressing a grinding wheel depending on the wheel specifications and the grinding operation, see section 1.2.3 for further information. Nevertheless, EP CBN wheel cannot be dressed because of the fact that they only have a single abrasive layer. This situation hampers the grinding process since the grinding conditions get worse as the wear on the wheel increases.

In the review of the state of the art some works that studied situations with the same grinding wheel, similar grinding parameters and nickel base alloys as workpiece material were cited [6],[38],[39],[43]–[45],[47],[50],[53]. The majority of them found the same wear types, namely, wear flat, grain fracture and grain pull-out. These wear types were measured in terms of different parameters.

In the state of the art, three different wear types were mentioned for EP CBN grinding wheels, namely, grain fracture, grain pull-out and wear flat. Their cause together with their consequences in the grinding process are explained in section 1.2.2.2.

Nevertheless, the wear types do not depend only on the grinding wheel but also on the grinding process itself. Taking this into account, the current grinding process was analyzed in order to pay special attention to the most likely wear types. On the one hand, the effect of the grinding parameters was taken into account. In CFG the high cutting speed and low feed rate result in a low chip thickness. It was explained before that a low chip thickness entails low grinding forces and as a consequence the wear flat is more likely to appear than other wear types.

On the other hand, grinding wheel configuration was addressed. The grinding wheel configuration is usually designed for adapting the wheel to the process so that achieving a stable solution. In this way, special bonding types, grain geometry and grain structure are being developed for reducing the need of dressing the wheel through self-sharpening phenomena. However, the nature of EP CBN wheels does not allow significant variation. The bonding material is a nickel base matrix that covers the grains up to the half of its size. This matrix is a mechanical

junction that provides a high retention. The grain size can be selected as a function of aspects such as the final roughness of the workpiece and the precision of the profile of the grinding wheel. The grain concentration comes from the plating process, so this usually depends on the grain size. Finally, as a consequence of the high retention force and the toughness of the CBN, these wheels present a good resistance to grain pull-out and grain fracture.

In conclusion, the grinding parameters and the grinding wheel show a favorable scenario for the wear flat. This assumption can be confirmed by problems occurred during the industrial process as vibration marks and thermal damage shown in Fig. 1 and Fig. 51.

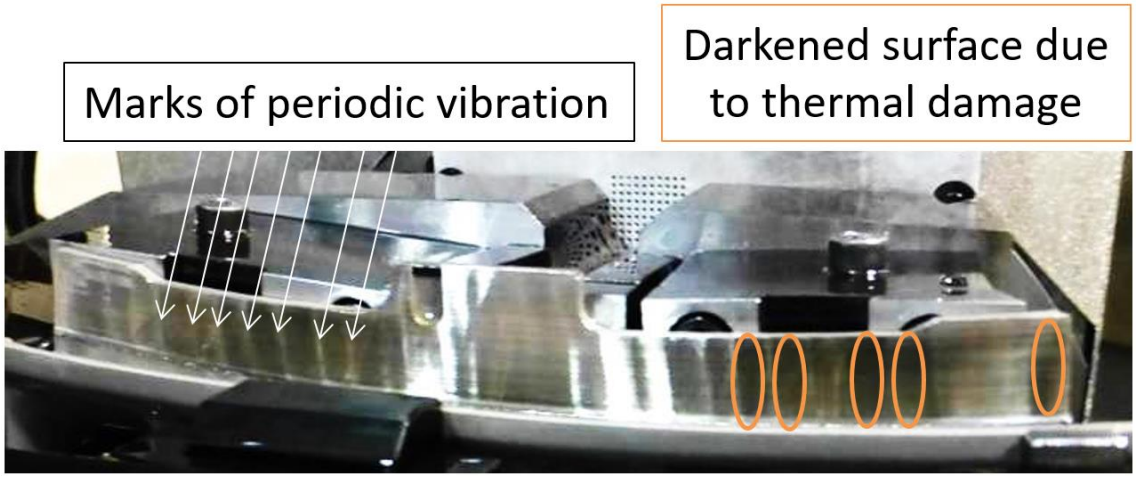

Fig. 51 Vibration marks marked with white arrows and darkened zoned due to thermal damage marked in orange.

For avoiding these problems, some modifications have been done on EP CBN grinding wheels. With the purpose of reducing the thermal loads on the contact, the coolant was transported right to the contact zone through radial holes manufactured on the wheel. Nevertheless, the grains around the hole suffered higher forces and a weaker retention force. Hence, eventual abrasive layer detachment took place beside the holes. This phenomenon was observed during the analysis and some examples are shown in Fig. 52 a) and b).

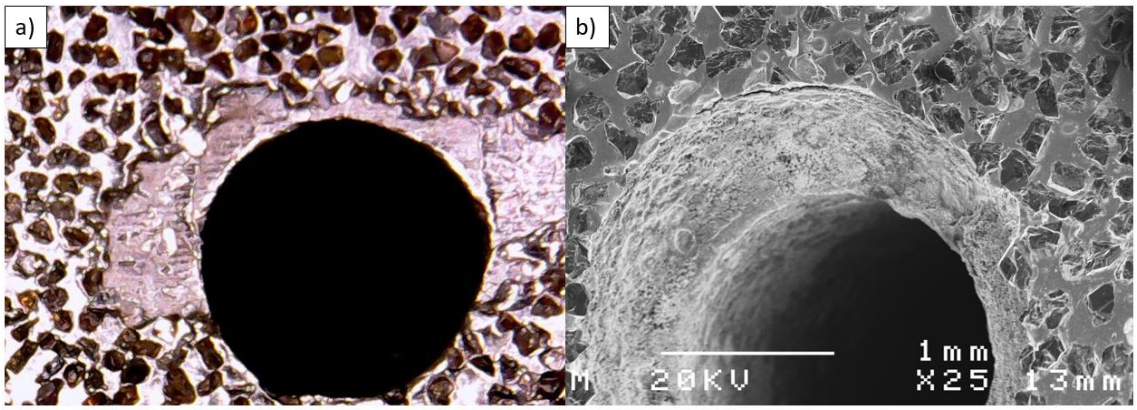

Fig. 52 a) Optical image of abrasive layer detachment next to a hole for lubrication of an EP CBN grinding wheel. b) a SEM image of abrasive layer detachment next to a hole for lubrication of an EP CBN grinding wheel.

The situations shown in Fig. 51 and Fig. 52 causes significant loses for the industry. On the one hand, the grinding operation is one of the last stages on the manufacturing sequence of this

part. In consequence, although the material can be casted again, the accumulated cost of the manufacturing time is completely lost. On the other hand, the EP CBN wheels have a cost significantly higher than the conventional grinding wheels due to their special manufacturing process and the abrasive material. These situations are unacceptable in the aeronautic industry, where the productivity and quality are getting more and more demanding. In spite of the fact that the problem is well known in the industry, there is a lack of understanding about what is taking place in the contact between the wheel and the workpiece; how the wear evolves during the wheel life and how the wear; and how the cutting parameters affect the grinding performance. The aim of this work is to understand this process with the purpose of being able to increase the productivity and avoid the problems mentioned previously. The first step of the study is addressed in this chapter. The methodology and results of a topographic analysis of the wheel surface are gathered in the following lines. The information obtained in this chapter will be a key point for the following chapters.

The topographic analysis was mainly focused on the wear flat given the favorable conditions for its appearance due to the grinding parameters and grinding wheel configuration. However, other wear types detected by other authors were also considered as plausible. The topographic analysis was carried out at different wear states of EP CBN grinding wheels used in ~~the~~ industry in order to register the evolution of both the wear types and the wear degree from the beginning to the end of the wheel working life. Standardized 3D roughness parameters from Standard ISO 25178 were used for characterizing the wheel. The most representative ones were selected through statistical methods and finally, the wear evolution along the wheel life was explained through the variation of those parameters.

2.2 METHODOLOGY

The wheel wear appears during the wheel life and gets more severe as the wheel removes more material. However, not only there is a variation on the severity of the wear types, but it also may be on the presence. That is to say that a specific wear type may be present only at a specific stage of the wheel life. This is characteristic feature of wheels with a single abrasive layer that cannot be dressed.

Taking that into account, the wear of EP CBN wheels has to be studied at different wear states, from a brand-new wheel to a completely worn wheel, i.e. at the end of its life. Furthermore, the wear of the wheels had to be caused by real working conditions since the process parameters have influence on the wear. For that purpose, wheels used in the aeronautic industry for grinding NGV were taken to the laboratory, analyzed and finally taken back to the industry. In this process, different wheel specifications were used, namely, 250 µm in grain size for roughing operations and 180 µm for finishing operations. Since more material per workpiece was removed by roughing operations, a faster wheel wear was expected on roughing wheels within the same number of parts. In consequence, the study was focused on the roughing wheels. The bonding material was a nickel matrix deposited by galvanization that provided a mechanical junction between the grains and the steel body of the wheel. The single abrasive layer covered around the half of the grain size as it can be seen in Fig. 53.

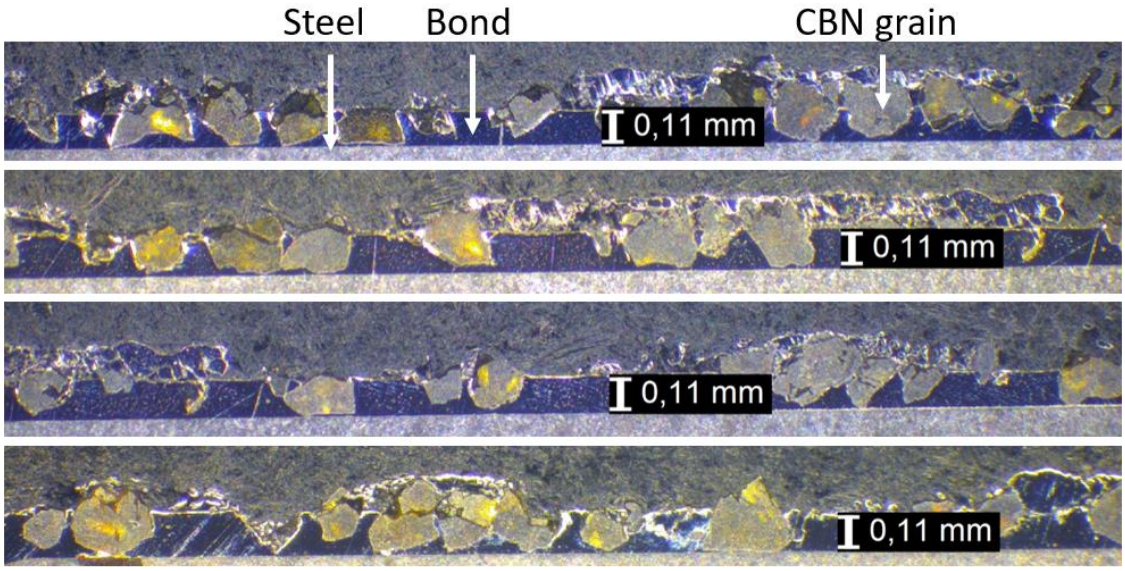

Fig. 53 Macroscope picture of sectioned EP CBN grinding wheels where the depth of the bonding layer can be measured.

The surface of the wheel can be digitalized by means of contact devices, such as a stylus profilometer, and optical devices, such as a confocal microscope. Each one has its own features and their suitability depends, on the one hand, on the sample to be digitalized and, on the other hand, on the needed information. For that purpose, the geometrical features of the grinding wheel were analyzed.

The size of the abrasive grain used in the wheels of the study was 250 µm. In Fig. 54 the number of grains on a 4.5x4.5 confocal digitalization of the wheel surface was counted. From that value, the grain density and the equivalent number of grains per mm in length was calculated. Also in that figure the maximum number of grains per mm considering only the grain size was calculated, namely, 4 grain/mm. The number of grains per mm calculated from the confocal digitalization was 3.26 grain/mm, what is more than the 80% of the maximum possible grain number per mm.

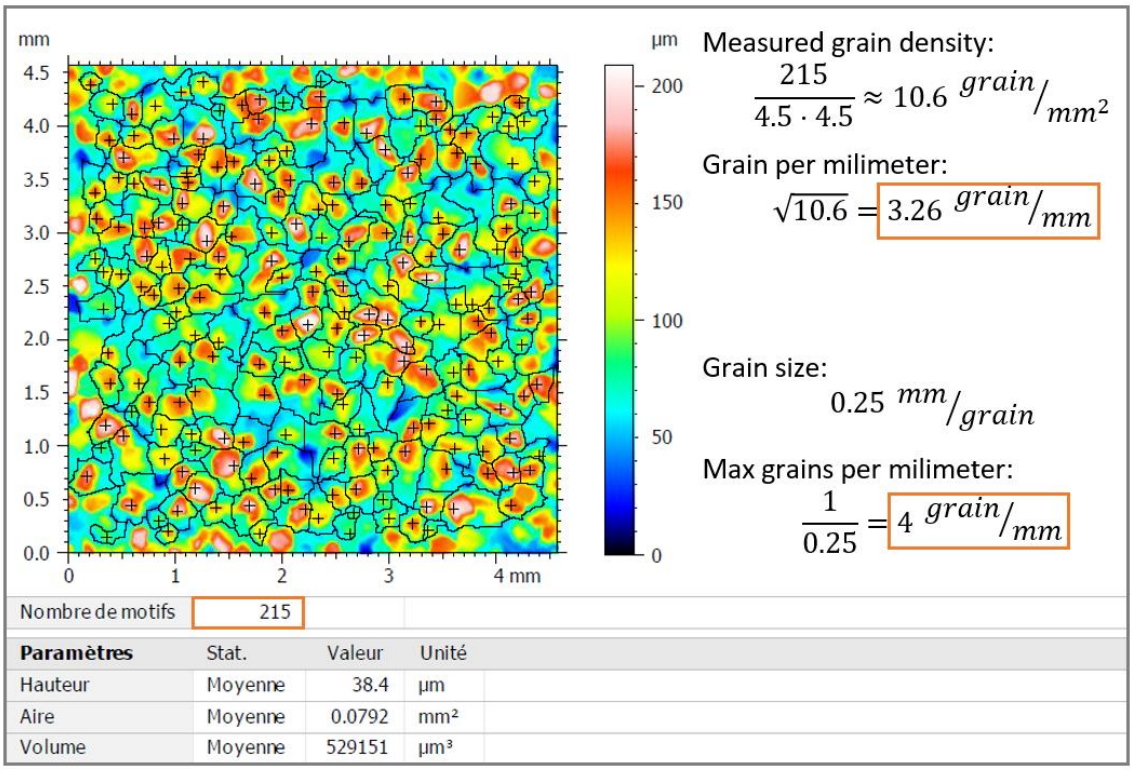

Fig. 54 Number of grains counted in a 4.5x4.5 confocal digitalization and a comparison of that value with theoretical maximum grain concentration for 0.25mm grain size.

The high grain density can hamper the measurement if a stylus profilometer is used for digitalizing the wheel surface. This problem has been noticed by Blunt and Ebdon [65] during the digitalization of a grinding wheel. By contrast, optical measuring devices do not suffer this limitation. Instead, they can be affected by the optical features of the samples e.g. a shiny surface can produce false peaks in the digitalization. Moreover, the time required for the digitalization was significantly higher for a contact device than for an optical device. Hence, the wheel surface was digitalized through optical devices and special attention was put on the optical features of the different elements. Among the wide range of optical devices that can be used for characterizing a surface, the following three were selected:

- Macroscope.
  A macroscope is an optical device that allows to take magnified pictures of a surface if it is used together with a digital camera. The images can be saved in a computer together with a metadata file that contains valuable information as the scale of the picture. This information can be used by picture analysis software for taking a wide range of measurement. It should be mentioned that the measurement available with this kind of technology can only be based on the optical properties of the pictures, namely, distances, areas, particle counting and image color treatment.
  That being said, in these pictures the elements of the wheel surface could be differentiated, which is helpful when the color of the elements is the most significant difference among them. For instance, workpiece adhered material can be detected on or among the grains. Furthermore, subtler aspects as the texture can be addressed as well. This can help to differentiate a worn grain from a new one or to detect whether the bonding material has been damaged during the process.

In this work a Leica DSM 300® was used for acquiring the pictures and Leica Application Suite was used for the analysis.

- Confocal microscope.

  A confocal microscope is an optical device capable of digitalizing surfaces in three dimensions; its functioning can be described as follows.

  The key component of a confocal microscope is called pinhole. The pinhole is a hole in a plate located between two lenses before the detector. The size and the location of the pinhole is critical so that only light coming from a plane located at the focal distance can pass through and reach the detector, green beam in Fig. 55. In order to find the focal plane of the point, the microscope must be moved in the light beam direction. Once the focal distance has been found and the detector has received the light, the height of the focal plane is registered together with the other two coordinates and the microscope moves to the next point. Both the size of the surface to be measured and the range in height covered by the microscope are defined by the user. The result of the digitalization is a cloud of points that can be opened either by any data analysis software or by specialized software provided by the microscope manufacturer.

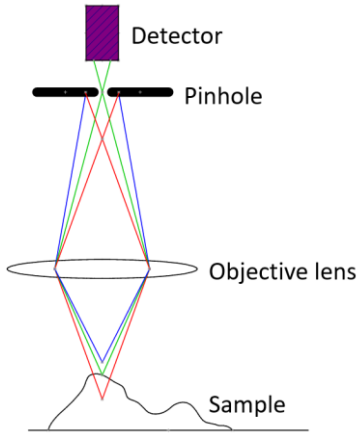

Fig. 55 Confocal microscope functioning schema.

In spite of the advantages of the confocal technology, wrong measurement can take place due to special optical features of the surface. As it registers the height of the point whose light beam passes through the pinhole, a shiny surface can cause inaccurate measurement. This is the case of the EP CBN wheels, where the elements on the surface, i.e. the nickel layer and the CBN grains, present different optical features. In Fig. 56 a) some peaks and valleys can be seen on both the bond and the grains, despite the fact that the majority of the surface resembles precisely the wheel surface, the presence of these false phenomena will affect the measurement. With the purpose of facilitating and improving the characterization process, the optical features were homogenized.

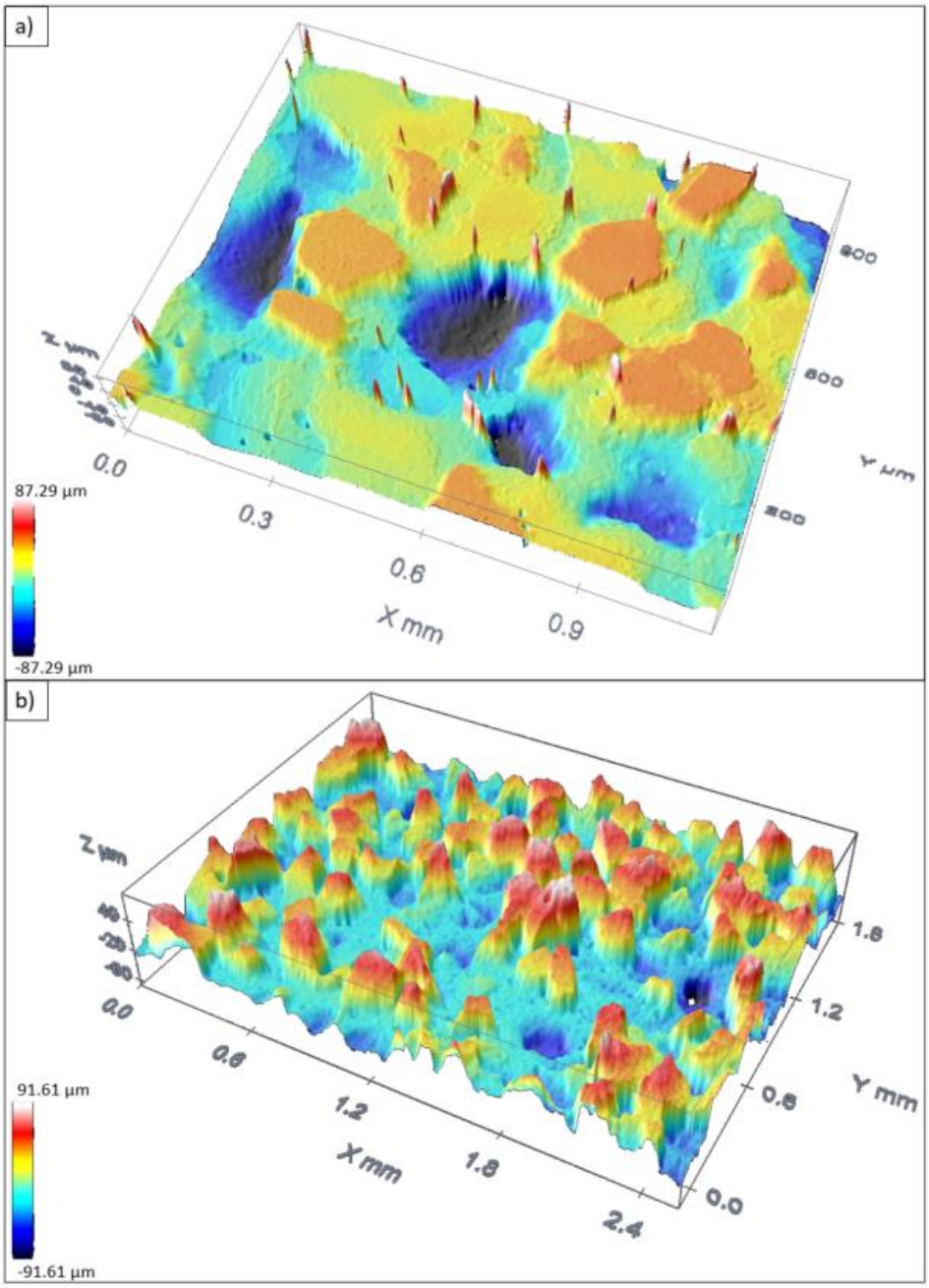

Fig. 56 a) A digitalized surface of an EP CBN grinding wheel with false peaks. b) A digitalized surface of an EP CBN grinding wheel without false peaks.

Resin replica was used as an alternative with the aim of obtaining the negative profile of the wheel surface for a later observation. Nevertheless, some grains were pulled-out from the wheel when the replica was removed because of the high adhesion force developed during the curing of the replica. As an alternative, the surface was covered with a black graphite layer applied with a spray that was easy to remove and did not have any influence when the wheel was later returned to the grinding process. In Fig. 57 a) there is a wheel surface painted in black, and the same wheel zone after being cleaned in Fig. 57 b). A slight mark can be seen where the graphite was applied but that had no influence in the grinding process.

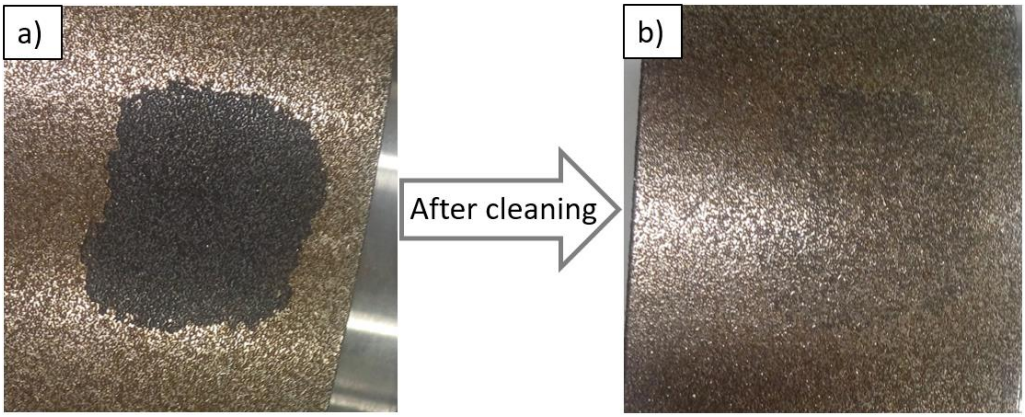

Fig. 57 a) The surface of an EP grinding wheel with the graphite layer applied on its surface. b) The same zone of the wheel after being cleaned.

In this way, the appearance of false peaks and valleys was avoided, as it can be seen in Fig. 56 b).

For this work, a confocal microscope Leica DCM 3D® was used whose acquisition software was Leica Scan® and the analysis software Leica Map®.

A surface size of 2.55 by 1.9 mm was established as standard for the digitalizations so that all the results were obtained from digitalizations with the same amount of data. An example of a digitalization can be seen in Fig. 58.

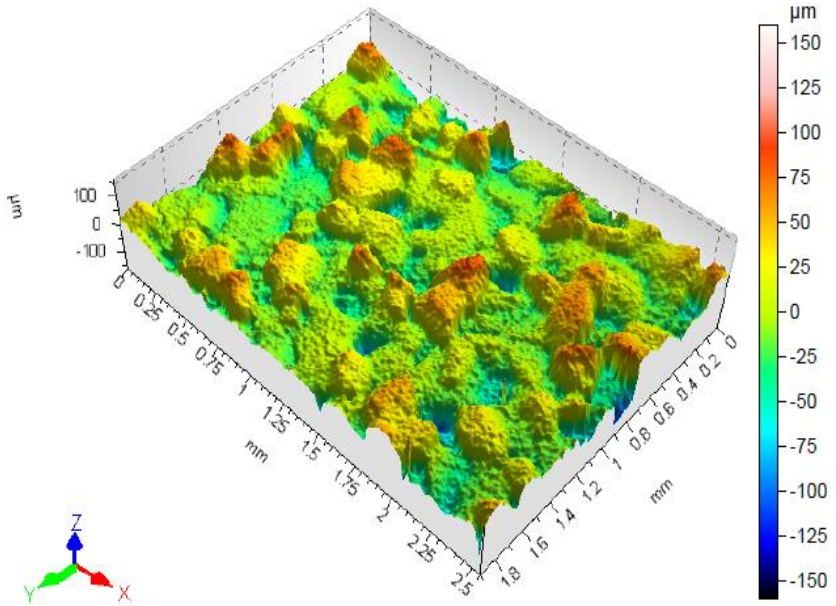

Fig. 58 An example of the digitalizations used for the topographic analysis.

- Scanning electron microscope

  A SEM is an optical device that uses electron beams instead of light in the visible spectrum. According to the Rayleigh criterion, the maximum resolution of a picture that can be taken from a body is directly proportional to the wavelength of the light used for the observation. The wavelength of the electron beam is in the range of 10^4 and 10^5 times shorter than the wavelength of the light within the range of the visible spectrum.

Therefore, higher magnification with a better resolution can be achieved by the electron beam. Furthermore, a SEM has more applications than taking only optical pictures.
When the electron beam collides against the sample surface, different types of electron beams are reflected back:

- Secondary electrons are the electrons reflected by the surface of the sample. The pictures obtained by these electrons are comparable to optical pictures; they can only be focused on a plane. Thus, the image gives information about the third dimension of the profile by the difference between the focused and unfocused elements. The pictures are plotted in white and black, see an example in Fig. 59.

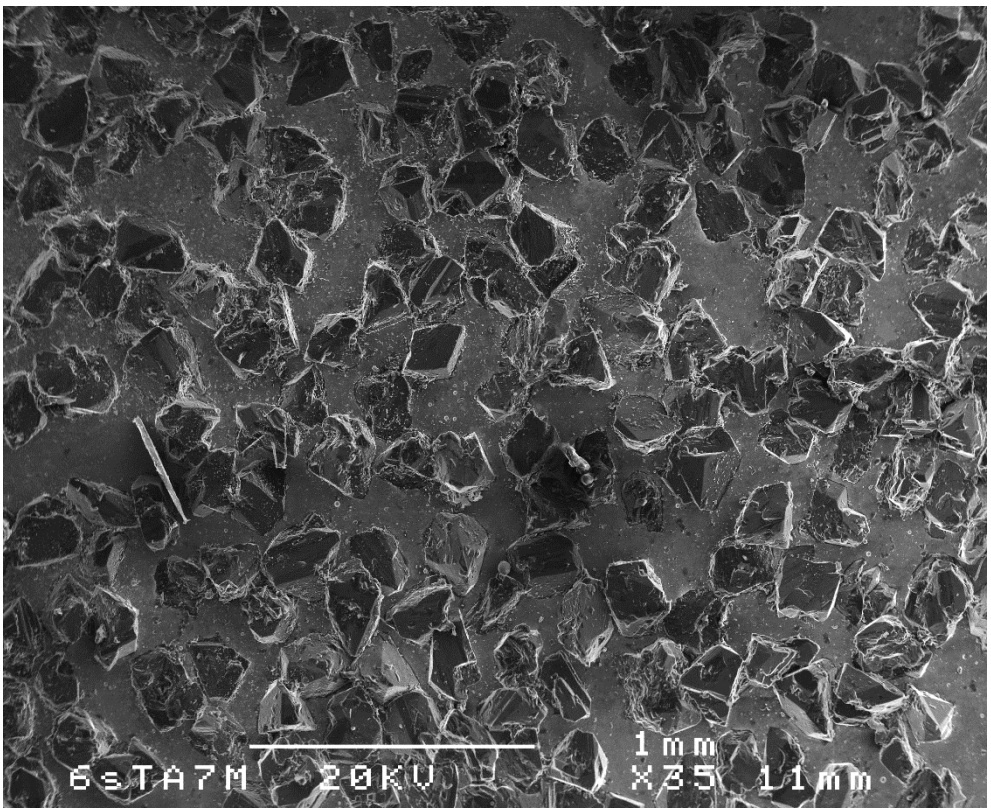

Fig. 59 The surface of an EP CBN grinding wheel digitalized with a SEM through secondary electrons.

- Backscattered electrons are the electrons that have penetrated the sample surface, reacted with the material and then scattered back outside the sample through the surface. The image composed by gathering this type of electrons is flat, i.e. there are no unfocused points. The energy of the backscattered electrons resembles to atomic number of the material they have reacted with. Hence, the materials of the sample can be easily differentiated by their density. These pictures are also plotted in black and white, see an example in Fig. 60.

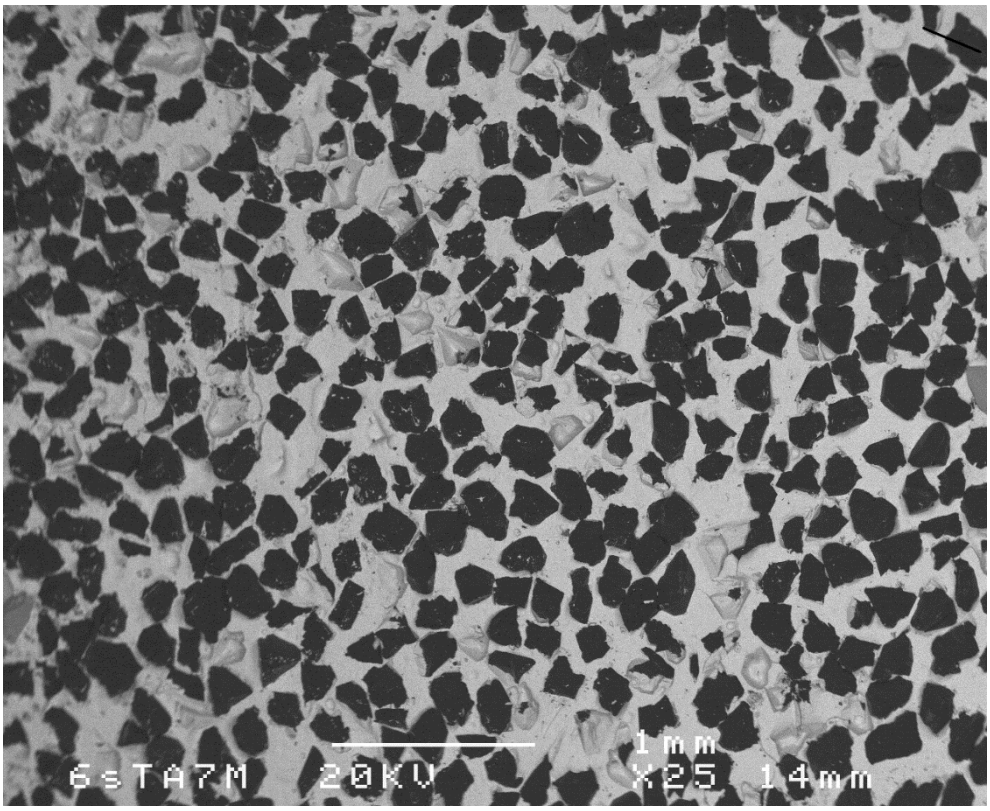

Fig. 60 The surface of an EP CBN grinding wheel digitalized with a SEM through backscattered electrons.

- Apart from the analysis done with the two types of the electron beams, energy-dispersive X-ray spectroscopy, EDXS, analysis can also be carried out in the majority of SEMs. When the electron beam hits the sample, a part of the energy of the beam is transmitted to the electrons of the atoms of the sample. As a consequence, the electrons of the lower shells are excited and can either jump to shells with higher energy or be kicked-off. If they are kicked-off, they leave a space with positive charge that attracts electrons from higher energy levels (shell). When the electron from the higher energy levels descends to fill the space left by the former electron, the difference in energy is released in form of x-rays. The energy is characteristic of the atomic number of the element; hence, the spectrum of the x-rays can be considered as the fingerprint of the element. SEMs usually are equipped with a detector of X-ray and a software for analyzing the spectrum. Depending on the aim of the study, qualitative or quantitative analysis can be performed. On the one hand, qualitative analysis reveals the chemical elements of the sample and their location superimposed on the secondary electron image. On the other hand, quantitative analysis adds the information of the concentration of each chemical element, so that the material of the sample can be revealed. Fig. 61 a) shows a secondary electron image, Fig. 61 b) shows the energy spectrum of the X-ray and Fig. 61 c) shows, in red, the location of nitrogen and, in blue, the location of nickel. Nitrogen is a component of CBN (cubic boron nitride) and nickel is the bonding material. In addition, the origin of the debris can be also deduced. Those made of nickel come from the workpiece since it is a nickel base superalloy, while those made of nitrogen are fractured pieces of grains.

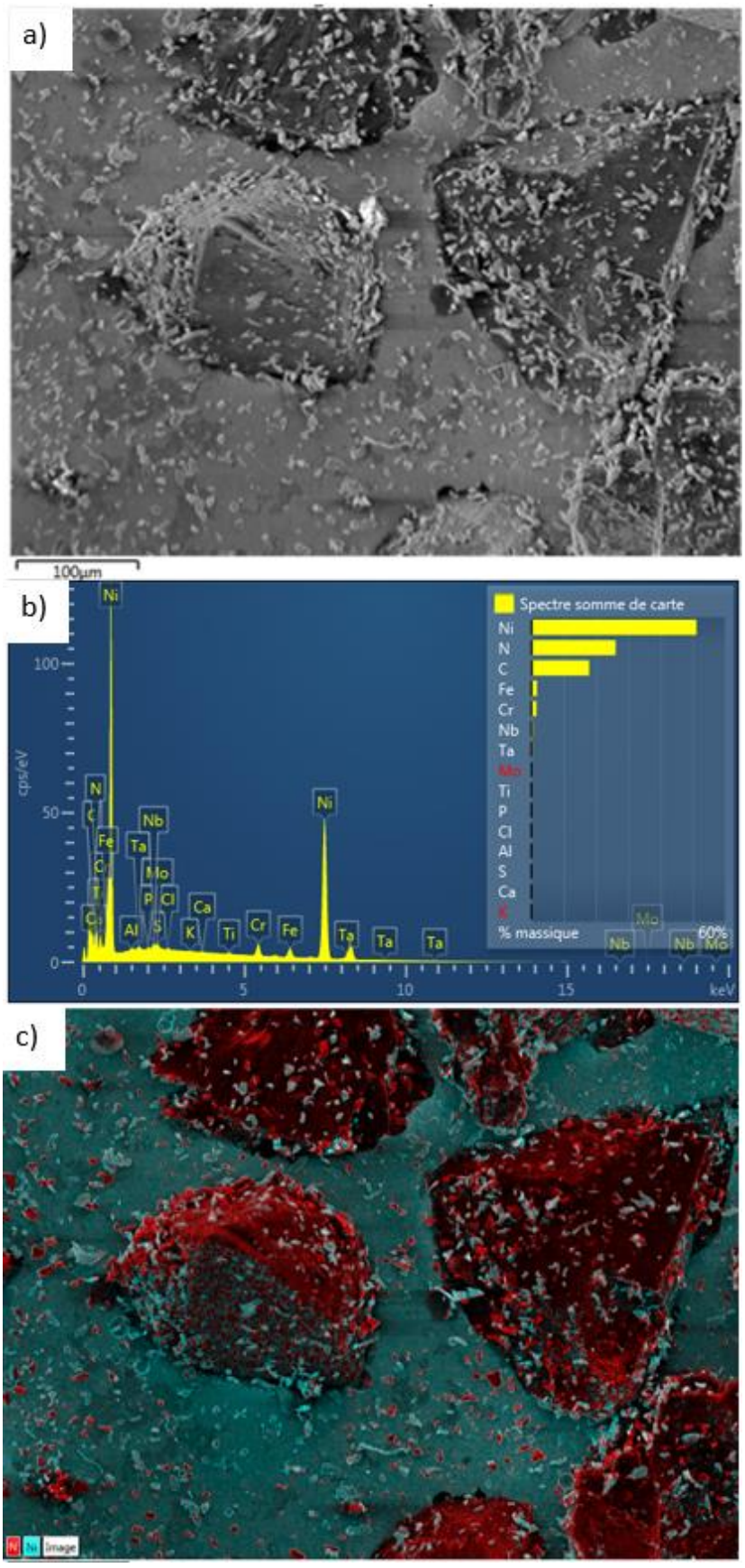

Fig. 61 a) A SEM image of CBN grains in the nickel bond matrix. b) The energy spectrum of the X-ray emitted by the surface. c) The image obtained from the X-ray spectrum superimposed with the original surface

The use of a SEM is more delicate in comparison with the two devices explained previously. The microscope is a sealed tube with a vacuum atmosphere inside for working in a cleaner environment. The sample size must be small, in the range of a few millimeters, since it must be loaded in a chamber where the vacuum must be done before being inside the microscope. The sample must be electrical conductor for being able to interact with the electron beam. If the sample is not conductor, it must be coated by a thin layer of gold or carbon.
In this work, some wheels were removed from the industrial process and small samples were extracted through wire electro discharge machining in order to be observed by SEM and analyze deeper the state of the wheel surface. The device used during this work was a Jeol® JSM 7100 F TTLS.

There are several surfaces with different geometry that are ground in an NGV. This process requires a specific wheel geometry for each one in spite of being ground under the same parameters. Taking this into account, wheels used for grinding two different surfaces were used for the topographic study.

As it was mentioned before, the grinding parameters and wheel specification are the same in every roughing operation. However, because of the geometry of the surface to be ground, the zone of the wheel to be measured must be chosen in order to correlate the wear observed with the corresponding accumulated volume of workpiece material removed.

One of them was a straight wheel of 150 mm in diameter and 50 mm in width. This was the responsible of grinding surfaces with irregular section called *wedge faces*, see the wheel in Fig. 62 a) and the wedge faces in Fig. 62 b) and c). If the workpiece material removed volume by each millimeter of wheel width is plotted, an important difference along the 50 mm can be seen. In this case, the difference between the center of the wheel and one of the ends of the wheel is in the range of 2.5 times higher, as it can be seen in Fig. 62 d).

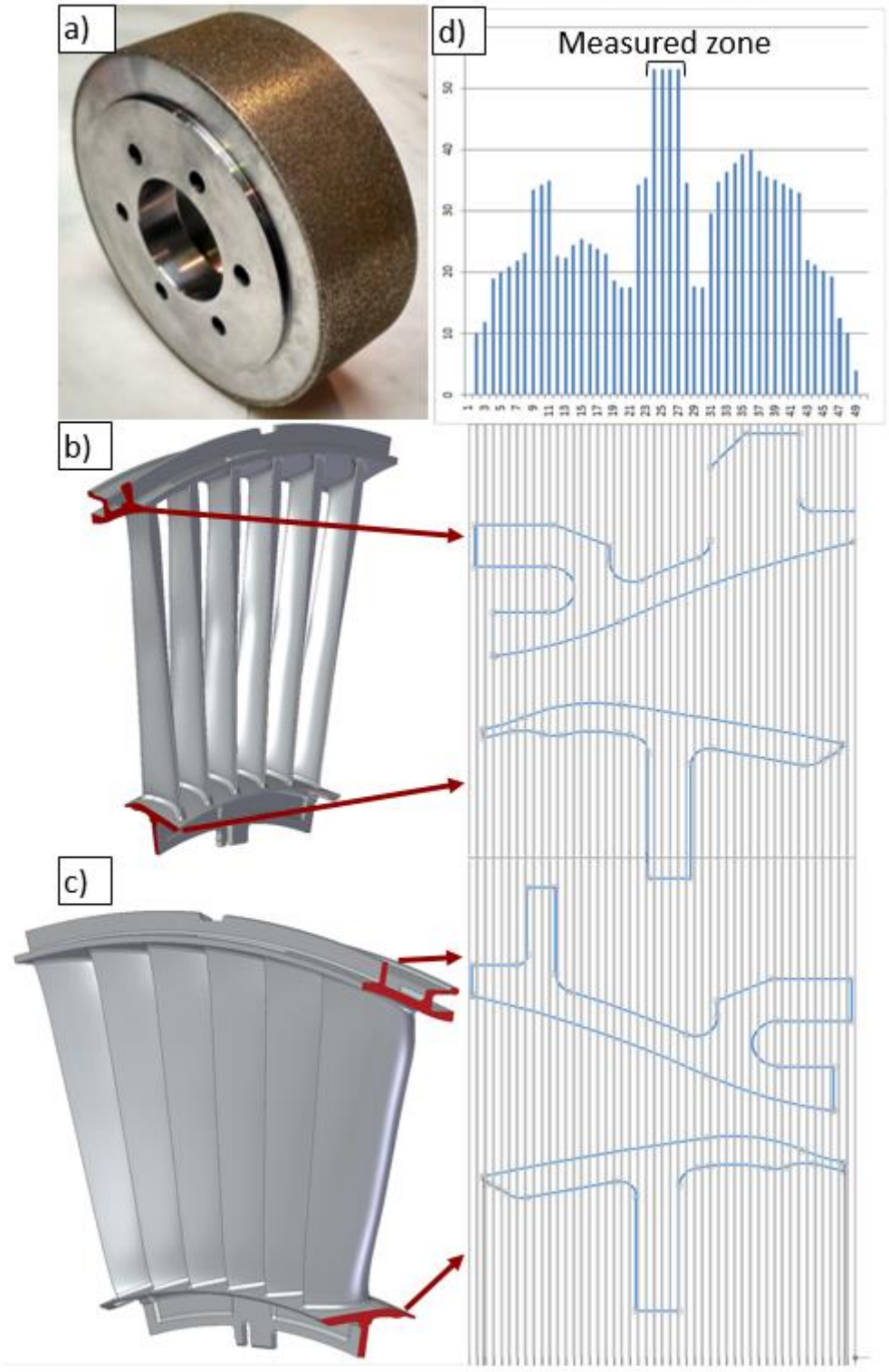

Fig. 62 a) The straight EP CBN wheel used for grinding the wedge faces. b) A view of a NGV and the wedge faces of one side marked in red. c) Other view of the NGV with the wedge faces of the other side marked in red. d) The corresponding workpiece material volume per wheel width.

The other wheel used for this analysis was the responsible of grinding the surface called *inner rail*, see the wheel in Fig. 63 a). The geometry of the inner rail, Fig. 63 b) and c), required a conical wheel, the outer diameter of the wheel was 180 mm in order to ensure the cutting speed in the

inner diameter. Similarly to the previous wheel, the wear was not constant in all the wheel width. In Fig. 63 d) two zones can be clearly distinguished. The clearer zone has more work load than the darker zone. For this study, the data obtained from the outer zone of the wheel was used.

Fig. 63 a) The wheel responsible of grinding the inner rail. b) and c) the two sides of the inner rail marked in red. d) The conical wheel with two differentiated zones as a consequence of the wear.

Moreover, the wheel should be measured on different zones along its circumference in order to have a global measurement of the wear. For this reason, every wheel was measured on 6 different zones of its circumference, i.e. at every 60^{o}.

The process of digitalizing the 6 points of the wheels on the most loaded zone was repeated at different wear states, i.e. accumulated workpiece material removed, along the wheel life. For this purpose, the wheels were taken from the industry to the university together with the HSK chuck used for clamping the wheel. In this way, the runout of the wheel when it was mounted again on the machine was reduced. The wheel of the inner rail during the digitalization process can be seen in Fig. 64.

Fig. 64 A conical wheel on the table of the confocal microscope during the digitalization process.

2.3 RESULTS

In this section, the results obtained during the topographic analysis are presented.

2.3.1 Qualitative and quantitative analysis of wear types

For a given grinding process, the wear type and grade may vary with the workpiece material removal. This phenomenon was addressed during the characterization of wheels at different wear state.

In this section, results of the characterization of wheels with different accumulated volume of workpiece material removed are shown. The wear types were firstly detected by means of optical images. Secondly, roughness parameters from standard ISO 25718 were proposed for evaluating the grade of each wear type. Finally, these parameters were calculated for the wear states found by optical images.

2.3.1.1 Qualitative analysis: Wear type detection

Five different wheel life steps were selected for this section.

- A brand-new wheel. The surface of a brand-new wheel was studied with the purpose of having a point of comparison. It was assumed that this surface did not present any wear type and that any change detected in the following observations is a consequence of wear. The data corresponding with this state is going to be called as *New* from this point on. See the box with dark edges in Fig. 65.

- A touch dressed wheel. A special process, similar to dressing, is conducted on every wheel when it is new. It is called touch dressing and consists of dressing the wheel with a resin bonded SiC stick. The stick is significantly softer than CBN and thus, the effect that it has on the wheel is not the same as it was a diamond dresser. Instead of modifying the grains, it is rather focused on improving the cutting ability of the wheel by means of removing excessive bonding material from the wheel surface and hence, enhance the space between the grains.
  The data corresponding with this state is going to be called S*tick* from this point on. See the box with orange edges in Fig. 65.
- A wheel after grinding 45 workpieces. This corresponds with an accumulated volume of workpiece removed material equal to 121,381 mm^3. The data corresponding with this state is going to be called as *A* from this point on. See the box with grey edges in Fig. 65.
- A wheel after grinding 1,875 workpieces. This corresponds with an accumulated volume of workpiece removed material equal to 5,070,060 mm^3. The data corresponding with this state is going to be called *B* from this point on. See the box with yellow edges in Fig. 65.
- A wheel after grinding 3,000 workpieces. This corresponds with an accumulated volume of workpiece removed material equal to 8,112,096 mm^3. According to the experience of the industry, this was established as a safe wheel life limit. The data corresponding with this state is going to be called as *C* from this point on. See the box with blue edges in Fig. 65.

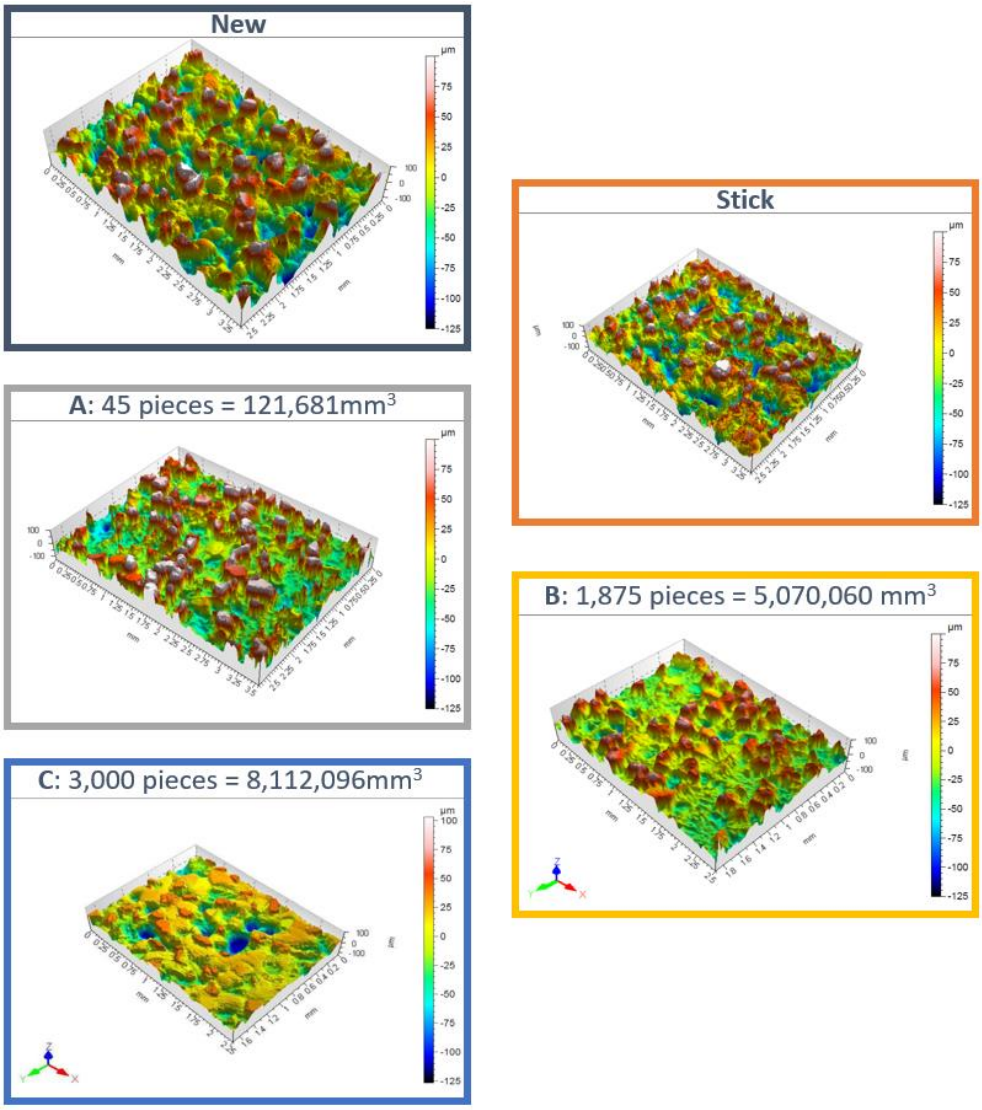

Fig. 65 A confocal digitalization of the five different wear levels studied.

The wear types found by other authors during similar applications were also found in this study.

- Grain fracture. It was found predominantly in *A* and in *B* rather than in *C*. In Fig. 66 there are some captures of the macroscope where fractured grains and untouched grains can be seen together. They are marked in red and in green respectively.

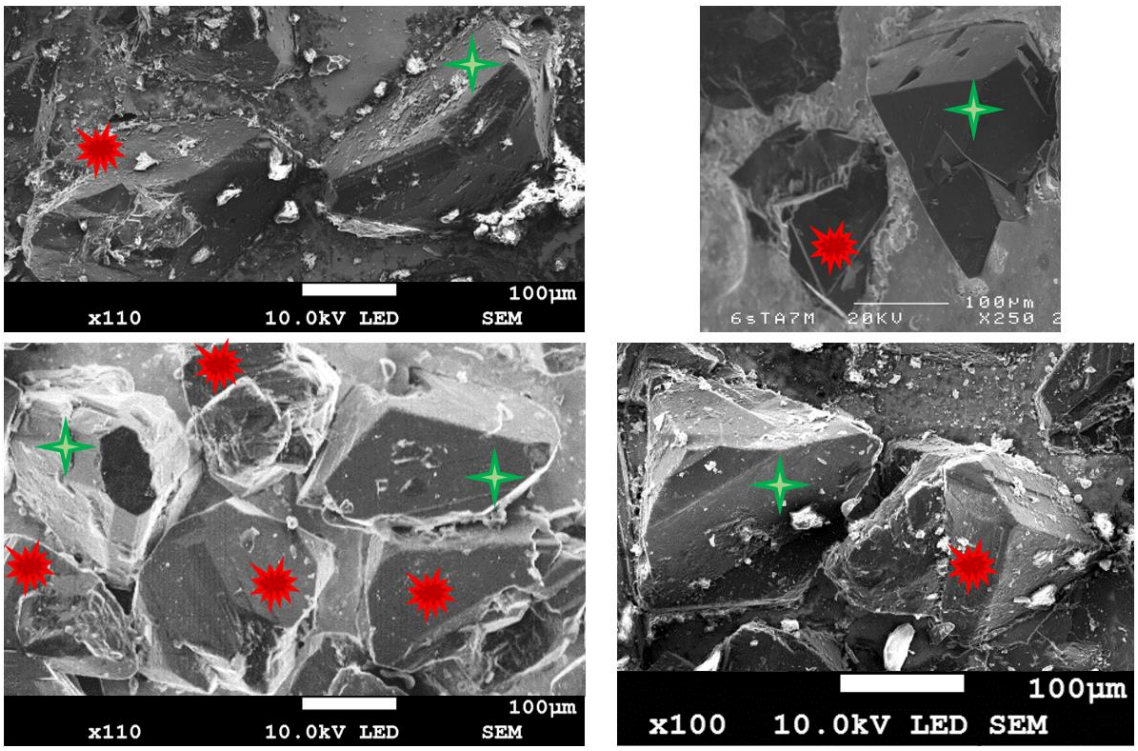

Fig. 66 SEM pictures of EP CBN wheels where there are fractured grains (marked in red) next to untouched grains (marked in green)

- Wear flat. Contrary to the appearance of grain fracture, a greater presence of this wear type was found especially in *C*. On the top left of Fig. 67 there is a 3D digitalization where the grains are flatly worn, on the bottom left there is a macroscope picture of similar grinding wheel where the wear flats are marked in orange. On the right there is a comparison between a flat untouched grain, on the top, and wear flats seen by macroscope and SEM, on the bottom respectively.

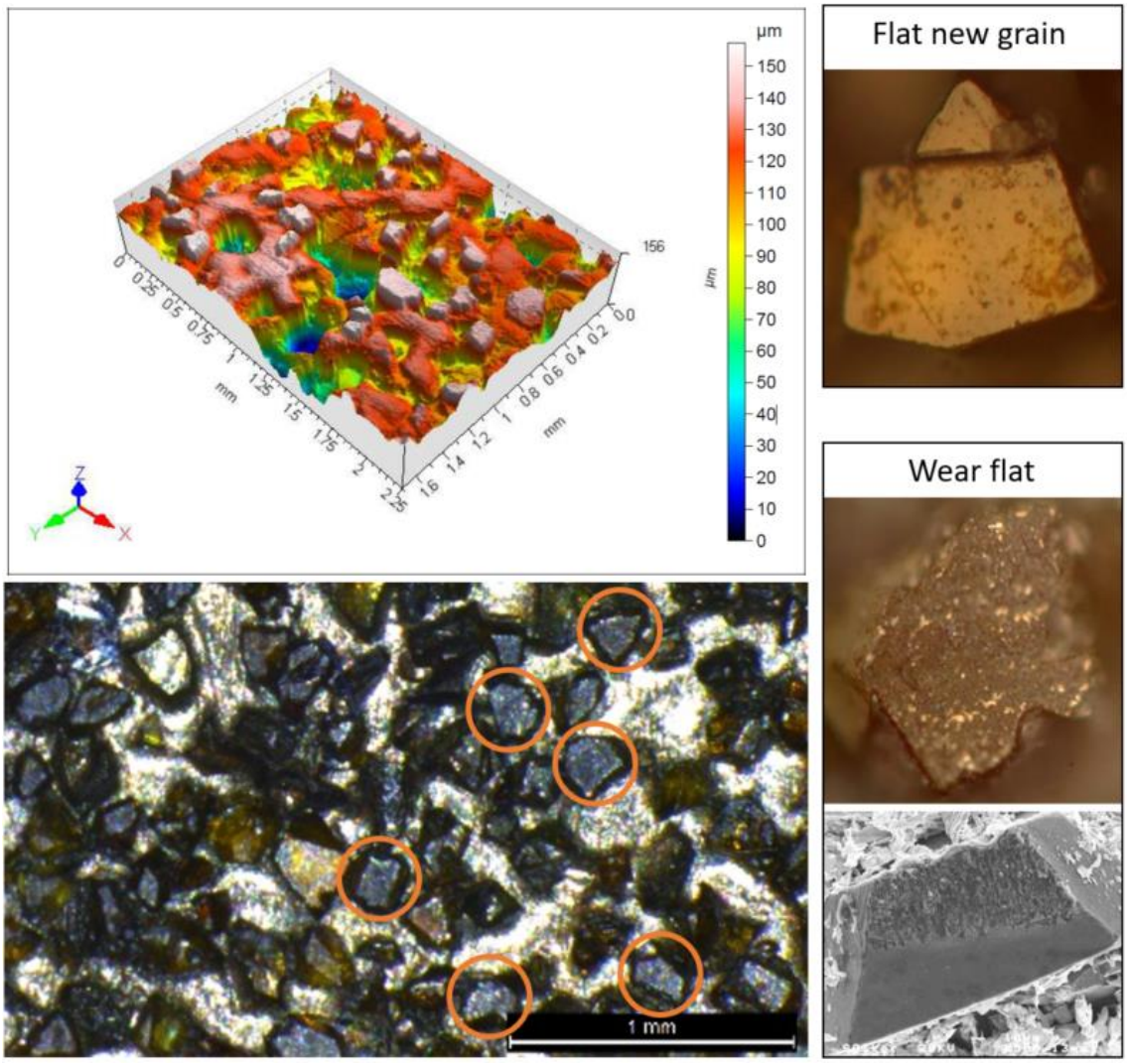

Fig. 67 On the top left a 3 D digitalization of an EP CBN grinding wheel with wear flat on its grains. On the left bottom, a macroscope picture of an EP CBN wheel with the wear flats marked in orange. On the right top there is a macroscope picture of an untouched flat grain. On the right bottom there is a macroscope and a SEM picture of wear flats.

- Grain pull-out. This wear type was hardly found on the observed wheel surfaces. Grain pull-out takes place when the grinding forces are higher than the retention force of the bond upon the grain. Fig. 68 shows the backscattered image of a wheel surface where grain pull-out was found. The holes left by the grains are marked with orange circles. However, the presence of this wear type did not show any correlation with the material removed volume.

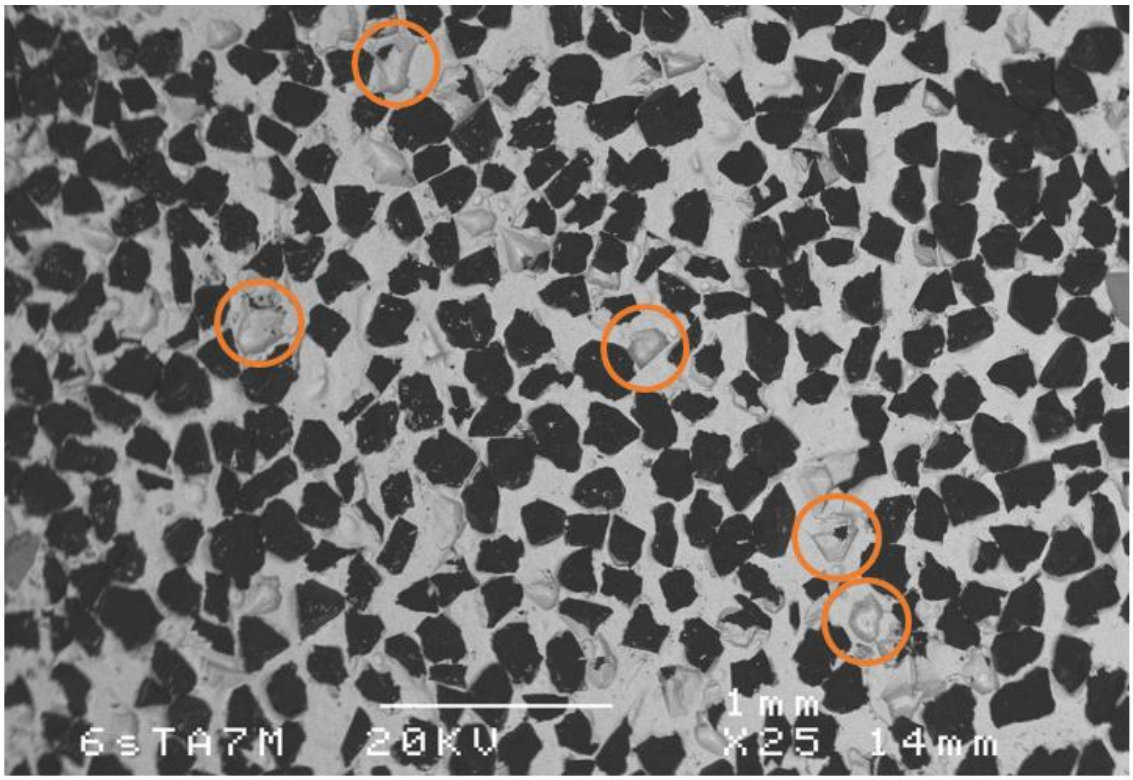

Fig. 68 Backscattered electron digitalization where grain pull-out can be seen marked in orange.

Apart from the previously mentioned wear types, particular catastrophic wears were also observed as a consequence of the severity of the process.

Nickel layer detachment around the holes used for the coolant was already mentioned in section 2.1. However, that phenomenon was also observed in other zones as a result of other adverse conditions.

In Fig. 69 and Fig. 70 the analysis of a nickel layer detachment on the edge and on the center of the wheel are shown respectively. Figures a) are general views of the wheel surface; figures b) are detailed pictures of the zone marked in red, taken with the macroscope; figures c) are the 3D views of the digitalization with the confocal microscope and figures d) show a profile extracted of the 3D digitalization where the step is measured. In both cases, the bonding layer was thicker than the half of the grain size, 149 and 145 µm respectively. This caused a lower grain protrusion grain and less void space for coolant and chips. One of the consequences of having less cutting fluid in the contact zone and less space for chip storage is the increase of the temperature on the cutting zone. The higher temperature in the contact zone in comparison with wheels with the appropriate bonding layer thickness likely caused a weakening of the nickel layer that eventually resulted in a complete detachment as a consequence of the grinding forces.

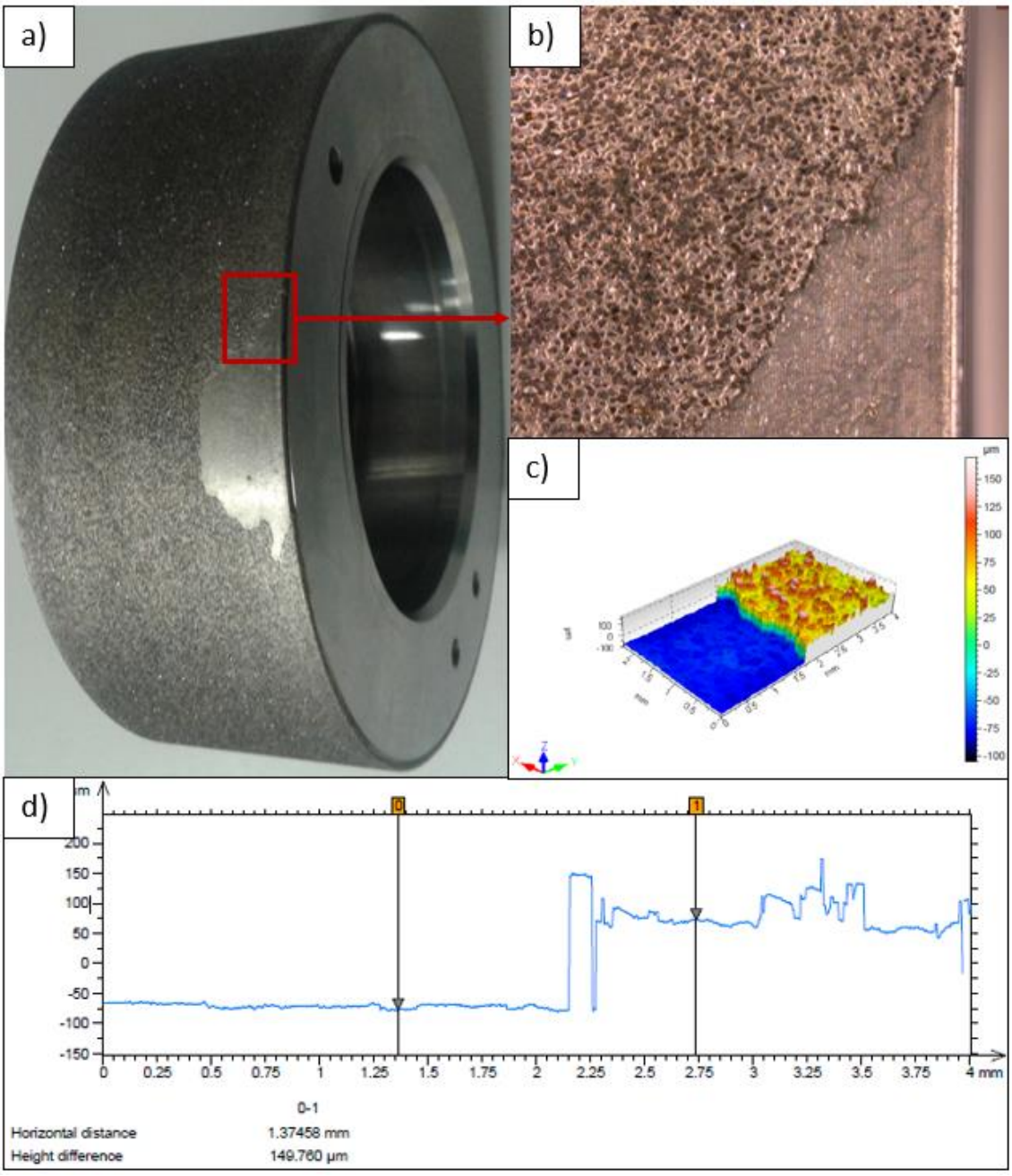

Fig. 69 a) A general picture of an EP CBN grinding wheel with a nickel layer detachment on the edge. b) A detailed macroscope picture of the zone marked in red in figure a). c) The 3D digitalization of the step with the confocal microscope. d) The profile of the step extracted from the 3d digitalization.

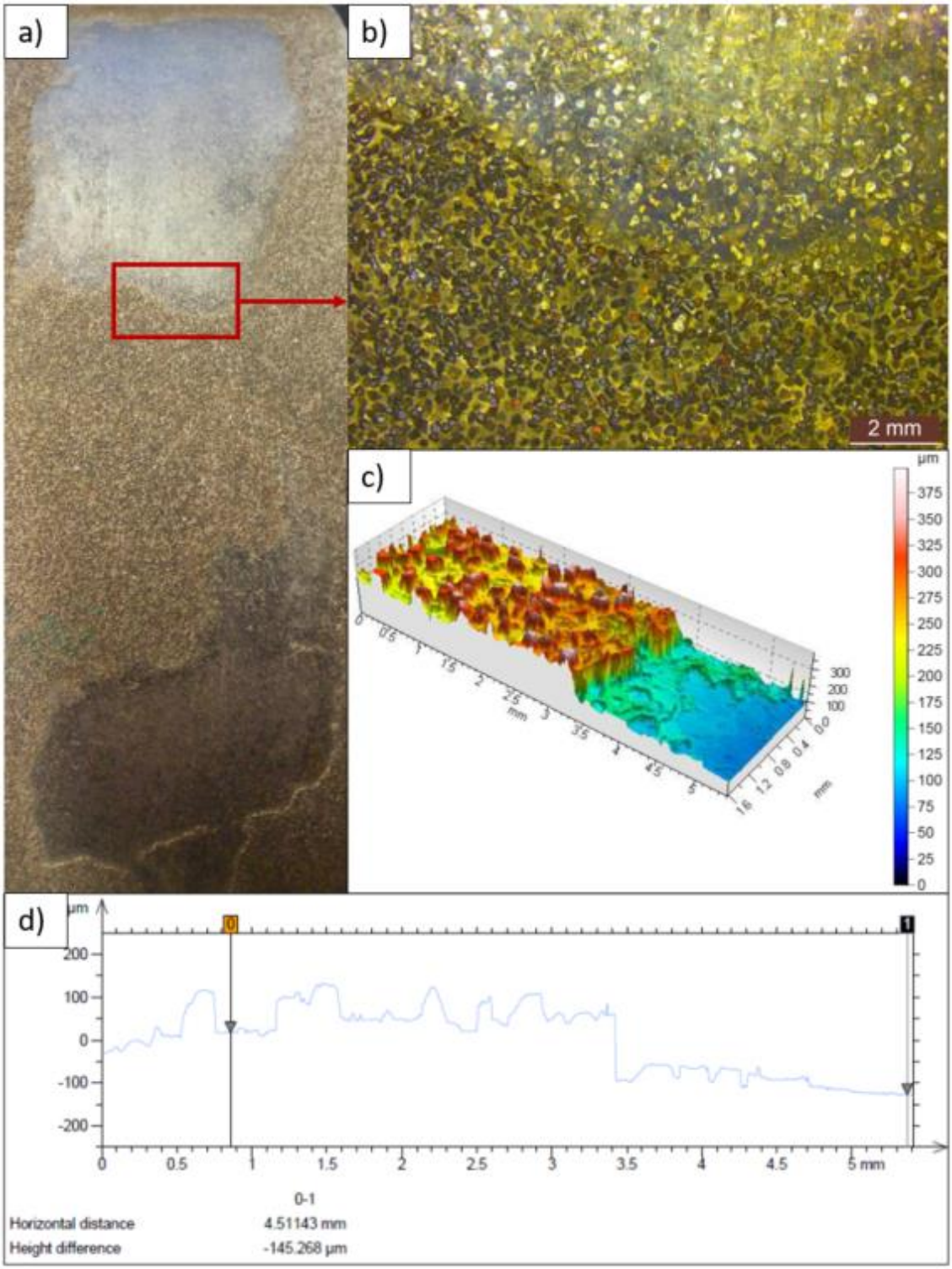

Fig. 70 a) A general picture of an EP CBN grinding wheel with a nickel layer detachment on the center. b) A detailed macroscope picture of the zone marked in red in figure a). c) The 3D digitalization of the step with the confocal microscope. d) The profile of the step extracted from the 3d digitalization.

This catastrophic wear can be foreseen thanks to the power consumption. A wheel with a low grain protrusion is expected to consume more power than a correctly manufactured wheel under the same accumulated workpiece material removal. Therefore, through an online comparison of the power consumed by the current wheel with the power consumed by a

correctly manufactured wheel under the same accumulated workpiece material removal, this phenomenon could be foreseen.

Nonetheless, this was not the only catastrophic wear observed during the topography analysis. A groove on some wheels was detected as it is gathered in Fig. 71 from a) to d).

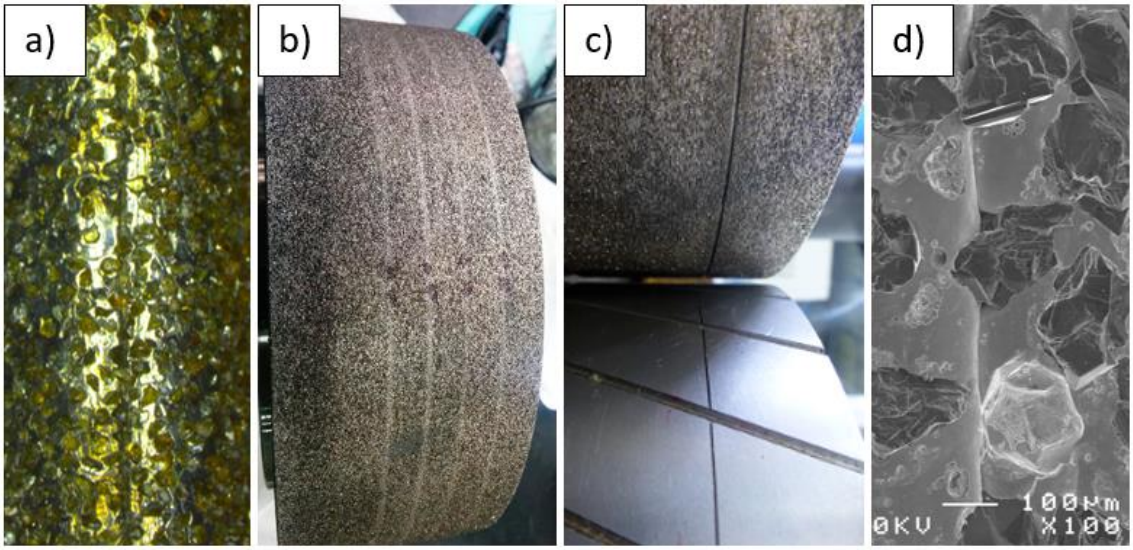

Fig. 71 a) A macroscope picture of a groove on an EP CBN wheel. b) An EP CBN wheel with four grooves on its surface. c) On the top, an EP CBN grinding wheel with a groove on its surface, on the bottom, the steel body of an EP CBN wheel where the groove reached to the steel body. d) A SEM picture of a groove on an EP CBN grinding wheel.

The grooves were caused by a cluster of reason that comprised the grinding process, the workpiece material and the grinding sequence. Firstly, CFG is a grinding process where, through a significant increase of the cutting depth, the process becomes more productive. In addition, as a consequence of the deep contact depth, the hot point of the contact length is located far from the workpiece, hence the risk of causing thermal damage on the workpiece is reduced. However, the combination of the high cutting speed with the low feed speed result in a low chip thickness. This condition coupled with the long contact length makes the process energetically poorly efficient with high temperatures on the cutting zone and important plastically deformed material.

Secondly, Inconel 718 is a nickel-based material used in the turbine parts that have to work at the highest temperatures. This is due to its ability to maintain its mechanical properties at high temperatures as it can be seen in Table 2.

Table 2 Yield and tensile strength of Inconel 718 at different temperatures [106].

Temperature (K)	Yield strength (MPa)	Tensile strength (MPa)
Room temperature	1123.8	1365.2
588.7	1075.6	1265.2
810.9	1020.4	1192.8

922.0	965.3	1103.2
977.6	930.8	1006.6
1033.1	799.8	851.5
1088.7	689.5	723.9

In consequence, instead of failing as a consequence of the stress and high temperature, Inconel 718 is more likely to form burrs when the wheel leaves the workpiece. This characteristic is favored by the cutting conditions explained previously. In Fig. 72 a chip generated on an edge of an NGV is shown.

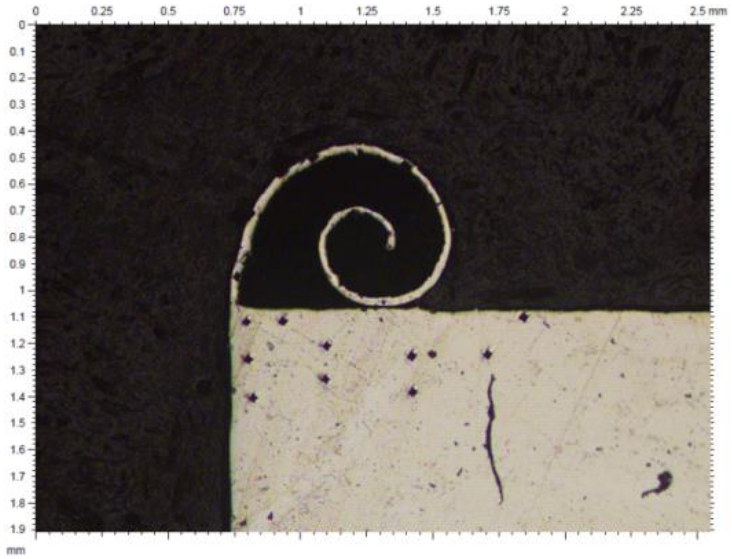

Fig. 72 A macroscope picture of a burr.

Finally, the sequence of the grinding operations may accumulate excessive burrs in the same zone of the workpiece. An NGV has numerous surfaces that are ground and most of them have the wedge faces at the beginning and at the end of the grinding operation. See the wedge face marked in red and the rest of ground zones of an NGV marked in green in Fig. 73.

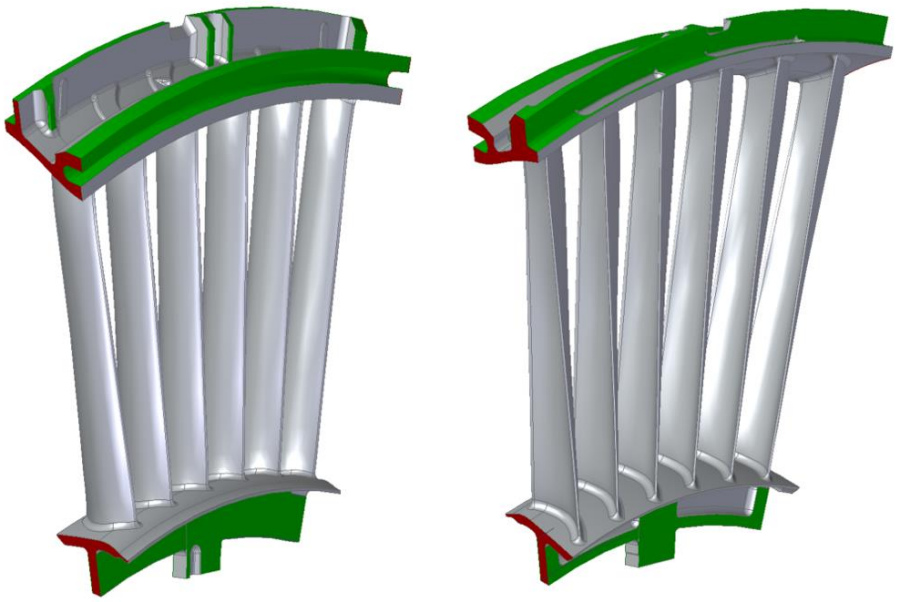

Fig. 73 Rear and front view of an NGV. In red, the wedge faces. In green the rest of ground zones.

As it can be deduced, the grinding wheel of the wedge face had to remove the burrs of all the operations. Every zone of the NGV was ground, at least, in two roughing operation and a single finishing operation given the high stock coming from the casting process. The first roughing operation usually barely removed workpiece material. Its objective was to remove the irregularities and the excessive material that could have the workpiece from the casting process. The subsequent roughing and finishing removed a determined cutting depth that could be excessive if the burrs were added to it. In conclusion, the grinding sequence was arranged in order to remove the burrs by the first roughing operation of the wedge faces.

2.3.1.2 Quantitative analysis: Wheel topography measurement

In this section, the wear state of the wheel is measured in terms of roughness parameters and the conclusions are compared with the wear types found in the previous section.

2.3.1.2.1 Roughness parameters

It has been revealed by means of optical and SEM pictures that the presence of the wear types varies along the wheel life. However, it should be quantified in order to verify numerically what was observed and in order to detect more clearly the progression.

The standard ISO 25718 addresses the characterization of the surfaces in 3D in terms of an extensive number of roughness parameters and diagrams. In that document, all the parameters and diagrams are defined together with the procedure for calculating them. Also in that document, information about surface measurement technologies and devices is included with the purpose of not only showing the wide range of possibilities but also with the purpose of using them correctly.

The parameters are listed in the part 2 of the standard. They are separated by the aspect of the surface they address. In this way, they are classified in:

- Height parameters, where the height of the surface profile is evaluated in 3D.
- Special parameters, where features as the horizontal projection of the highest slopes are measured.
- Hybrid parameters, where the gradient of the surface is evaluated.
- Functional and related parameters, where parameters obtained from the Abbott-Firestone curve are gathered. These parameters analyze separately the upper, the center and the lowest part of the profile giving a global image of it.

Among the wide range of roughness parameters, the most relevant were considered for this study. That being said, the height parameters were taken into account since they are the most widely used parameters in industry for evaluating the roughness of surfaces. These parameters address the height and shape of the whole profile. Furthermore, the functional parameters were also considered for the study. Through these parameters, the height of the profile is partitioned in three sections so that information can be taken from each section. By contrast, special and hybrid parameters were not considered for this study. They were not directly given by the analysis software, hence, the equations for calculating these parameters must be developed. However, it was considered that the features of the profile were appropriately addressed by the height and functional parameters, thus, these parameters were finally dismissed for the study. The height and functional parameters are explained in the following lines. In the following section, some of the explained parameters are chosen for analyzing the changes suffered in the wheel surface in a simple and effective manner.

- Height parameters.
    - Mean Roughness, S_a, [µm]. This parameter is calculated dividing by the measured area the sum of the volume of peaks and valleys above and below the mean line. Mathematically, it is calculated through the division of the double integral of the profile and the horizontal projection of the measured surface, see Eq. (10).

$$S_a = \frac{1}{A}\iint_A |z(x,y)|dxdy \tag{10}$$

    - Root Mean Square Roughness, S_q, [µm]. It is equivalent to the standard deviation of the heights. It is calculated through Eq. (11).

$$S_q = \sqrt{\frac{1}{A}\iint_A |z^2(x,y)|dxdy} \tag{11}$$

    - Maximum Peak Height, S_p, [µm]. It is the height of the highest peak.
    - Maximum Valley Depth, S_v, [µm]. It is the depth of the deepest valley, it is given in negative value.
    - Maximum Height of the Surface, S_z, [µm]. It is the maximum height of the surface. It is calculated from the Eq. (12).

$$S_z = S_p - S_v \tag{12}$$

    - Skewness, S_{sk}, [-]. This parameter is a measure of the symmetry of the profile in terms of the height of the measured points. As an example, a positive skewness is the result of a surface where the height of the peaks is higher than the depth of the valley, a negative skewness means the opposite scenario while a

symmetrical surface leads to a skewness equal to zero. This roughness parameter is calculated through Eq. (13).

$$S_{sk} = \frac{1}{S_q^3}\left[\frac{1}{A}\iint_A z^3(x,y)dxdy\right] \tag{13}$$

- Kurtosis, S_{ku}, [-]. This parameter represents the variation of the height or depth of the valleys. A height distribution that fits a bell-shaped function lead to S_{ku} equal to 3, if there are extreme peaks or valleys S_{ku} will have values above 3 and if the height and depth of the valleys is constant, S_{ku} will be below 3. It is calculated through Eq. (14).

$$S_{ku} = \frac{1}{S_q^4}\left[\frac{1}{A}\iint_A z^4(x,y)dxdy\right] \tag{14}$$

- Functional parameters. As explained before, these parameters are calculated from the Abbott-Firestone curve. Hence, before explaining the parameters, the Abbott-Firestone curve should be introduced.

  Abbott-firestone curve shows the percentage of material in the abscissa axis while the height of the profile is plotted in the ordinate axis. In this way, the curve starts from the 0% at the highest point and finishes at 100% at the lowest point of the profile. The shape of the curve gives the information of the profile and it is separated in three zones through the equivalent line with the purpose of analyzing in detail the peaks, the core and the valleys of the profile, as depicted by Fig. 74.

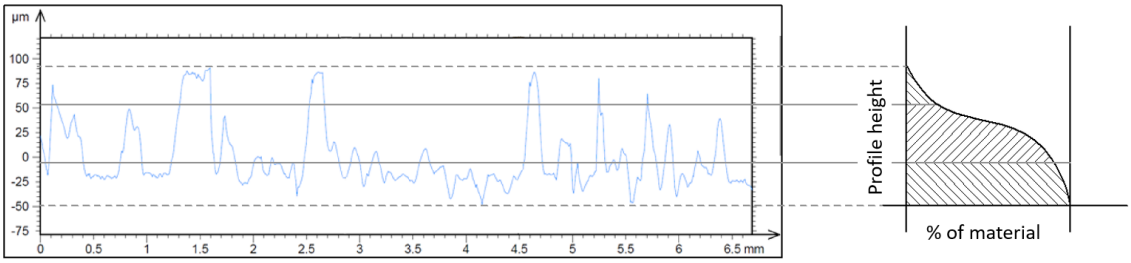

Fig. 74 An EP CBN grinding Wheel profile (left) and the corresponding Abbott-Firestone curve (right).

The equivalent line must fulfill the following conditions:

- It must cut the curve in two points
- The distance between the projection of these two points on the X axis must cover the 40% of the areal material, see Fig. 75 a).
- The equivalent line is the one with the lowest slope that accomplishes the previous conditions.
- If there is more than one line with the lowest slope, the one closest to the left Y axis must be selected as the equivalent line.

Once the line is traced, the intersection with the two Y axes defines the limits of each zone. The curve fraction above the intersection point with the left Y axis corresponds to

the peaks while the intersection point with the right Y axis corresponds to the valleys. The curve fraction between these two points is called the core of the profile. See an example of the Abbott-Firestone curve with the equivalent line in Fig. 75 a).

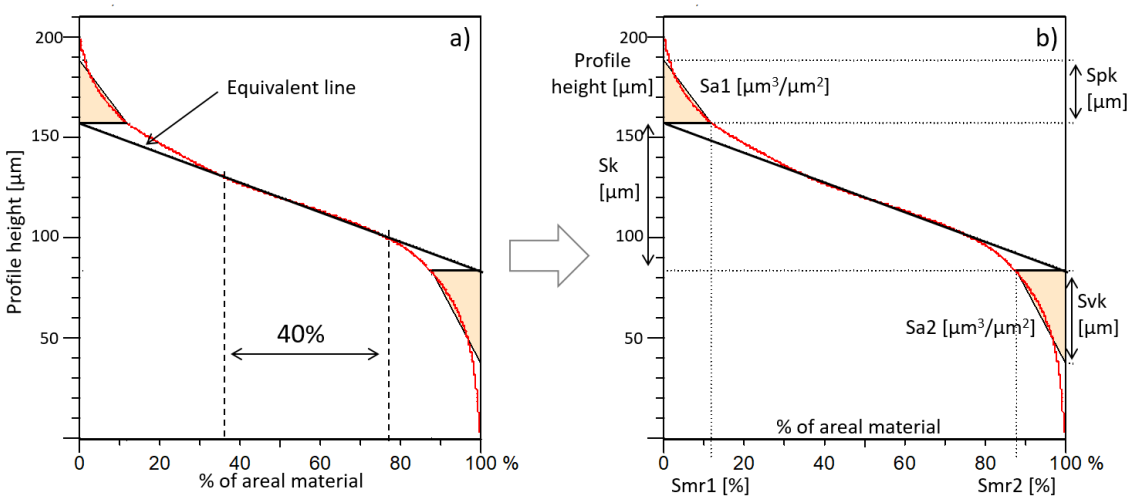

Fig. 75 a) Equivalent line in the Abbott-Firestone curve. b) Functional parameters obtained from the equivalent line in the Abbot-Firestone curve.

Several parameters can be taken from that partition of curve, as it can be seen in Fig. 75 b). These parameters are explained in the following lines:

- Core roughness, S_k, [µm]. This parameter is the height comprised between the two intersection points of the equivalent line with the left and right axes.
- Reduced peak height, S_{pk}, [µm]. The value of this parameter is the height of the triangle whose area is equal to the area between the curve above the core and the upper limit of the S_k. The base of this triangle is S_{mr1} that is the horizontal line from the left axis to the curve at the upper limit of S_k.
- Reduced valley depth, S_{vk}, [µm]. The value of this parameter is the height of the triangle whose area is equal to the area between the curve below the core and the lower limit of the S_k. The base of this triangle is S_{mr2} that is the horizontal line from the right axis to the curve at the lower limit of S_k.
- Peak Material Portion, S_{mr1}, [%]. It is the percentage of the measured surface covered by peaks.
- Valley Material Portion, S_{mr2}, [%]. It is the percentage of the measured surface covered by the valleys.
- Upper Volume, S_{a1}, [µm^3/ µm^2]. This parameter is the area of the triangle formed by S_{pk} and S_{mr1}. It corresponds to the ratio of the volume of the peaks above S_k to the percentage of the whole area indicated by S_{mr1}.
- Lower Volume, S_{a2}, [µm^3/ µm^2]. This parameter is the area of the triangle formed by S_{vk} and S_{mr2}. It corresponds to the ratio of the volume of the valleys below S_k to the percentage of the whole area indicated by 1-S_{mr2}.

In spite of using parameters of the Standard ISO 25718 for characterizing the wheel in a universal manner, the treatment of the digitalized files must be detailed since it affects the results of the parameters. A profile can be considered as the sum of form, waviness and roughness of the

sample. The background form of the digitalized surfaces was cylindrical due to the shape of the grinding wheel. It was removed through a specific option of the analysis software for removing cylinder form. Then, the parameters were obtained after applying a Gaussian filter. The cutoff length of the filter was selected following the recommendation of the part 3 of the Standard ISO 25718. It is mentioned in that document that the cutoff length should be five times larger than the size of the coarser particle to be measured. The grain size of the EP CBN analyzed in this work was 250 µm but it was shown in Fig. 53 that the grain is covered up to 110 µm. Therefore, considering a grain protrusion in the range of 140 µm, the resulting cutoff length should be 700 µm. The cutoff length used in this work was 0.8 mm since the next lower available value was 0.5 mm.

2.3.1.2.2 Wear evolution along the wheel life

The wear evolution observed qualitatively in section 2.3.1.1 was quantified by means of the most representative functional parameters, namely S_{pk}, S_k and S_{vk}. As explained in the previous section, these parameters are complementary, they cover all the range in height of the profile. Therefore, they were considered as valid for evaluating the change in height and shape of the grains in a simple and effective manner. Taking this fact into account, they were selected for evaluating the evolution of wear along the five wear states. The numerical values will help to determinate the presence of each wear type during the different steps of the wheel life.

The result of S_{pk}, S_k and S_{vk} are plotted in Fig. 76, Fig. 77 and Fig. 78 respectively.

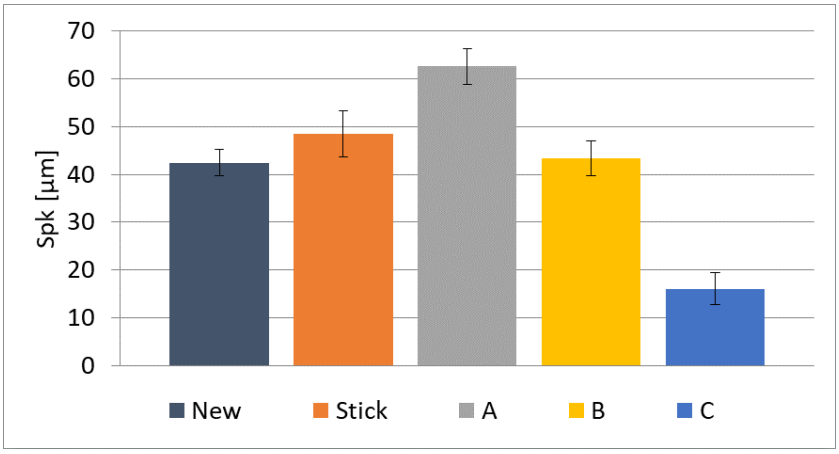

Fig. 76 S_{pk} and standard deviation values of New, Stick, A, B and C states of the grinding wheel.

S_{pk} increases from *New* to *A*. This means that the grains are progressively sharpen due to subsequent fractures. However, from *A* to *B*, the sharpening process stops and the peak height of the grains starts to diminish. The trend is confirmed with the decrease of S_{pk} from *B* to *C*, where wear flat is spread over more grains. It was also confirmed that the conditioning sharpens the grains and increases the cutting ability.

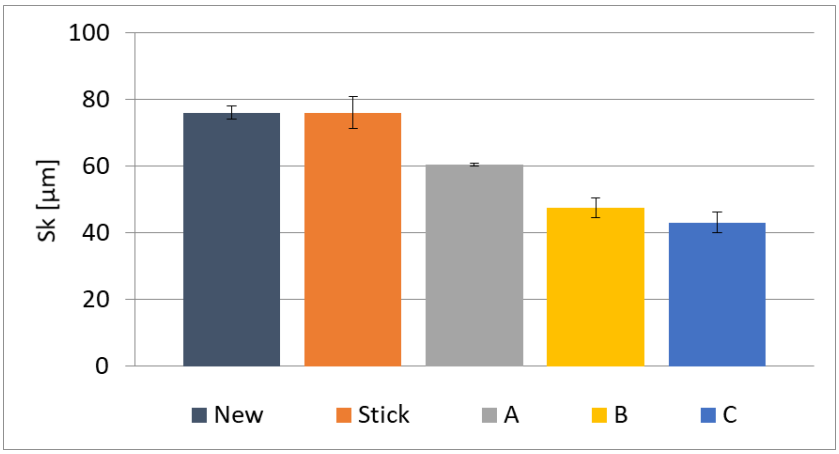

Fig. 77 S_k and standard deviation values of New, Stick, A, B and C states of the grinding wheel.

The progressive decrease of S_k from *New* to *C* is a consequence of the decrease of the height of the peaks. From *New* to *Stick* there is not a significant difference in S_k average value. However, the increase in the range of the standard deviation indicates that there is a randomness in the shape of the peaks as a consequence of the fractures caused by the conditioning.

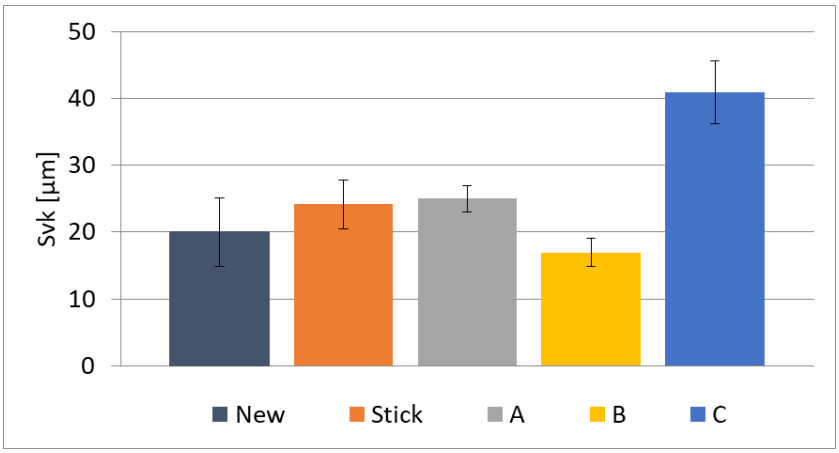

Fig. 78 S_{vk} and standard deviation values of New, Stick, A, B and C states of the grinding wheel.

Finally, S_{vk} shows a progressive increase. This increase is a consequence of the decrease of S_k. The lowest part of the grains is not worn since it does not contact the workpiece, therefore the equivalent line pivot in a zone between the upper and the lower limit of the core. This provokes the decrease of S_k value and the increase of S_{vk}.

Analyzing the three graphs as a whole, the conclusions drawn from the qualitative analysis match with the conclusions drawn from this analysis. At the first stages, the sharpening phase seen in Fig. 76 occurs thank to the microfractures observed on the grain tips. This is accompanied by a progressive decrease in the height of the grains, as detected by S_k in Fig. 77. Eventually, the height of the grains is equaled on the whole wheel surface. As a conclusion, the forces per grain become lower and thus, the wear type switches form microfractures to wear flat. This is confirmed at first by optical, confocal and SEM observation in Fig. 67 and then by both the sudden decrease of S_{pk} and the increase of S_{vk}, see Fig. 78.

2.3.2 Determination of the wheel life limit

2.3.2.1 Mathematical background

In the previous section the evolution of the wear types along the wheel working life was studied through the functional parameters. It was demonstrated that the wear flat is the predominant wear type in the states *B* and *C*. However, a finer analysis of roughness parameters must be done when two wear flat states must be differentiated and a numerical roughness value of the wheel life limit is needed.

In this section, an extensive comparison of various roughness parameters is presented with the aim of finding the most representative parameter for distinguishing two different wear flat states. A statistical method explained by Leach et al. [107] was used in order to reduce the time and ensure a correct result. Once the most significant parameter was found, the value of that parameter that establishes the threshold between the two wear levels was calculated.

This method is called standard deviation method and it is suitable for a binary classification, where two classes, i.e. two wear states, are compared.

In the current study there are two wear states called *B* and *C*. Each wear state has its own feature vector that comprises the parameters that must be compared, from s_1 to s_m. There should also be several samples of each wear state; they are numbered from *1* to *n*. An example of the feature vector of different samples of both wear states is shown in Eq. from (15) to (17).

$$p^{B1} = (s_1^{B1}, s_2^{B1}, \dots, s_m^{B1}) \qquad p^{C1} = (s_1^{C1}, s_2^{C1}, \dots, s_m^{C1}). \tag{15}$$

$$p^{B2} = (s_1^{B2}, s_2^{B2}, \dots, s_m^{B2}) \qquad p^{C2} = (s_1^{C2}, s_2^{C2}, \dots, s_m^{C2}). \tag{16}$$

$$\dots \qquad \dots$$

$$p^{Bn} = (s_1^{Bn}, s_2^{Bn}, \dots, s_m^{Bn}) \qquad p^{Cn} = (s_1^{Cn}, s_2^{Cn}, \dots, s_m^{Cn}). \tag{17}$$

The next step is to rearrange the vectors of each class. A new vector should be created for each s_i parameter that gathers its corresponding value of each sample, from *1* to *n*. as it is done in Eq. from (18) to (20).

$$s_1^B = (s_1^{B1}, s_1^{B2}, \dots, s_1^{Bn}) \qquad s_1^C = (s_1^{C1}, s_1^{C2}, \dots, s_1^{Cn}) \tag{18}$$

$$s_2^B = (s_2^{B1}, s_2^{B2}, \dots, s_2^{Bn}) \qquad s_1^C = (s_1^{C1}, s_1^{C2}, \dots, s_1^{Cn}) \tag{19}$$

$$\dots \qquad \dots$$

$$s_m^B = (s_m^{B1}, s_m^{B2}, \dots, s_m^{Bn}) \qquad s_m^C = (s_m^{C1}, s_m^{C2}, \dots, s_m^{Cn}) \tag{20}$$

For each new vector *i* the mean value and the standard deviation must be calculated through the Eq. (21) and (22).

$$\mu_i^B = \frac{1}{n}\sum_{k=1}^{n} s_i^{Bk} \qquad \mu_i^C = \frac{1}{n}\sum_{k=1}^{n} s_i^{Ck} \tag{21}$$

$$\sigma_i^B = \sqrt{var(s_i^B)} \qquad \sigma_i^C = \sqrt{var(s_i^C)} \tag{22}$$

The average and the standard deviation values are then used together with the coverage factor *k* for calculating the interval, I_i, of the normal distribution of each parameter according to the probability density function. See Eq. (23).

$$I_i^B = \mu_i^B \pm k\sigma_i^B \qquad I_i^C = \mu_i^C \pm k\sigma_i^C \tag{23}$$

The confidence level of the normal distribution function depends on the value of *k*. In this study the following coverage values were used:

k = 1. The 68% is comprised between μ-σ and μ+σ.

k = 2. The 95% is comprised between μ-2σ and μ+2σ.

k = 3. The 99.7% is comprised between μ-3σ and μ+3σ.

The resulting two intervals can be separated or not. If not, there is a region of uncertainty, see Fig. 79, where the same value of the plotted parameter can belong to both wear states. Therefore, it can be assumed that this parameter is not significant of the wear suffered by the wheel since it will lead to unclear conclusions.

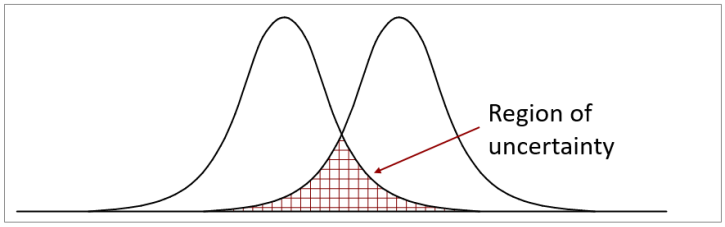

Fig. 79 Region of uncertainty between two probability density functions.

If the bells are separated one from the other there is not a zone where the parameters of both classes are in the same range of values. In that case, the parameter is suitable for differentiating between the two classes. However, the suitability of the parameters depends on the separation between the curves of the two classes. Hence, the distance among the two intervals of each parameter must be evaluated in order to find the most significant.

The suitability of the parameters is called significance, S_i, and it is calculated through the Eq. (24). Where $d\left(I_i^B, I_i^C\right)$ is the difference between the upper limit of the lowest interval and the lower limit of the highest interval.

$$S_i = \frac{d(I_i^B, I_i^C)}{\frac{1}{2}(\mu_i^B + \mu_i^C)}. \tag{24}$$

The parameter with the highest significance value should be considered as the most representative. However, it should be noted that the significance value depends not only on the

mean value of the two states but also on the standard deviation and the coverage factor. As a consequence, the roughness parameters with higher standard deviation are more likely to have poor significance values when high coverage factors are used.

The last step is to calculate the threshold. This value is the theoretical limit between two wear states, which is useful when a third wheel surface is measured and is wanted to be classified inside class *B* or *C*. The threshold, τ, is calculated through Eq. (25).

$$\frac{(\tau-\mu_i^W)^2}{2\sigma_i^W}-\frac{(\tau-\mu_i^N)^2}{2\sigma_i^N}=\frac{\sigma_i^N}{\sigma_i^W}. \tag{25}$$

All the parameters explained in section 2.3.1.2 were included in this study for an extensive analysis of the wheel topography. The results are gathered in the following section.

2.3.2.2 Results

The input data was formed by an extensive amount of data arranged in matrices, which could not be managed without the help of a computational tool. For that purpose, Matlab® (Matrix Laboratory) software was chosen because of its suitability with this type of data. Therefore, the mathematical sequence was programmed in Matlab® code and the roughness parameters were introduced from Excel® tables. The output of the program was also a table where the parameters were displayed together with their significance value for the three coverage factors mentioned previously. The result of the significance is arranged from the highest to the lowest in Table 3 and plotted in Fig. 80 a).

Table 3 Significance value of the studied parameters at different coverage factors from the comparison between B and C.

k = 1		**k = 2**		**k = 3**	
S_{sk} (-)	6.396	S_{sk}	4.776	S_{sk}	3.157
S_{a1} (µm³/mm²)	1.143	S_{a1}	0.642	S_{mr1}	0.384
S_{a2} (µm³/mm²)	1.010	S_{mr1}	0.610	S_{vk}	0.262
S_{mr1} (%)	0.837	S_{a2}	0.514	S_p	0.230
S_{pk} (µm)	0.630	S_{vk}	0.444	S_{a1}	0.140
S_{vk} (µm)	0.625	S_p	0.400	S_{a2}	0.018
S_p (µm)	0.570	S_{pk}	0.127	S_{mr2}	–0.021
S_a (µm)	0.111	S_{mr2}	0.033	S_a	–0.179
S_{ku} (-)	0.104	S_a	-0,034	S_q	-0.273
S_{mr2} (%)	0.087	S_q	–0.130	S_z	–0.329
S_z (µm)	0.058	S_z	–0.136	S_{pk}	–0.375
S_q (µm)	0.013	S_v	–0.323	S_v	–0.559
S_v (µm)	–0.088	S_{ku}	–0.329	S_k	–0.753
S_k (µm)	–0.232	S_k	–0.492	S_{ku}	–0.761

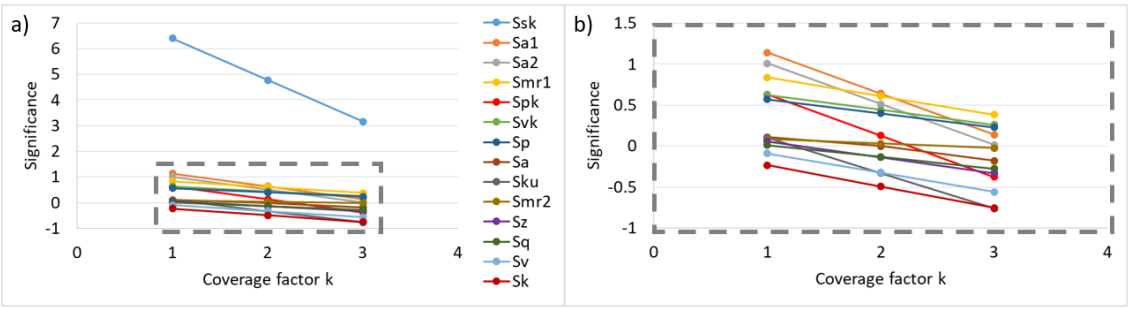

Fig. 80 a) Significance value of the studied parameters versus coverage factors. b) Detailed view of the parameters with the lowest significance value.

The following conclusions can be drawn from this table:

- The negative significance values correspond to parameters whose normal distribution curves are overlapped to some extent. The influence of the coverage factor can also be observed, the higher the confidence level, the less parameters will have a positive significance.
- The standard deviation takes more importance when the coverage factor increases. Thus, the order of the parameters varies as Fig. 80b) shows. The lines of the parameters with higher standard deviation present higher slope. This can also be deduced developing Eq. (24) as follows in Eq. (26).

$$S_i = \frac{d(I_i^B, I_i^C)}{\frac{1}{2}(\mu_i^B + \mu_i^C)} \rightarrow \frac{\mu_i^C - k\sigma_i^C - \mu_i^B + k\sigma_i^B}{\frac{1}{2}(\mu_i^C + \mu_i^B)} = 2\frac{\mu_i^C - \mu_i^B}{\mu_i^B + \mu_i^C} + \frac{\sigma_i^B - \sigma_i^C}{\mu_i^B + \mu_i^C}k \rightarrow y = A + Bx \quad (26)$$

- The skewness is the parameters with the highest significance. It should be noted that it presents the highest slope, this means that it has the highest standard deviation. However, the mean values are so distanced that there is no overlap of the distribution bells despite the high standard deviation.
  Regarding the important difference in the significance value with respect to the rest of parameters, skewness must be chosen as the most significant parameter for evaluating the wear grade of an EP CBN grinding wheel when it mainly presents wear flat.

In the average and standard deviation method, an expression for calculating the threshold between the two classes was included, namely, Eq. (25). The threshold calculated from that formula was -0.058. According to the definition of the skewness value, a negative value indicates the predominance of the valleys. For a global vision of the evolution of the skewness value along the wheel life, the values for the five studied wheel states are plotted in Fig. 81 versus the accumulated volume of workpiece material removed. It should be mentioned that a symbolic volume of 10 mm^3 was given to the state *Stick* for separating from *New*.

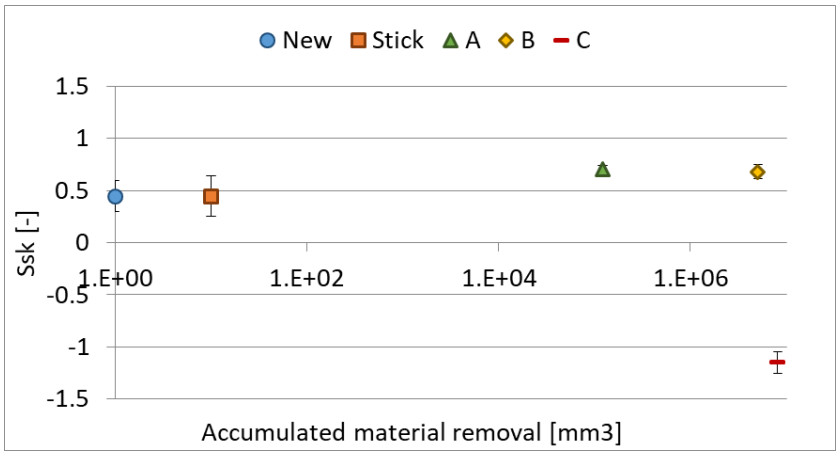

Fig. 81 S_{sk} evolution along the wheel life.

Skewness does not present a progressive evolution from *New* to *C*. This confirms the results of the study carried out along the whole wheel life where wear flat was mainly detected in the advanced wear states of the wheel as the predominant wear type.

Taking everything into account, the skewness was found as the most representative roughness parameter for the wear suffered by EP CBN grinding wheels during the CFG of nickel-base alloys. A value of S_{sk} was found through a mathematical analysis of the results that indicates a safety wheel life limit. This limit was stablished at S_{sk} = -0.058. If the wheel surface presents skewness values above -0.058, the wear flat level is not considered as dangerous. However, for values below -0.058, the good performance of the wheel is not ensured, since it is in the wear range of the wheels considered by the industry as too worn for grinding. If wheels with wear level in an intermediate point between *B* and *C* were used for this study, a threshold value closer to *C* could be found. Nevertheless, given the standard deviation, the significance could be below 1.

2.3.3 Study and evaluation of the wheel conditioning

The progressive increase in the wear state makes the cutting conditions variable during the wheel life. As a result, problems on the workpiece are more likely to take place as the wear increases. One of them is the vibration marks appeared on a specific part of the workpiece.

There are three factors that cause this problem.

Firstly, the increase in the grinding forces as a consequence of the wear. The flattening of the grains required an increase in the normal force in order to reach the minimum contact pressure for initiating the penetration of the grain into the workpiece material.

Secondly, the low rigidity of that part of the workpiece. As it can be seen in Fig. 82 marked in red, that zone is only joined to the rest of the workpiece by one side and its width to length ratio makes it unrigid.

Finally, the deficient clamping of that part. That zone can only be supported by the opposite side in contact with the wheel.

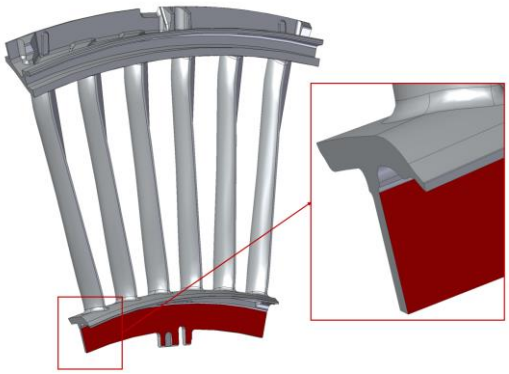

Fig. 82 A nozzle guide vane. The zone of the workpiece where vibration appears is marked in red.

These marks leave the workpiece out of the required tolerances, which sometimes can be corrected by grinding again that surface. If not, the workpiece must be scrapped. However, this problem is avoided by modifying the surface of the wheel when the marks appear.

It has been previously explained that EP wheels cannot be dressed due to their characteristics. However, it was explained in the state of the art that these wheels can be conditioned by various methods. In this case, a mechanical conditioning process similar to the process applied to the *Stick* wheel was used for trying to recover the cutting ability of the worn grains.

The effect of this conditioning process was studied in terms of wheel power consumption and wheel topography in the following sections.

2.3.3.1 Power consumption

To understand the meaning of the change of the power curve, the stages of a tool wear curve must be known. A typical tool wear curve, see Fig. 83, has in the X axis an indicator of the wheel life such as workpiece material removal or working time and in the Y axis an indicator of the wear. Regarding its shape, three different zones can be distinguished. The first one, at the beginning of the wheel life, is a zone where the wear advances rapidly until a stationary state. In a grinding wheel this happens due to the sharpness of the grains and the unevenness of the grain protrusion height. The second zone takes place when the tool reaches a steady state where its performance during the process is stable and the wear advances slowly. In grinding wheels, this zone can be related with a state where the grains are at the same level and grinding forces are equally distributed among all of them. Finally, the last zone is related with a rapid wear evolution which eventually leads to the failure of the tool, which can be related with the drastic change in the Skewness value seen in Fig. 81.

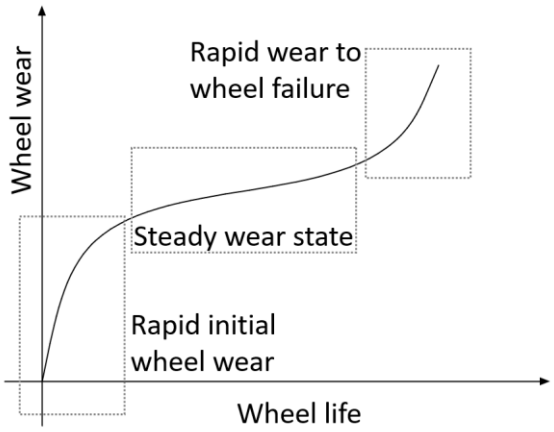

Fig. 83 A generic wear curve of a grinding wheel.

Taking this into account, the change in the power consumption plotted in Fig. 84 can be analyzed as follows.

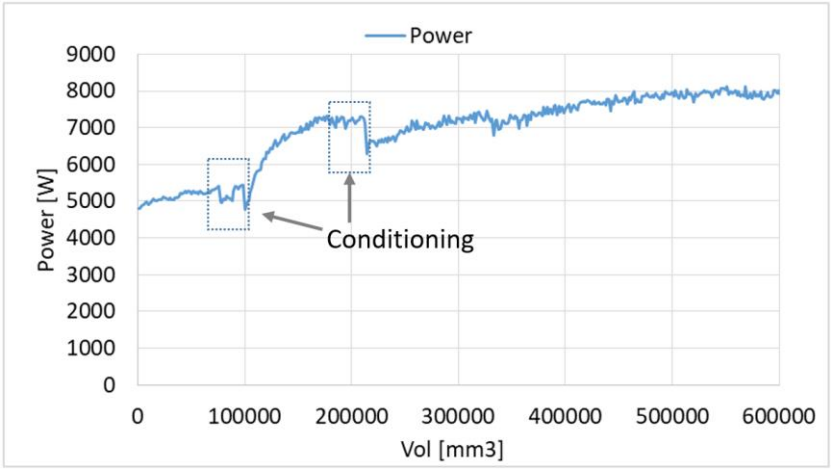

Fig. 84 Power consumption versus the accumulated workpiece material removal. Two conditioning are marked in dotted rectangles.

The wheel was conditioned two times. In each time, the wheel reaches its steady wear states where the slope of the curve decreases. In that situation, the power and consequently the grinding forces are higher than before because of the progressive loss of cutting ability. When the conditioning process is carried out, a sudden decrease in the power is registered caused by an increase in the cutting ability of the wheel. The wheel is able to remove material more easily. However, that decrease is followed by another phase of sudden increase similar to the beginning of the wheel life.

It can be considered that after conditioning a new wear curve starts. After the first conditioning it should be noted that the new curve has a higher power consumption when it reaches the new steady state than the extension of the former curve, see the orange curve in Fig. 85. However, after the second conditioning, the steady wear state matches the theoretical extension of the curve generated after the first conditioning, yellow curve in Fig. 85.

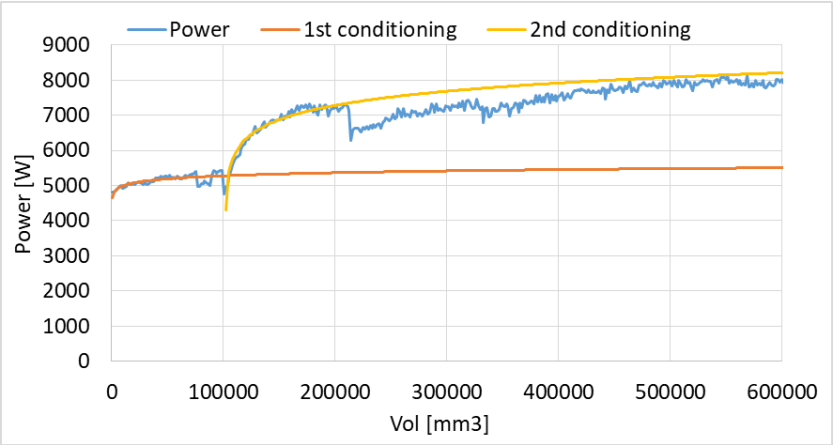

Fig. 85 Power consumption versus the accumulated workpiece material removal. The curves before the two conditioning are extended with orange and yellow curves.

The two conditionings had different effect on the power consumption. The difference between the steady wear state of the two conditionings is caused by the different state of the grains before the conditioning process itself. If the accumulated volume of the workpiece material removed is compared with the volume of Fig. 81, it can be seen that the conditionings take place when the wear flat starts to be predominant. In this way, it can be deduced that the first conditioning takes place when there are still grains without wear flat. By contrast, the second conditioning takes place when the majority of grains present wear flat, this is the reason why when the wheel reaches again the steady wear state, the power cannot rise more.

2.3.3.2 Topographic analysis

The wheel surface was digitalized before and after the conditioning process following the same procedure as in the previous wheel surface analysis. Later on, the average and standard deviation method was used again upon the same roughness parameters analyzed in section 2.3.2.2. The results of the significance are listed in Table 4.

Table 4 Significance value of the studied parameters at different coverage factors from the comparison of wheels before and after conditioning.

k = 1		**k = 2**		**k = 3**	
	Significance		Significance		Significance
S_v	0.074	S_z	–0.064	S_{mr2}	–0.102
S_z	0.060	S_{mr2}	–0.066	S_z	–0.188
S_{ku}	0.000	S_v	-0.082	S_{ku}	-0.224
S_p	–0.020	S_{ku}	–0.112	S_v	–0.238
S_{mr2}	–0.031	S_p	–0.166	S_p	–0.311
S_{pk}	–0.079	S_{pk}	–0.277	S_{pk}	–0.474
S_q	–0.154	S_q	–0.334	S_q	–0.515
S_a	–0.158	S_a	–0.359	S_a	–0.560
S_{vk}	–0.194	S_{mr1}	–0.482	S_{mr1}	–0.754
S_{mr1}	–0.210	S_k	–0.488	S_k	–0.757

S_k	–0.219	S_{vk}	–0.520	S_{vk}	–0.845
S_{a2}	–0.304	S_{a2}	–0.784	S_{a2}	–1.263
S_{a1}	–0.626	S_{a1}	–1.412	S_{a1}	–2.198
S_{sk}	–1.351	S_{sk}	–4.000	S_{sk}	–6.650

The majority of parameters listed in Table 4 are negative, only S_v and S_z have positive significances. However, their value is close to zero, 0.074 and 0.060 respectively, and they belong to the lowest coverage factor. The difference between this table and Table 3 is caused by the slight change suffered by the wheel surface during the conditioning. The standard deviation of the mean parameters takes the probability density function to a range in common before and after the conditioning process. Therefore, another methodology should be used for achieving the most representative values of the change generated by the conditioning process.

In the same book [107], Leach defined another mathematical method as an alternative to the average and standard deviation method. It was called correlation coefficient. It was defined as a less robust method but simpler. Eq. (27) should be applied on the parameters for calculating the correlation coefficient, r_{GB}. The maximum r_{GB} achievable value is 1, hence a value close to 1 indicates a high suitability of the parameter. By contrast, a parameter with an r_{GB} value close to 0 should not be used.

$$r_{GB}(s_i) = \frac{\sum_{j=1}^{n}\left(s_i^{Bc,j} - \mu^{Bc}\right)\left(s_i^{Ac,j} - \mu^{Ac}\right)}{\sqrt{\sum_{j=1}^{n}\left(s_i^{Bc,j} - \mu^{Bc}\right)^2 \sum_{j=1}^{n}\left(s_i^{Ac,j} - \mu^{Ac}\right)^2}}. \tag{27}$$

Eq. (27) gives the correlation coefficient value for a parameter s_i measured in samples from 1 to n on a wheel before being conditioned, superscript *Bc*, and on a wheel after being conditioned, superscript *Ac*. The Greek symbol μ corresponds to the average value. The correlation coefficients of the studied roughness parameters are listed in Table 5.

Table 5 r_{GB} values of the studied roughness parameters

	r_{GB}
S_a	0.812
S_k	0.800
S_z	0.744
S_{mr1}	0.685
S_{vk}	0.632
S_{mr2}	0.625
S_q	0.551
S_{ku}	0.448
S_v	0.425
S_p	0.164
S_{a1}	0.126
S_{sk}	–0.095

S_{pk}	–0.129
S_{a2}	–0.211

The author classified this method as less robust, therefore the evaluation of only the most significant parameter was considered insufficient for understanding the change on the wheel surface. In order to carry out a more reliable analysis, the parameters with the five highest r_{GB} where evaluated, namely, S_a, S_k, S_z, S_{mr1} and S_{vk}. The mean value before and after conditioning are listed in Table 6 together with the percentage variation of the mean value after conditioning with respect to before conditioning.

Table 6 Average values before and after conditioning and the percentage variation of the parameters chosen for the study of the conditioning process

	Before conditioning	After conditioning	Percentage variation
S_a	21.9	22.9	4.4%
S_z	246.6	205.1	-16.8%
S_k	55.2	58.0	5.1%
S_{vk}	31.1	35.5	14.1%
S_{mr1}	17.7	18.8	6.3%

The percentage variation is plotted in Fig. 86 it was calculated through Eq. (28).

$$\% = \frac{\mu^A - \mu^B}{\mu^B} x100 \tag{28}$$

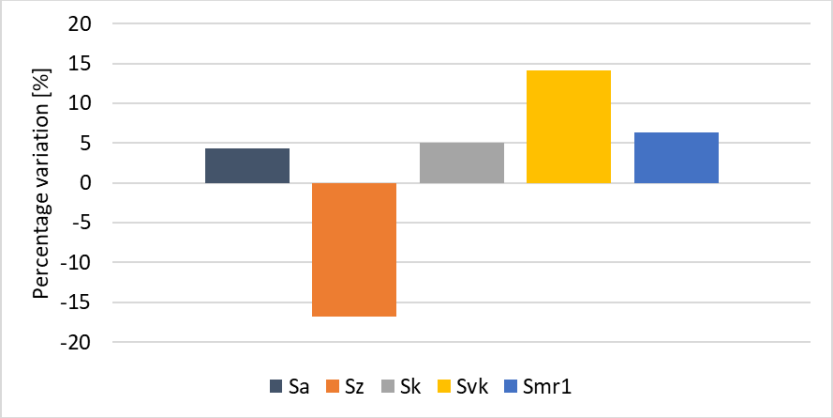

Fig. 86 Percentage variation of the average of the parameters chosen for the study of the conditioning process.

The parameters were analyzed one by one and the conclusion taken from each one was put in common for an understanding of the global situation. The analysis was based on the following facts observed on the wheel surface and depicted in Fig. 88:

- There is no material addition to the wheel during the wheel conditioning.

- The bonding layer is a flat surface as it can be seen in the SEM capture of Fig. 87, from where only the grains protrude. The presence of any other element on the bond as the red lines in Fig. 88 b) is dismissed.

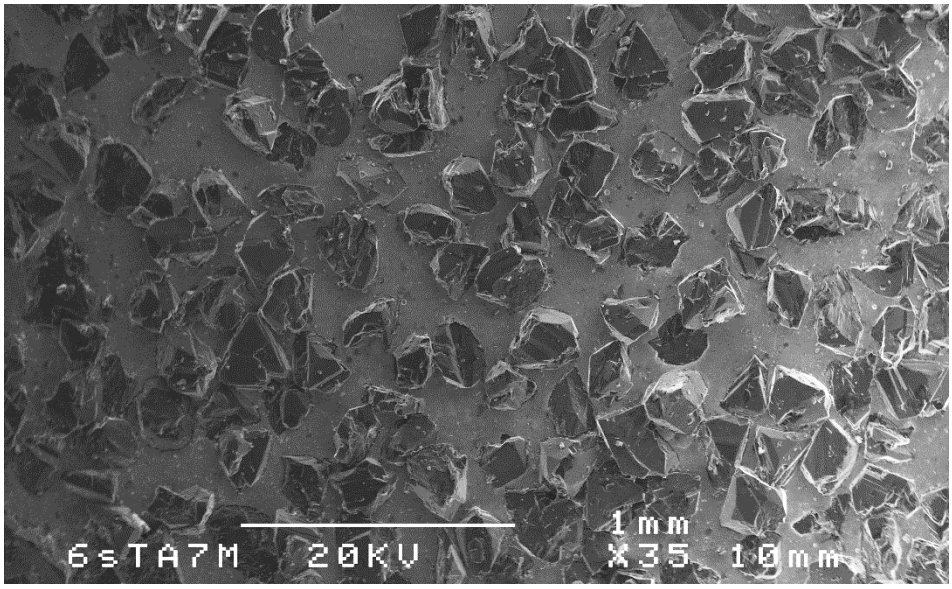

Fig. 87 A SEM capture of an EP CBN grinding wheel.

- Grain material removal is considered to take place on the tips. Material of the lower part, marked in red in Fig. 88 c), was not considered to be removed if there is still grain material above.

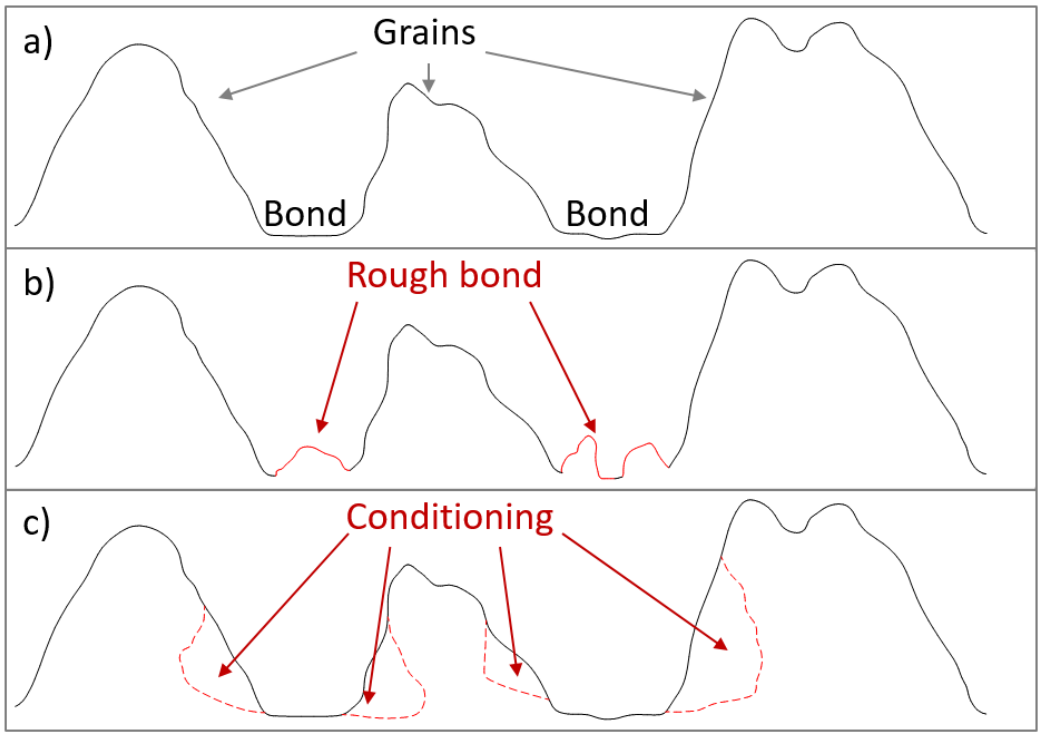

Fig. 88 a) A Wheel profile with flat bond Surface. b) A wheel profile with rough elements on the bond. c) A wheel profile with grain material removed only from the lowest part of the grains

S_a increases after conditioning. Regarding the mathematical expression of S_a, Eq. (10), this augmentation can be justified as an increase in the volume of the profile either on the peaks or on the valleys. Because of the nature of the conditioning process, material cannot be added to the profile. Therefore, this change must be caused by the removal of the bonding material.

S_z suffers an important decrease after conditioning. S_z is the distance between the highest peak and the deepest valley of the profile. This variation contradicts what was deduced from the variation of S_a. It should be noted that when a surface suffers a decrease in S_a, S_z does not necessarily have to change, it can be either lower, Fig. 89, or even maintain the same value, Fig. 90. However, when a surface with a flat bottom zone suffers an increase in S_a without any addition of material, S_z must increase. It should be mentioned that S_z is named R_z in Fig. 89 and Fig. 90 because it is its equivalent roughness parameter for a 2D profile.

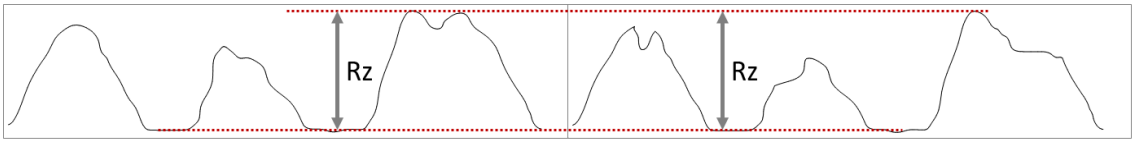

Fig. 89 A hypothetical wheel profile after and before conditioning. The profile on the right has the same R_z but lower R_a.

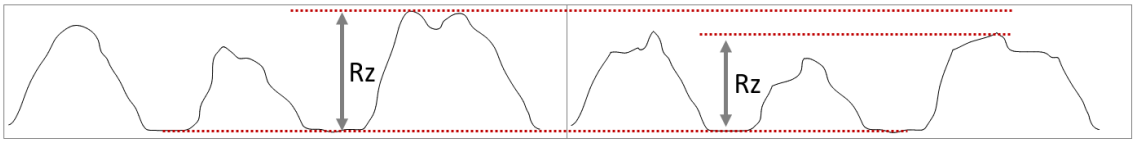

Fig. 90 A hypothetical wheel profile after and before conditioning. The profile on the right has lower R_a and R_z.

S_k increases after conditioning. S_k is the height between the two end points of the equivalent line. Thus, the increase of this parameter in this scenario is caused by an increase in the slope of the equivalent line.

S_{vk} increases significantly. This contradicts the variation seen in S_k. A decrease of S_k and an increase of S_{vk} means that the slope of the equivalent line has been reduced. This is due to fractures on the grain tips, in this way, the curve descends faster until the height where the body of the grain is reached, see Fig. 91 b). At that point, the percentage of the material (X direction of the curve) increases rapidly with small variation in depth (Y direction). This change can be considered as an aggressive sharpening of the grains. By contrast, an increase of S_k, as it has been mentioned before, is caused by an increase in the slope of the equivalent line. This situation represents the profile of grain with sharp but solid grain tips unlike the previous situation, see Fig. 91 c). Hence, the increase on material percentage as the curve descends in height is more progressive resulting in a higher slope. This change can be considered as a soft sharpening. An increase of S_{vk} can only be propitiated by a significant removal of bonding layer that compensates the loss of S_{vk} caused by the higher slope of the equivalent line. These two situations are explained in Fig. 91 using the hypothetical profile of a wheel with wear flat.

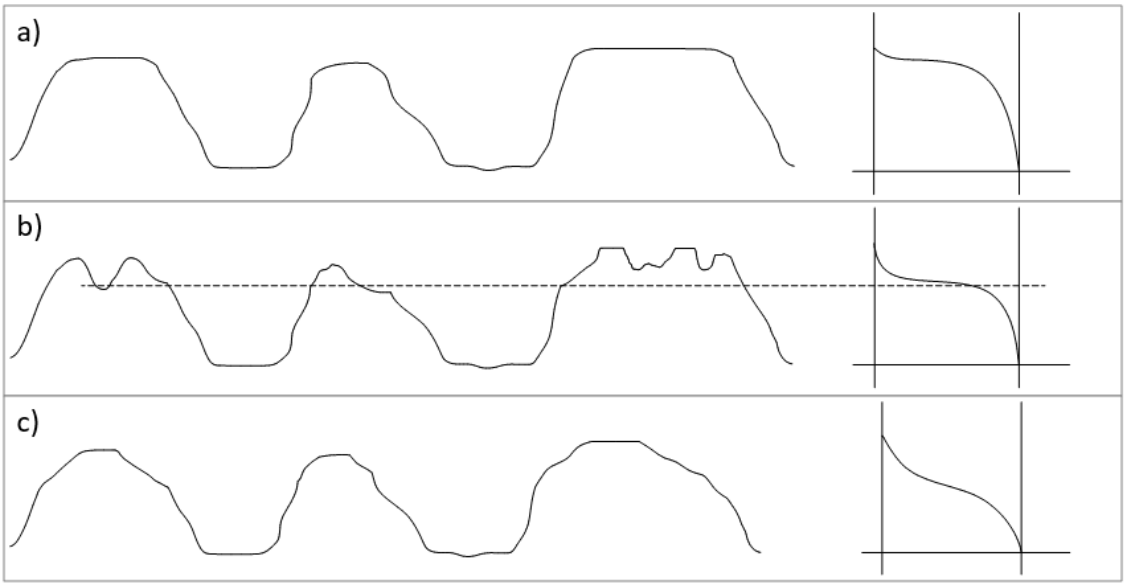

Fig. 91 a) The hypothetical profile of a grinding wheel under wear flat and the corresponding Abbott-Firestone curve. b) The profile of the grinding wheel after aggressive grinding. c) The profile of the grinding wheel after soft sharpening.

An aggressive sharpening in comparison with a soft sharpening creates a sharper state of the grains. However, the resulting grains from an aggressive sharpening are weaker and tend to lose easier the new cutting edges, resulting in wear flat sooner. By contrast, soft sharpening creates stronger grains that will maintain longer the sharpness before reaching a critical wear flat grade. In terms of power consumption, the aggressive sharpening causes a more sudden decrease, nevertheless, they will reach the steady wear state sooner because of a faster rise of the power.

S_{mr1} increases in comparison with the wheel after conditioning. The increase in S_{mr1} is caused by an aggressive sharpening rather by a soft sharpening considering the assumptions of this study. A higher slope of the equivalent line takes the upper limit of the core closer to the upper part of the curve where the curve is closer to the left Y axis. This leads to a lower S_{mr1}.

Taking everything into account it is evident that the output of this method is not as clear as that of the average and standard deviation method. However, it is helpful if the results are analyzed carefully and extra information as the power consumption and optical images can be used.

In this study, the conclusions that can be drawn from some parameters contradict the conclusion that can be drawn from others. With the purpose of finding which of the contradictory parameters are reliable, the standard deviation of the average values must be regarded.

During the analysis of the parameters, S_a and S_z showed contrary results. However, the average value before grinding and after conditioning of S_z are more differentiated one from the other than the average value before and after conditioning of S_a. This can be visually observed with the probability density function, as plotted in Fig. 92.

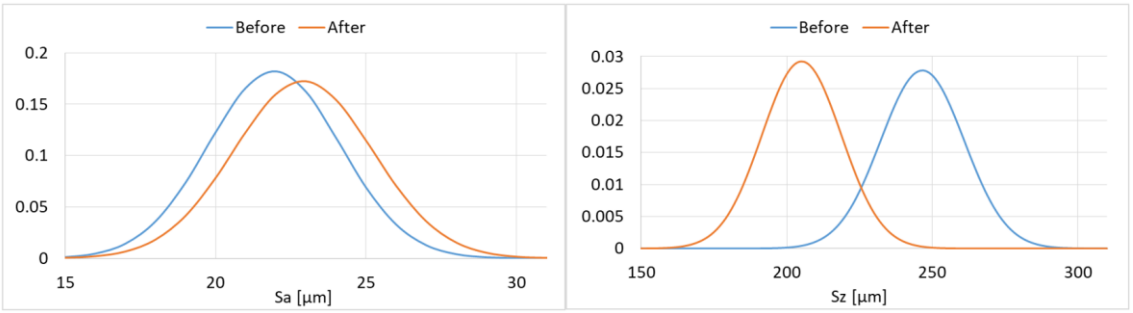

Fig. 92 Probability density functions of S_a (left) and S_z (right).

Therefore, the conclusions taken from the variation of S_z were considered as correct. None of the remaining parameters showed a difference between the two states as clear as S_z, hence only the parameters whose change was consistent with the wheel situation defined by S_z were considered as suitable for the analysis.

Similarly, S_k and S_{vk} were contradictory. The decrease of S_z, involves that the increase in S_k can only happen if material of the lowest part of S_k has been removed which was disregarded in the assumptions. Therefore, the variation of S_{vk} should be considered instead of the variation of S_k. As it was explained previously, this indicates that the grains have been suffered aggressive sharpening.

Finally, the variation of S_{mr1} was consistent with the aggressive sharpening.

2.4 CONCLUSIONS

In this chapter, the evolution of the wear of an EP grinding wheel used for CFG Inconel 718 was studied. Wheels used in aeronautic industry were taken to the laboratory and analyzed by means of optical measuring devices namely, macroscope, confocal microscope and SEM, and then returned to the industry. The surface analysis was carried out in terms of 3D roughness parameters of the standard ISO 25178 with the purpose of using standardized concepts. During the analysis the following questions were addressed.

Wear types and wear evolution along the wheel life. It was confirmed that the wear type that takes place on a grinding wheel depends on the wear state of the grinding wheel. At the beginning of the wheel life, the main wear type is the fracture of the grains until the height of them is leveled. Then, the forces decrease because of a lower chip thickness and the wear flat appears and gets more and more common as the grain protrusion height diminishes. For this analysis, the functional parameters were used since the different parts of the profile, i.e. the peaks, the core and the valleys, can be evaluated.

The most representative wear parameter of the wear state at the wheel life limit was found by means of comparing the roughness parameters of two wheels close to the wheel life limit. A wide range of parameters were compared, for that purpose, a mathematical method called average and standard deviation method was programed in Matlab® matrix analysis software. Thanks to this method, S_{sk} was found as the most representative parameter of the wear state at the end of the wheel life. In addition, the average and standard deviation method also provided

an equation for calculating the threshold value of the significant parameter for classifying the grinding wheels. With that threshold, a wheel can be classified as a function of its wear flat level.

The conditioning process of EP grinding wheel with resin bonded SiC stick was analyzed. This process was performed as a solution of the vibration and thermal problems on a specific part of the workpiece. The effect of this process was analyzed in terms of power consumption and wheel topography. The curve of the power consumption registered sudden decreases after conditioning process. However, the reduction was followed by a rapid increase until a new steady wear state. It was concluded that when the conditioning was performed on a wheel with wear flat not completely spread on the grains, the power consumption during the new steady wear state was higher than the tendency before the conditioning. However, when the conditioning was performed on a wheel with wear flat present on the majority of the grains, the power consumption during the new steady wear state returns to the same tendency that it had before conditioning. Regarding the topographic analysis, the change on the wheel surface was too slight to be able to apply the average and standard deviation method. As an alternative, another method called correlation coefficient was used on the same roughness parameter quantity as in the previous study. The five most representative parameters were analyzed in order to understand the change suffered by the wheel during the conditioning. It was concluded that the grains suffered microfractures that increased the cutting ability momentarily but soon they were broken and wear flat appeared again. This was related with the sudden decrease of the power and with the subsequent rapid increase to the new steady wear state.

EXPERIMENTAL APPROACH

3 EXPERIMENTAL APPROACH

3.1 INTRODUCTION

The empirical experimentation is a necessary source of information when either a physical or a chemical phenomenon is being studied. According to the scientific method, the hypothesis that is the origin of the scientific study comes from the background research and the observation of the process. Once the hypothesis is posed, specific experiments must be designed and carried out for testing whether the hypothesis corresponds to the empirical phenomenon or not.

The experiments should be planned for addressing two important aspects of the scientific work. On the one hand, the experiment must reproduce the real conditions of the process that has been the origin of the hypothesis. On the other hand, the experiments must allow the measurement of the output parameters for the evaluation of the hypothesis.

Taking these two basics into account, grinding process has been studied by means of both real condition grinding tests and laboratory tests. While the real grinding conditions can be reproduced by the first option, some simplifications based on theoretical assumptions must be done when laboratory tests are used as a source for empirical data. Nevertheless, the laboratory tests permit to take very specific information from the process that is difficult or even impossible to take from a real grinding operation.

There are numerous aspects of the grinding process that can be measured during and after grinding operation. The main ones are explained in the following lines.

Grinding forces are normally measured on the workpiece, they are usually divided in two components. The force in the radial direction of the wheel is called normal force while the force in the direction of the cutting speed is called tangential force. Because of the abrasive nature of the material removal in grinding, the normal force is higher than the tangential force, unlike other machining processes such as turning or milling. The third component of the force, i.e. the force in axial direction, is considered negligible.

The grinding power consumption can also be measured easily during the grinding process. It must be calculated in two steps. At first, the power needed just for rotating the wheel at the required speed must be measured. Then, this power must be subtracted to the power consumed during the grinding operation. In this way, the power required only for removing material can be obtained. There is a relation between the power consumption and the tangential force that allows to obtain one of them from the other. This relation is shown by Eq. (29) where F_t is the tangential force, v_s is the cutting speed, i.e. the peripheral speed of the wheel, and P is the net power consumption.

$$F_t = v_s \cdot P \tag{29}$$

From these output parameters, indirect parameters such as specific grinding energy and force ratio can be calculated. The specific grinding energy is defined as the energy needed for removing a mm^3 of workpiece material. It is written as e_c and its expression can be seen in Eq. (30), where Q_v is the material removal rate. The force ratio is the ratio of normal force, F_n, to tangential force, F_t, see Eq. (31).

$$e_c = \frac{P}{Q_w} \tag{30}$$

$$Force\ ratio = \frac{F_n}{F_t} \tag{31}$$

Grinding temperature can be measured through different technologies. Optical devices such as laser pyrometer and thermographic camera can be used for this purpose. However, normally, the cutting fluid blocks the visual access to the contact zone and the measurement cannot be succeeded. Thermocouples are considered as the alternative method for measuring the temperature near the contact zone. Nevertheless, the disadvantage of this method in comparison with the optical devices is the higher thermal inertia.

Apart from the in-process measurements, valuable information can also be gathered after the grinding process.

The grinding wheel wear can be addressed through optical or contact devices. A wheel wear analysis with optical devices was carried out in chapter 2.

Besides the state of the wheel, the state of the workpiece surface can also be addressed by the same devices. Usually, the state of the workpiece surface is analyzed in terms of two aspects. On the one hand, the roughness of the ground surfaces is important for the subsequent stage of the manufacturing sequence of the workpiece. Grinding is usually one of the latest machining operations of the manufacturing sequence, if not the latest. Therefore, the roughness achieved during the grinding process must be controlled since the performance of the workpiece will depend on this aspect. Thus, the workpiece roughness as a function of the process parameters has been extensively studied [2],[11],[48],[61],[94],[97],[108]–[116]. Similarly to the wheel wear, it can be measured by means of optical and contact devices.

On the other hand, the structural quality of the material may be damaged during the grinding process, so it must also be controlled. Grinding is a process with significant thermal loads in the contact zone and important workpiece material deformation during the chip generation. As a consequence, the surface and subsurface of the material may be thermally affected. A correctly performed grinding operation should generate compressive stresses on the workpiece surface. These stresses are beneficial for the workpiece working life since the material is more resistant to phenomena such as crack propagation. However, if the thermal stresses are too aggressive, thermal damage can appear on the workpiece surface and/or subsurface. The consequences of

such phenomenon are tensile stresses that may create cracks on or even below the surface [28],[104],[117],[118]. In metallic materials this is usually accompanied by microstructural changes [29],[53]. These phenomena can be studied by means of destructive and non-destructive methods.

Depending on the scope of the study, the grinding process can be reproduced in terms of equivalent chip thickness, h_{eq}, speed ratio, q_s, and specific material removal rate Q'_w, which are the most common industrial indicators of the grinding process. See Eq. (32), Eq. (33) and Eq. (34) respectively where a_e is the cutting depth, v_w is the feed speed and v_s is the cutting speed.

$$h_{eq} = a_e \frac{v_w}{v_s} \tag{32}$$

$$q_s = \frac{v_w}{v_s} \tag{33}$$

$$Q'_w = a_e \cdot v_w \tag{34}$$

Laboratory tests often use a configuration where no grinding wheel is used, therefore, the application of the previously mentioned indicators is not possible. Instead of a grinding wheel, a single grit is usually used. These tests, also called single grit tests, are focused on topics such as the physical and chemical phenomena suffered either by the grain or by the workpiece as a result of the contact, see section 1.4.

The forces can be measured in the same way as in grinding tests. However, in this case, they just correspond to the grain in contact and they can be related to more specific factors such as the amount of material removed per pass [85],[104]. However, the real situation of having multiple abrasive grains contacting the workpiece cannot be addressed. In consequence, effects as the increase in the temperature or the strain hardening of the material as a result of the contact with previous grains is disregarded.

The wear can be studied as well through this type of test. Nevertheless, due to the short time of the interaction grain-workpiece, the analysis of wear generation or evolution is not the focus of these studies. Instead, it should be considered as an input parameter.

The material behavior is one of the main targets of the single grit tests. Unlike a grinding process, the groove left by a grain on the workpiece material is not altered by the subsequent grains so it can be studied. On the one hand, the deformation suffered by ductile materials is studied in order to address factors as the cutting efficiency or surface roughness. On the other hand, the avoidance of cracks and material removal in the ductile regime are two of the objectives addressed with brittle materials, see section 1.4.

In addition, single grit tests are normally carried out without cutting fluid, for simplifying the setup and measurement systems. The majority of the articles mentioned in section 1.4 were conducted without cutting fluid.

Taking the single grit tests as a reference for studying the interaction between the abrasive grain and the workpiece material at a micro scale, a specific tribometer was developed for this work. The new tribometer was designed for improving previously mentioned limitations of the single grit tests. The whole process from the initial design to the definitive tests is gathered in this chapter. The initial situation that motivated the new tribometer is explained in the following lines.

This work addresses the contact during CFG of Inconel 718 with EP CBN grinding wheels. This is a complex process in terms of equipment and materials. A high-quality grinding machine must be used for being able to reproduce the industrial process while both the EP CBN grinding wheels and Inconel 718 have a high cost and delivery time. In addition, the information needed for this study is not possible to obtain from grinding tests because of the reasons mentioned before. In consequence, a specific laboratory test configuration was prepared for addressing the required information.

In laboratory tests, the relative translation between the tool and the workpiece can be linear or rotary. [119] compared the two types and concluded that linear tests are more appropriate when the influence of the shape and the angles of the grains must be studied, while the rotatory test allows to use cutting speed and trajectories similar to the actual grinding process. In addition, they also observed that the tool replacement and setup was easier in the linear tests. Taking these conclusions into account, a new test bench was designed for this work where the relative translation between the tool and the workpiece was linear but the sliding speed could be raised up to CFG cutting speeds. Furthermore, with the purpose of making the contact during the tests as close as possible to the contact during the grinding process, a multigrain surface was used instead of a single grit. The description of the tribometer is gathered in the following section.

3.2 NEW TRIBOMETER DESIGN

As concluded in the previous section, a tribometer for analyzing the contact between the grinding wheel and the workpiece is required. Tests benches for analyzing the contact have been used on numerous research fields in addition to grinding. For instance, it is extensively used for analyzing wear and friction between contacting surfaces in the fields of transportation and machinery. Because of this reason, there are numerous commercial tribometers which procedure, both for using and for taking the results, is already established and validated by numerous scientific works.

However, the suitability of these tribometers must be studied before planning the test from both the economical and the technical point of view. These are the reasons why there is still wide range of scientific works whose results come from “homemade” tribometers, some of them are mentioned in section 1.4. In the book Friction Science and technology [120], Peter J. Blau addressed this topic and gave valuable information of the existing tribometer configurations and the points to be considered before planning the tests. In the following lines some of the indications presented in that book are gathered and used for designing the tribometer for this work.

Taking into consideration the assumption that the tribometer is not able to resemble exactly the real situation, according to Peter J. Blau, a tribometer must be selected after having evaluated the following three points:

- The target of the tests.
- The physical limitations of the tribometer, namely, the normal force, the magnitude and direction of the relative velocity, the acceleration, the humidity and temperature of the tribometer, the stiffness of the system and the presence of lubricants and loose particles among others.
- The friction is characteristic of a tribosystem and not of the materials. Therefore, the tribometer itself has influence on the results.

This works has some characteristics already established by the components of the test, especially the grinding wheel, and by the grinding process parameters. Therefore, some of the tribometer configurations gathered by the American Society of Lubrication Engineers (ASLE) can be directly dismissed. They sorted the tribometers in the following list.

- Multiple sphere.
- Crossed cylinders.
- Pin-on-flat.
- Flat on flat.
- Rotating pins-on-disks.
- Pin-on-rotating disk.
- Cylinder-on-cylinder.
- Rectangular flat-on-rotating cylinder.
- Disk-on-disk.
- Multiple specimens.
- Miscellaneous.

In the previous section it was concluded that with the purpose of addressing the effect of the adjacent grains in the contact, the tribometer must be capable of using a multigrain surface instead of a single grain. The multigrain surface must be taken from a real grinding surface with the purpose of using the same grain size, grain density and grain protrusion height as in the real process. The way of using a small surface of the grinding wheel for the tests is to extract pins from it.

The high cutting speed of CFG process is easier to reach with a rotating component. Otherwise, extremely high accelerations or extremely long samples would be needed if the moving components were moved with a linear motion.

The rotating component must be correctly balanced in order to avoid instabilities during the tests. Therefore, setting the pin as a rotating component hampers the tribometer setup. It is more sensible to manufacture a balanced disk made of the workpiece material.

Taking all the considerations into account, the most appropriate tribometer configuration for this work is a pin-on-rotating disk.

Regarding how the contacting surfaces change along the test, it can be divided in two types [120]. The conformal tests are those where the apparent contact area does not vary during the test. By contrast, the tests where the apparent contact area varies as a consequence of wear are qualified as nonconformal. This takes place when the section of the component to get worn is not constant, such as spheres or cylinders. The conformal tests maintain a constant contact pressure during all the test; however, it is more difficult to align correctly the two surfaces. By contrast, in nonconformal tests, the tangency point is found automatically thanks to the geometry or wear, but the pressure varies along the test. Due to the short duration of the tests and the difference in hardness between the workpiece and the abrasive grains, it was considered that the grains of the pin do not suffer wear during the test. Hence, these tests can be classified as conformal.

In conclusion, given the geometry and process parameter limitations, the optimal tribometer configuration is a pin-on-rotational disk where the abrasive surface is on the pin and the disk is made of workpiece material. The development of the "homemade" tribometer is explained in the following sections.

3.2.1 Design and development of a new tribometer

There are several aspects that must be taken into account when a new tribometer is developed for a specific purpose. Some of them are foreseen during the conception, but others are detected during the use of the tribometer. In the following lines the whole process is summarized and only the most relevant information for the reader is included with the purpose of improving the readability.

3.2.1.1 Setup and procedure

The setup was designed for being mounted inside a machine tool. In this way, only the static elements had to be designed. The disk was clamped to the workhead spindle and the pin was mounted in the table of the machine. The driving axes of the machine were used for controlling the relative position of both elements.

However, a constant contact pressure must be carried out during the tests. This requirement was not possible to fulfill with the driving axes of the machine since they go to the specified distance no matter the force needed. On the one hand, taking into account that a certain disk material removal is expected, the relative position at the beginning of the test cannot be maintained during all the tests without losing contact pressure. On the other hand, the pressure lost by the material removal could not be recovered by moving the axes of the machine during the test because of the reason explained previously. As a solution, the pin was mounted on a pneumatic cylinder and a constant movement of the disk toward the pin was carried out during the tests. For improving the rigidity of the setup, a cylinder with double rod was used, see Fig. 93.

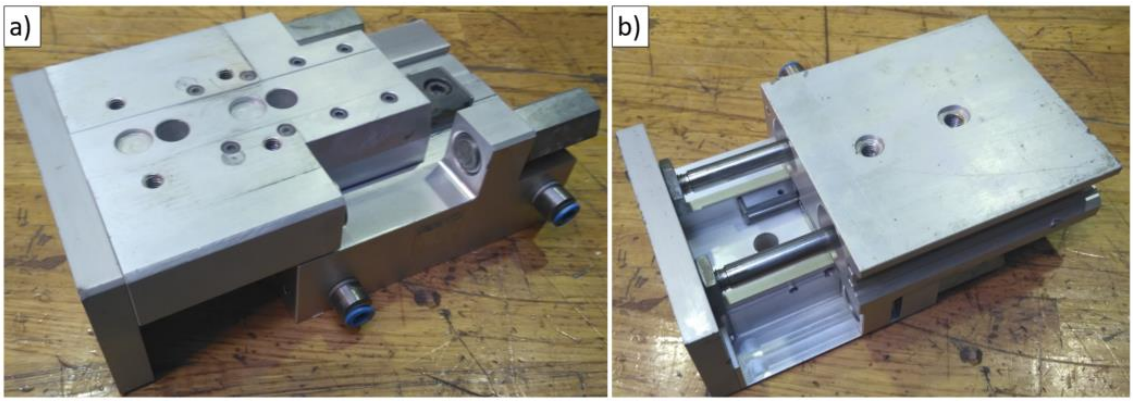

Fig. 93 a) Upper view of the double rod cylinder. b) Lower view of the double rod cylinder.

A homemade clamping device was manufactured for fixing the pin to the pneumatic cylinder, however, the orientation of the pin had to be established before the tests. Given the curvature of the grinding wheel the pin could have two orientations as shown in Fig. 94.

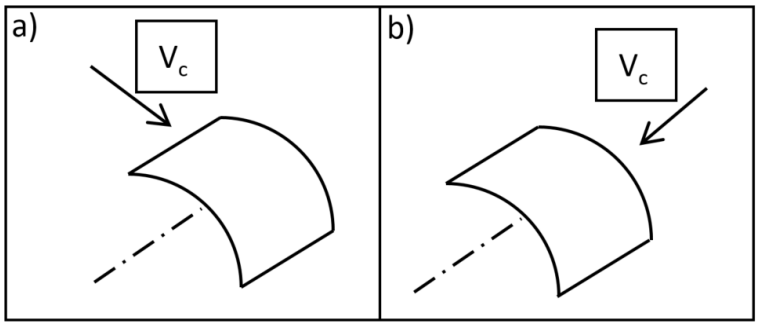

Fig. 94 a) The axis of the pin is perpendicular to the sliding speed direction. b) The axis of the pin is parallel to the sliding speed direction.

- The axis of the pin perpendicular to the linear speed of the disk, Fig. 94 a).
  With this configuration, there is a progressive increase in the cutting depth of the grains while the material approaches to the tangent point. That is to say that the disk material that contacts the grains has already been in contact with previous grains. The efficiency of the material removal process will have influence on the amount of material that the subsequent grains are going to interact with. This is the phenomenon that takes place during a real grinding operation, where the material to be removed by a grain has already been modified by the previous grains in both aspects thermally and mechanically.
- The axis of the pin parallel to the linear speed of the disk, Fig. 94 b).
  With this configuration, the result of different cutting depth can be studied in a single test thanks to the curvature of the pin. There are also several grains that will contact the disk material after having been interacted with other pins. However, the progressive increase in the cutting depth from a grain to the next one is more complicated to achieve in a controlled manner.

Comparing the two setups, the first one provides a scenario closer to the real grinding process. In addition, the preparation of the setup is easier in the option show in Fig. 94 a) since only the tangent point in all the width of the pin must be found, see Fig. 95 a) and b). By contrast, with

the option shown in Fig. 94 b) the pin should be slightly tilted for ensuring a contact with the grains instead of with the edge of the pin, see Fig. 95 c) and d).

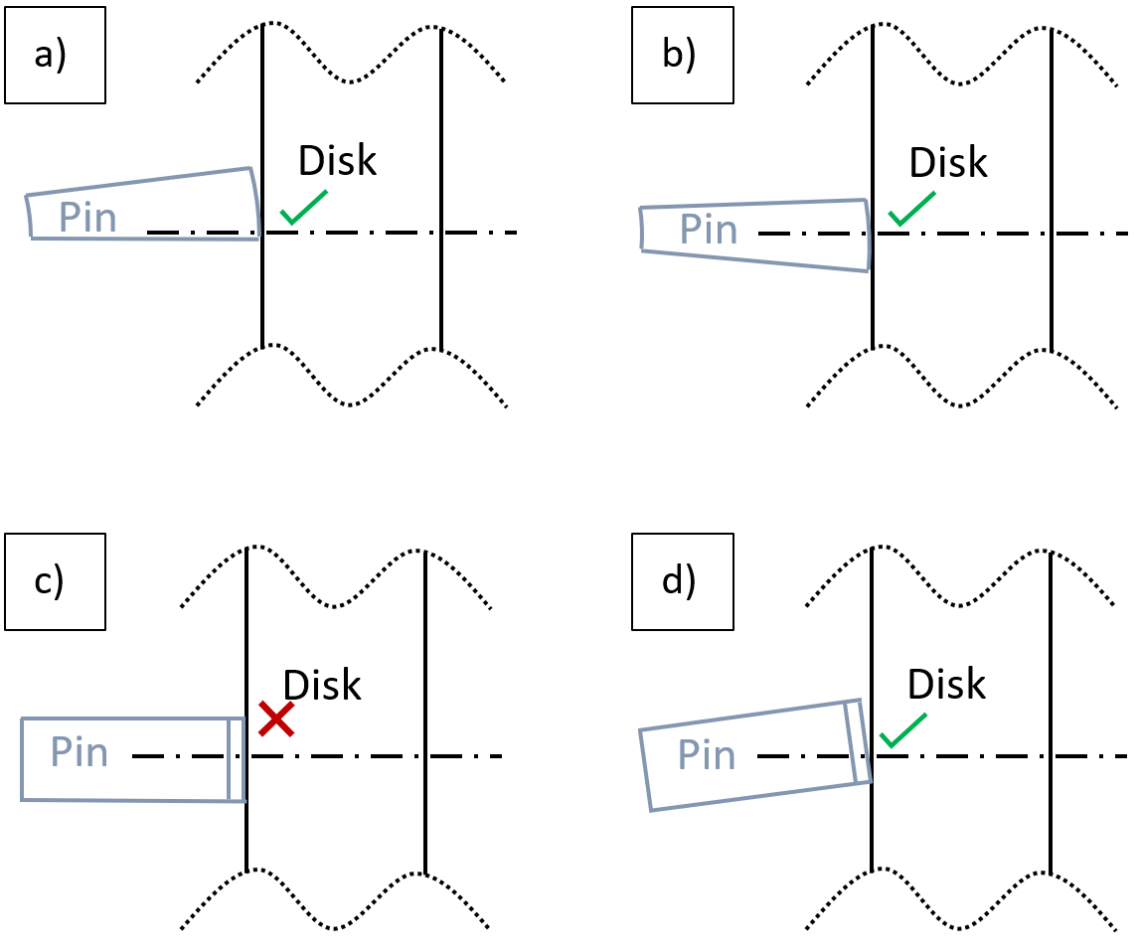

Fig. 95 a) and b) correct positions for the pin with respect to the disk with the configuration shown in Fig. 94a). c) and d) incorrect and correct position respectively for the pin with respect to the disk with the configuration shown in Fig. 94 b)

As depicted in Fig. 95, the contact was decided to be carried out on the flat face of the disk instead of on the periphery. Several tests were going to be carried out on the same disk, hence the scratches made on the disk had to be removed for the subsequent tests. Taking everything into account the following three reasons motivated this decision:

- The fact of performing the tests on the flat surface allowed to carry out several tests before having the need for removing the scratches.
- The process for removing the scratches was easier as it is going to be explained in section 3.2.1.4.
- The process of removing the scratches implies also a removal of the disk material. If the scratches were done on the periphery, the diameter of the disk would be reduced after every test.

Once defined the setup, the input parameters were selected. Considering the components of the tribometer, three input parameters could be modified:

- Sliding speed.
  The speed has influence on the material mechanical behavior and on the temperature generated during the grinding process due to the speed effect [14],[16],[82],[105]. Therefore, a range of speeds comparable to the speeds used in grinding operations was selected. The grinding speed used in the industry for this CFG application was 80 m/s, this value was set as the maximum speed. The lower speed values were 75, 60, 40 and 20 m/s.
- Contact time.
  The number of laps in contact depends on the contact time and the rotational speed of the disk. It was not possible to keep constant the number of laps and the contact time in every test given the range of speeds to be tested. Therefore, this aspect was fixed as a function of the methods for evaluating the tests. A constant contact time was useful for evaluating the wear on the pins while a constant number of laps is more appropriate for evaluating the scratches created on the disk. Due to the high performances of CBN, it was considered that no significant wear was going to take place on the pin. In consequence, the tests were programmed so that the same number of laps were carried out in every test, namely 10 laps.
- Pressure of the cylinder.
  The pressure of the cylinder controls the cutting depth of the pin. Similarly to the speed, this input should be coherent with the real process in order to obtain consistent results. The values of the pressure set on the cylinder are explained later in section 3.2.1.3 together with the definition of the size of the pin.

Before the preliminary tests, a methodology was established and followed step by step in every test. The sequence is the following:

1. Put the pin in the holding system and activate the cylinder with the pressure to be used during the test.
2. Approach the disk and the pin until the very first contact takes place. The disk is still during this step.
3. Check if the contact between both components is carried out all along the width of the pin. If not, they must be separated and the position of the pin must be adjusted until the contact is all along the width.
4. Once the contact is correct, the elements must be separated again and the rotation of the disk must be started.
5. When the disk reaches the speed programmed for the test, the test can be done.

Despite having every aspect of the tribometer defined, the performance at the required speeds and force was uncertain in terms of safety and reliability of the results. With the aim of checking these two aspects of the tribometer, a first batch of low speed tests (LST) was carried out with a simpler setup. The results obtained in these tests were analyzed and took into account for the later and definitive high-speed tests (HST).

It should also be mentioned that the tests were carried out with two different types of pins in order to assess the influence of the wear. Pins extracted from a brand-new grinding wheel, called from this point on as *new*, and pins extracted from a wheel at the end of its working life, called from this point on as *worn*.

3.2.1.2 Evaluation methods

The data for evaluating the tests was obtained by means of online and offline acquisition methods. They are sorted in the following lines:

- Power sensor (online measurement). A capacity power sensor was connected to the three phases of the workhead spindle of the machine, see Fig. 96. This device registered the power consumed by the spindle and sent this information to an acquisition card that allowed to register the data in a computer. For recording the real magnitude of power values, the hardware and the software must be adjusted according to the maximum power of the spindle engine of the machine.

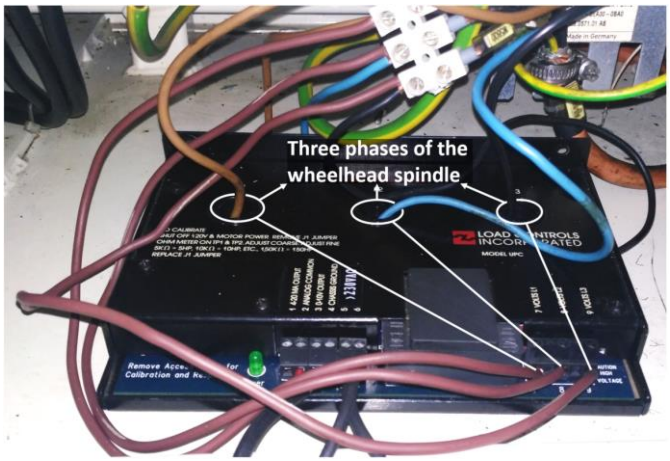

Fig. 96 The power sensor connected to the three phases of the wheelhead spindle.

- Force sensor (online measurement). A piezoelectric force sensor was used for registering the forces suffered by the pin. Although the tangential force could be obtained from the power consumed by the spindle by Eq (29), a specific device was needed for registering also the normal force. The third component of the force was also registered by the sensor, but it was not used for the study since the tribometer did not produced a force in that direction.
  The force ratio was used for evaluating the changes in the forces. This parameter is calculated with Eq. (35) and has been used by other authors as an indicator of the cutting ability of the wheel [1],[18],[23],[29],[43],[79],[116],[118],[121].

$$Force\ ratio = \frac{F_n}{F_t} \tag{35}$$

- Stylus roughness tester (offline measurement). The scratches made on the disk were digitalized through a stylus roughness tester. This was used for evaluating the behavior of the material in terms of plastically deformed material and removed material. The suitability of the diamond tip was verified by comparing its geometry with the geometry of several CBN grains with no wear. If the diamond tip was sharper than the CBN grains, it was capable for reaching the lowest part of the marks created by the grains. For that purpose, the angle of twelve CBN grains was measured in two directions with a confocal microscope. Given the irregular shape of the grains, the angle was evaluated in the first

10 µm in depth. An example of the measurement is depicted in Fig. 97 and the results are gathered in Table 7.

The pile-up ratio was used for comparing the scratches. This parameter is calculated with Eq. (36) and has also been used by other authors as an indicator of the material removal efficiency in terms of material behavior [14],[81],[83],[84],[100],[112].

$$Pile - up\ ratio = \frac{Piled\ section}{Groove\ section} \tag{36}$$

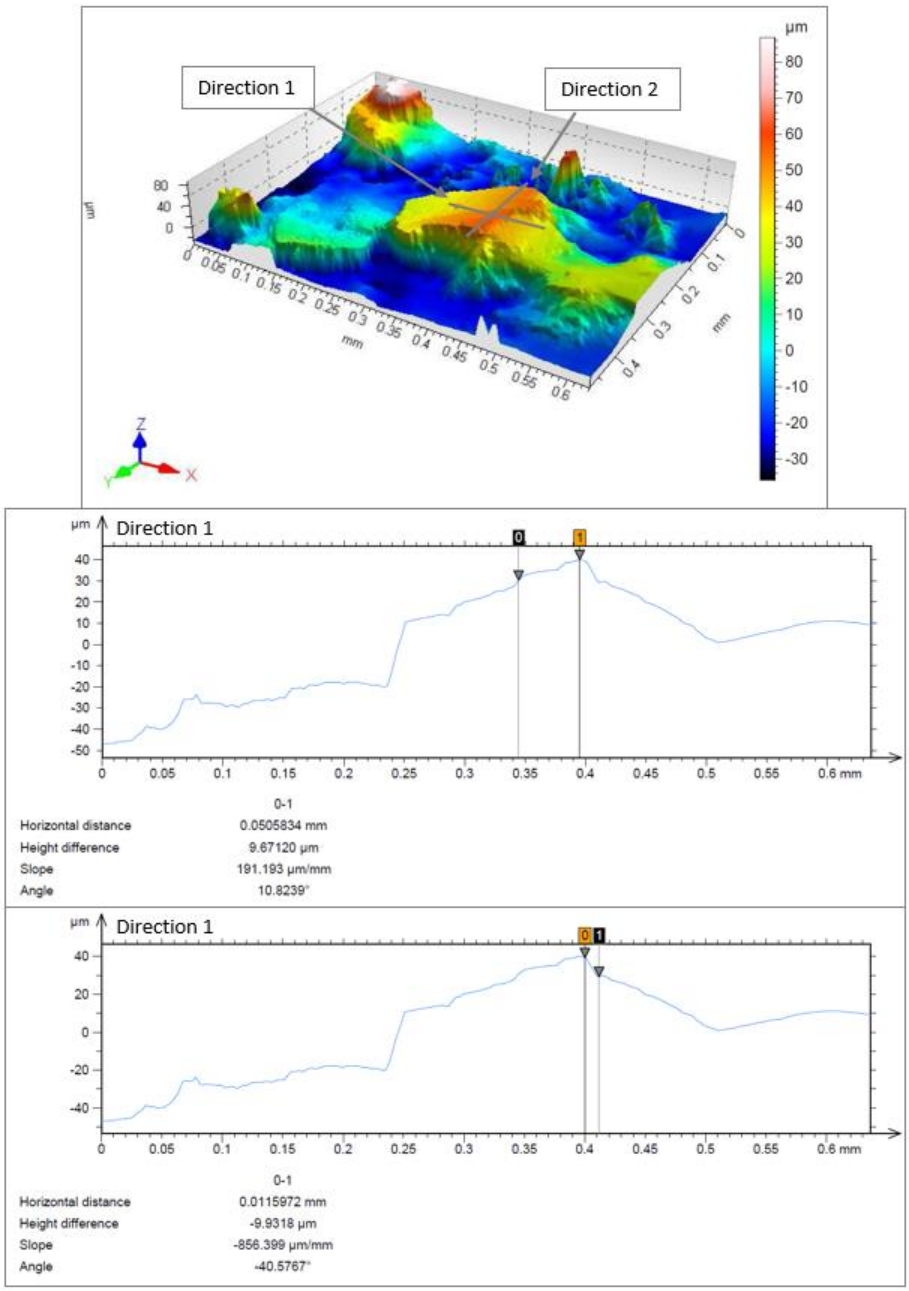

Fig. 97 Digitalization and measurement of the CBN grains tip. This grain corresponds with the Grain 1 of Table 7.

Table 7 CBN grains tip angle.

Grain	Grain tip angle in direction 1 [°]	Grain tip angle in direction 2 [°]
1	128.6	68.1
2	56.6	98.5
3	80.3	153.5
4	158.1	136.6
5	139.5	101.2
6	131.5	119.9
7	99.1	103.8
8	124.3	35.6
9	80.7	131.6
10	153.3	94.5
11	131.0	117.1
12	99.1	140.3
Average	115.2	108.4

The majority of the angles measured on the grains are above 60°, hence, a diamond tip of 60° was used for measuring the scratches, see Fig. 98.

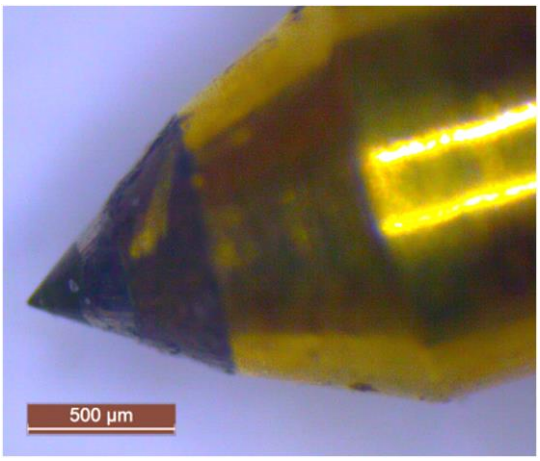

Fig. 98 Diamond type used in the stylus roughness tester.

- Optical devices (offline measurement). Optical devices were included in the evaluating methods for observing the surface of the pins after the tests. The same macroscope and SEM used in chapter 2 were used for this purpose.

3.2.1.3 Pin

As explained in the previous section, the abrasive pin must be extracted from a grinding wheel in order to have the same abrasive surface as in the actual grinding process. The procedure for extracting the pins from the grinding wheel must fulfill the following conditions:

- It must be ensured that no harm or modification was going to take place on the abrasive surface. Otherwise, the contact conditions could not be comparable with a real grinding wheel condition.
- It must be an accurate process with the purpose of reducing as much as possible the waste of the grinding wheel. The EP CBN grinding wheels have a cost around 10 or 20 times higher than a conventional grinding wheel. Besides, the delivery time is also significantly longer, hence, the number of pins extracted from a grinding wheel should be maximized.

Taking these two conditions into account, the process was defined taking advantage of the particular features of an EP grinding wheel.

Unlike the conventional vitrified grinding wheels, whose entire body is formed by abrasive grains, bonding material and pores, EP grinding wheels have only one abrasive layer. A nickel layer is the responsible of bonding the abrasive grains to the core the wheel. The core of the wheel has a mechanical purpose on the whole composition of the grinding wheel. For improving the wheel performance, it must contribute rigidity for avoiding the wheel deformation due to either normal force or centrifugal force. Nevertheless, the it must also be capable of dumping the vibrations created during the grinding process. Carbon fiber and steel are the most typical materials used for the core of the wheels. Carbon fiber is rather used for wheels with large dimensions with the purpose of reducing the weight thanks to the lower density in comparison with the steel. Nevertheless, the wheels used in this application by the industry have a steel core since they are 150 mm in diameter and 50 mm in width.

Taking advantage of the electric conductivity of the steel, electro discharge wire machining was used for extracting the pins. This technology allows to machine electric conductive materials with very particular characteristics in comparison with the typical machining processes. Electro discharge machining technology uses an electrode as one of the poles and the workpiece as the other. Then, a dielectric fluid is supplied to the zone to be machined and an electric current is sent to the electrode. The electrode is approximated to the workpiece until the difference in the voltage between the electrode and the workpiece ionizes the fluid where eventually a spark is created between the two bodies. Finally, the high temperatures created by the spark cause the material removal. As the workpiece material is removed, the electrode is moved according to the programmed trajectory. This machining process fulfills the two conditions mentioned before.

On the one hand, no harm is produced on the abrasive surface. There is not a physical contact between a tool and the workpiece, therefore the grains are not damaged or modified. In

addition, the temperature created by the spark for the material removal is very local and does not produces any modification in the structures of steel or nickel. On the other hand, the path created by the wire on the workpiece, was around 0.25 mm in width. In this width the diameter of the wire and the gap from the wire to the workpiece are comprised. Thus, the wasted proportion of the wheel was considered as negligible. An Ona Prima E-250 machine was used for this purpose.

Nevertheless, CBN is not a conductive material so it could not be cut by the wire. As a solution, the trajectory of the wire was programmed from the inner hole of the wheel to the abrasive layer. Once the nickel layer was reached, a special configuration of the machining parameters was used for having a gap higher than the grain size. See in Fig. 99 a) a sectioned wheel and in Fig. 99 b) some pins numbered for the tests.

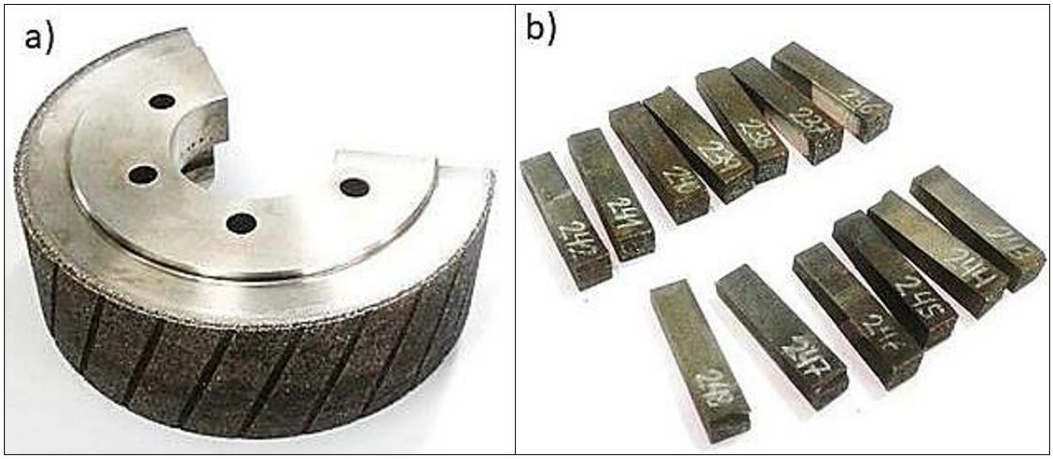

Fig. 99 a) A sectioned wheel. b) Some pins numbered for the tests.

With the purpose of simplifying the process and enhancing the number of pins that could obtained from the wheel, the pins where obtained with square section. However, the size of the pins together with the pressure set on the pneumatic cylinder was important for reproducing the mechanical loads of the real process. For this purpose, the power consumption of a grinding wheel during the real grinding process was analyzed. Then, an equivalence was calculated as a function of the pin size and the pressure of the pneumatic cylinder.

The power consumption and the corresponding ground geometry used or the calculation are shown in Fig. 100. It is the same surface as shown in Fig. 63 and called *inner rail*. The wheel used for grinding this surface is a conical wheel, unlike the one used for taking the pins. Nevertheless, the specifications of the wheel and the grinding parameters were the same. The reason why this grinding operation was chosen for this calculation was that there is a constant geometry that allowed to relate clearly a power value with a workpiece geometry. Other surfaces to be ground on the workpiece with same specification wheels present irregular geometry or more complex operation such as inner radius.

This power signal was obtained by means of a power sensor connected to a 5-axis grinding machine used in the industry. The power signal plotted in Fig. 100 was registered with a new wheel, thus, the influence of the wear was avoided.

The procedure for calculating the equivalence is explained in the following four steps:

1. From the subtraction between P_1 and P_{void} the power consumption spent only for grinding, P_{net}, is calculated, see Eq. (37).

$$P_{net} = P_1 - P_{void} = 12000 - 3000 = 9000W \tag{37}$$

2. The tangential force was calculated by dividing the power by the cutting speed, 80 m/s, see Eq. (38).

$$F_t = \frac{P_{net}}{v_s} = \frac{9000}{80} = 112.5N \tag{38}$$

3. Then, the normal force was calculated using a force ratio equal to 0.3, [8], in the Eq. (39).

$$F_n = \frac{F_t}{0.3} = \frac{112.5}{0.3} = 375N \tag{39}$$

4. Finally, the width of the grinding operation taken from Fig. 100 was used for calculating the normal force per mm in Eq. (40), this is called specific grinding force.

$$F'_n = \frac{F_n}{R_{out} - R_{in}} = \frac{375}{284.27 - 265.26} = 19.7N/mm \tag{40}$$

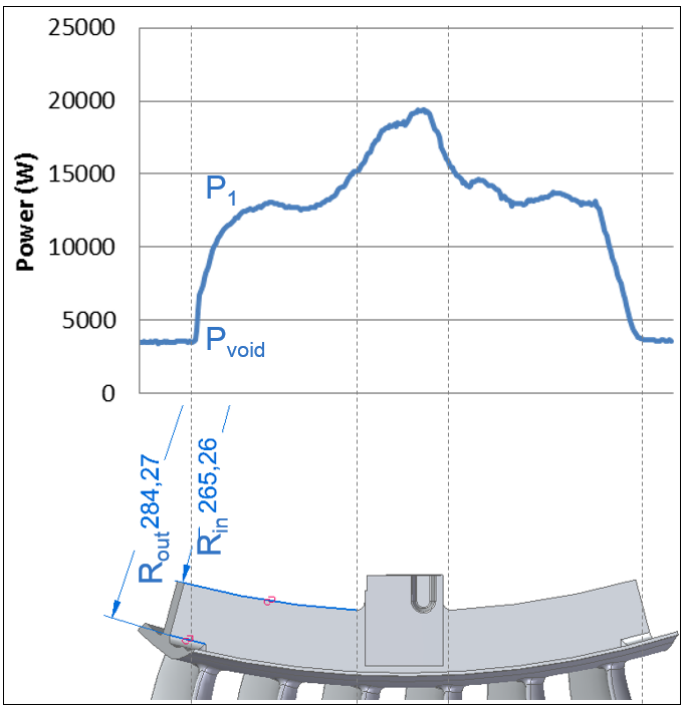

Fig. 100 On the top it is plotted the grinding power consumption that corresponds with the workpiece geometry depicted on the bottom.

Once the specific grinding force was calculated the corresponding contact width of the pin was calculated. The range from the lowest to the highest force of the cylinder as a function of the pressure was calculated for that purpose. Taking that value as a reference the corresponding pin width was finally calculated. All the information is gathered in Table 8.

Table 8 Force range of the cylinder as a function of the air pressure and the corresponding pin width for achieving the specific normal force calculated from the grinding process.

Air pressure in the cylinder [MPa]	Force given by the cylinder: F_{cyl}. [N]	Corresponding pin width: (F_{cyl}/F'_n). [mm]
0.1	98.3	5
0.2	196.6	10
0.3	294.9	15
0.4	393.2	20
0.5	491.5	25
0.6	589.8	30

The width of the pin was established at 7 mm because of two reasons. On the one hand, it was preferable to have low forces in the tribometer. Lower forces make the tests less demanding for the structure of the tribometer in terms of mechanical properties. On the other hand, given a grinding wheel width of 50 mm, it was possible to obtain 7 complete pins from each section without any waste of the wheel, see a depiction in Fig. 101 together with a picture of a pin.

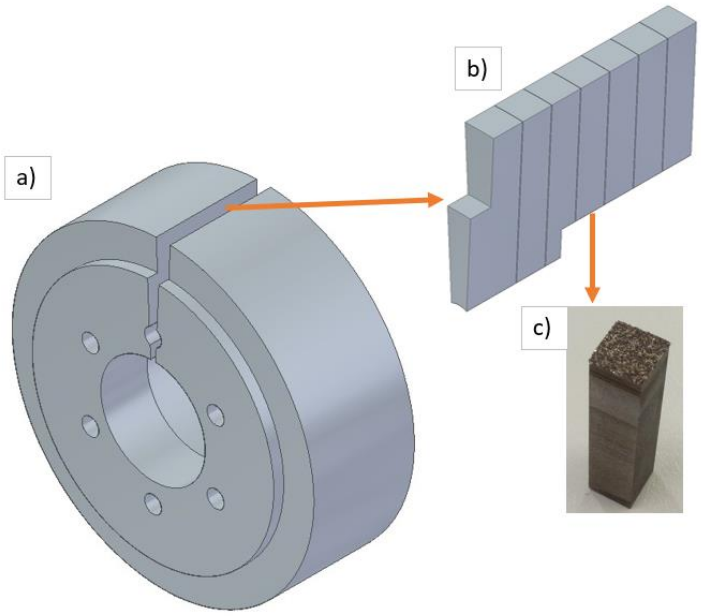

Fig. 101 a) A depiction of an EP grinding wheel with a section removed. b) A section of the wheel divided in seven pins. c) A picture of a real pin

3.2.1.4 Disk

The material of the disk was Inconel 718. Once received, the raw disks had to be modified with the purpose of adapting to the clamping system of the machine and reducing the unbalancing and runout error. The preparation of the disks for LST and HST was different

3.2.1.4.1 Disk for LST

In these tests the raw material was supplied as a rod with 160 mm in diameter. At first, the rod was machined in a lathe where the outer and inner diameters were machined. By machining the outer diameter, the irregularities from the rolling process were removed while the central hole was required for the HSK clamping system. Secondly, the rod was cut by electro discharge machining for obtaining the disks. Finally, the two faces of the disk were ground in a surface grinding machine for reducing the axial runout with respect to the clamping hole and for diminishing the roughness of the disk surface.

3.2.1.4.2 Disk for HST

Unlike the one used for the LST, the diameter of this disk was larger for achieving higher speed without the need of having a rotation speed extremely high. Thus, a disk with 450 mm in diameter and 20 mm in width was used. Instead an HSK, the flanges used for a high-speed grinding wheel were used for clamping the disk. In this case, a 3-axis milling machine was used for machining the required holes on the disk. The last step was to minimize the axial runout and reduce the roughness on the face of the disk where the tests were going to be carried out. This operation was done with a surface grinding machine for the previous tests, however, this resulted in a deficient process, as it is explained in section 0. As an alternative, the tribometer was used also for grinding the disk through a vitrified alumina pin, see Fig. 102.

Fig. 102 An alumina pin used for grinding the disk surface.

The pin shown in Fig. 102 was clamped in the same place as the pin of CBN and subsequent passes were carried out on the surface of the disk until the runout and the roughness were in acceptable values, $\leq$ 10 µm and $R_a \leq$ 0.2 µm respectively. Furthermore, the same procedure could be used for cleaning the surface of the disk after doing a batch of tests.

3.2.2 Low speed tests

The LST tests were carried out in a horizontal milling machine Comau® UGV MT1. A special geometry was machined on the Inconel 718 for been clamping by an HSK chuck, see Fig. 103. The disk was 110 mm in diameter and 10 mm in width.

Fig. 103 The Inconel 718 disk fixed on the HSK chuck used for the LST.

A piezoelectric force sensor Kistler 9347C was used for registering the forces transmitted to the pin, both components were fixed as it is shown in Fig. 104.

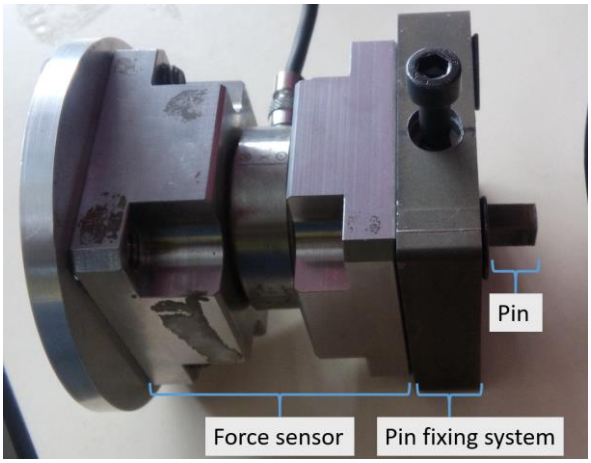

Fig. 104 Assembly of the force sensor, the pin fixing system and the pin.

This was attached to the pneumatic cylinder and the whole assembly was fixed on the table of the machine as it can be seen in Fig. 105.

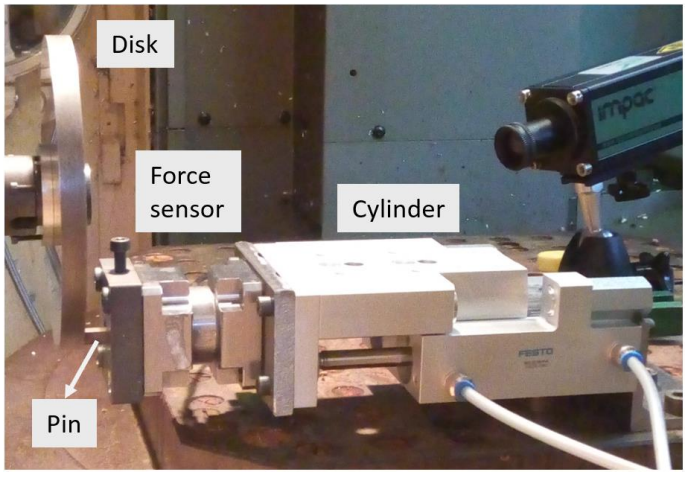

Fig. 105 Setup of the LST.

The speed was limited to 20 and 40 m/s because of the size of the disk and the maximum rpm of the workhead spindle. Nevertheless, the pressure calculated in section 3.2.1.3 was used, i.e. 0.1 and 0.2 MPa. Although these results were essential information for the final design of the tribometer and HST, they do not give valuable information to the reader. Therefore, only the most relevant aspects noticed from the results are going to be mentioned for improving the readability of the document. The definitive results obtained in the HST will be shown later in section 3.3.

3.2.2.1 Forces

The forces registered by the sensor showed an extremely high vibration specially on the tests carried out at 40 m/s and 0.2 MPa. A Fourier analysis was carried out with the aim of finding the cause of the vibration. The result of the Fast Fourier Transform (FFT) analysis of two normal force signals is shown in Fig. 106 a) and b).

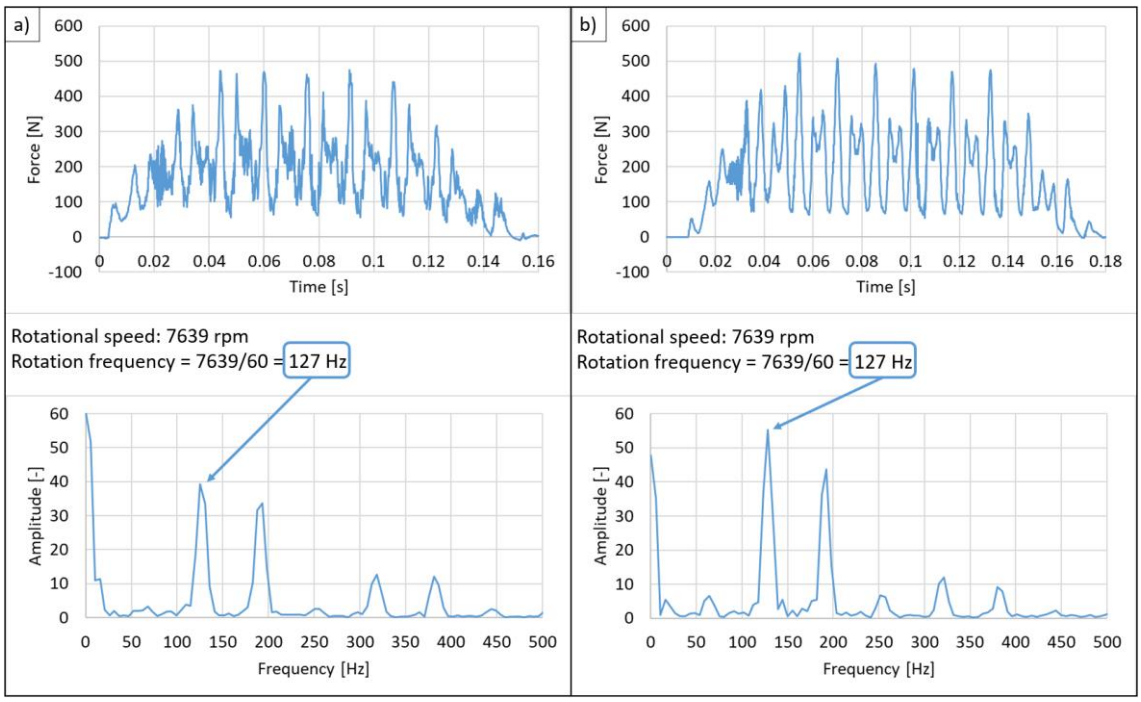

Fig. 106 On the top, the normal force signal of two tests at 40 m/s and 0.2 MPa. On the bottom, Fast Fourier Transform of the signals.

The first harmonic revealed by the FFT matched with the rotation frequency. Therefore, it was concluded that the cause of this harmonic was the axial runout of the disk. Both tests were carried out on the same disk, hence, the reason may be a deficient manufacture. In spite of the fact that the manufacturing process was carefully designed for avoiding this problem, the quality was not good enough for ensuring a good performance. As a solution, it was concluded that the face of the disk must be finished after having the disk mounted in the tribometer. The process is explained in section 3.2.1.4.2.

The second harmonic at 193 Hz could not be related to a specific factor, therefore it was tried to be solved by a stiffer setup.

3.2.2.2 Wear of the pins

The state of the pins after the tests was observed with the aim of seeing the effect that the tests had on the CBN grains. This was carried out through a macroscope and a SEM.

In Fig. 107 the macroscope pictures of two pins are shown. It can be noticed that the alignment of the pins with respect to the surface of the disk is correct since there is disk material in all the pin width.

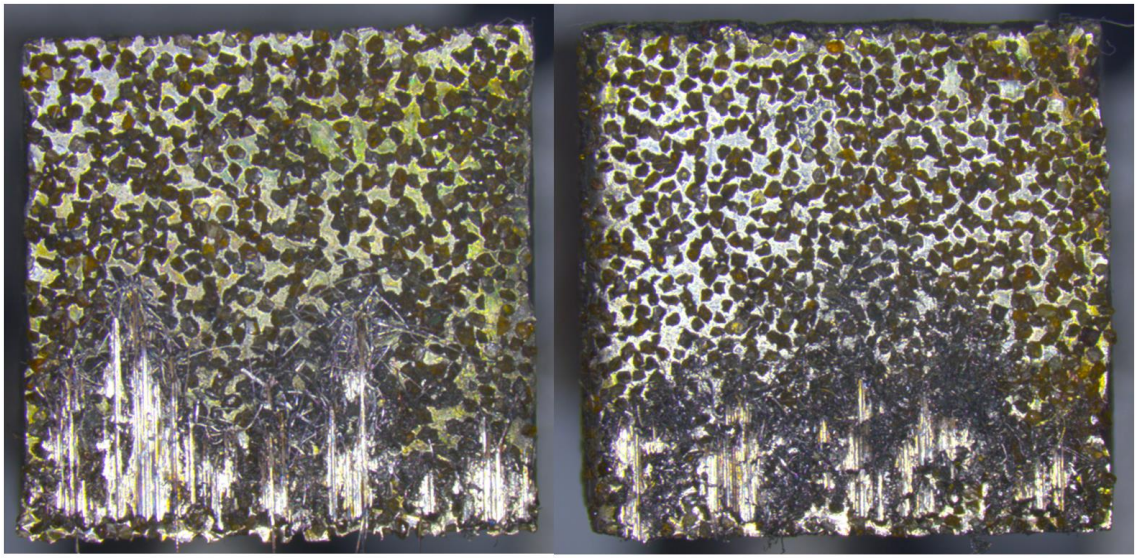

Fig. 107 A macroscope picture of two pins after LST,

In Fig. 108 two SEM pictures of the contacting zone are shown. In these pictures it is evident that the disk material attached to the pin covered the void space between the grains and also the grains in the contact zone. Therefore, as it was expected, the wear of the pins could not be considered as an output.

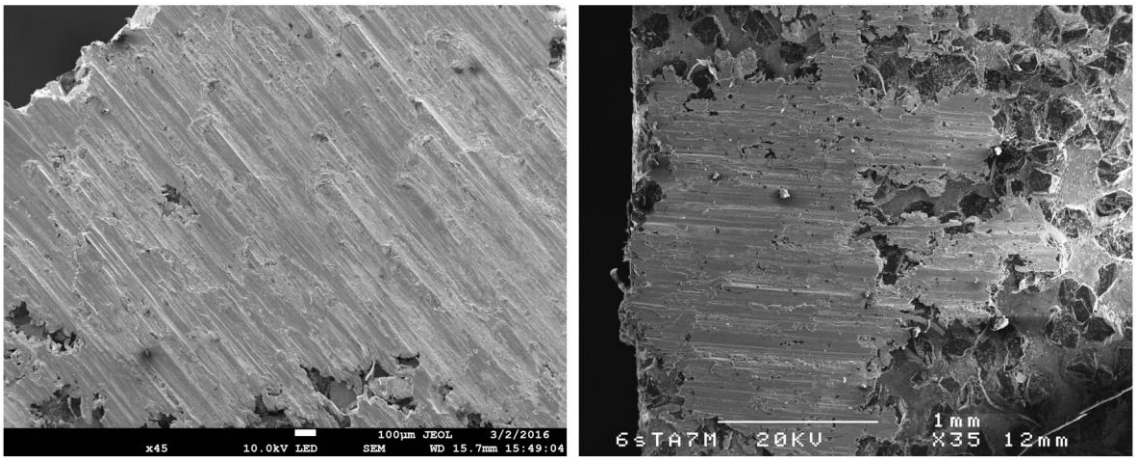

Fig. 108 SEM pictures of the loaded zones of the pin after LST.

The attachment phenomenon does not take place in the real grinding process unless too worn wheels are used, inappropriate grinding parameters are used or deficient cutting fluid rate is delivered. There are three factors that promoted this result:

- The ductility of the material. A ductile material, in comparison with a brittle material, suffers more plastic deformation before the failure. When a fragile material is machined, the resulting chips are smaller because there is less plastic deformation before the creation of the chip. By contrast, the chips of a ductile material are longer and are more likely to get attached to the tool.
- The kinematics of the tests. During a grinding process, despite having a constant contact between the wheel and the workpiece, the contact between the grains and the workpiece is discontinuous. Thus, the chips created from the interaction between the grain and the workpiece are removed from the contact zone when the grains leave the workpiece. Nevertheless, in the tribometer, the contact between the grains and the disk is constant. This situation hampers the removal of the chips from the contact zone and facilitates the attachment phenomenon.
- The absence of cutting fluid. Despite using cutting fluid in the industrial process of CFG of Inconel 718, the tests were carried out in dry conditions. The cutting fluid used in the industry is oil, what requires specific safety equipment for fires. The tribometer was designed for being used inside a machine tool, hence the use of cutting fluid during the tests was feasible. Nevertheless, the use of oil was dismissed because of safety reasons. Thus, the first battery of tests was planned to be carried out in dry conditions. The use of water based cutting fluid will be considered for future tests.

3.2.2.3 Measurement of the scratches

After having performed the tests, the scratches of the disk were digitalized by means of a stylus roughness tester. The digitalization of the scratches was then used for calculating the pile-up ratio. According to Eq. (36), this is the ratio of the piled material section to the groove section. Hence, the piled material must be differentiated from the groove, the area of both parts must be calculated and finally the values must be divided.

The analysis software of the stylus roughness tester allowed to separate the profile in an upper and a lower section. However, the profile could only be separated with the mean line. The mean line is placed at the height where the material section above equals the void section below. This is used for calculating roughness parameters such as the mean roughness, R_a, but was not suitable for the current study. As a solution, the profiles were analyzed in Matlab® software.

The process had the following steps:

1. Levelling the profile. The disk and the stylus roughness tester were not perfectly aligned in consequence, the profile presented a slope that had to be removed.
2. Establishing the zero level. The height of the virgin surface had to be used for differentiating the piled material from the grooves. Thus, the positive values of the profile corresponded to the piled material and the negative values to the groove section. The first and the second steps were carried out at the same time as it is depicted in Fig. 109.

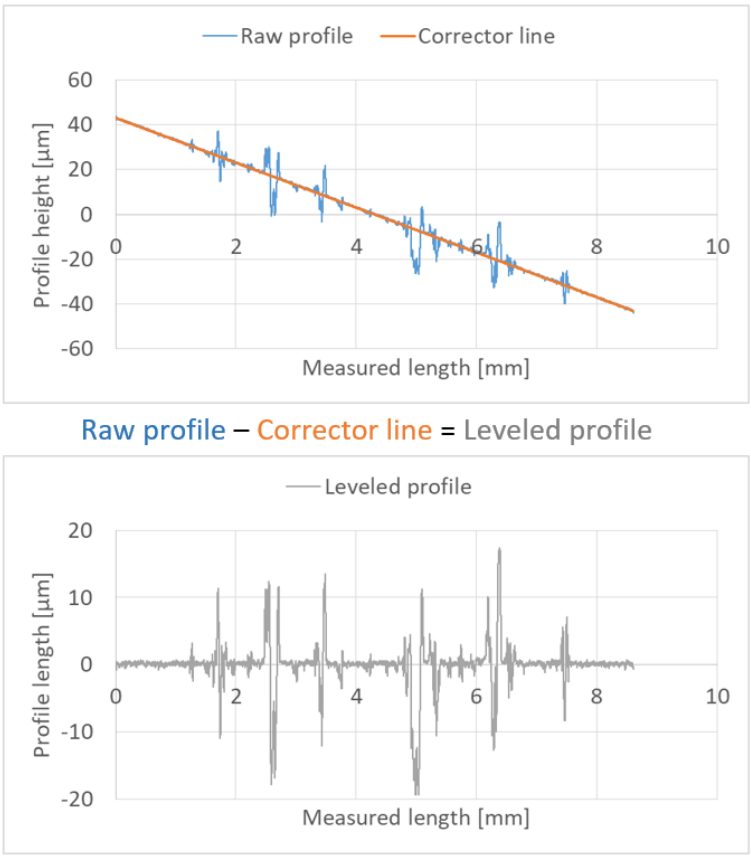

Fig. 109 On the top, the raw profile of a mark is plotted together with its corresponding corrector line. On the bottom it is plotted the leveled profile.

3. Removing the roughness. Due to the nature of the pin surface, there were some zones where no contact was occurred. Nevertheless, those zones presented a roughness that came from the finishing process of the disk. Therefore, this roughness had to be dismissed for the calculation of the pile-up ratio. For this purpose, every value within the range of -1 to 1 µm was substituted by zero. See the final profile in Fig. 110.

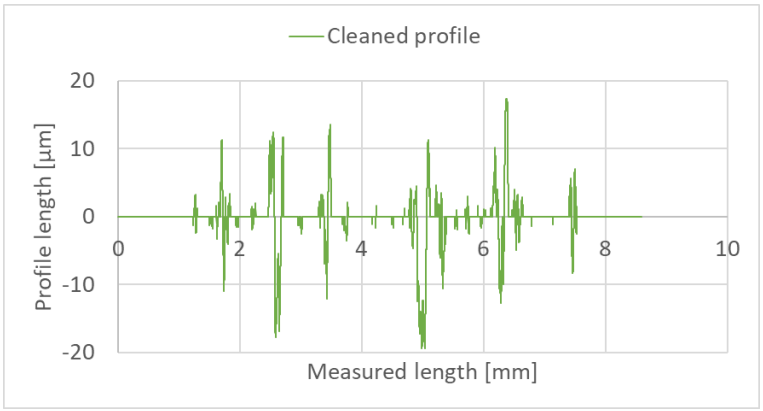

Fig. 110 The profile shown in Fig. 109 with the roughness of the untouched zones removed.

3.2.3 High speed tests

In this section the details of the HST are explained. There are some differences with respect to the LST for improving the results.

The HST were carried out in a cylindrical grinding machine Danobat® FG-600-S. In comparison with the milling machine used for the LST, the grinding machine had better mechanical properties thanks to the granite structure. A granite structure is stiffer and has a better behavior for damping the vibrations than a steel structure among other benefits.

As explained before, the disk was significantly higher that the disk used in the LST. This allowed to reach higher speeds without the need of especially high rpm in the spindle. The dimensions and weight of the disk, around 40 kg, were not a problem since they were in the range of a grinding wheel. However, it had to be balanced before being mounted inside the machine. This process is also carried out with grinding wheels.

The last modification concerned the piezoelectric force sensor, in this case a Kistler® 9257B device was used. The setup was modified because of the force sensor. Instead of being mounted between the pin and the cylinder, it was used as the base for the cylinder, see the setup in Fig. 111.

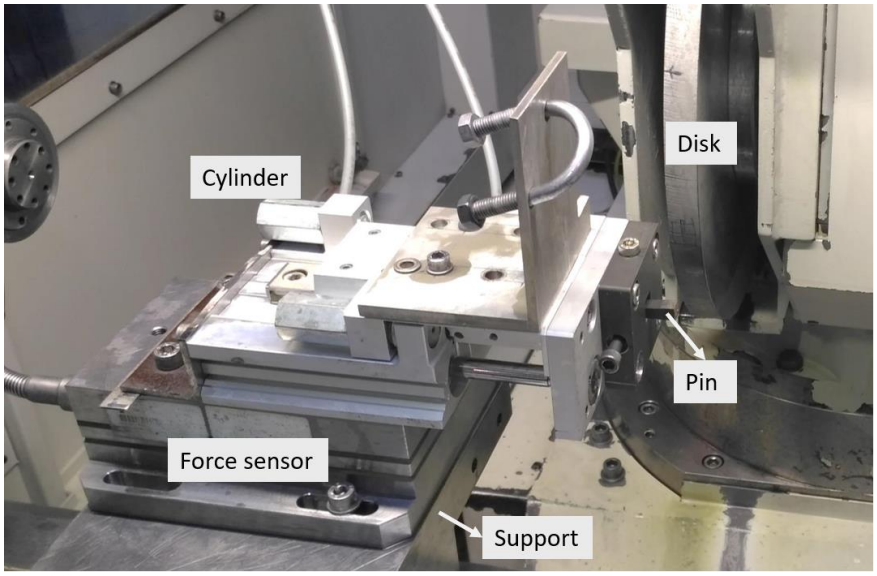

Fig. 111 Tribometer setup for HST.

The vibration problems observed in the LST were avoided thanks to the different process for removing the axial runout of the disk and the new setup. In Fig. 112 a) a normal force of a test carried out at 40 m/s and 0.2 MPa is plotted together with the FFT. The same graphs are shown in Fig. 112 b) of a test at 80 m/s where no harmonics with significant amplitude can be seen.

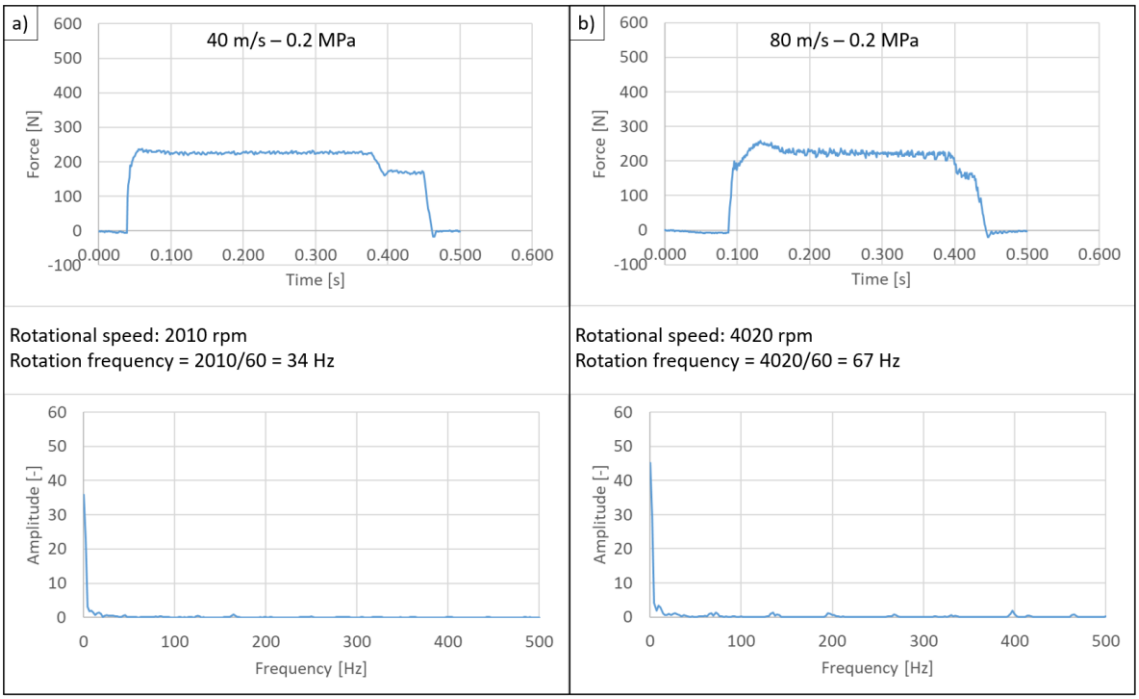

Fig. 112 a) On the top, the normal force registered during a test at 40 m/s and 0.2 MPa in the HST tribometer is plotted. On the bottom the FFT that signal is plotted. b) On the top, the normal force registered during a test at 80 m/s and 0.2 MPa in the HST tribometer is plotted. On the bottom the FFT that signal is plotted.

Regarding the digitalization of the scratches, the procedure was changed due to the size and weight of the disk. Instead of taking the disk to the stylus roughness tester, resin replicas of the scratches were done after every batch of tests and before cleaning the surface of the disk for the subsequent tests. See a picture of the process in Fig. 113. Then, the replicas were digitalized by the stylus roughness tester using the same procedure as in the LST. The resin was the result of mixing a powder (Technovit® 3040) and a liquid (Technovit® Universal liquid) in a proportion 2 to 1. Once mixed, the mixture needed 30 minutes for curing. The green material is a modelling clay used as a mold where the yellow resin was poured and cured.

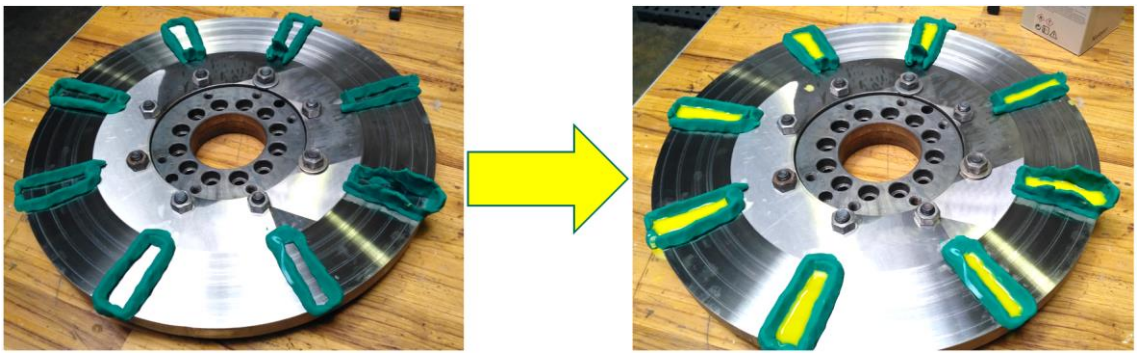

Fig. 113 On the left, the modelling clay is put on eight zones of the disk. On the right, the molds are filled with the liquid resin.

The signals of registered by the power sensor were compared with the tangential force measured by the force sensor. The result of the tangential force obtained from the power consumptions are plotted in orange in Fig. 114, while the results of the tangential force are plotted in blue. The acquisition frequency of both systems was 1000 Hz.

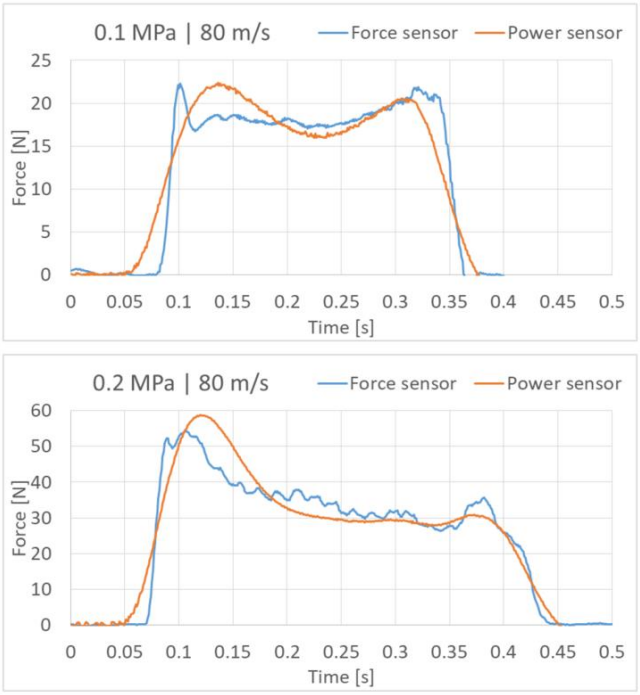

Fig. 114 On the top, the signal of the force sensor, in blue, is plotted together with the signal of the power sensor, in orange, of a test at 0.1 MPa and 80 m/s. On the bottom, the signal of the force sensor, in blue, is plotted together with the signal of the power sensor, in orange, of a test at 0.2 MPa and 80 m/s

Unlike the LST, the HST covered the whole range in speed mentioned in section 3.2.1.1. The parameters used for this test battery are gathered in Table 9

Table 9 The test parameters used in the HST.

Speed (m/s)	Pressure (MPa)	Number of repetitions
20	0.1	x2
	0.2	
40	0.1	
	0.2	
60	0.1	x4
	0.2	
75	0.1	
	0.2	
80	0.1	
	0.2	

3.3 RESULTS

The influence of the cutting speed and the contact pressure on the process was evaluated in terms of pile-up ratio and force ratio as follows.

3.3.1 Pile-up ratio

The replicas of the disk used in the HST were carried out on eight points of the marks, see Fig. 113, and one profile was digitalized on each replica. The average values together with the standard deviation of the tests with *new* and *worn* pins are plotted in Fig. 115.

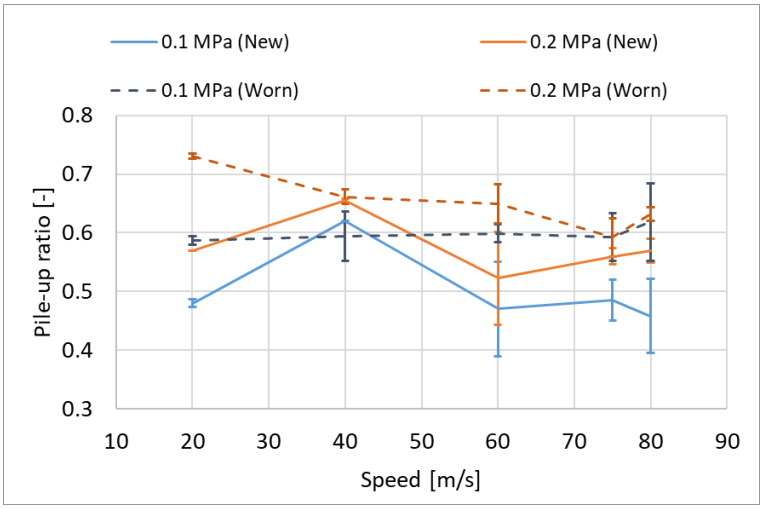

Fig. 115 Pile-up ratio of the HST with new and worn pins.

The following comparisons can be done from the graph plotted in Fig. 115. It should be mentioned that the efficiency is evaluated only in terms of material deformation in this section:

- 0.1 MPa (New) vs 0.1 MPa (Worn): There is a constant pile-up ratio for both wear states except the peak observed at 40 m/s with *new* pin. Therefore, it can be concluded that the influence of the speed is negligible for a given wear state and contact pressure. Nevertheless, the wear of the pin has an important influence. The pile-up ratio with a *worn* pin is around a 20% higher than with *new* pin. This means that the proportion of plastically deformed material to the actually removed material is a 20% higher.
- 0.2 MPa (New) vs 0.2 MPa (Worn): The same phenomenon as in the previous point was observed. The pile-up ratio is higher when the wear of the grains of the pins is higher.
- 0.1 MPa (New) vs 0.2 MPa (New): Both pressures show the same pattern, hence, the influence of the speed is the same at both pressures. In addition, the pile-up ratio has a nearly constant value no matter the speed except for the sudden increase at 40 m/s. However, there is less proportion of plastically deformed material with 0.1 MPa, that means that the material removal process is more efficient in terms of material behavior with lower contact depth.
- 0.1 MPa (Worn) vs 0.2 MPa (Worn): The results observed in this comparison are similar to what was observed in the previous point. The material removal process is more efficient with lower contact depth. However, in this case, the pile-up ratio obtained with deeper contact depth shows a decrease when the speed is increased. Eventually, the

pile-up ratio at 75 and 80 m/s is the same at both contact depths. This means that the efficiency of the material removal may improve with the speed.

From these comparisons, the effect of wear, contact depth and speed can be assessed.

3.3.1.1 Effect of wear on the pile-up ratio

The pile-up ratio is higher with *worn* pins than with *new* pins at both 0.1 and 0.2 MPa. One of the differences between both surfaces concern the height of the grains. As observed in chapter 2, the protrusion height of the grains is different when the wheel is new. This difference tends to disappear as the wheels gets worn. As a consequence, the number of grains that contact the workpiece in the same operation increases. The increase in the active grains results in a reduction of the material that every grain finds along the contact length. Therefore, it is more difficult to reach the critical chip thickness. As a result, there is more proportion of plastically deformed material with higher wear level.

Moreover, higher contact temperature is expected due to two reasons. On the one hand, there are more grains that contact with material that has already been in contact with a grain. When there is a contact between a grain and the material, there is an energy transmission to the workpiece in form of heat. Hence, the temperature of the disk material increases after every grain-disk interaction. On the other hand, there is also contact between the flat surface of the grains and the disk. This contact generates only friction, since the material plastic deformation and removal occur ahead the grain. This friction is also a heat source that modifies the physical properties of the disk material. That being said, the yield stress of Inconel decreases with higher temperatures [122]–[124], hence, more plastic deformation can also be expected as a consequence of this phenomenon.

Finally, taking into account the predominant wear type observed at advanced wear states of EP CBN wheel, it can be deduced that the real contact surface is larger with *worn* pins. The normal force performed by the cylinder is the same, therefore, the penetration depth is shallower. This facilitates the presence of plastic deformation at the expense of the chip generation.

3.3.1.2 Effect of contact depth on the pile-up ratio

The contact depth is related with the pressure set on the cylinder, the higher the pressure, the deeper the contact depth is.

In general terms, it is accepted that the increase in the chip thickness leads to a more efficient material removal. However, the chip thickness can be increased by means of different manners and not all of them have the same results. This topic was addressed by Rabiey during his thesis [125]. He compared the result of increasing the chip thickness by means of cutting depth and feed speed. When the cutting depth was augmented, eventually thermal damage occurred on the workpiece. However, when the feed speed was augmented, the process became energetically more efficient. In these tests, the increase of the pressure is directly related with the increase in the cutting depth, therefore, higher temperature can be expected according to the results observed by Rabiey. This is caused by a deeper engagement where the contact between the grains and the disk material takes place in zones where no material removal occurs.

The results shown in Fig. 115 agree with this phenomenon, since the pile-up ratio is higher with 0.2 MPa. The rise in temperature explained in the previous paragraph leads to more plastic deformation. Despite the higher temperature, no signs of thermal damage were observed on the disk.

3.3.1.3 Effect of speed on the pile-up ratio

The speed can have different effects in grinding [14],[16],[82],[105]. On the one hand, the rise in the speed can cause a strain rate hardening, which makes the material more brittle. On the other hand, the increase in the temperature caused by the increase in the speed can overcome the hardening effect and cause a thermal softening effect on the material. If this takes place, the material softens and presents higher plastic deformation.

In this study, the influence of the speed was observed in two situations.

The first situation concerns the tests with *new* pin. There is an increase in the pile-up ratio of the test carried out with *new* pins when the relative speed is 40 m/s. For both slower and faster speeds, the pile-up ratio remains around constant values. This trend cannot be explained using the theory of strain rate hardening and thermal softening. According to this theory, a material can experience a hardening phase up to a certain speed while the softening phase can take place after this phase. The sequence must follow that order, however, what is shown in Fig. 115 occurs in the contrary sequence.

This particular peak can be caused by a microstructural change of Inconel 718; however, the microstructure of the disk could not be analyzed, hence this hypothesis cannot be confirmed. Other possible reason may be caused by a mistake during the performance of the tests. An error in the programming of the CNC of the machine may lead to an incorrect number of laps of the contact and thus, to another result on the pile-up ratio. This must be checked with the result of the force ratio.

The second situation concerns the tests with *worn* pins. The pile-up ratio at 0.2 MPa present a progressive decrease as the speed is increased. By contrast, the ratio at 0.1 MPa presents a constant value at every speed. The descent observed at 0.2 MPa means that there is an improve in the efficiency when the speed is increased. This shows a strain rate hardening of the material that does not take place at 0.1 MPa. Nevertheless, a slight increase can be observed at both pressures when the relative speed is increased to 80 m/s. This can be considered as the start point of the thermal softening for the given wear state.

3.3.2 Force ratio

A moving average was applied on the raw force signals for removing the slight ripple in order to facilitate the calculation of the force ratio. Two examples are shown in Fig. 116.

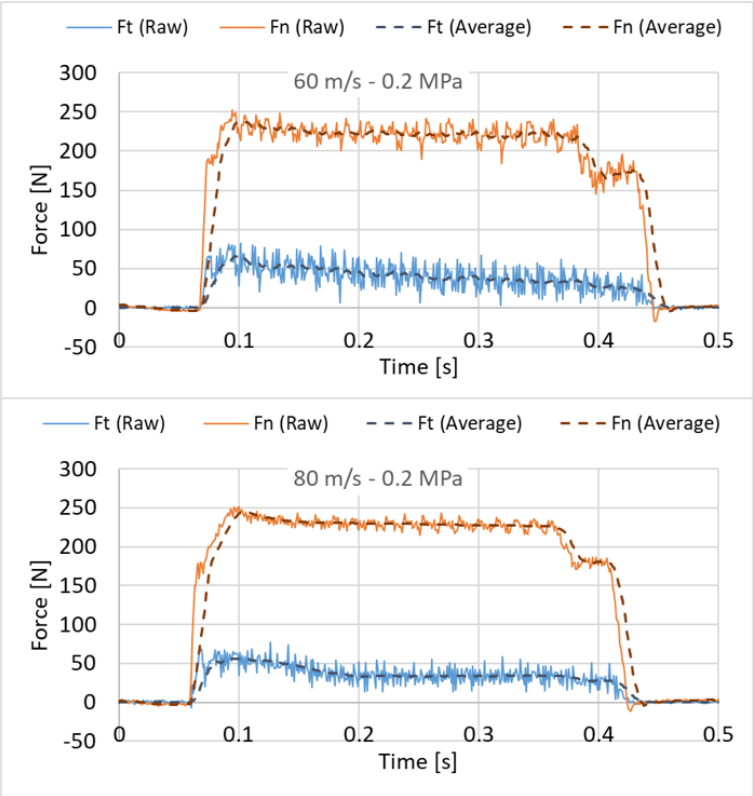

Fig. 116 On the top, the tangential and normal force before and after applying the moving average of a tests carried out in the HST at 60 m/s and 0.2 MPa with a new pin. On the bottom, the tangential and normal force before and after applying the moving average of a tests carried out in the HST at 80 m/s and 0.2 MPa with a new pin.

The result of the force ratio of the HST are plotted in Fig. 117.

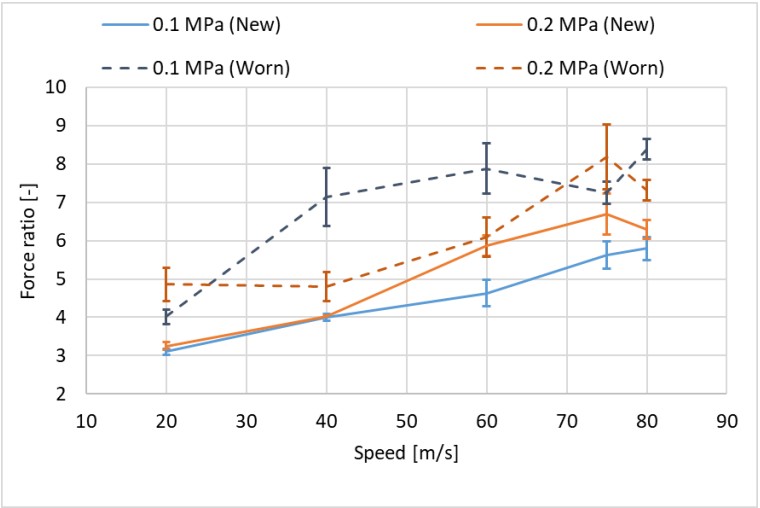

Fig. 117 Force ratio values obtained in the HST.

This graph is evaluated following the same schema as followed with the pile-up ratio.

- 0.1 MPa (New) vs 0.1 MPa (Worn): The force ratio is significantly higher with *worn* pin. The normal force is considered the same thanks to the pneumatic cylinder, hence, this difference can be understood as a lower tangential force registered with *worn* pins. This

result is consistent with the results observed in the pile-up ratio. The higher temperature assumed with *worn* pins softens the material of the disk, which results in lower tangential force.

- 0.2 MPa (New) vs 0.2 MPa (Worn): In this comparison, the same situation as with 0.1 MPa can be seen. However, in this case, the difference between both lines is smaller. This phenomenon is explained in the following two points.
- 0.1 MPa (New) vs 0.2 MPa (New): Despite having similar values at the lowest speeds, the 0.2 MPa shows higher force ratio. The normal force is twice higher than in 0.1 MPa, nevertheless, the tangential force does not increase correspondingly. Instead, the tangential force increases in a lower proportion. This is caused by the higher temperature acknowledged in the previous section, which softens the material.
- 0.1 MPa (Worn) vs 0.2 MPa (Worn): Unlike the previous comparison, the effect of the temperature is not high enough for resulting in a higher force ratio. Instead, the tangential force is proportionally higher at 0.2 MPa than at 0.1 MPa. The friction created by the high amount of plastically deformed material together with the higher force needed as a result of the deeper contact depth resulted in lower force ratio.

3.3.2.1 Effect of wear on the force ratio

The tests with *worn* pins present a higher force ratio, what means a lower tangential force. This implies a lower power consumption during the process, but this does not mean that the process is more efficient. The tests with *worn* pins showed also the highest pile-up ratio, thus, the efficiency should be analyzed in terms of the specific grinding energy for assessing both aspects at the same time.

3.3.2.2 Effect of contact depth on the force ratio

Different conclusions can be drawn from tests with *new* pins and from tests with *worn* pins.

When the contact depth is increased with *new* pins, less tangential force is required during the tests. This may be a consequence of the increase of the temperature that softens the disk material.

However, the effect of the increase in temperature is not high enough for overcoming the friction in the case of *worn* pins. The combination of the deformed material that is contacting the pin together with the friction with the flat surface of the grains, results in a tangential force proportionally higher than what is needed at 0.1 MPa.

3.3.2.3 Effect of speed on the force ratio

The increase in the speed leads to an increase in the force ratio. As previously explained, this is caused by a decrease in the tangential force for a given normal force. Therefore, there is not any evidence of material hardening with the speed i.e. strain rate hardening. Instead, the material becomes softer when the speed increases.

Both Fig. 115 and Fig. 117 give information about the efficiency of the process, however, the first one addressed the material behavior and the second one the tool performance. In grinding processes, the specific energy is used for evaluating the performance of a grinding process in a global manner. The specific energy is the energy needed for removing a unit of workpiece

material volume. The specific grinding energy of the HST was calculated through Eq. (41), were t is the contact time, V_{groove} is the volume of the groove and V_{pile} is the volume of the piled material.

$$e_c = \frac{\int_0^t P}{V_{groove} - V_{pile}} \tag{41}$$

The specific energy obtained in the HST is plotted in Fig. 118.

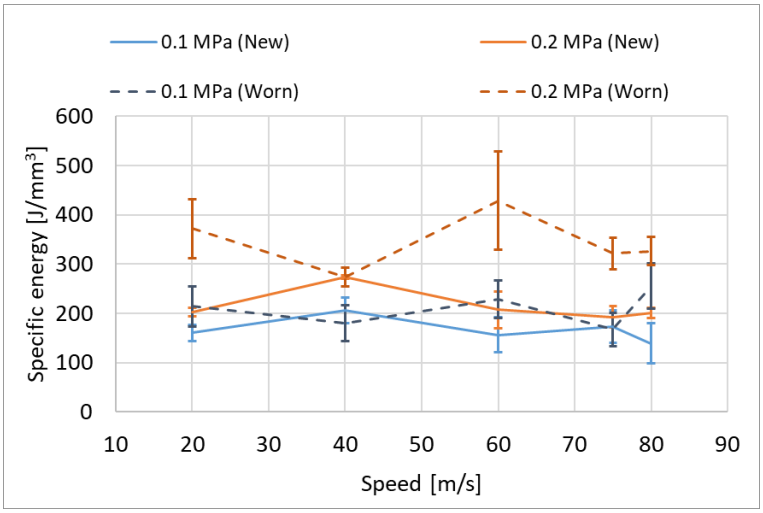

Fig. 118 Specific energy calculated from the HST.

Low values of specific energy mean that removing material is less expensive in terms of energy. Therefore, it can be concluded that the best results have been obtained with the lowest pressure set on the cylinder. The friction produced by the higher amount of plastically deformed material led the tests at 0.2 MPa to less efficient.

Similarly, the tests with *worn* pins were less efficient as a consequence of the energy lost in the friction caused by the flat surfaces.

3.4 CONCLUSIONS

It should be mentioned before drawing any conclusion that these results cannot be numerically extrapolated to the actual grinding process because of the difference in the kinematics. However, it is considered that the trends seen in these tests can be extrapolated to the grinding process.

One of the objectives of this work was to analyze the material behavior as a function of the speed with different wear states and cutting depths. The cutting speed may cause opposite phenomena as the strain rate hardening and thermal softening. The first one is a hardening of the material that entails a brittle behavior, while the second one is a softening of the material that entails a ductile behavior. It should be mentioned that thermal softening is a result of the increase of temperature, the increase in the cutting speed is only one of the factors that can cause this phenomenon.

The relation between these two phenomena can be better understood through Johnson-Cook expression, Eq. (42). This expression is widely used for calculating the flow stress as a function of the current strain (first bracket), strain rate (second bracket) and temperature (third bracket) of the material. Further details and explanations are given in chapter 4.

$$\sigma = [A + B \cdot \varepsilon^{n}]\left[1 + C \ln {\dot{\varepsilon}}/{\dot{\varepsilon}_0}\right][1 - T^{*m}] \tag{42}$$

The increase in the strain rate, $\dot{\varepsilon}$, causes an increase in the flow stress while the increase in the temperature, *T*, reduces the flow stress of the material. As it can be seen, the influence of each factor depends also on some constant of the material, namely, *C* and *m*. Thus, the increase in the speed causes a hardening of the material by itself. However, if the increase in the temperature caused by the speed overcomes the hardening effect, the softening starts to take place.

Under the conditions tested in this chapter, the rise in the speed causes a softening of the material that results in a reduction of the tangential force.

Having a lower tangential force could be understood, at a first glance, as a better performance of the process. The same conclusion may be drawn from a lower value of the pile-up ratio. However, it must be verified if the combined effect of two parameters gives as a result a better or a worse efficiency of the process. For this purpose, the specific grinding energy was calculated using the power consumption and the net volume removed. The results showed that the deeper engagement between the disk and the pin as a consequence of having a higher pressure on the cylinder, give as a result higher specific energy. As it was deduced from the pile-up ratio, there is more deformed material at 0.2 MPa than at 0.1 MPa. The power consumed by the friction with the deformed material did not result in material removal, thus, the resulting process was less efficient.

Wear led to a less efficient process, as it was expected. As confirmed in chapter 2, the wheel surface at an advanced wear state is covered by wear flats. One of the consequences of this wear type is the friction generated in the contact between the flat surface of the grain and the workpiece. The power consumed by this phenomenon is not the responsible of removing material. Instead, it is the responsible of increasing the temperature in the contact zone. However, it should be mentioned that the difference between *worn* and *new* pins is not very significant due to the nature of the tribometer. There is an important friction with the deformed material, as a consequence, the adverse effect of the flat surfaces of the grain tips is partially hidden.

Finally, there is not a clear conclusion from the speed concerning the efficiency since there is not a clear trend in the specific energy. If these results are applied to a grinding process, using a higher cutting speed is would be an improvement for the process. Increasing the speed does not entail any adverse effect and by contrast, the feed speed of the grinding process can be increased in the same proportion under the condition of keeping constant the equivalent chip thickness.

The results obtained in this chapter are going to be used as information for validating the numerical modelization of the process addressed in chapter 4.

TOPOGRAPHIC CHARACTERIZATION AND WEAR ANALYSIS OF ELECTROPLATED CBN GRINDING WHEELS

4 MODELIZATION

4.1 INTRODUCTION

In previous chapter 3 a tribometer was developed for reproducing the cutting conditions of the CFG process used in aeronautical industry for grinding NGVs. A number of different parameters were used with the purpose of covering a wide range of input parameters and thus, understand the interaction between the grains and the workpiece. However, the conclusions taken from an empirical study can hardly be extrapolated to situations where the conditions are not the same. For that reason, the analysis of the results of the tribometer should be coupled with a modelization of the process where the input parameters can be modified and the influence on the process of such modifications can be observed.

The modelization must be consistent with the empirical results in terms of input and output parameters. It must be capable of addressing thermal and mechanical loads since both of them had influence on the results observed in chapter 3. The geometry of the grains is an important factor since it resembles the wear, however, not only the wear has influence on the process but also other features of the wheel surface such as grain size and grain density. As it was mentioned in the state of the art, section 1.5, the surface of the grinding wheel has been reproduced by means of statistical approaches and geometrical simplifications. However, although this method leads to acceptable results, the use of the real wheel surface was considered as a more appropriate manner for reproducing correctly the tests. This implies that the model must be created in a 3D environment where the surface of the grinding wheel can be easily and accurately modified.

Once the model has been created, it will have to be validated with the results of chapter3. Taking this into account, the model must be designed so that to reproduce the same kinematics as the tribometer under the same input parameters. Furthermore, the output obtained for the model must be comparable with the outputs of the tribometer.

The different methods used by other authors for modeling the grinding process have been extensively addressed in the state of the art, section 1.5. In the following lines each method is briefly summarized with the purpose of finding the most appropriate modeling method for the current case study.

An analytical model is based on mathematical expressions that define the geometry of the parts and control the relation between the input and output parameters. This relation can be formed either by a single equation or by intermediate iterations for more complex thermo-mechanical models. The geometry of the grinding wheel is commonly reproduced by means of statistical values taken from grinding wheel specification or wheel digitalization. Taking everything into account, the intricate system of equations that would be required for this model must be coupled with a mathematical definition of the actual grinding surface. In addition, that mathematical definition must be modifiable with the purpose of changing the wear degree of the wheel. Taking this aspect into account, the analytical models were not the most suitable method for this work [51],[90]–[94].

Grinding process has also been modeled through kinematic models [11],[48],[96]–[102]. The geometry of the parts is graphically defined either in 2D or in 3D. Hence, the topography of the virtual wheel can be modified so that it resembles the topography of the actual grinding wheel. Furthermore, it can be modified with the purpose of having a consistent degree of wear flat [101] thanks to computer aided design (CAD) software. Once the geometry of the parts of the model is defined, the result of this type of model comes from the kinematic intersection of the different parts. In consequence, geometrical aspects such as chip thickness or workpiece roughness as a function of the geometry and kinematics of the cutting process can be directly calculated with a kinematic model. However, when the study must address something else than the geometrical aspects of the process, the model must be coupled with other type of model, namely, analytical or FEM. In such cases, the output of the kinematic model can be used as input for the complementary method, e.g. chip thickness, or vice versa, e.g. vibration as input for the kinematic model. In this way, thermal and mechanical loads can be addressed.

The FEM is another method widely used for machining models [71],[84],[86],[103]–[105]. On the one hand, mechanical and thermal loads can be addressed in the same model. On the other hand, it is relatively versatile in terms of the geometry of the parts that can be designed. The basic functioning of this method can be simplified through Eq. (43) assuming a mechanical problem. This is the general equation of motion and comprises the position along the time through the term $r(t)$, the velocity along the time through $\dot{r}(t)$ and the acceleration along time by $\ddot{r}(t)$.

$$M[r(t), \dot{r}(t), \ddot{r}(t)] = 0 \tag{43}$$

The Eq. (43) can hence be solved through numerical time integration methods. Depending on the type of solver used for the modelization, the calculation time may depend on the number of elements, on the size of the elements and on the density of the elements. The density is given by the materials of the modelization. However, the size and number of elements have a direct influence on the result of the model. The type of solver and the corresponding affecting factors are discussed later in section 4.2.1.

In the recent years discrete element method (DEM) has also been used in research works about grinding. This method substitutes the bodies of the model by discrete elements that normally have spherical shape. Depending on the simulation, the elements can be free or can be bonded together. In that case, the properties of the bond must be defined correctly in order to have consistent results. Nevertheless, this method is more recent than FEM and therefore, the available software is less developed. The commercial softwares for FEM models have predefined options that allow to customize the model to the particularities of the process to be modelled. As it is going to be explained in the following sections, a special methodology was followed for creating the surface of the pin. The options of the advanced FEM software facilitated this step of the study.

Taking everything into account, FEM was chosen for modeling the CFG process since the real wheel geometry and wear could be reproduced in the model and the influence of the temperature and grinding forces could be addressed in the same model. In the following sections, the details of the model are explained, later, the input and output parameters and the

trials carried out for adjusting the model are shown and finally the results of the adjusted model are gathered.

4.2 FEM MODEL

The model was developed within the commercial software Abaqus® 6.14 where a coupled thermo-mechanical 3D explicit analysis was used for complementing the results obtained in chapter 3.

Although the goal of the whole work is to understand and to improve the CFG process with EP CBN wheel of superalloys, the model was focused on the tests carried out in the tribometer developed in chapter 3 in order to be validated by means of the results obtained with the tribometer. Therefore, the model should have the same kinematics as the tribometer i.e. a linear relative displacement, instead of the trochoidal movement traced by an abrasive grain during a surface grinding.

4.2.1 Solver type

In Abaqus, a dynamic thermomechanical problem can be solved by two different solvers. On the one hand, the implicit solver is unconditionally stable. That is to say that the conditions of equilibrium are ensured during every increment of the calculation. For this purpose, the solver checks the stability after every increment. If the conditions of equilibrium in a certain increment are not satisfied, the solver reduces the loads corresponding with that increment and recalculates it. This is done iteratively until the equilibrium conditions are fulfilled in that increment. In this way, the results of an implicit calculation are always stable, but the computational costs and hence, the computational time, might be extremely large.

On the other hand, the explicit solver is conditionally stable. That is to say that the equilibrium is not checked after every increment. The stable time increment must satisfy a condition linked to the material mechanical properties, and the size of the elements in the mesh. The solver may continue time incrementation loop, but there is no guaranty of the results validity. Nevertheless, the computational cost is lower, also due to the fact that it is preferred to use reduced integration elements.

The explicit solver was chosen for this work since it allowed to run the simulation faster than the implicit solver. In this way the calibration of the model could be done faster. The time required for calculating the model depends on the stable time increment. Since the stability of the model is not verified after every calculation, as it is done in the implicit analysis, the stable time increment is calculated through Eq. (44) and it is used as the time increment for every step. A model with a large stable increment time would need a smaller number of increments for completing the calculation, hence, the calculation time would be shorter.

$$\Delta t_{stable} = \frac{L_{min}}{c_d} \tag{44}$$

In this equation two factors can be differentiated. On the one hand, the minimum element size, written as L_{min}, makes a calculation longer when it has small values. In consequence, the size of

the elements must be checked with the purpose of using the appropriate element size in order to have a good accuracy of the results with an acceptable calculation time.

The element size depends on the geometry of the bodies and on the results and load of the model. According to the Courant-Friedrichs-Lewy condition [126], the smaller the element size is, the larger the computational costs. The element size and shape topics are addressed later in sections 4.2.2.1.5 and 4.2.2.2.3.

On the other hand, there is the wave propagation speed, written as c_d. This parameter is calculated through Eq. (45).

$$c_d = \sqrt{\frac{E}{\rho}} \tag{45}$$

From this equation it can be concluded that the ratio of Young's modulus, E, to the density, ρ, has an inverse influence on the stable time increment. Therefore, a light material that can be hardly deformed within the elastic region results in a higher wave propagation speed and thus, in a lower stable time increment. However, these parameters depend on the physical properties of the material, hence, they are given input that cannot be modified for reducing the computational costs.

Despite they are given input data, the influence of the density can be mitigated through an option in Abaqus® called mass scaling. Nevertheless, this option was not used in this analysis.

It should be mentioned that bodies defined as rigid are not considered for calculating the stable time increment.

That being said, the details of the model are explained in the following section. They are separated in two subsections, namely, the disk and the pin.

4.2.2 Input parameters

4.2.2.1 Disk

4.2.2.1.1 Geometry

The disk was represented by a plate in the model. If the disk with the dimensions of the one used in the tribometer was created for the model, the calculation time would be extremely long. Instead, the plate was designed to have a shorter length but long enough for the model to achieve stable results. The results of the force ratio in chapter 3 were obtained from the steady zone observed in the force signals, see Fig. 119. Therefore, as an alternative, a smaller part was considered valid for the simulation as long as the steady zone was reached.

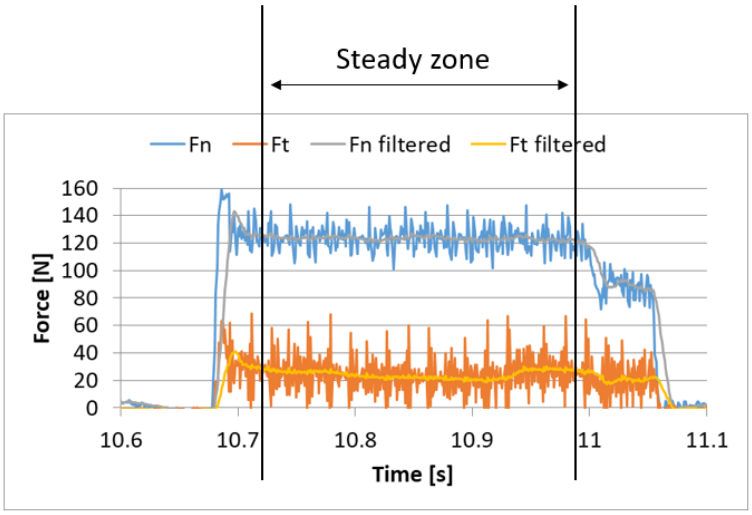

Fig. 119 A force signal where the steady zone is marked in black.

Furthermore, the disk shape was no longer necessary. In chapter 3 a pin-on-disk configuration was chosen because of the technical resources available for reaching the needed speed. However, in the model, the workpiece could be designed as a square plate whose length was determined as a function of the contact length needed for the forces to reach the steady zone as it is explained later in section 4.2.4.

The width of the plate was designed according to the width of the abrasive surface in order to reduce the number of elements of the model.

The third dimension of the plate was determined with two conditions. The first one was related with the forces. The displacement in the normal direction on the bottom of the plate had to be avoided in order to reproduce the stiffness of the disk. However, the lack of displacement in that direction could affect the stress transmission across the plate if it was defined as too thin. Hence, the thickness of the plate should be enough for avoiding the mentioned phenomenon but, at the same time, as thin as possible for reducing the computational time.

The second condition was related with the thermal aspects. In chapter 3 the important role of the temperature in the material behavior was observed. Its effect is increased due to the fact that there are numerous grains in contact at the same time. In this way, the first grains modify geometrically the workpiece but also thermally and this affects the interaction of the subsequent grains. The model should be able to reproduce this phenomenon, for that purpose, the plate should be thick enough for ensuring that the whole abrasive surface has been passed over a contact point before the temperature created in that point in the first contact reaches the bottom of the plate. Otherwise, the thermal conduction through the material will be affected by the thermal conduction of the environment.

The establishment of the dimensions is explained by means of data obtained from the model in section 4.2.4.

4.2.2.1.2 Physical properties

The plate was expected to reproduce the behavior of the disk; therefore, the thermal and mechanical properties of Inconel 718 should be assigned to it. Given the wide range of temperature expected and the dependence of the process on it, some of the mechanical properties were set as a function of temperature. Table 10 and Table 11 gather the physical properties of the plate considered for the model [106].

Table 10 Constant physical quantities of Inconel 718.

Physical quantity	Unit	Value
Density	kg/m^3	8,220
Specific heat	J/(kg·K)	435

Table 11 Temperature dependent physical quantities of Inconel 718.

Temperature [K]	Young's modulus [MPa x 10^3]	Poison's ratio [-]	Thermal conductivity [W/(K·m)]
294.3	200.0	0.294	11.1
310.9	198.6	0.291	-
366.5	195.8	0.288	12.4
422.0	193.1	0.280	-
477.6	190.3	0.280	14.1
533.2	186.9	0.275	-
588.7	184.1	0.272	16.0
644.3	180.6	0.273	-
699.8	177.9	0.271	17.7
755.4	174.4	0.272	-
810.8	171.0	0.271	19.5
866.5	166.9	0.276	-
922.0	163.4	0.283	21.2
977.6	158.6	0.292	-
1033.2	153.8	0.306	23.1
1088.7	146.9	0.321	-
1144.3	139.3	0.331	25.0
1199.8	129.6	0.334	-
1255.4	120.0	0.341	26.7
1310.9	109.6	0.366	-
1366.5	98.6	0.402	28.3

4.2.2.1.3 Constitutive model

Inconel 718 is a viscoplastic material. This means that its plastic behavior depends on the strain rate at which it is being deformed. For instance, the yield stress value obtained at different strain rates varies significantly, see Fig. 120 a). However, the yield stress value does not only depend on the strain rate but also on the working temperature, as it can be concluded from the comparison between Fig. 120 a) and Fig. 120 b) [122].

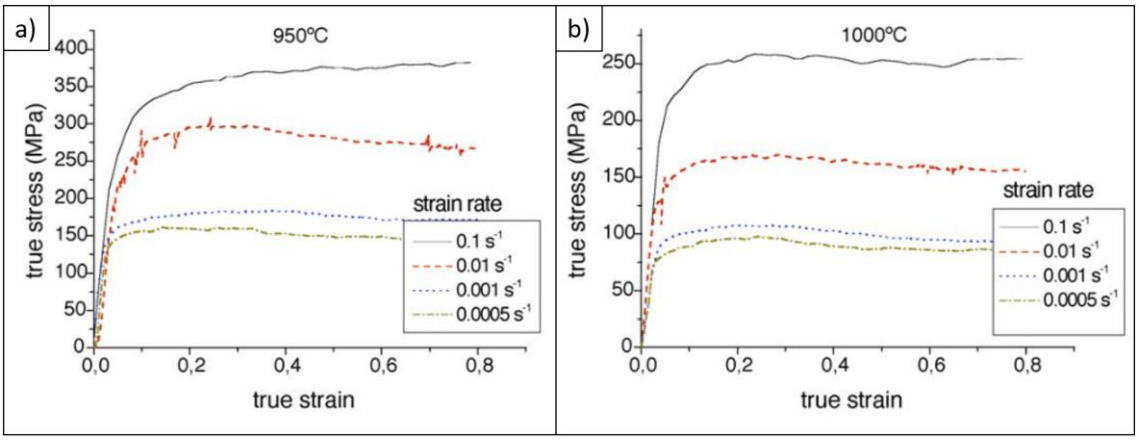

Fig. 120 a) True stress- true strain curve of Inconel 718 at 950°C and different strain rates. b) True stress- true strain curve of Inconel 718 at 1000°C and different strain rates. "High temperature deformation of Inconel 718"

For a consistent reproduction of the material behavior, the influence on the strain rate and the temperature on the material response have to be taken into account.

Many authors have developed constitutive models, one of the most used for large strains, high strain rates and high temperatures is the Johnson-Cook (JC) model [127]. This model was developed in 1983 by the need of reducing the empirical test needed for adjusting the increasingly complex numerical simulations allowed by the advances in the computers. They proposed the expression shown in Eq. (42) for calculating the flow stress, σ, as a function of the current strain, ε, the current strain rate, $\dot{\varepsilon}$, and the homologous temperature, T^*. T^* is calculated from Eq. (47) where T_m is the melting temperature of the material, T_r is the temperature below which the temperature has no longer effect on the response of the material, also called reference temperature or transition temperature, and T is the current temperature.

$$\sigma = [A + B \cdot \varepsilon^n]\left[1 + C \ln {\dot{\varepsilon}}/{\dot{\varepsilon}_0}\right][1 - T^{*m}] \tag{46}$$

$$T^* = \frac{T - T_r}{T_m - T_r} \tag{47}$$

Each one of the three brackets address the effect of a particular phenomenon. The first one is related with the strain hardening effect. A is the initial yield stress in MPa, B is the hardening modulus also in MPa and n is the strain hardening exponent. All the parameters in the first bracket are obtained for a reference strain rate, $\dot{\varepsilon}_0$, and T_r. The second one refers to the strain rate hardening effect where C is a dimensionless strain hardening coefficient. The last one

corresponds to the thermal softening caused by adiabatic softening, where the thermal softening parameter is written as *m*.

The constants were found for several materials through torsional and tensile tests carried out by Split-Hopkinson Pressure Bar at different strain rates and temperatures. The same strain rate and temperature could not be used in both testing devices. Then, they validated the recently obtained expression comparing the results of cylinder impact tests with numerical simulations based on their expressions.

Despite the JC model takes into account the effect of the strain hardening, strain rate hardening and thermal softening, they are considered as independent factors. That is to say, for instance, that the temperature does not affect the strain rate hardening. This aspect was modified by other authors with the purpose of enhancing the sensitivity of the JC model to very particular conditions. In consequence, several JC modifications have been developed for machining processes thanks to the simplicity and coherence of the model.

There was such a variety of JC models for machining processes that in [128] Jafarian et al. compared different already developed JC models for Inconel 718 with the purpose of finding the one with less error for their turning application. They compared the empirical results with model results in terms of chip geometry and process forces. The one with less error was used later for a research work about turning Inconel 718. The JC models compared in that work are sorted in Table 12 following the same order and naming as in the original article.

Table 12 The parameters of the JC models compared by Jafarian et al. [128]

Material model	A [MPa]	B [MPa]	C	N	m	$\dot{\varepsilon}_0$	Other constants
M1	1290	895	0.016	0.5260	1.55	0.030	-
M2	963	937	Variable	0.3300	1.300	0.001	C=Eq. (48)
M3	1485	904	0.0134	0.7770	1.589	0.001	-
M4	1241	622	0.0134	0.6522	1.300	1.000	-
M5	1241	622	0.0134	0.6522	1.300	1.000	D=0.6, S=0, $\dot{s}$=5, r=10, Eq. (49)
M6	1562	300	0.0134	0.2500	1.300	1.000	-
M7	1241	622	0.0134	0.6522	1.300	1.000	F=18, G=1.36, Eq. (50)

$$C = 0.0232 - \left(0.00372 + 0.0021\, Sin\left(\frac{\dot{\varepsilon} - 5000}{3000}\pi\right)\right) Sin\left(\frac{T - 500}{150}\pi\right) \quad (48)$$

$$\sigma = [A + B \cdot \varepsilon^n]\left[1 + C \ln {\dot{\varepsilon}}/{\dot{\varepsilon}_0}\right][1 - T^{*m}]\left\{D + (1 - D)\dot{s} \tanh\left[\frac{1}{(\varepsilon + S)^r}\right]\right\} \quad (49)$$

$$\sigma = [A + (F + 200) + G\varepsilon + B \cdot \varepsilon^n]\left[1 + C \ln {\dot{\varepsilon}}/{\dot{\varepsilon}_0}\right][1 - T^{*m}] \quad (50)$$

M1 showed the least error in the two mentioned aspects and therefore it was the selected model for their work. In this work, the same model was used since the kinematics of the model are the same, and it showed the best correlation with the empirical values of the forces. The expression of that model is shown in Eq. (51).

$$\sigma = [1290 + 895 \cdot \varepsilon^{0.526}][1 + 0.016 \ln {\dot{\varepsilon}}/{0.03}][1 - T^{*1.55}] \quad (51)$$

4.2.2.1.4 Inelastic heat fraction

In addition to the constitutive model, the inelastic heat fraction is needed for a model where deformation and heat generation are addressed. The inelastic heat fraction, also called Taylor-Quinney coefficient, was firstly quantified for several metals back in 1937 [129] by Taylor and Quinney through a specific test bench. Although their research work on the latent energy started before in 1933 [130] by analyzing the cold work on copper tubes. They developed the following methodology for quantifying the so-called Taylor-Quinney coefficient.

The latent energy of a sample is released in form of temperature when the sample is heated above the annealing temperature. Therefore, they put two similar samples inside a furnace, one of the samples was cold worked and the other was already annealed. They heated the furnace in vacuum conditions above the annealing temperature of the samples and measured the temperature of each one. They repeated the process in order to assure that the difference of the temperatures observed was caused by the release of the latent energy. Once measured the temperature difference, the corresponding energy per mass was calculated using the specific heat of the material at that temperature. That value was subtracted to the energy per mass used during the cold working process. The difference in the energy per mass was assumed to be transformed into heat during the cold working process.

They quantified the latent energy for copper, nickel, iron, aluminum and brass. The tests with aluminum resulted unreliable because of the volatilization of the material in the vacuum furnace. Nevertheless, for the rest of materials, the latent energy was in the range of 5 (nickel) to 15% (iron) of the energy used in the deformation of the material. In consequence, it was concluded that around a 90% of the energy used for deforming the material was transformed into heat. Thus, a Taylor-Quinney coefficient of 0.9 was considered as appropriate for metals.

However, later in 1984, Shaw [131] stated that those results extrapolated to chip formation strain energy levels, led to a percentage of latent energy in the range of 1 to 3 %, what results

in a Taylor-Quinney coefficient equal to 0.97. This value was later mentioned by Guo and Malkin [93] as a more realistic approach than the coefficient 1 commonly used in grinding.

4.2.2.1.5 Meshing

The bodies of a FEM model have to be discretized in finite elements so that the Eq. (1) can be completed. The zone of the part where more information is needed is usually meshed with smaller elements. This increases the output information that can be taken from that zone but increases as well the number of elements of the model. This is why it is common to use an incremental seeding along some of the edges of the part. In this way, the mesh is refined as it gets closer to the critical zone.

In addition to the size, the geometry and type of the elements must be defined. Among the different 3D elements, the most used for this type of application are the tetrahedral and the hexahedral elements, see Fig. 121. In general terms, hexahedral elements provide more accurate solution while tetrahedral elements are able to adapt better to complex geometries.

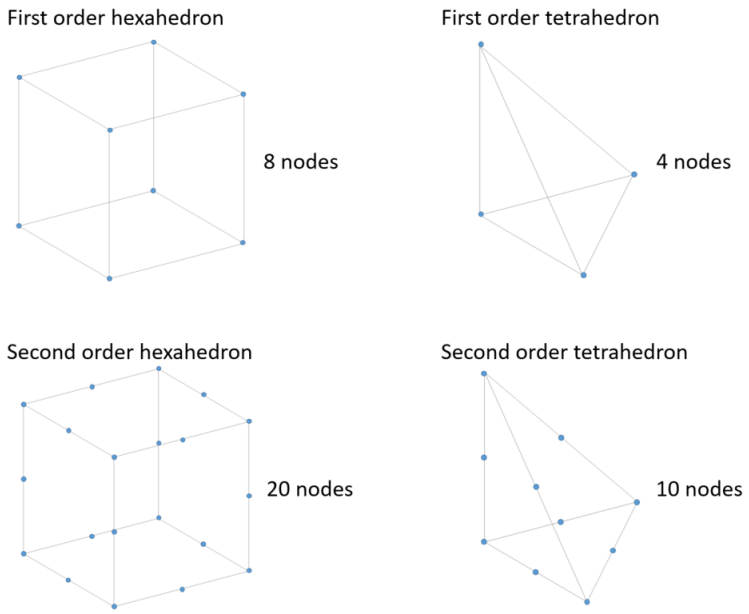

Fig. 121 On top, first order hexahedron element (left) and tetrahedron element (right). On the bottom, second order hexahedron element (left) and tetrahedron element (right).

Moreover, these elements can be linear, as those in Fig. 121 top, or quadratic, as those in Fig. 121 bottom. The accuracy of the quadratic or second order elements is improved by adding extra nodes on the center of the edges of the elements. In this way, a quadratic tetrahedron has 10 nodes instead of the 4 nodes of a linear tetrahedron, and a quadratic hexahedron has 20 nodes instead of the 8 nodes of a linear hexahedron. As it can be seen in Fig. 122, second order elements adapt better to irregular forms and consequently to the deformation that elements can undergo, thus, the accuracy of the models improves. As a drawback, in comparison with a mesh of linear elements of the same size and number of elements, the computational costs of the quadratic elements is higher since they have more nodes and more integration points. Tetrahedral quadratic elements have 4 integration points instead of 1 and hexahedral quadratic elements 27 instead of 8.

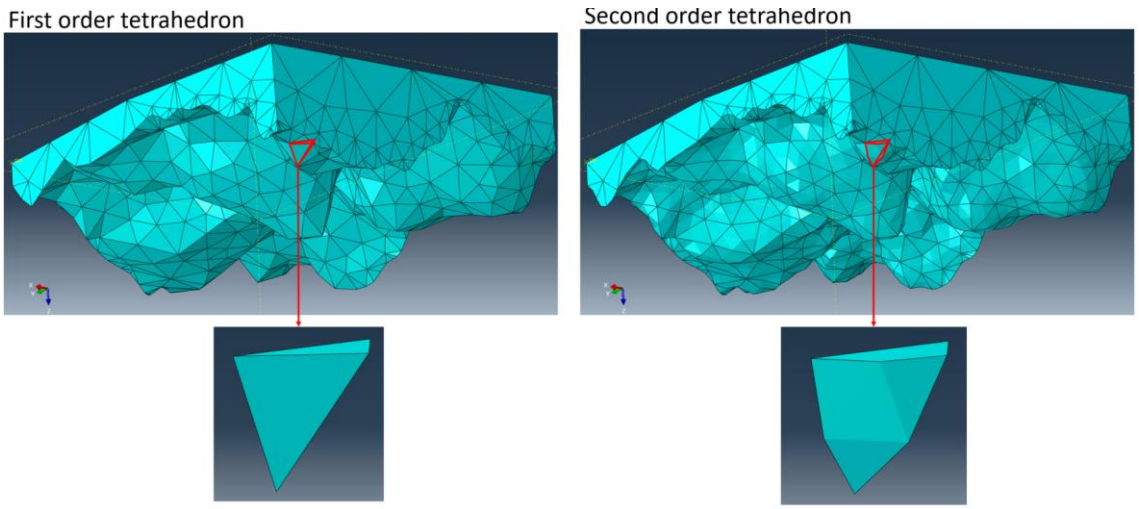

Fig. 122 Left, the pin meshed with first order tetrahedron. Right, the pin meshed with second order tetrahedron.

Regarding the type of element, it is selected as a function of the analysis. This model was defined as a thermo-mechanical approach of the pin-on-disk test, thus, the elements had to be able to address thermal and mechanical loads. Among the element library of Abaqus®, second order coupled temperature-displacement tetrahedral elements C3D10MT were used for meshing the plate.

4.2.2.2 Pin

4.2.2.2.1 Geometry

The wheel configuration is an important factor of the process. The size, the shape, the grain concentration, the material, the porosity and the bonding have a strong influence on the wheel performance and on the result of the operation. Hence, the grinding wheel features had to be reproduced with a maximum fidelity when the grinding process is being modeled. Some of these aspects refer to the geometry while others refer to the physical properties. In this section, the geometry of the surface used in the model is addressed.

One of the advantages of the FEM is that the user can design any geometry for the parts of the model. In previous works, other authors have developed different 3D surfaces for modeling grinding processes, see section 1.5.3. However, all of them were simplifications of the real grinding wheel topography. Although they obtained remarkable results, a simplified surface adds another uncertainty to the model that have to be supported through the adjustment of the model.

In this work, that negative point was avoided since the geometry of a real grinding wheel was imported directly to the model.

The first step for including the actual topography of a real grinding wheel in the model was to convert the wheel topography in digital format. The same procedure used in chapter 2 with the confocal microscope was used for this purpose. One of the files generated by the confocal microscope is a matrix of three columns of numbers. The first and the second columns indicate the points of the horizontal plane where information has been obtained. The first column can be considered as the X axis and the second one as the Y axis. The third column gathers the height

at which the material has been detected at every XY point. The way in which the values appear in the three columns can be seen in Fig. 123 together with a depiction of the 3D surface.

X axis	Y axis	Z axis
0	0	0
1	0	10
2	0	30
3	0	50
4	0	70
5	0	90
0	1	20
1	1	61
2	1	37
3	1	51
4	1	88
5	1	86
0	2	50
1	2	67
2	2	64
3	2	66
4	2	35
5	2	81
0	3	20
1	3	84
2	3	59
3	3	43
4	3	31
5	3	41
0	4	50
1	4	51
2	4	42
3	4	62
4	4	38
5	4	36
0	5	20
1	5	82
2	5	77
3	5	66
4	5	33
5	5	77

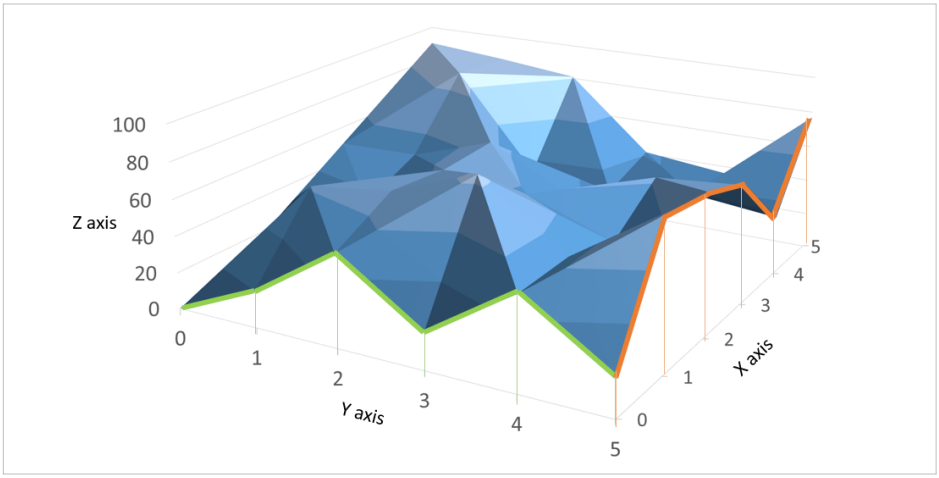

Fig. 123 A depiction of the .dat file and its graphical representation.

Despite having the surface of the wheel as a data file, only universal CAD software formats could be imported to the FEM software. Therefore, the three columns file was processed through CAD software that could transform the cloud of points into a solid body.

At first, the digitalization, see Fig. 124 a), was opened in Catia®. This software allowed to open the data file and visualize the surface as a cloud of points, see Fig. 124 b). The cloud of points was then transformed into a canvas, as it is shown in Fig. 124 c), and imported to another CAD software called NX®. Although it could be opened by different CAD software, it was not possible to be modified since it remained as numerically undefined. For allowing the software to recognize it, the canvas was substituted as a sum of polynomic expressions. For enhancing the accuracy of this conversion, the canvas was separated in smaller sections so that the polynomial expressions resulted simpler. At this point, the mathematical expressions could be intersected with an extruded square so that it resulted in a solid with the geometry of the wheel in one of its faces. The final result is shown in Fig. 124 d). This body could be exported to a file format that could be finally opened with the FEM software.

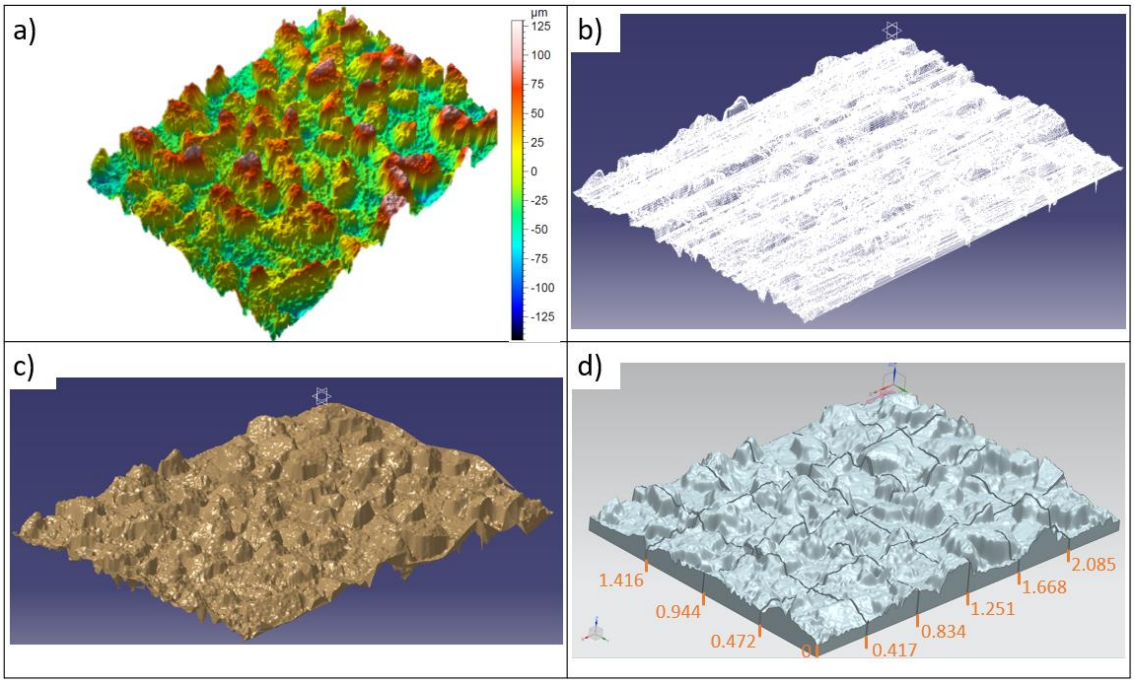

Fig. 124 A 3D confocal digitalization of an EP CBN wheel. b) The cloud of points generated by the confocal microscope imported to Catia®. c) The "canvas" used for covering the cloud of points. d) The solid body created from the mathematical approach.

The size of the wheel surface imported into the model could not be as large as the digitalized surface in chapter 2 since it would result in a huge number of elements. As an alternative, one of the sectioned portions was used as the pin for the model. The section was a square of 0.417x0.472 mm.

However, the aim of using the real wheel surface on the model involves that the wear phenomena must be addressed. According to the analysis carried out in chapter 2 the wheel suffered different wear types, but the most detrimental for the grinding process was wear flat. From the wear flat appearance to the end of the wheel life limit, the percentage of the wheel surface covered by this wear type increased as a consequence of the progressive reduction in the height of the grains. This evolution has a noticeable influence on the process performance as it can be deduced from the power consumption curve shown in section 2.3.3.1. Therefore, the wear must be considered as an input variable of the model for a complete modelization of the process.

One of the options for obtaining the worn surface for the model was to repeat the same process upon a digitalization of a worn wheel. However, the process of substituting the 3D surface by polynomial expressions took a long time, since it had to be done manually. The polynomial expression for each section of the canvas was selected one by one varying the grade and the discretization of the canvas until the lowest error was found. Moreover, with the purpose of isolating the effect of the wear, it was better to use different wear grades of the same surface.

Therefore, wear flat was created on the model following the same methodology used by Aurich et al. [101]. The 3D body was cut with a horizontal plane in order to create flat planes on the tips of the grains. Despite being demonstrated in chapter 2 that Skewness is the most representative standardized roughness parameters for recognizing wear flat, it was not feasible to use that

parameter with the purpose of evaluating the coherence between the wear flat created on the 3D body and the wear flat level observed on the grinding wheel. In consequence, a simpler and more effective parameter was used, namely wear flat percentage.

This parameter indicates the percentage of the surface that is covered by wear flat. Nevertheless, the height where the horizontal plane was set at is related with the resulting wear flat percentage. The height was established after iterative trials until the wear flat percentage created on the 3D body was in the range of the percentage measured on the grinding wheel. The percentage on the wheel was calculated from optical analysis of the digitalizations, some examples of the wear flat percentage measurement on a worn wheel are gathered in Fig. 125.

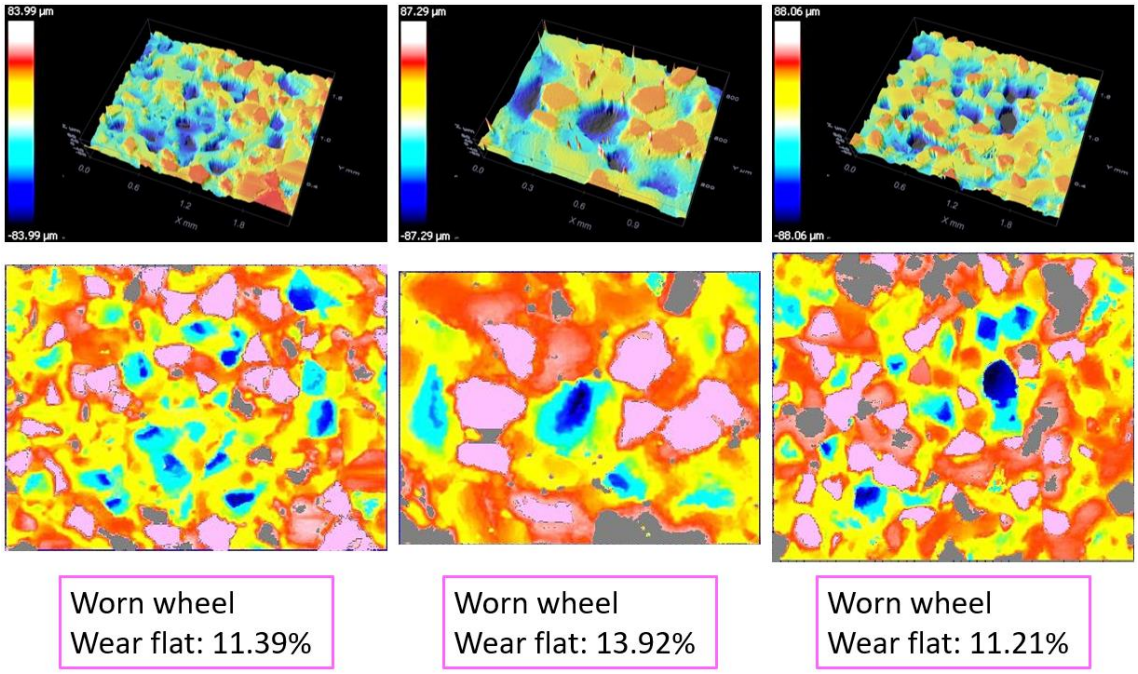

Fig. 125 The wear flat percentage measured on three digitalization of a grinding wheel at the end of its life. On top there are the 3D pictures of the digitalizations. In the middle there are the top views of the digitalization, the wear flats are marked in pink. On the bottom, the value of the wear flat.

From Fig. 125 can be stated that the wear flat percentage of a worn wheel, i.e. at the end of its life, is around 12%. It should be mentioned that the digitalizations shown in Fig. 125 correspond to the most advanced wear state analyzed in chapter 2. After subsequent trials, a wear flat percentage in the same range was created on the 3D body, as it can be seen in Fig. 126.

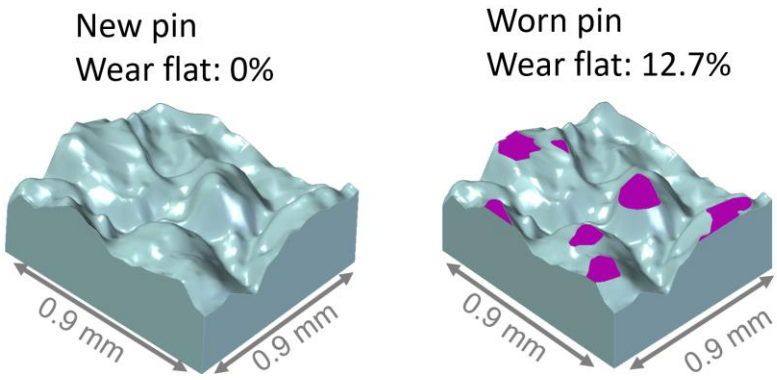

Fig. 126 Left, the pin geometry imported to the model. Right, the modified pin geometry with a resulting wear flat percentage of 12.3%.

Considering 12.3% as the maximum wear flat percentage that a grinding wheel can have while it is still be capable of grinding acceptably, lower wear flat percentages could be used in the model for addressing the influence of the wear. The additional wear flat percentages were created by modifying slightly the height of the horizontal plane instead of values obtained from grinding wheels.

4.2.2.2.2 Physical properties

Apart from the geometry, the physical properties of the wheel must be defined. Since the contact only takes place on the grains, the properties of the CBN was assigned to all the abrasive body. The thermal and mechanical properties of CBN are listed in Table 13 [132],[133].

Table 13 Constant physical quantities of CBN.

Physical quantity	Unit	Value
Density	kg/m^3	3460
Specific heat	J/(kg·K)	670
Young modulus	$MPa \cdot 10^3$	706
Poisson's ratio	-	0.3
Thermal conductivity	W/(K·m)	1300

Given the short duration of the simulation and the endurance of CBN while grinding Inconel 718 seen in chapter 2, the wear of the abrasive grains during the simulation was not considered. In addition, due to the hardness of CBN and nature of EP grinding wheels, the abrasive part was defined as a rigid body in the model.

4.2.2.2.3 Meshing

As it was explained in the previous section, the pin was defined as a rigid body. Hence, the duties of the mesh were simpler than in the case of the disk. On the one hand, it had to transmit the proportion of the heat generated on the contact zone that was evacuated by the pin. On the other hand, it had to reproduce correctly the geometry of the pin. For that purpose, a finer mesh was used on the part of the pin that contacted the disk, see Fig. 127, while much larger elements where used in the opposite side.

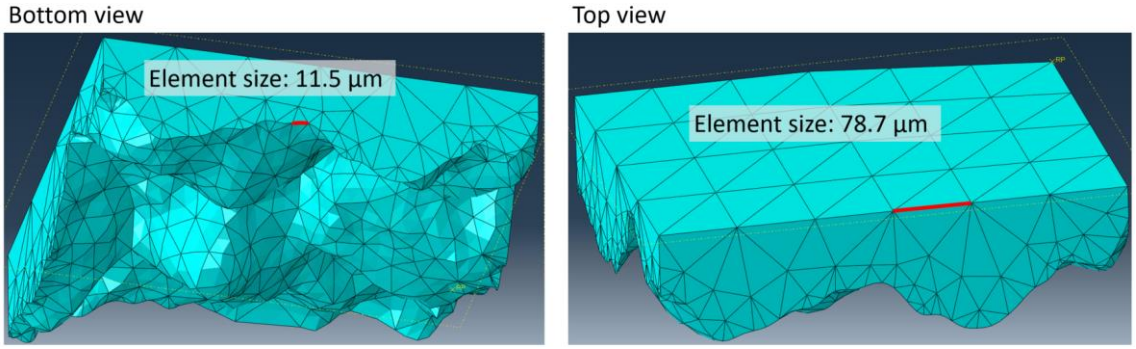

Fig. 127 Left, a bottom view of the mesh of the pin. Right, a top view of the mesh of the pin. The size of the elements marked in red is written on each image.

Despite of having variable size, the same elements as the ones used in the plate were used in the pin, namely C3D10MT. The fact that the pin was defined as a rigid body reduced the high computational costs of the quadratic elements.

4.2.3 Output parameters

The FEM software gives a huge amount of output parameters based on the properties of the model. In this case, the model was a thermo-mechanical approach of the pin-on-disk test, therefore, parameters related with forces and stresses, with the temperature generation and transmission and with displacements could be obtained. First of all, parameters suitable for the validation of the model should be evaluated. Once the model has been validated, the rest of the output parameters can be observed with the purpose of having information of modelled process that could not been obtained from the experimental tests.

The experimental tests were evaluated in terms of force ratio and pile-up ratio, as explained in chapter 3. Nevertheless, the same criteria could not be used for evaluating the model as it is explained in the following lines.

The normal force could not be used since the size of the pin used in the model was smaller than the actual pin's size.

Moreover, the tangential force could not be used for this purpose because of the nature of the grinding process and the model. In grinding, the material removal takes place when the shearing stress resulting from the material deformation exceeds the stress bearable by the material. However, the elements of the model could not reach the plastic deformation obtained during the tests as it is going to be explained in section 4.2.4.4.2. Hence, the tangential force obtained on the model was the result of different conditions.

Taking into account the incapacity for modelling the plastic deformation of the material, the parameter used for evaluating the profile of the scratches, i.e. the pile-up ratio, was also dismissed for validating the model.

As a consequence, the model must be evaluated by means of other output parameters that allowed to recognize the same phenomena observed in the experimental tests. The following four parameter were selected for evaluating the different aspects of the model:

- von Mises stress. von Mises stress is a useful parameter for evaluating the stress on a material at complex stress states.
- Equivalent plastic strain. The equivalent plastic strain is analogous to von Mises stress. This is a dimensionless parameter that is a result of the plastic strain suffered by the material on the different cartesian directions.
- Maximum temperature. The temperature was included in the output parameters since it gives information about how the input parameters affects the temperature.
- Heat flux. This parameter was used for studying how the input parameters affect the heat transmitted to the plate.

4.2.4 Model adjustment

The conception and general definition of the model was done in the previous sections. Nevertheless, there were several points of the model whose full definition must be based on the results of the model itself. In this section, the analysis of the preliminary modelizations and the adjustment of the FEM model is gathered. The pending aspects of the simulation were defined and other unexpected phenomena were detected and solved as follows.

4.2.4.1 Speed trials

The speed used in the pin-on-disk tests was in the range of 20 to 80 m/s. One of the reasons for developing a FEM model of the pin-on-disk was that the speed would be limited by the tribometer. However, given the large number of simulations expected, the phases of acceleration and contact had to be shortened as much as possible in order to reduce the calculation time of each simulation.

In the tribometer, the moving element was the disk. However, what actually matters is the relative velocity between both bodies. In the model, the pin was defined as the moving element while the nodes of the lowest surface of the plate were defined as immobile. See the beginning of a simulation in Fig. 128, the pin moves at 80 m/s while the plate is at 0 m/s.

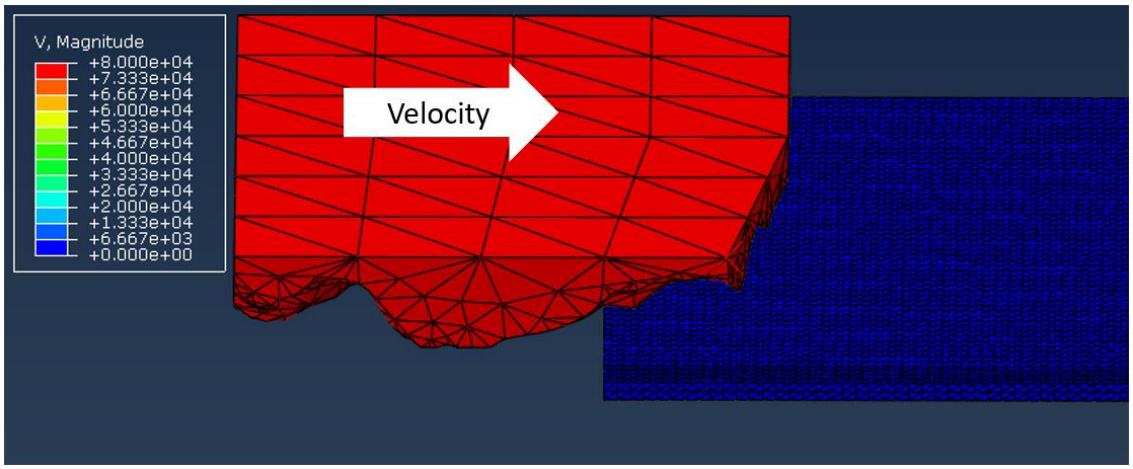

Fig. 128 A 3D view of a model where the speed was applied on the pin.

4.2.4.2 Contact depth

The contact depth in the experimental tests was the result of the force produced by the pneumatic cylinder and the contact area. At first, the same principle was followed for achieving the contact depth in the model. That is to say that it was defined by defining a normal force between the pin and the plate. However, this method resulted in problems of stabilization since there was a phenomenon of rebound between both bodies caused by the elastic recovery. In consequence, this method was dismissed and substituted by imposing the depth as a relative position between the lowest point of the pin and the surface of the plate before starting the calculation. The cutting depth was calculated empirically through the procedure explained in the following lines.

The profiles of the scratches digitalized during the chapter 3 could not be used for this purpose since they corresponded to several passes of the pin over the same zone. Instead, indentation trials were performed with new pins on an Inconel 718 disk. Taking Vickers microhardness tests as reference, the input parameters that affect the result are the contact pressure and the contact time. On the one side, the contact pressure used for the indentations was the same as the pressure used for the pin-on-disk tests, namely 0.1. On the other side, the contact time was established at 0.5 s with the purpose of avoiding the phenomena of a crash tests and with the purpose of not extending the contact for too long, it should be noted that the contact time during the pin-on-disk tests was around 0.5 s.

The pressure set on the pneumatic cylinder resulted in a contact force, however, the contact pressure depended also on the contact surface. The contact surface could be considered as a constant that depends on the macro geometry of the pin. However, if the abrasive surface is accounted, the actual contact surface depended on the wear state of the pin. For achieving coherent contact depth values, indentation tests were carried out with pins extracted from a new wheel and pins extracted from a wheel at the end of its life.

The indentation marks were digitalized by the confocal microscope in order to measure the depth. Some marks carried out with new pin at 0.1 MPa are shown in Fig. 129.

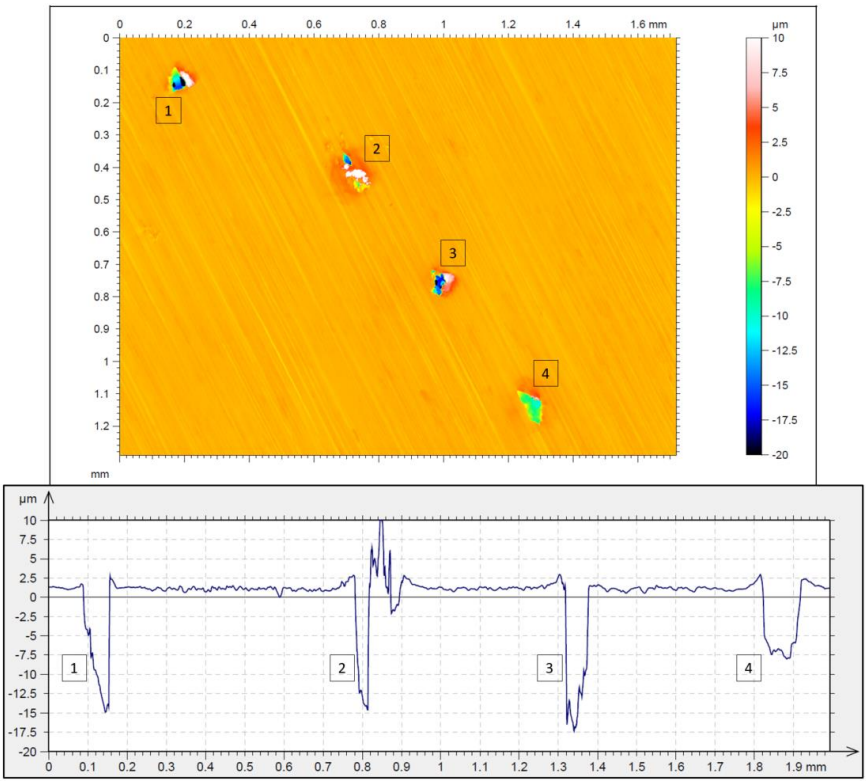

Fig. 129 Confocal digitalization and depth measurement of indentation tests at 0.1 MPa with new pins.

From Fig. 129, the contact depth for a new pin working at 0.1 MPa can be established at 16 µm. The starting situation of a model reproducing this contact conditions is depicted in Fig. 130

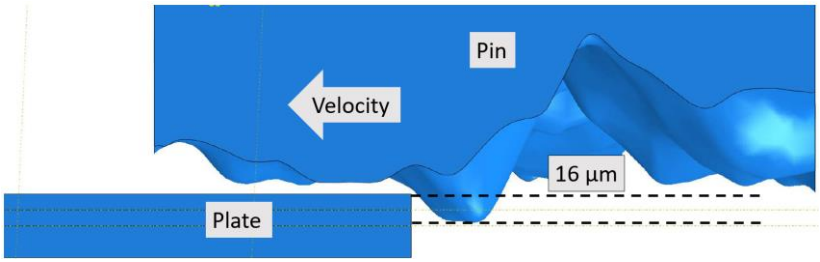

Fig. 130 A side view of the initial relative position of the model with the new pin and the plate at 0.1 MPa.

Concerning the indentation with worn pins, the indentation at 0.1 MPa can be seen in Fig. 131.

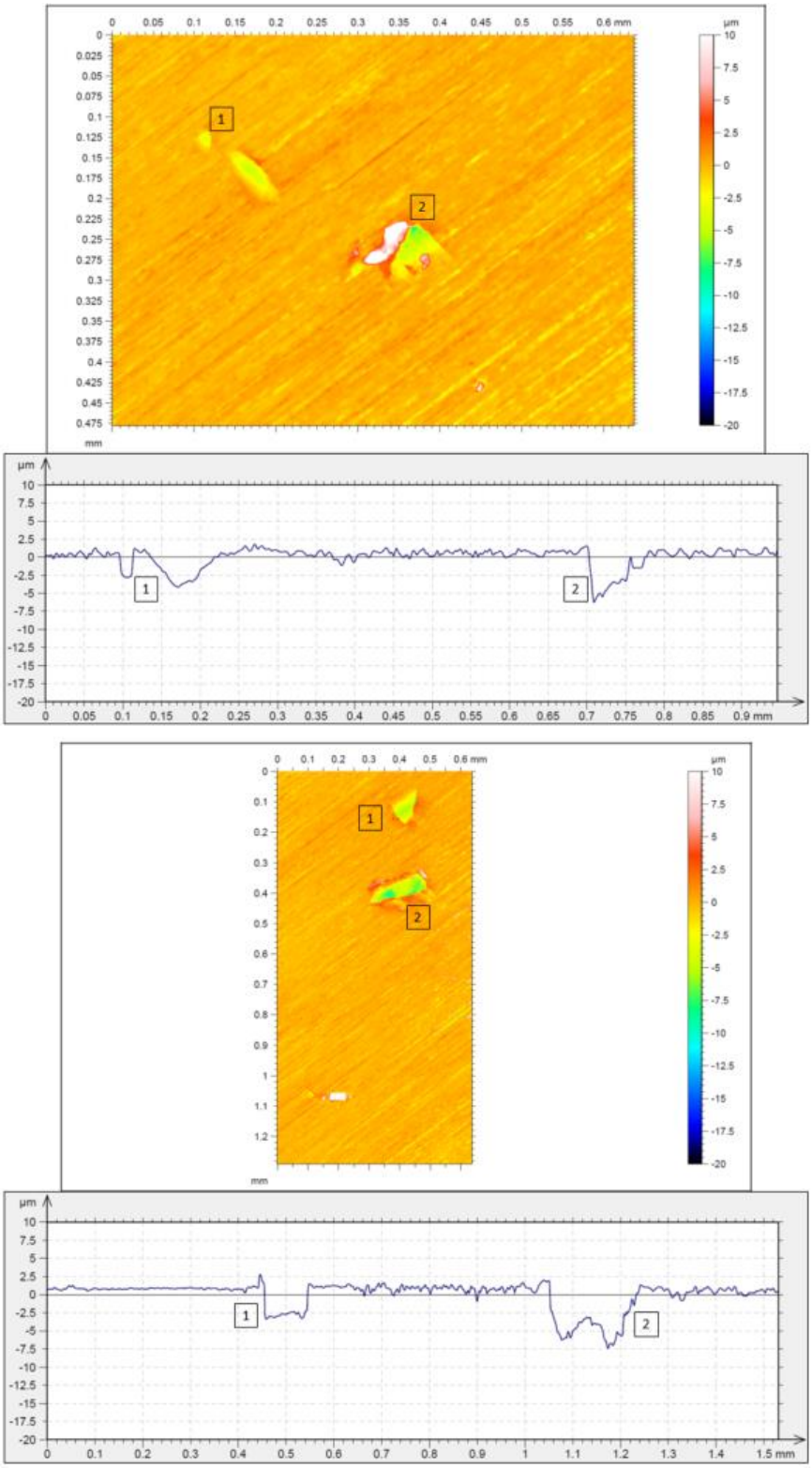

Fig. 131 Confocal digitalization and depth measurement of two indentation tests at 0.1 MPa with worn pins.

The contact depth in this case was set at 5 µm. Fig. 132 shows the initial position of the pin and the plate on the model.

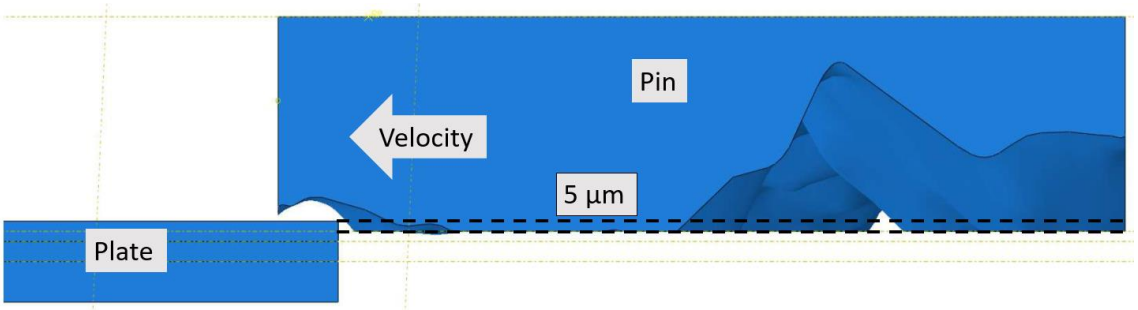

Fig. 132 A side view of the initial relative position of the model with the worn pin and the plate

4.2.4.3 Dimension of the plate

The requirements for the dimension of the plate were mentioned in section 4.2.2.1.1.

On the one hand, the plate must be long enough for ensuring a steady zone on the result of the force in order to be able to compare with the empirical data. The length of the plate used in the first trial was 0.9 mm. The result of the normal force obtained from that calculation is plotted in Fig. 133.

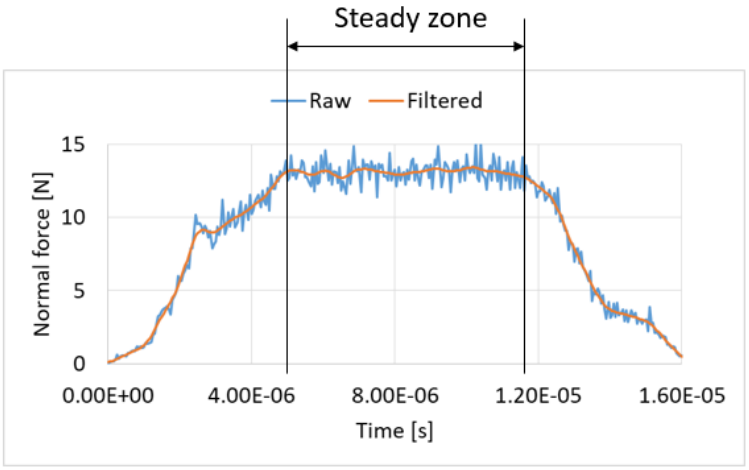

Fig. 133 In blue there is a normal force signal acquired after a preliminary calculation. In orange there is the same signal after being filtered by a Butterworth filter at 1,000,000. In black there is the steady zone.

A steady zone can be clearly seen on the central part of the signal plotted in Fig. 133, hence the original distance of 0.9 mm was considered as valid for the model. In addition, among all the filters available in Abaqus®, Butterworth filter with a filtering parameter equal to 1,000,000 was selected for smoothing the force signals. The orange curve plotted in Fig. 133 is the result of applying that filter to the raw signal, plotted in blue.

On the other hand, the plate must be thick enough for avoiding the heat to reach the lower surface of the plate. For that purpose, two calculations were launched, one at 573K and other one at 1273K. The solution of those calculations was analyzed in order to see if the heat flux resulting from the contact reached the lower surface, the images are gathered in Fig. 134.

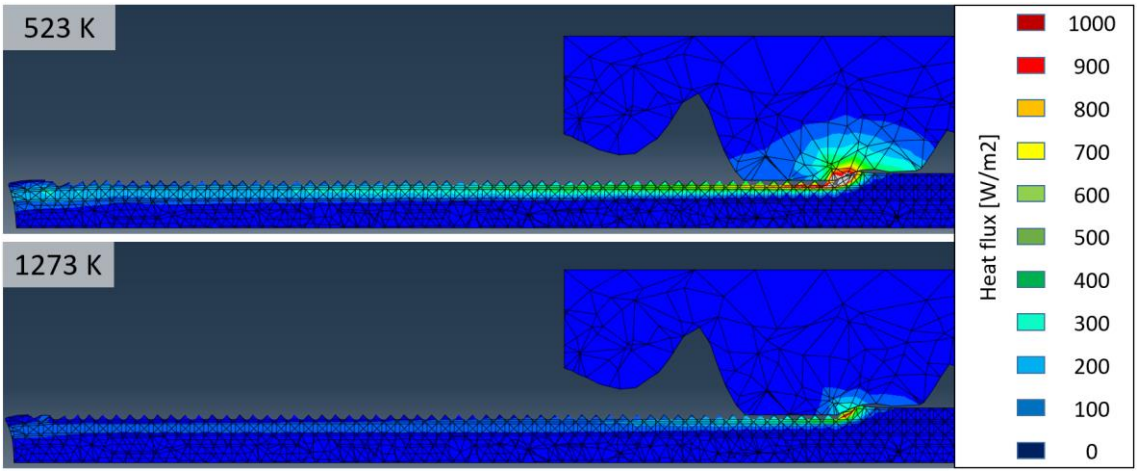

Fig. 134 Two side views of a slice of the model where the heat flux is colored according the color scale of the left. On top, a model with 523K as starting temperature. On the bottom, a model with 1273K as starting temperature.

Through Fig. 134, the thickness of the plate used on those trials was confirmed as valid for the subsequent simulations since the heat transmission along the plate is not affected by the plate thickness. As expected, the heat transmission was higher at lower temperature. However, even at that conditions, the low thermal conductivity of Inconel 718, allowed to have only a thin layer of material affected by the heat.

4.2.4.4 Analysis of sensitivity

An analysis of sensitivity was carried out for establishing the input parameters that could not be taken from bibliography and needed an iterative process for establishing their value. This analysis was carried out on two aspects of the model, namely, the material failure and the element size. The procedure and results are summarized in the following lines.

4.2.4.4.1 Element size

It was mentioned before in this chapter, that a compromise must be stated between the computational costs and the accuracy of the results. Therefore, the size of the elements should be adapted to the features of the modelization.

Through the static indentations, the minimum contact depth was established at 5 µm for the case of 0.1 MPa and worn pins. The rest of the combinations led to deeper contact depth because of higher pressure of lower contact surface. Therefore, it was concluded that the maximum element size in the direction of the contact depth should not exceed 5 µm. Nevertheless, as mentioned in section 4.2.1, the lower the element size is, the larger the calculation costs for an explicit calculation.

With the purpose of establishing the minimum size of the elements in the direction of the contact depth, the result of two different sizes were compared, namely, 5 and 2.5 µm. It should be mentioned that the same contact depth was used in both cases, 5 µm.

The model with the minimum element size of 2.5 µm suffered an excessive distortion on some of the elements and the calculation crashed due to an excessive temperature rate occurred while solving the heat transfer equations. By contrast, the model with 5 µm in minimum element

size was calculated successfully and the results of the normal force were stable, as shown in Fig. 135 together with the normal force of 2.5 µm.

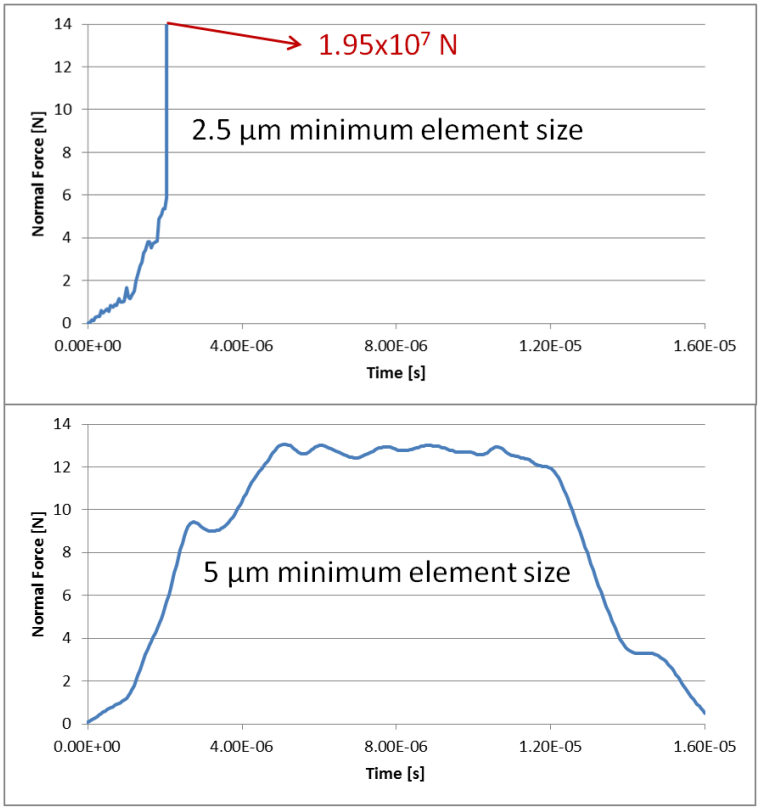

Fig. 135 Resulting normal force of two different minimum element size. On top, 2.5 µm. On the bottom, 5 µm.

As a consequence, the plate was seeded in such a way that the elements on the contact zone had 5 µm in size in the contact depth direction. Along the other two directions, 10 µm were set. The elements furthest from the surface were designed with 10x10x10 µm. In Fig. 136 the tetrahedrons from both zones are compared.

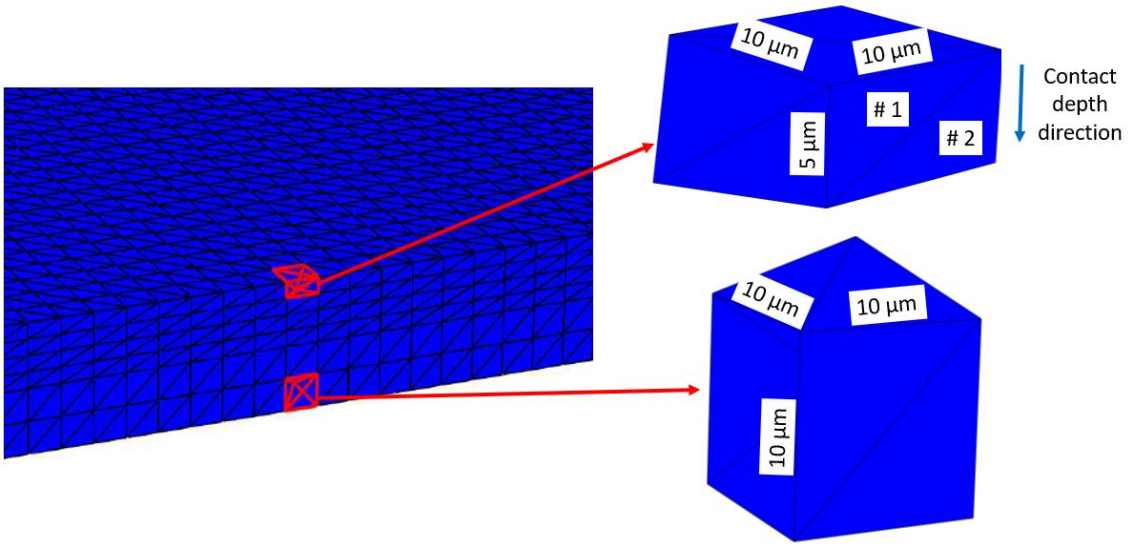

Fig. 136 Element size distribution along the direction of the cutting depth.

From Fig. 136 can also be seen that, in spite of using elements with the same size as the contact depth, there is more than a single element along the contact depth. This leads to a finer discretization of the contact.

4.2.4.4.2 Material failure

The material removal was needed to be addressed by the model for two reasons. On the one hand, the pin-on-disk involved a significant amount of material removed that affects directly to mechanical and thermal results. On the other hand, the material removal affects the contact conditions of the grains that are not in the first line of contact. Moreover, not only the material removal but also the plastic deformation of the material affected the result of the multigrain simulation. In this model the combined effect of the material removal and plastic deformation was controlled by the failure criterion and friction coefficient.

The failure criterion determines when the material starts to fail and loses all or a part of its physical properties. The simplest way in which FEM models represent this phenomenon is by deleting the elements that have reached the limit established by the failure criterion. However, the limit can be defined as a function of various physical properties and it can be defined either as a constant or as a variable parameter. Given the wide range of variability, this is also a case of study of FEM models where many authors have worked [86],[104],[134]. The failure criterion used in this work was a predefined JC shear failure model.

The friction coefficient is a parameter that must be defined when the contact between two surfaces is defined. It should be mentioned that this parameter is not comparable with the friction coefficient calculated from the division of the normal and tangential force resulting from the model. The result of that division can be considered as a macro friction coefficient while the parameter addressed in this section can be considered as a micro friction coefficient. Thus, this parameter has a direct influence on the local friction between the two surfaces. That is to say that a lower friction coefficient allows the material of the plate to slip easier on the surface of the pin. By contrast, with a higher friction coefficient, the pin drags easier the material of the plate. Therefore, it can be deduced that the macro friction coefficient depends on the micro friction coefficient as it depends on the rest of the input parameters.

The values gathered in Table 14 were combined in order to find the optimal combination.

Table 14 Input parameters for the analysis of sensitivity for the material removal.

JC shear failure	0.01-0.75-1.5-2.25-3
Friction coefficient	0.01-0.3-0.6

The results of the 15 trials are gathered in Table 15. Two pictures are in every box, one with a front view of the groove and the other one with the normal force along all the contact time.

Table 15 Results of the analysis of sensitivity for the material removal.

		Friction coefficient		
		0.01	0.3	0.6
JC shear failure	0.01	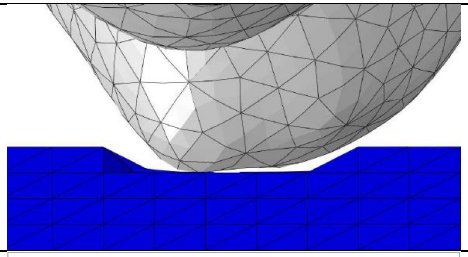	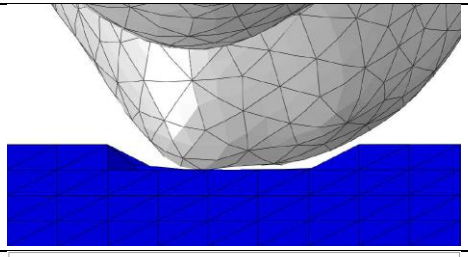	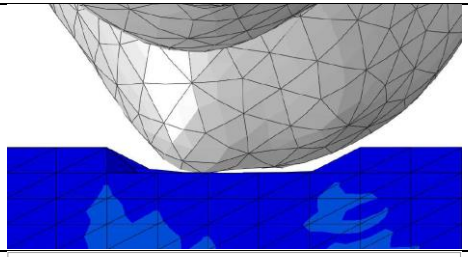
	0.75	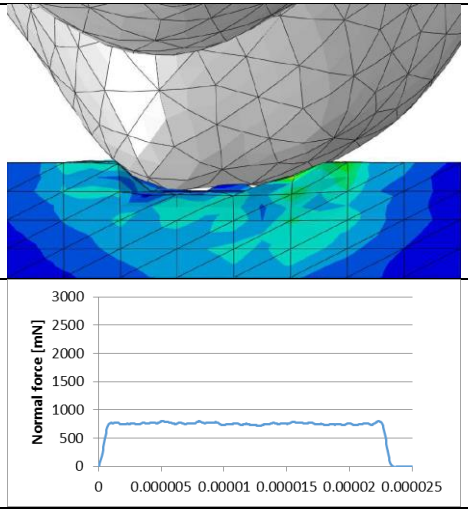	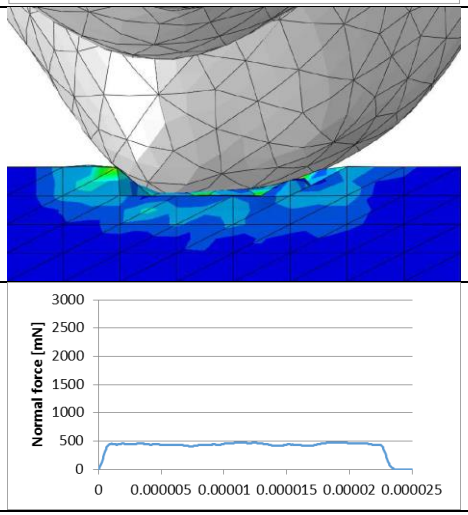	Not calculated

	1.5	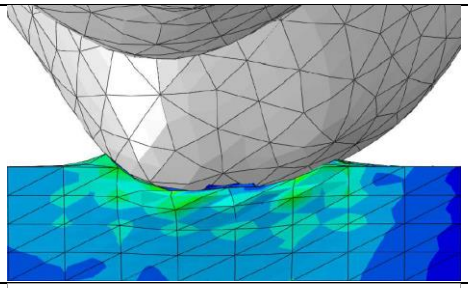	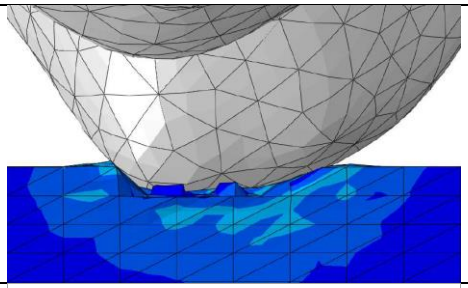	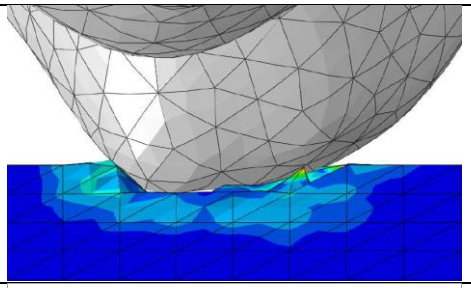
	1.5	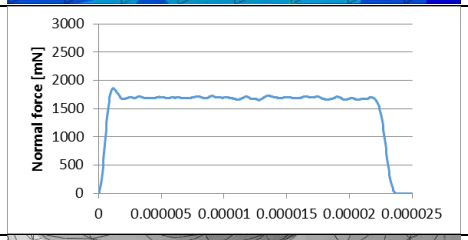	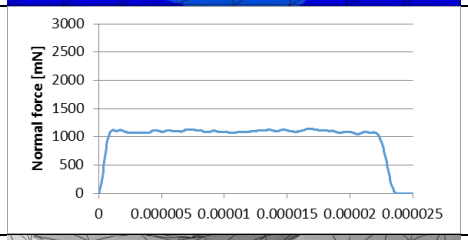	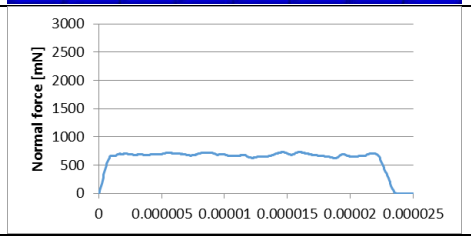
	2.25	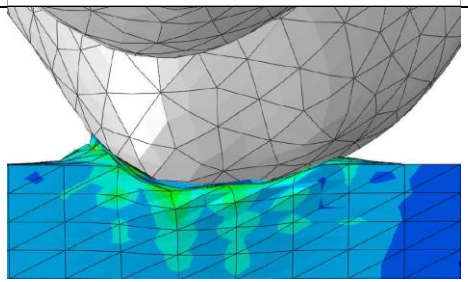	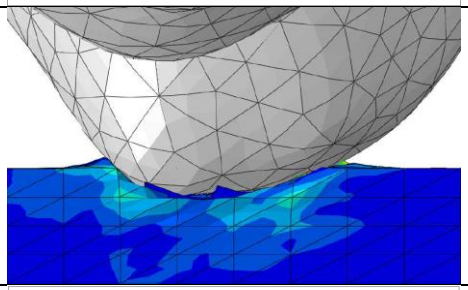	Not calculated
		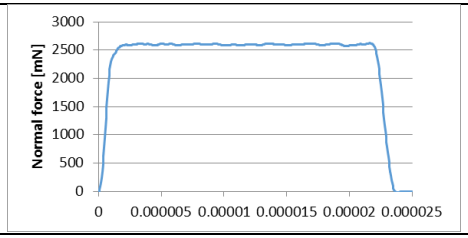	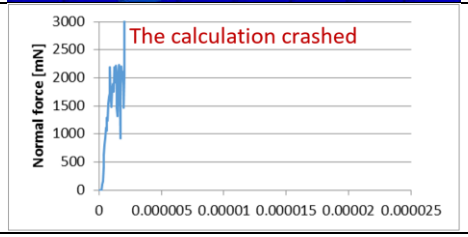	

	3	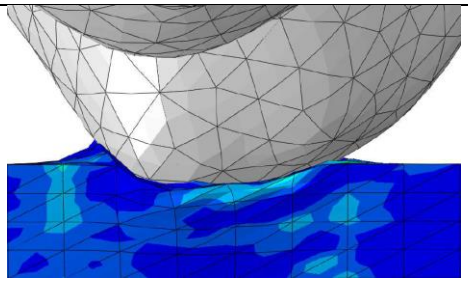	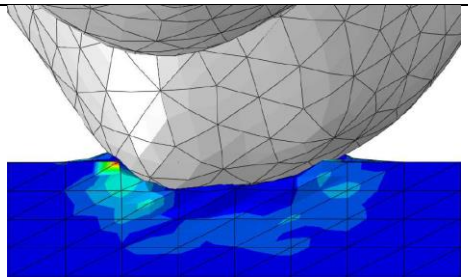	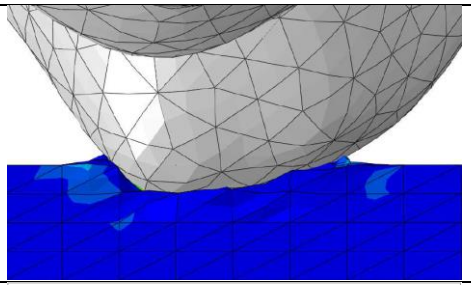
		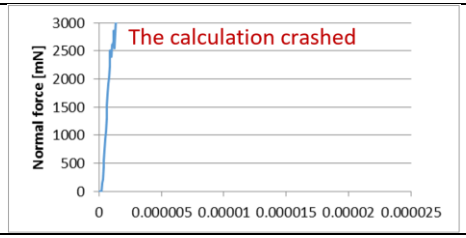 The calculation crashed Normal force [mN] 3000 2500 2000 1500 1000 500 0 0 0.000005 0.00001 0.000015 0.00002 0.000025	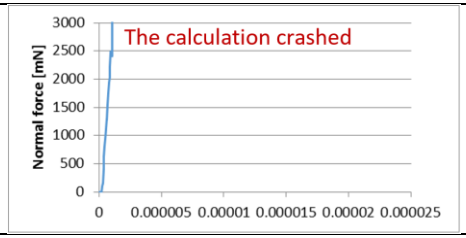 The calculation crashed Normal force [mN] 3000 2500 2000 1500 1000 500 0 0 0.000005 0.00001 0.000015 0.00002 0.000025	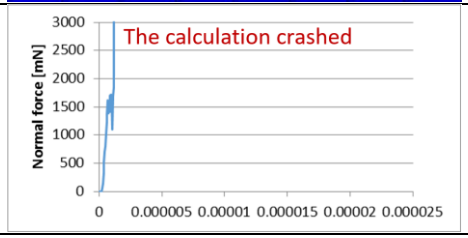 The calculation crashed Normal force [mN] 3000 2500 2000 1500 1000 500 0 0 0.000005 0.00001 0.000015 0.00002 0.000025

When the JC shear failure was small, i.e. 0.01, the deformation of the plate is small, which means that there is almost no plastic deformation. As a consequence of this fragile behavior, it can be seen that the groove left on the plate, is wider than the pin. This is because every element that contacted the pin failed and was deleted from the model. The effect of the excessive fragility led to discontinuous value of the normal force. A zero value of normal force could be assumed as a lack of contact, this scenario could not be considered as valid.

When the shear failure increased, the resistance of the elements increased and thus, the normal force registered was constant all along the sliding time, as it can be seen in shear failures 0.75 and 1.5. The friction coefficient was found to be influential also on the material deformation. The higher deformation for a given shear failure value took place at a friction coefficient equal to 0.01. When the friction coefficient increased to 0.3, the deformation on the elements of the plate was lower. In this case, the friction between the elements of the surface of the plate and the elements on the surface of the pin was higher. Because of this reason, the elements of the plate were dragged towards the speed direction rather than pushed aside the pin.

The plastic deformation took place in an important proportion in the experimental tests; therefore, its presence should be maximized in the model. Taking this into account, some calculations with 0.6 in friction coefficient were not launched since the deformation was going to be lower than with 0.3.

Taking up the analysis of the shear failure values, there is an important difference between 0.75 and 1.5. 0.75 gives a constant normal force as a result, but the plastic deformation of the material is negligible. By contrast, 1.5 allows more plastic deformation, especially for friction coefficient 0.01.

However, when the shear failure value increased excessively, the elements were able to bear more stress and therefore, the resulting deformation was larger. If the deformation is too high, some of the elements may present an excessive distortion, which results in problems for solving the thermal part of the model.

Despite the calculation with friction coefficient 0.01 could be succeeded for shear failure 2.25, friction coefficient 0.3 led to the error mentioned in the previous paragraph. Therefore, 2.25 was considered as an unstable input parameter for the model.

Finally, shear failure equal to 3 was too high whatever the friction coefficient.

Taking everything into account JC shear failure 1.5 and friction coefficient 0.01 were used in the model.

4.3 RESULTS AND VALIDATION

The parameters selected for evaluating the model were introduced back in section 4.2.3. In this section these results are plotted and discussed.

4.3.1 von Mises stress

Maximum values of von Mises stress are plotted in Fig. 137.

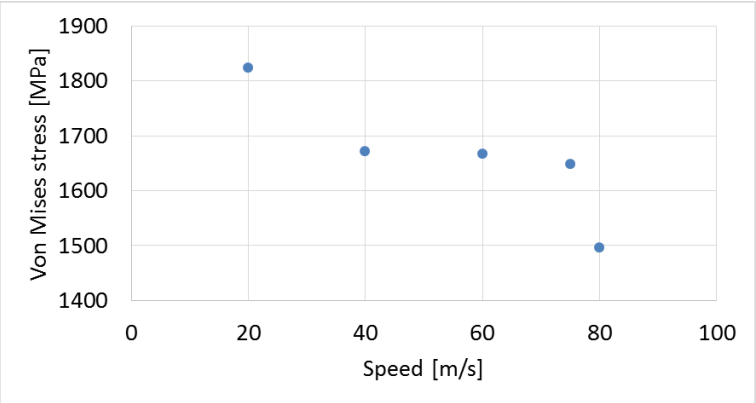

Fig. 137 von Mises stress obtained in the model.

The stress decreases with the increase in the cutting speed. This phenomenon is a result of the softening of the material. The von Mises stress obtained in the models was compared with the force ratio obtained in the experimental tests with the purpose of evaluating the changes in the material hardness. The comparison is shown in Fig. 138. The von Mises stress is plotted in blue by dots while the inverse of the force ratio is plotted by an orange line. From this figure it can be stated that the softening observed in the model matches with the different stages that can be differentiated in the force ratio. There is a sudden change from 20 to 40 m/s, then the variation is less severe and finally there is a slight increase at 80 m/s. See Fig. 138.

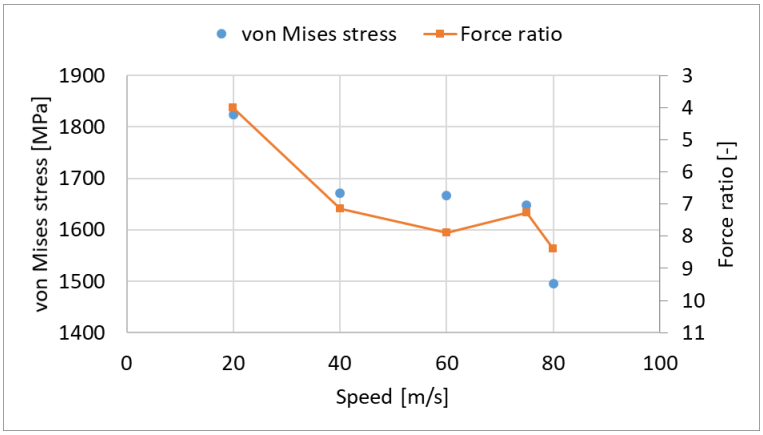

Fig. 138 von Mises stress values obtained from the numerical simulation with a worn pin and 5 µm in cutting depth. In orange is superimposed the inverse of the force ratio.

This comparison indicates that the model is capable of reproducing qualitatively the softening phenomenon of Inconel 718.

4.3.2 Equivalent plastic strain

Maximum values of equivalent plastic strain are plotted in Fig. 139. Those values were obtained on the plastically deformed material left on the plate on the sides of the scratch, as it can be seen in Fig. 140.

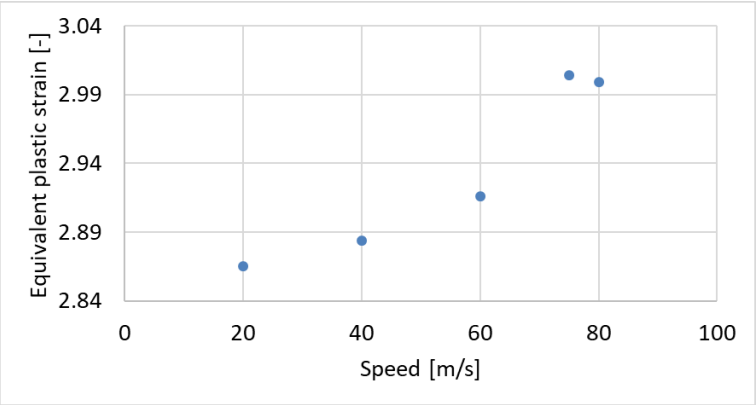

Fig. 139 Equivalent plastic strain obtained in the model.

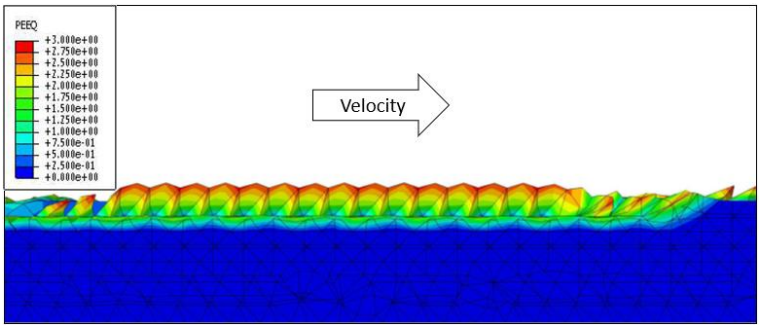

Fig. 140 A side view of the equivalent plastic strain on the plate.

This graph indicates that the softening of the material involves an increase of the plastically deformed material. These results match with the assumption that the material is mainly affected by thermal softening.

4.3.3 Maximum temperature

Maximum temperatures are plotted in Fig. 141. Those values were obtained on the same element located on the ridge created besides the abrasive grains as it can be seen in Fig. 143.

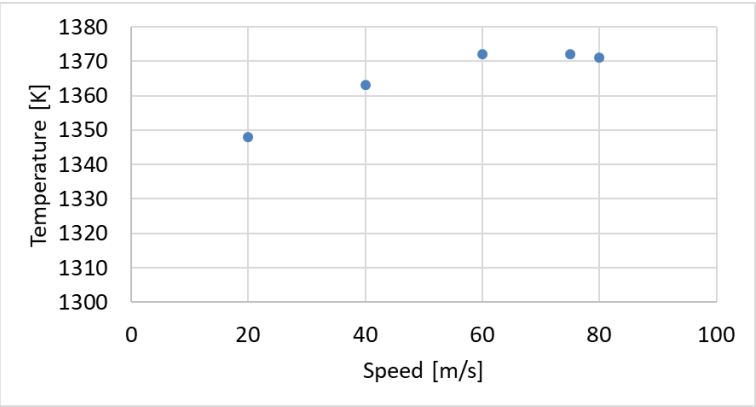

Fig. 141 Maximum temperature obtained in the model.

The maximum temperature achieved in the model increases with the cutting speed to an asymptote close to the melting temperature of the material. These results cannot be

quantitatively validated since there is no temperature data during the experimental tests. However, it can be stated through the following two reasons that temperatures in the same range of values are reached during the tests.

On the one hand, it is accepted by many authors in grinding that the material reaches temperatures in the range of the melting temperature before becoming chip [135]. This is also considered on the expression used for calculating the heat evacuated by the chips, Eq. (52).

$$q_{ch} = \rho \cdot c \cdot T_m \left(\frac{a_e \cdot v_w}{l_c} \right) \tag{52}$$

On the other hand, it was optically confirmed by the videos and pictures taken during the tests that the chips were created in form of sparks, see Fig. 142. This phenomenon confirms the high temperatures reached during the process.

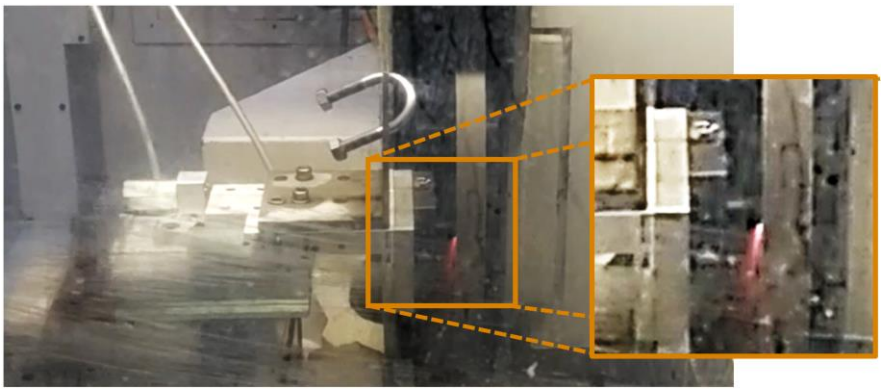

Fig. 142 Sparks generated during a pin-on-disk test as a consequence of the high temperature.

The melting temperature in the model for Inconel was set at 1573 K. Despite it is considered that the chip reaches the melting temperature when it is created, such value could not be obtained in the model since the chip generation could not be completely simulated. That is to say that the final part of the chip generation, when the strain takes the highest values, was not addressed in this model.

Taking everything into account the model is in accordance with the statement of the temperature at the onset of the chip generation. Thus, the values plotted in Fig. 141 must be considered as the maximum temperatures on the elements before reaching the failure criteria defined on the model, instead as the maximum temperature during the actual process. Even if a relationship with the cutting speed may be deduced from Fig. 141, it is more sensitive to look at the heat flux in order to analyze the thermal loads created during the process.

It should be mentioned, that the values of von Mises stress shown in section 4.3.1 and the values of the maximum temperature were not taken from the same zone. The von Mises stress of the material at the zone of the maximum temperature was significantly lower, as it can be seen in Fig. 143. In this picture, for instance, the maximum stress, around 1000MPa, is on an element that is at 1100K, while the stress on the elements at higher temperatures is substantially lower.

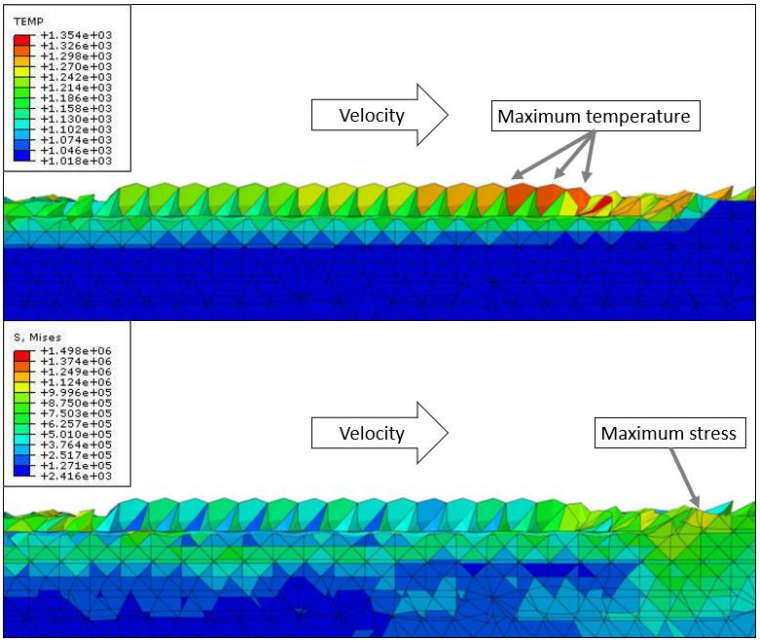

Fig. 143 Side view of the temperature (top) and von Mises stress (bottom).

4.3.4 Heat flux

The trend of the temperature has been analyzed in the previous section; nevertheless, it is limited by the melting temperature of the material. In addition, it was measured on the material that later was going to become chip. In this section, the heat flux is analyzed with the purpose of addressing the thermal loads on the part. The heat flux is plotted in Fig. 144.

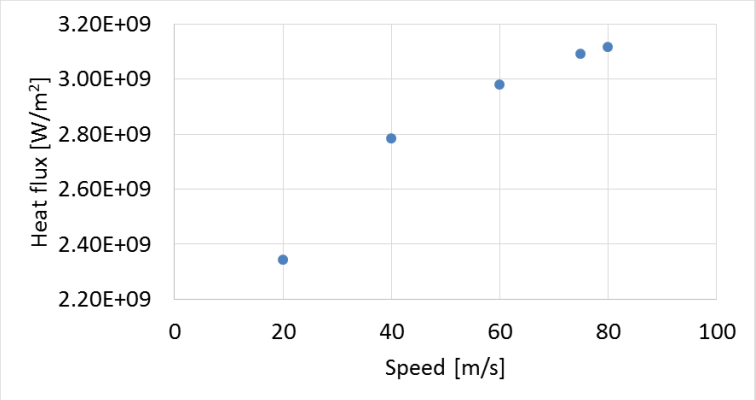

Fig. 144 Heat flux obtained in the model.

From Fig. 144, the effect of the speed on the thermal softening is more evident. When the speed increases, more energy is transmitted to the part. This energy is transformed into heat on the part and thus, the properties of the material are modified. The modification does not only affect the interaction with the grain that have created this increase in the temperature but it also affects the interaction of the subsequent grains. This phenomenon can be successfully addressed thanks to the use of a multigrain surface.

4.4 CONCLUSIONS

A FEM model was created for reproducing the interaction between the abrasive grains of an EP CBN grinding wheel with the actual geometry of a real grinding wheel. The simulation was evaluated in terms of von Mises stress, equivalent plastic strain, maximum temperature and heat flux. The results were compared to the results obtained on the pin-on-disk test for finding a correlation and thus, verifying the consistency of the model. The conclusions are gathered in the following lines.

During the tests carried out in the tribometer, a softening of the material was observed when the cutting speed was increased. The same phenomenon was observed on the model, through the reduction of the von Mises stress according to the increase of the cutting speed.

One of the aspects that should be mentioned is that the softening did not follow a constant progression. The pattern followed by the softening in the experimental tests was also achieved in the model.

Taking everything into account, it was concluded that, in general terms, thermal softening controls the material behavior at different cutting conditions instead of strain rate hardening. However, analyzing in detail the progression of the softening, the presence of the strain rate hardening can be acknowledged at the intermediate speeds. Although there is not an actual hardening of the material, there is a reduction on the softening progression that can be attributed to the strain rate hardening.

This statement was confirmed by means of the equivalent plastic strain. The increase observed with the increase of the cutting speed was considered as an increase of the ductile behavior instead of the fragile behavior that would have been caused by the strain rate hardening.

This indicates that the material removal process is less efficient. In grinding process, the plastic deformation of the material can be related with beneficial and detrimental phenomena. The plastic deformation leads to better finishing surface, i.e. less roughness. Nevertheless, a huge plastic deformation can result in higher temperatures and in workpiece material adhesion on the grinding wheel.

Regarding the thermal loads created during the interaction, the heat flux gives more consistent information than the maximum temperature. In accordance to the theory of grinding processes, the maximum temperature is reached on the chip generation, which is not addressed by the model. By contrast, the results of the heat flux demonstrate more clearly the increase in the thermal loads caused by the speed.

Taking everything into account, the efficiency of the material removal should be assessed in order to account what these results would involve on the grinding process.

The efficiency of the material removal process is evaluated in terms of specific energy. This was already introduced in this manuscript and defined as the energy needed for removing a unit volume of the workpiece material. The material softening observed in this process, in both experimental and numerical results, leads to a reduction of the force needed for the pin to scratch the plate. This could be considered as a beneficial aspect if the reduction of the

tangential force was high enough for diminishing the resulting energy spent in the cutting. However, this reduction would have to be at least the same as the increase in the cutting speed, which was not observed.

Moreover, the increase of the speed entails higher temperatures in the cutting zone as a result of an increase of the heat flux to the part. The increase in the temperature may be a result of a change in the partition ratio, hence it may not modify the specific energy of the cutting process. Nevertheless, it has a direct influence on the process performance. High temperature in the contact zone softens the material and it becomes more ductile, which facilitates the adhesion of the workpiece material to the wheel. In addition, the high temperature is the responsible of several problems in grinding such as tractive residual stresses on the workpiece or changes in the workpiece material composition such as oxidation or changes in the microstructure.

Finally, the increase in the plastic deformation affects negatively the specific energy. Less proportion of the material that comes in contact with the grains is removed, instead, it is plastically deformed. This phenomenon facilitates problems of heating and workpiece material adhesion to the grinding wheel.

In conclusion, the increase in the cutting speed does not have advantages from the point of view of the specific grinding energy. Although the productivity of the process would be enhanced since faster feed speeds can be used. It should be taken into account that these conclusions are based on a grinding process without cutting fluid. The presence of cutting fluid would lead to different results and thus, to different conclusions.

Apart from the technical conclusions gathered in the previous paragraphs, this work can also be analyzed in general terms, an overview is given in the following lines.

The model is able to predict the evolution of the thermal and dynamic phenomena involved in the contact of a grinding operation as a function of the cutting speed and contact depth. This was achieved using a real multigrain grinding wheel surface in the FEM environment under a real level of wear, what has not been done so far.

The results of the model must be correlated with the real performance during the grinding process. In this way, the results of the model can be related with important factors for the industry as the end quality achieved on the workpiece and the influence on the grinding wheel life. In doing so the primary goal of the study would be fulfilled.

It must be kept into account that the plastic deformation of the workpiece material could not be reproduced. Therefore, the adverse consequences that can be caused by this phenomenon, must be observed empirically and related with the outputs of the model.

CONCLUSIONS AND FUTURE WORKS

5 CONCLUSIONS AND FUTURE WORKS

In this section the conclusion that have been drawn along the several chapters of this manuscript are gathered in the following lines. In addition, the future works to do on the research lines opened by this thesis are also listed in the final section of this chapter.

5.1 CONCLUSIONS

The work carried out in this thesis has been separated in three parts, namely the wheel characterization, the experimental approach and the numerical modelization. Each chapter has a final section where the conclusions are commented. In the following lines, those final sections are summarized:

- The wear types suffered by EP CBN grinding wheel as a consequence of CFG nickel base alloys were detected by means of different optical devices. Grain fracture and wear flat were found as the main wear types. Grain pull-out was found occasionally, but no relation with the working life was found.
- The topography of the grinding wheel was measured in terms of roughness parameters comprised in the standard ISO 25178. The digitalizations made with the confocal microscope were used for obtaining the roughness parameters.
- The evolution of the wear types along the wheel working life was registered. The predominance of different wear types was found at different wear grades of the wheel. This was confirmed through an analysis of the roughness parameters obtained from the wheel surface. Grain fracture was found at the first wear stages of the wheel. Once the uneven height of the grains decreased to similar values, wear flat appeared as the main wear type until the end of the wheel life.
- The most representative parameter for the particular wear observed on the wheel was found through a mathematical analysis of an extensive number of roughness parameters. S_{sk} was resulted as the clearest indicator of the wear flat level on the wheel surface.
- The effect of the SiC stick conditioning process was studied on two aspects, namely the wheel surface and the power consumption. It was found that the conditioning process modified only the tips of the flattened grains. The conditioning process resulted in a significant decrease in the power consumption. However, this beneficial effect disappeared fast and the power curve returned to the power consumption values before the conditioning.
- Two different statistical mathematical methods developed by other authors were successfully used for the wheel wear analysis. They allowed to discern the most representative parameters among a wide number of them to differentiate two grinding wheel wear states.
- A tribometer was developed for studying the material removal under CFG conditions. The tribometer was able to use multigrain surfaces and extreme cutting conditions as high speeds and deep cutting depths.

- The material removal was studied as a function of wear and cutting parameters. Pins extracted from a brand-new wheel and from a worn wheel were used for this study. The results were analyzed in terms of forces, scratch profiles and specific energy.
- The specific energy increased when the cutting depth was increased. Therefore, the material removal rate should be increased by means of the feed rate instead of the cutting depth.
- As expected, the higher wear resulted in higher specific energy. The friction with the flat surfaces and the increase in the number of contacting grains consumed additional energy that did not result in material removal.
- The effect of the speed in the specific energy was not noticeable. However, the tangential forces decreased when the speed increased, although not in a constant manner. This variable evolution was considered as a proof of the struggle between thermal softening and strain rate hardening. Although the thermal softening controls the material behavior.
- A FEM model was developed where a real surface of a grinding wheel was defined. The digitalizations obtained in the wear analysis were transformed to a format that could be read by the modelization software.
- Similarly, a wheel wear level measured in real wheels was used as an input of the FEM model. The wear level could be easily adjusted to different wear flat levels.
- The model was adjusted using an internal parameter of the software called friction coefficient and the failure criterion.
- The FEM model was validated through qualitative trends of the mechanical loads, plastic deformation and heat flux. Due to the difference in the scale, a quantitative validation could not be carried out.
- The trend shown by the forces registered in the experiments and the von Mises stress obtained in the model showed the same trend as a function of the cutting speed. The same softening pattern was found.
- The temperatures were not considered as the most representative parameter for evaluating the thermal loads. In grinding, the chip removal occurs at temperatures near the melting point, which was not able to be modelled. Instead, the heat flux was used for this purpose. A higher heat flux to the workpiece was found when the cutting speed increased, which was considered as higher temperatures in the contact zone.
- The material deformation was evaluated by means of the equivalent plastic strain, although the model was not able to reproduce the high deformations observed in the experiments. The trends observed were consistent with the thermal softening of the material deduced from the result of the mechanical and thermal loads. The equivalent plastic strain increased with the cutting speed.

5.2 FUTURE WORK

The work carried out in this thesis has opened new opportunities for studying the contact in a wide range of grinding applications by means of experimental works and grinding modelization. In the following lines, the immediate research works to do concerning these two aspects are sorted:

- To model an intermediate wear level and evaluate the variation of the output parameters. The calculations are already finished, but the results
- The influence of the cutting fluid on the tribometer results must be addressed. Cutting fluid is a paramount factor in grinding. It helps to keep the grinding temperature within admissible limits. It also has influence on the force ratio since it provides a lubrication effect in the cutting zone.
- A rigid and accurate tribometer has been developed in this thesis. However, it should be improved in the following aspects:
    - Kinematics: The contact between the disk and the pin was constant during a certain period of time, which is not the real situation in a CFG grinding operation. This should be corrected by a new configuration of kinematics or by a different preparation.
    - Chip thickness: The power consumption was used for calculating the pin size and contact pressure so that the cutting depth was in the same range as in the industrial process. Then, the pin orientation was carefully selected for trying to reach the same uncut chip thickness values as in the industrial process. If the kinematics or preparation processes are modified, the resulting chip thickness should also be calculated in order to have representative values.
    - Temperature measurement: The layout of the tribometer was not compatible with any reliable temperature measurement device. It was considered the use of a thermographic camera, but the layout of all the elements left no space inside the machine for that. If the sense of the turning speed of the disk is changed and the pin holding system is shifted 180^{o}, a thermographic camera may be used during the tests.
- The changes carried out on the experiments are going to be taken to the FEM model.
    - The cutting fluid must set as another input of the model. At a first glance, it will have influence:
        - on the heat evacuation from the workpiece.
        - on the friction coefficient that has been used as one of the adjusting parameters of the model.
    - The temperature measurements will help to support the validation of the model not only on mechanical measurements.
- The definitive results must be extrapolated to the industrial process in order to be able to solve the problems that motivated this thesis:
    - The values of the output parameters must be related to the actual performance of the process. In doing so, the output parameters of the model that mean the optimal grinding performance can be established.
    - The input parameters must be studied in order to find the combination that lead to the optimal output values in order to be improved the efficiency and productivity of the process. It must be taken into account that the optimum input parameters are likely to vary as a function of the wear of the wheel.
- NGVs have historically been made of Inconel 718. However, nowadays, different nickel-base alloys are been used for these components. One of these materials is C1023, which has not been studied. The methodology developed in this thesis can be applied to the study is the CFG process of that innovative material:
    - C1023 alloy can only be obtained in small quantities and size that usually come from the waste or control samples of the casting process. Currently it is not

possible to manufacture a disk with 400 mm in diameter. Therefore, the setup should be designed again in order to be able to use inserts of this material in a dummy steel disk. The steel disk is already manufactured.

- There is not any research work in bibliography focused on the characterization of this material. Hence, there are not any constitutive equations for defining this material in a numerical model. Thus, prior to model the grinding process, this material must be characterized under high temperatures strain and strain rates. The response of the material is going to be used for calculating a constitutive model. Samples for those tests are already manufactured and heat treated under the same conditions as the NGVs.
- The same structure of the FEM model can be used for modeling the CFG process of C1023. The only changes to do are going to be the material properties and constitutive model. Then, the model is going to be adjusted again according to the empirical results obtained in the tribometer.

6 NOMENCLATURE

A:	Initial yield stress
a_e:	Cutting depth
a_{gmax}:	Uncut chip thickness
A_r:	Groove section
a_{zsr}:	Elementary cutting depth
A_1:	Piled material section
A_2:	Piled material section
B:	Hardening modulus
B_{kr}:	Active grinding wheel length
C:	Active grain density
	Dimensionless strain hardening coefficient
c:	Specific heat capacity
c_d:	Wave propagation speed
D:	Additional parameter of Johnson-Cook model
d_e:	Diameter of the grinding wheel
d_{eq}:	Equivalent diameter
d_g:	Diameter of the grain
E:	Yong's modulus
e_c:	Specific grinding energy
f_{ab}:	Relative chip volume
F_{cyl}:	Force generated by the pneumatic cylinder
F_n:	Normal force
F_t:	Tangential force
F'_n:	Specific normal grinding force

h_{cu}:	Undeformed chip thickness
h_{eq}:	Equivalent chip thickness
K_{afgw}:	Ratio of cutting ability
l_c:	Contact length
L_{min}:	Minimum element size
l_s:	Mean abraded length
l_w:	Mean distance between abrasive grain vertices
m:	Thermal softening parameter
n:	Strain hardening exponent
P:	Power
P_{net}:	Net power consumption
P_{void}:	Power consumption in void
P_1:	Overall power consumption
q_{ch}:	Heat evacuated by the chips
q_s:	Speed ratio
Q_w:	Material removal rate
Q'_w:	Specific material removal rate
r:	Ratio of width to thickness of the chip
	Position along the time
r_{gb}:	Correlation coefficient
R_{in}:	Inner radius of the Inner Rail
R_{out}:	Outer radius of the Inner Rail
R_z:	Maximum height of the surface in a 2D profile
$\dot{r}$(t):	Velocity along the time
$\ddot{r}$(t):	Acceleration along the time
S:	Additional parameter of Johnson-Cook model

S_a:	Mean roughness
S_{a1}:	Upper volume
S_{a2}:	Lower volume
S_{ds}:	Summit density
S_{ha}:	Mean hill area
S_{hv}:	Mean hill volume
S_k:	Core roughness
S_{ku}:	Kurtosis roughness parameter
S_{mr1}:	Peak material portion
S_{mr2}:	Valley material portion
S_{sc}:	Summit curvature
ss_{opt}:	Optimum sample size
S_p:	Maximum peak height
S_{pd}:	Density of peaks
S_{pk}:	Reduced peak height
S_q:	Root mean square
S_{sk}:	Skewness roughness parameter
S_v:	Maximum valley depth
S_{vk}:	Reduced peak valleys
S_z:	Maximum height of the surface
T:	The temperature at an instant in a model
T_m:	The melting temperature
T_r:	Reference temperature in J
T^*:	The homologous temperature
V_{groove}:	Volume of the groove
V_{pile}:	Volume of the piled material

v_s: Cutting speed

v_w: Feed speed

w_i: M

ean amount of abrasive grain vertex

Δt_{stable}: Stable time increment

ε: Strain

$\dot{\varepsilon}$ Strain rate

$\dot{\varepsilon}_0$: Reference strain rate

ρ: Density

7 ACRONYMS

AE	Acoustic emissions
CBN	Cubic Born nitride
CFG	Creep feed grinding
EDXS	Energy-dispersive X-ray spectroscopy
EP	Electroplated
FEM	Finite element method
FFT	Fast Fourier transform
HST	High speed tests
JC	Johnson-Cook
LST	Low speed tests
LTC	Laser touch conditioning
SEM	Scanning electron microscope
SiC	Silicon carbide
USV	Ultrasonic vibrations

8 BIBLIOGRAPHY

1. Kannappan, S. & Malkin, S. Effects of grain size and operating parameters on the mechanics of grinding. *J. Manuf. Sci. Eng. Trans. ASME* **94,** 833–842 (1972).

2. Liu, Y., Warkentin, A., Bauer, R. & Gong, Y. Investigation of different grain shapes and dressing to predict surface roughness in grinding using kinematic simulations. *Precis. Eng.* **37,** 758–764 (2013).

3. Ahmed, O. I. & Dugdale, D. S. Performance of Silicon Carbide Wheels in Grinding Tool Steels. in *Proceedings of the Seventeenth International Machine Tool Design and Research Conference: held in Birmingham 20th -- 24th September, 1976* (ed. Tobias, S. A.) 165–169 (Macmillan Education UK, 1977). doi:10.1007/978-1-349-81484-8_20

4. Tanaka, T., Ikawa, N. & Tsuwa, H. Affinity of Diamond for Metals. *CIRP Ann. - Manuf. Technol.* **30,** 241–245 (1981).

5. Herman, D. & Markul, J. Influence of microstructures of binder and abrasive grain on selected operational properties of ceramic grinding wheels made of alumina. *Int. J. Mach. Tools Manuf.* **44,** 511–522 (2004).

6. Ichida, Y., Sato, R., Morimoto, Y. & Inoue, Y. Profile Grinding of Superalloys with Ultrafine-Crystalline cBN Wheels. *JSME Int. J. Ser. C* **49,** 94–99 (2006).

7. Malkin, S. & Cook, N. H. The Wear of Grinding Wheels L Part1-Attritious Wear. 3–7 (2016).

8. Marinescu, I., Hitchiner, M. & Uhlmann, E. *Handbook of machining with grinding wheels*. (2006).

9. Zhenzhen, C., Jiuhua, X., Wenfeng, D. & Changyu, M. Grinding performance evaluation of porous composite-bonded CBN wheels for Inconel 718. *Chinese J. Aeronaut.* **27,** 1022–1029 (2014).

10. Ding, W. F. *et al.* Fabrication and performance of porous metal-bonded CBN grinding wheels using alumina bubble particles as pore-forming agents. *Int. J. Adv. Manuf. Technol.* **67,** 1309–1315 (2013).

11. Chen, X. & Rowe, W. B. Analysis and simulation of the grinding process. Part II: Mechanics of grinding. *Int. J. Mach. Tools Manuf.* **36,** 883–896 (1996).

12. Denkena, B., Köhler, J. & Kästner, J. Chip formation in grinding: An experimental study. *Prod. Eng.* **6,** 107–115 (2012).

13. Ohbuchi, Y. & Obikawa, T. Surface Generation Model in Grinding with Effect of Grain Shape and Cutting Speed. *JSME Int. J.* **49,** 114–120 (2006).

14. Tian, L., Fu, Y., Xu, J., Li, H. & Ding, W. The influence of speed on material removal mechanism in high speed grinding with single grit. *Int. J. Mach. Tools Manuf.* **89,** 192–201 (2015).

15. Hecker, R. L., Liang, S. Y., Wu, X. J., Xia, P. & Jin, D. G. W. Grinding force and power

modeling based on chip thickness analysis. *Int. J. Adv. Manuf. Technol.* **33,** 449–459 (2007).

16. Brinksmeler, E. & Glwerzew, a. Chip Formation Mechanisms in Grinding at Low Speeds. *CIRP Ann. - Manuf. Technol.* **52,** 253–258 (2003).

17. Ghosh, S., Chattopadhyay, A. B. & Paul, S. Modelling of specific energy requirement during high-efficiency deep grinding. *Int. J. Mach. Tools Manuf.* **48,** 1242–1253 (2008).

18. Ghosh, S., Paul, S. & Chattopadhyay, A. B. Experimental investigations on grindability of bearing steel under high efficiency deep grinding (HEDG). *Int. J. Abras. Technol.* **2,** 154–172 (2009).

19. Ren, Y. H., Zhang, B. & Zhou, Z. X. Specific energy in grinding of tungsten carbides of various grain sizes. *CIRP Ann. - Manuf. Technol.* **58,** 299–302 (2009).

20. Balogun, V. A. & Mativenga, P. T. Impact of un-deformed chip thickness on specific energy in mechanical machining processes. *J. Clean. Prod.* **69,** 260–268 (2014).

21. Sinha, M. K., Kumar, P., Ghosh, S. & Ventakeswara Rao, P. An Improved Model for Specific Energy Estimation in Surface Grinding of Inconel 718. (2015).

22. Ni, J., Yang, Y. & Wu, C. Assessment of water-based fluids with additives in grinding disc cutting process. *J. Clean. Prod.* **212,** 593–601 (2019).

23. Setti, D., Sinha, M. K., Ghosh, S. & Venkateswara Rao, P. Performance evaluation of Ti-6Al-4V grinding using chip formation and coefficient of friction under the influence of nanofluids. *Int. J. Mach. Tools Manuf.* **88,** 237–248 (2015).

24. Kim, H.-J., Kim, N.-K. & Kwak, J.-S. Heat flux distribution model by sequential algorithm of inverse heat transfer for determining workpiece temperature in creep feed grinding. *Int. J. Mach. Tools Manuf.* **46,** 2086–2093 (2006).

25. Guo, C., Wu, Y., Varghese, V. & Malkin, S. Temperatures and Energy Partition for Grinding with Vitrified CBN Wheels. *CIRP Ann. - Manuf. Technol.* **48,** 247–250 (1999).

26. Kim, N. K., Guo, C. & Malkon, S. Heat Flux Distribution and Energy Partition in Creep-Feed Grinding. *CIRP Ann. - Manuf. Technol.* **46,** 227–232 (1997).

27. Ortega, N., Bravo, H., Pombo, I., Sánchez, J. A. & Vidal, G. Thermal Analysis of Creep Feed Grinding. *Procedia Eng.* **132,** 1061–1068 (2015).

28. Cameron, a., Bauer, R. & Warkentin, A. An investigation of the effects of wheel-cleaning parameters in creep-feed grinding. *Int. J. Mach. Tools Manuf.* **50,** 126–130 (2010).

29. Zhang, L., Suto, T., Noguchi, H. & Waida, T. A study of creep-feed grinding of metallic and ceramic materials. *J. Mater. Process. …* **48,** (1995).

30. Uhlmann, E. & Spur, G. Surface Formation in Creep Feed Grinding of Advanced Ceramics with and without Ultrasonic Assistance. *CIRP Annals - Manufacturing Technology* **47,** 249–252 (1998).

31. Upadhyaya, R. P. & Fiecoat, J. H. Factors Affecting Grinding Performance with Electroplated CBN Wheels. *CIRP Ann. - Manuf. Technol.* **56,** 339–342 (2007).

32. Mohamed, A.-M. O., Bauer, R. & Warkentin, A. Application of shallow circumferential grooved wheels to creep-feed grinding. *J. Mater. Process. Technol.* **213,** 700–706 (2013).

33. Bhaduri, D. *et al.* 5 th CIRP Conference on High Performance Cutting 2012 A study on ultrasonic assisted creep feed grinding of nickel based superalloys. **1,** 359–364 (2012).

34. Bhaduri, D. *et al.* Ultrasonic Assisted Creep Feed Grinding of Inconel 718. *Procedia CIRP* **6,** 615–620 (2013).

35. Paknejad, M., Abdullah, A. & Azarhoushang, B. Effects of high power ultrasonic vibration on temperature distribution of workpiece in dry creep feed up grinding. *Ultrason. Sonochem.* **39,** 392–402 (2017).

36. Liao, T. W., Tang, F., Qu, J. & Blau, P. J. Grinding wheel condition monitoring with boosted minimum distance classifiers. *Mech. Syst. Signal Process.* **22,** 217–232 (2008).

37. Furutani, K., Ohguro, N., Hieu, N. T. & Nakamura, T. In-process measurement of topography change of grinding wheel by using hydrodynamic pressure. *Int. J. Mach. Tools Manuf.* **42,** 1447–1453 (2002).

38. Fujimoto, M. & Ichida, Y. Micro fracture behavior of cutting edges in grinding using single crystal cBN grains. *Diam. Relat. Mater.* **17,** 1759–1763 (2008).

39. Yu, T., Bastawros, A. F. & Chandra, A. Modeling Wear Process of Electroplated CBN Grinding Wheel. *Proc. ASME 2015 Int. Manuf. Sci. Eng. Conf.* **1,** 1–7 (2015).

40. Brinksmeier, E. & Werner, F. Monitoring of Grinding Wheel Wear. *CIRP Ann. - Manuf. Technol.* **41,** 373–376 (1992).

41. Yang, Z., Zhang, Z., Yang, R. & Liu, A. Study on the grain damage characteristics of brazed diamond grinding wheel using a laser in face grinding. *Int. J. Adv. Manuf. Technol.* **87,** 853–858 (2016).

42. Malkin, S. & Cook, N. H. The Wear of Grinding Wheels Part 2-Fracture Wear. 3–7 (2016).

43. Ding, W. F., Xu, J. H., Chen, Z. Z., Su, H. H. & Fu, Y. C. Wear behavior and mechanism of single-layer brazed CBN abrasive wheels during creep-feed grinding cast nickel-based superalloy. *Int. J. Adv. Manuf. Technol.* **51,** 541–550 (2010).

44. Shi, Z. & Malkin, S. Wear of Electroplated CBN Grinding Wheels. *J. Manuf. Sci. Eng.* **128,** 110 (2006).

45. Puerto, P., Kirsch, B. & Aurich, J. C. A Comparison of Techniques to Measure the Wear Flat Area of Conventional and Superabrasive Grinding Wheels. **137,** 1–7 (2017).

46. Sutowski, P. & Plichta, S. An investigation of the grinding wheel wear with the use of root-mean-square value of acoustic emission. *Arch. Civ. Mech. Eng.* **6,** 87–98 (2006).

47. Shi, Z. & Malkin, S. An lnvestlgatlon of Grinding with Electroplated CBN Wheels.

48. Chen, X., Rowe, W. B., Mills, B. & Allanson, D. R. Analysis and simulation of the grinding process. Part IV: Effects of wheel wear. *Int. J. Mach. Tools Manuf.* **38,** 41–49 (1998).

49. Furutani, K., Trong Hieu, N., Ohguro, N. & Nakamura, T. Automatic compensation for grinding wheel wear by pressure based in-process measurement in wet grinding. *Precis. Eng.* **27,** 9–13 (2003).

50. Fujimoto, M., Ichida, Y., Sato, R. & Morimoto, Y. Characterization of Wheel Surface Topography in cBN Grindig. *JSME Int. J. Ser. C* **49,** 106–113 (2006).

51. Yu, T., Bastawros, A. F. & Chandra, A. Experimental characterization of electroplated cBN grinding. 1–8 (2014).

52. Badger, J. Factors affecting wheel collapse in grinding. *CIRP Ann. - Manuf. Technol.* **58,** 307–310 (2009).

53. Guo, C., Shi, Z., Attia, H. & McIntosh, D. Power and Wheel Wear for Grinding Nickel Alloy with Plated CBN Wheels. *CIRP Ann. - Manuf. Technol.* **56,** 343–346 (2007).

54. Wegener, K. *et al.* Conditioning and monitoring of grinding wheels. *CIRP Ann. - Manuf. Technol.* **60,** 757–777 (2011).

55. Ghosh, A. & Chattopadhyay, A. K. Experimental investigation on performance of touch-dressed single-layer brazed cBN wheels. *Int. J. Mach. Tools Manuf.* **47,** 1206–1213 (2007).

56. Ghosh, A. & Chattopadhyay, A. K. On Cumulative Depth of Touch-Dressing of Single Layer Brazed cBN Wheels with Regular Grit Distribution Pattern. *Mach. Sci. Technol.* **11,** 259–270 (2007).

57. Kitzig, H., Tawakoli, T. & Azarhoushang, B. A novel ultrasonic-assisted dressing method of electroplated grinding wheels via stationary diamond dresser. *Int. J. Adv. Manuf. Technol.* **86,** 487–494 (2016).

58. Dold, C. *et al.* A study on laser touch dressing of electroplated diamond wheels using pulsed picosecond laser sources. *CIRP Ann. - Manuf. Technol.* **60,** 363–366 (2011).

59. Deng, H. *et al.* A theoretical and experimental study on the pulsed laser dressing of bronze-bonded diamond grinding wheels. *Appl. Surf. Sci.* **314,** 78–89 (2014).

60. Deng, H., Chen, G. Y., Zhou, C., Li, S. C. & Zhang, M. J. Processing parameter optimization for the laser dressing of bronze-bonded diamond wheels. *Appl. Surf. Sci.* **290,** 475–481 (2014).

61. Pfaff, J. *et al.* Laser Touch Dressing of Electroplated CBN Grinding Tools. *Procedia CIRP* **46,** 272–275 (2016).

62. Zhao, Q. & Guo, B. Ultra-precision grinding of optical glasses using mono-layer nickel electroplated coarse-grained diamond wheels. Part 1: ELID assisted precision conditioning of grinding wheels. *Precis. Eng.* **39,** 56–66 (2015).

63. Lu, Y. J., Xie, J. & Si, X. H. Study on micro-topographical removals of diamond grain and metal bond in dry electro-contact discharge dressing of coarse diamond grinding wheel.

Int. J. Mach. Tools Manuf. **88,** 118–130 (2015).

64. Linke, B. & Klocke, F. Temperatures and wear mechanisms in dressing of vitrified bonded grinding wheels. *Int. J. Mach. Tools Manuf.* **50,** 552–558 (2010).

65. Blunt, L. a. & Ebdon, S. The Application of Three-Dimensional Surface Measurement Techniques to Characterizing Grinding Wheel Topography. *Int. J. Mach. Tools …* **36,** 1207–1226 (1996).

66. Butler, D. ., Blunt, L. ., See, B. ., Webster, J. . & Stout, K. . The characterisation of grinding wheels using 3D surface measurement techniques. *J. Mater. Process. Technol.* **127,** 234–237 (2002).

67. Darafon, A., Warkentin, A. & Bauer, R. Characterization of grinding wheel topography using a white chromatic sensor. *Int. J. Mach. Tools Manuf.* **70,** 22–31 (2013).

68. Cui, C. *et al.* Extraction of the grains topography from grinding wheels. *Measurement* **46,** 484–490 (2013).

69. Ye, R., Jiang, X., Blunt, L., Cui, C. & Yu, Q. The application of 3D-motif analysis to characterize diamond grinding wheel topography. *Meas. J. Int. Meas. Confed.* **77,** 73–79 (2016).

70. Bifano, T. G., Dow, T. a. & Scattergood, R. O. Ductile-Regime Grinding: A New Technology for Machining Brittle Materials. *J. Eng. Ind.* **113,** 184 (1991).

71. Zhang, X., Yao, B., Feng, W., Shen, Z. & Wang, M. Modeling of a virtual grinding wheel based on random distribution of multi-grains and simulation of machine-process interaction. *J. Zhejiang Univ. Sci. A* **16,** 874–884 (2015).

72. Kita, Y., Ido, M. & Hata, S. The mechanism of metal removal by an abrasive tool. *Wear* **47,** 185–193 (1978).

73. Wang, H., Subhash, G. & Chandra, A. Characteristics of single-grit rotating scratch with a conical tool on pure titanium. *Wear* **249,** 566–581 (2001).

74. Wang, H. & Subhash, G. An approximate upper bound approach for the single-grit rotating scratch with a conical tool on pure metal. *Wear* **252,** 911–933 (2002).

75. Subhash, G., Loukus, J. E. & Pandit, S. M. Application of data dependent systems approach for evaluation of fracture modes during a single-grit scratching. *Mech. Mater.* **34,** 25–42 (2002).

76. Briscoe, B. J., Delfino, A. & Pelillo, E. Single-pass pendulum scratching of poly ž styrene / and poly ž methylmethacrylate /. 319–328 (1999).

77. Pandit, S. M. & Wu, S.-M. *Time Series and System Analysis with Applications*. (Krieger Pub Co, 2001).

78. Zum Gahr, K.-H. *Microstructure and Wear of Materials*. *Tribology Series 10* (Elsevier, 1987).

79. Patnaik Durgumahanti, U. S., Singh, V. & Venkateswara Rao, P. A New Model for Grinding Force Prediction and Analysis. *Int. J. Mach. Tools Manuf.* **50,** 231–240 (2010).

80. Singh, V., Venkateswara Rao, P. & Ghosh, S. Development of specific grinding energy model. *Int. J. Mach. Tools Manuf.* **60,** 1–13 (2012).

81. Aurich & Steffes. Single Grain Scratch Tests to Determine Elastic and Plastic Material Behavior in Grinding. *Adv. Mater. Res.* **325,** 48–53 (2011).

82. Chen, Z. Z., Xu, J. H., Ding, W. F., Cheng, Z. & Fu, Y. C. High Speed Grinding of Nickel-Based Superalloy with Single Diamond Grit. *Adv. Mater. Res.* **325,** 140–146 (2011).

83. Öpöz, T. T. & Chen, X. Experimental investigation of material removal mechanism in single grit grinding. *Int. J. Mach. Tools Manuf.* **63,** 32–40 (2012).

84. Öpöz, T. T. & Chen, X. Experimental and numerical study on scrtaching test. *Proc. 11th Int. Conf. Manuf. Res.* 461–466 (2013).

85. Rasim, M., Mattfeld, P. & Klocke, F. Analysis of the grain shape influence on the chip formation in grinding. *J. Mater. Process. Technol.* **226,** 60–68 (2015).

86. Akbari, M., Buhl, S., Leinenbach, C. & Wegener, K. A new value for Johnson Cook damage limit criterion in machining with large negative rake angle as basis for understanding of grinding. *J. Mater. Process. Technol.* **234,** 58–71 (2016).

87. Cheng, J., Wu, J., Gong, Y. D., Wen, X. L. & Wen, Q. Experimental study on the single grit interaction behaviour and brittle-ductile transition of grinding with a diamond micro-grinding tool. *Int. J. Adv. Manuf. Technol.* 1–18 (2016). doi:10.1007/s00170-016-9816-5

88. Wang, W. *et al.* Elastic stress field model and micro-crack evolution for isotropic brittle materials during single grit scratching. *Ceram. Int.* **43,** 10726–10736 (2017).

89. P., S. P. A., Arunachalam, N. & Vijayaraghavan, L. Evaluation of grinding strategy for bioceramic material through a single grit scratch test using force and acoustic emission signals. *J. Manuf. Process.* **37,** 457–469 (2019).

90. Steffens, K. & König, W. Closed Loop Simulation of Grinding. *CIRP Ann. - Manuf. Technol.* **32,** 255–259 (1983).

91. Koshy, P., Jain, V. K. & Lal, G. K. Stochastic simulation approach to modelling diamond wheel topography. *Int. J. Mach. Tools Manuf.* **37,** 751–761 (1997).

92. Guo, C. & Malkin, S. Inverse Heat Transfer Analysis of Grinding, Part 1: Methods. *J. Eng. Ind.* **118,** 137–142 (1996).

93. Guo, C. & Malkin, S. Inverse Heat Transfer Analysis of Grinding, Part 2: Applications. *J. Eng. Ind.* **118,** 143–149 (1996).

94. Agarwal, S. & Ventakeswara Rao, P. A probabilistic approach to predict surface roughness in ceramic grinding. *Int. J. Mach. Tools Manuf.* **45,** 609–616 (2005).

95. Gibb, A., St-Jacques, M., Nourry, G. & Johnson, M. A Comparison of Deterministic vs

Stochastic Simulation Models for Assessing Adaptive Information Management Techniques over Disadvantaged Tactical Communication Networks. *7th ICCRTS* 1–16 (2002).

96. Chen, X. & Rowe, W. B. Analysis and simulation of the grinding process. Part I: Generation of the grinding wheel surface. *Int. J. Mach. Tools Manuf.* **36,** 871–882 (1996).

97. Chen, X., Rowe, W. B., Mills, B. & Allanson, D. R. Analysis and simulation of the grinding process. Part III: Comparison with experiments. *Int. J. Mach. Tools Manuf.* **36,** 897–906 (1996).

98. Warnecke, G. & Zitt, U. Kinematic Simulation for Analyzing and Predicting High-Performance Grinding Processes. *CIRP Ann. - Manuf. Technol.* **47,** 265–270 (1998).

99. Nguyen, T. A. & Butler, D. L. Simulation of precision grinding process, part 1: Generation of the grinding wheel surface. *Int. J. Mach. Tools Manuf.* **45,** 1321–1328 (2005).

100. Nguyen, T. A. & Butler, D. L. Simulation of surface grinding process, part 2: Interaction of the abrasive grain with the workpiece. *Int. J. Mach. Tools Manuf.* **45,** 1329–1336 (2005).

101. Aurich, J. C. & Kirsch, B. Kinematic simulation of high-performance grinding for analysis of chip parameters of single grains. *CIRP J. Manuf. Sci. Technol.* **5,** 164–174 (2012).

102. Mohamed, A. M. O., Warkentin, A. & Bauer, R. Prediction of workpiece surface texture using circumferentially grooved grinding wheels. *Int. J. Adv. Manuf. Technol.* **89,** 1149–1160 (2017).

103. Ding, W. *et al.* Stress characteristics and fracture wear of brazed CBN grains in monolayer grinding wheels. *Wear* **332–333,** 800–809 (2014).

104. Sun, D. W. *et al.* Finite element analysis of machining damage in single-grit grinding of ceramic knee implants. *43rd Proc. North Am. Manuf. Res.* **1,** 644–654 (2015).

105. Dai, J., Ding, W., Zhang, L., Xu, J. & Su, H. Understanding the effects of grinding speed and undeformed chip thickness on the chip formation in high-speed grinding. 995–1005 (2015).

106. Www.specialmetals.com. INCONEL® Alloy 718 Data Sheet- Special Metals Company. 1 (2017).

107. Leach, R. *Characterization of Areal Surface Texture*. (2013). doi:10.1007/978-3-642-36458-7

108. Cao, Y. *et al.* Modeling and simulation of grinding surface topography considering wheel vibration. *Int. J. Adv. Manuf. Technol.* **66,** 937–945 (2013).

109. Tuffy, K. & O'Sullivan, M. Abrasive machining of ductile iron with CBN. *Ind. Diam. Rev.* **66,** 33–37 (2006).

110. Uhlmann, E., Borsoi Klein, T. & Koprowski, S. Tilt angle effects in surface grinding with mounted points. *Prod. Eng.* **8,** 431–442 (2014).

111. Uhlmann, E., Koprowski, S., Weingaertner, W. L. & Rolon, D. A. Modelling and Simulation of Grinding Processes with Mounted Points: Part I of II - Grinding Tool Surface Characterization. *Procedia CIRP* **46,** 599–602 (2016).

112. Li, H., Yu, T., Zhu, L. & Wang, W. Analysis of loads on grinding wheel binder in grinding process: insights from discontinuum-hypothesis-based grinding simulation. *Int. J. Adv. Manuf. Technol.* **78,** 1943–1960 (2015).

113. Chakrabarti, S. & Paul, S. Numerical modelling of surface topography in superabrasive grinding. *Int. J. Adv. Manuf. Technol.* **39,** 29–38 (2008).

114. Gong, Y. ., Wang, B. & Wang, W. . The simulation of grinding wheels and ground surface roughness based on virtual reality technology. *J. Mater. Process. Technol.* **129,** 123–126 (2002).

115. Inasaki, I. Grinding Process Simulation Based on the Wheel Topography Measurement. *CIRP Ann. - Manuf. Technol.* **45,** 347–350 (1996).

116. Li, Q., Xu, J., Su, H. & Lei, W. Fabrication and performance of monolayer brazed CBN wheel for high-speed grinding of superalloy. *Int. J. Adv. Manuf. Technol.* **80,** 1173–1180 (2015).

117. Caggiano, A. & Teti, R. CBN Grinding Performance Improvement in Aircraft Engine Components Manufacture. *Procedia CIRP* **9,** 109–114 (2013).

118. Zhao, Q. & Guo, B. Ultra-precision grinding of optical glasses using mono-layer nickel electroplated coarse-grained diamond wheels. Part 2: Investigation of profile and surface grinding. *Precis. Eng.* **39,** 56–66 (2015).

119. Hambi, H., Dursapt, M. & Zohuani, H. Characterization of abrasive grain's behavior and wear mechanisms. *Wear* **254,** 1294–1298 (2003).

120. Blau, P. J. *Friction Science and Technology: from Concepts to Applications*. (2009).

121. Aslan, D. & Budak, E. Surface roughness and thermo-mechanical force modeling for grinding operations with regular and circumferentially grooved wheels. *J. Mater. Process. Technol.* **223,** 75–90 (2015).

122. Thomas, A., El-Wahabi, M., Cabrera, J. M. & Prado, J. M. High temperature deformation of Inconel 718. *J. Mater. Process. Technol.* **177,** 469–472 (2006).

123. Wang, X. *et al.* Dynamic behavior and a modified Johnson–Cook constitutive model of Inconel 718 at high strain rate and elevated temperature. *Mater. Sci. Eng. A* **580,** 385–390 (2013).

124. Lin, Y. C. *et al.* New constitutive model for high-temperature deformation behavior of inconel 718 superalloy. *Mater. Des.* **74,** 108–118 (2015).

125. Rabiey, M. *Dry Grinding with CBN Wheels , The Effect of Structuring*. (2010).

126. Courant, R., Friedrichs, K. & Lewy, H. On the partial difference equations of mathematical physics. *New York* (1959).

127. Johnson, G. R. & Cook, W. H. A constitutive model and data for metals subjected to large strains, high strain rates and high temperatures. *7th International Symposium on Ballistics* 541–547 (1983). doi:10.1038/nrm3209

128. Jafarian, F. *et al.* Finite element simulation of machining Inconel 718 alloy including microstructure changes. *Int. J. Mech. Sci.* **88,** 110–121 (2014).

129. Quinney, H. & Taylor, G. I. The Emission of the Latent Energy due to previous Cold Working when a Metal is Heated. **CLX,** (1937).

130. Taylor, G. I. & Quinney, H. The Latent Energy Remaining in a Metal after Cold Working. *Proc. R. Soc. A Math. Phys. Eng. Sci.* **143,** 307–326 (1933).

131. Shaw, M. C. *METAL CUTTING PRINCIPLES*. *New York* (1984). doi:10.1037/023990

132. Beiss, P., Ruthardt, R. & Warlimont, H. Materials: Powder Metallurgy Data. Refreactory, Hard and Intermetallic Materials. *Powder Metall. Data. Refract. Hard Intermet. Mater.* 118–139 (2005). doi:10.1007/10858641_7

133. D'Evelyn, M. P. & Zgonc, K. Elastic properties of polycrystalline cubic boron nitride and diamond by dynamic resonance measurements. *Diam. Relat. Mater.* **6,** 812–816 (1997).

134. Liu, Q., Roy, A., Tamura, S., Matsumura, T. & Silberschmidt, V. V. Micro-cutting of single-crystal metal: Finite-element analysis of deformation and material removal. *Int. J. Mech. Sci.* **118,** 135–143 (2016).

135. Marinescu, I. D., Rowe, W. B., Dimitrov, B. & Inasaki, I. *Tribology of Abrasive Machining Processe*. (2004).